THE UNIVERSITY OF WARWICK

Electrochemical Characterisation of Single Crystal Boron Doped Diamond

Lucy Inglett Tomlinson

A thesis submitted for the degree of Doctor of Philosophy

Department of Chemistry

August 2012

TABLE OF CONTENTS

LIST OF FIGURES

LIST OF TABLES

ACKNOWLEDGEMENTS

Firstly I am indebted to those who started my belated journey into higher education, thank you Neil Austin for giving me the courage to believe in myself, change things for the better. Without the unconditional support of my A' Level chemistry teacher and now I am proud to say my long term friend - Gary Gray, I would have faltered in my first steps of the journey, thank you for guiding me through UCAS. I must acknowledge Gary's support, encouragement and friendship, thank you for always listening, I will be eternally grateful for everything you have ever done for me.

I must say a huge thank you to my friends and family who have been there for the highs and the lows of undergraduate and postgraduate education, a special mention for; Sally, Abbie, Big Dave, Paul, Huw and Michelle for all the good times shared. Thank you to everyone for keeping me going when it got hard and for always believing in me.

Steve, your love, encouragement and understanding has been wonderful, thank you for being you and keeping me smiling.

Our research group is quite large and diverse, I would like to thank everyone for their help, support and friendship during my time spent at Warwick, special mentions for Hollie, Laura, Mike O'C, Kim, James and Dario, the latter especially for *i-t* curves, we did laugh at our accents.

Finally, I must thank my academic supervisors Professor. Julie Macpherson and Professor. Mark Newton along with my industrial sponsors Element Six Ltd and the EPSRC for this great opportunity and the experiences it gave me.

DECLARATION

The work contained within this thesis is entirely original and my own work, except where acknowledged. I confirm that this thesis has not been submitted for a degree at another university. The Raman spectroscopy mapping and cathodoluminescence in Chapter 3 were performed with James Iacobini. Finite element modelling simulations in Chapter 3 were written by Rob Channon and Dr Hollie Patten who also facilitated some of the programming. Katherine Meadows developed the finite element modelling simulations for intermittent contact-scanning electrochemical microscopy mapping leading to k^0 values reported in Chapter 4 and 6. White light interferometery was performed by Dr Maxim Joseph. The electrodeposition of nanoparticles in Chapter 5 was guided by Dr Petr Dudin.

Parts of the work reported were presented;

L. Tomlinson, L. Hutton, J.V. Macpherson, M. E. Newton, N. Palmer and T. Mollart, *The effect of boron dopant concentration on the electrochemical behaviour of MW-CVD grown single crystal boron doped diamond*, 63rd Diamond Conference, July 2012.

ABSTRACT

Interest and employment of boron doped diamond (BDD) as an electrode material has grown rapidly over the last decade, due to its unique advantageous properties over traditional electrode materials. BDD has minimal background currents and can offer an increased potential range allowing for the detection of an increased range of analytes. Furthermore BDD stability in harsh conditions, elevated temperatures and pressures offers a wealth of applications.

Polycrystalline BDD (pBDD) is commercially available in large wafers for industrial applications. This material is comparatively easy to grow when compared to single crystal BDD (scBDD) which requires careful homoepitaxial growth. This thesis aims to characterise scBDD grown with differing boron dopant densities, crystal orientation and growth procedures; with a view to determining the most suitable scBDD material for employment in electroanalytical applications.

Characterisation is performed using high resolution microscopic and spectroscopic techniques which show sample variations relating to growth parameters. No non-diamond like carbon is detected and boron concentrations are all ~10^{20} cm^{-3} or greater. Electrochemical characterisation is performed using the scBDD in disc electrode format, where wide potential windows, minimal background currents and close to reversible behaviour is observed for outer sphere mediators $FcTMA^{+/2+}$, $IrCl_6^{2-/3-}$ and $Ru(NH_3)_6^{3+/2+}$. Electrode pre-treatments demonstrate the importance of surface termination supporting faster or slower electron transfer kinetics of selected inner sphere mediators.

scBDD was functionalised with gold nanoparticles to aid in sample homogeneity determination, highlighted some heterogeneities as a direct result of a failed growth process. This was performed at both macro and micro scales, giving rise to differing nucleation theories.

Finally electrochemical imaging using scanning electrochemical microscopy is reported, enabling the determination of $FcTMA^{+/2+}$ and $Ru(NH_3)_6^{3+/2+}$ kinetic electron transfer rates at well-defined tip-substrate distances.

ABBREVIATIONS

AFM	atomic force microscopy
atm	atmospheres
BDD	boron doped diamond
bpy	bipyridine
CE	counter electrode
CH-SECM	constant height-scanning electrochemical microscopy
CL	cathodoluminescence
CM-AFM	contact mode-atomic force microscopy
C_{meas}	capacitance
CNTs	carbon nanotubes
CV	cyclic voltammetry / current-voltage
CVD	chemical vapour deposition
DAQ	data acquisition
DICM	differential interference contrast microscopy
E6	Element Six Ltd
ET	electron transfer
FE-SEM	field emission-scanning electrochemical microscopy
FEM	finite element modelling
GC	glassy carbon
H-terminated	hydrogen terminated
HET	heterogeneous electron transfer
HFCVD	hot filament chemical vapour deposition
HOPG	highly orientated pyrolytic graphite
HPHT	high pressure-high temperature
IC-SECM	intermittent contact-scanning electrochemical microscopy
LDOS	local density of states
MCEM	microcapillary electrochemical method
MWCVD	microwave assisted chemical vapour deposition
NPs	nanoparticles
O-terminated	oxygen terminated
pBDD	polycrystalline boron doped diamond
ppm	parts per million
RE	reference electrode
RMS	relative mean square
sc	single crystal
SCE	saturated calomel electrode

scBDD	single crystal boron doped diamond
SECM	scanning electrochemical microscopy
SEM	scanning electron microscopy
SG-TC	substrate generation-tip collection
SH	Scharifker and Hills
SICM	scanning ion conductance microscopy
SIMS	secondary ion mass spectrometry
TM-AFM	tapping mode atomic force microscopy
UME	ultra micro electrode
WE	working electrode
XPS	x-ray photoelectron spectroscopy

GLOSSARY OF TERMS

a	radius of electrode
A	area of electrode
A_w	atomic weight
[B]	boron concentration / cm^{-3}
c, c*, c_j	concentration
C	double layer capacitance
CB	conduction band
d	tip-substrate separation
D, D_j	diffusion coefficient
E	potential
E_A	acceptor level
E_C	conduction band
E_F	Fermi level
E_{fb}	flat band potential
E_s	substrate bias
E_t	tip bias
E_V	valence band
E°'	formal potential
E_0	incident energy
$E_{½}$	half wave potential
F	Faraday constant
h	height
i	current
i_b	current-backward sweep
i_f	current-forward sweep
i_{lim}	limiting current
i_m	maximum current
i_p	peak current
i-t	current - time
j	active species
J_j	flux
k_b	backward rate constant
k_f	forward rate constant
k_t	heterogeneous rate constant
k^0	standard rate constant
l	length

$\underline{n}$	inward pointing vector
n	number of electrons
N_{oj}	total flux
O	oxidised species
r	radial direction
R	gas constant / reduced species
rg	ratio of glass
RG	ratio of insulating material to conducting
R_j	reaction rate
r_t	tip radius
s	seconds
T	temperature
t	time
t_{dep}	deposition time
t_m	maximum time
V	potential / velocity vector
VB	valence band
V_{dep}	deposition potential
Z	atomic number
z	coordinate
z_j	charge on species
α	transfer coefficient
ΔE_p	peak to peak separation
η	overpotential
φ	electrostatic potential
π^*	anti-bonding orbital
ρR	mass range
ν	sweep rate
χ	function of RG

1 Introduction

1.1 INTRODUCTION TO BORON DOPED DIAMOND

The first diamond stones were discovered in India ~ 2700 years ago and were used in commerce.[1] Jewellery using diamonds came a few centuries later followed by faceting and polishing techniques which were developed in the 14th-15th century[1] thereby exposing diamonds true natural beauty. The fascination with diamond originally stemmed from its gemstone perspective, but also because diamond has extraordinary physical and chemical properties. Numerous reviews[2] detail the properties of diamond which include the highest thermal conductivity at room temperature (2×10^3 W m^{-1} K^{-1}), its optical transparency and resistance to chemical corrosion. As such diamond has found a myriad of uses both in the intrinsic state and doped form; for example cutting tools,[3] X-ray windows[3] and electrochemical sensors.[4]

1.1.1 Diamond Synthesis

In 1772, Lavoisier[5] proved that diamond was an allotrope of carbon and due to the rarity of natural diamonds various methodologies have been developed to synthesise this material. Thereby increasing its usability significantly, both from an availability and cost perspective. Synthetic diamonds are grown with a specific use in mind, with control over doping levels (if applicable), size and morphology leading to designer properties and applications. There are many techniques used to grow synthetic diamond, however the two most common methods are high pressure-high temperature (HPHT) and chemical vapour deposition (CVD).

Natural diamonds are formed at extremely high temperature and pressures deep within the earth's crust which over time, through plate tectonics, travel towards the earth's surface and are mined.[5] This knowledge was used during the development of the industrialised HPHT growth technique. The HPHT method has been used for decades to produce industrial diamonds suitable for cutting, machining, polishing and grinding given their small size.[6]

The HPHT growth method compresses graphite in the presence of a metal catalyst solvent,[7] in a hydraulic press (as shown in Figure 1.1) to tens of thousands of atmospheres (atm), simultaneously heated to over 1700 °C until diamond crystals form.[2] Extraordinary growth control is needed to produce large (> 1 carat) single crystal (sc) HPHT diamond, with comparatively few defects or impurities.[8]

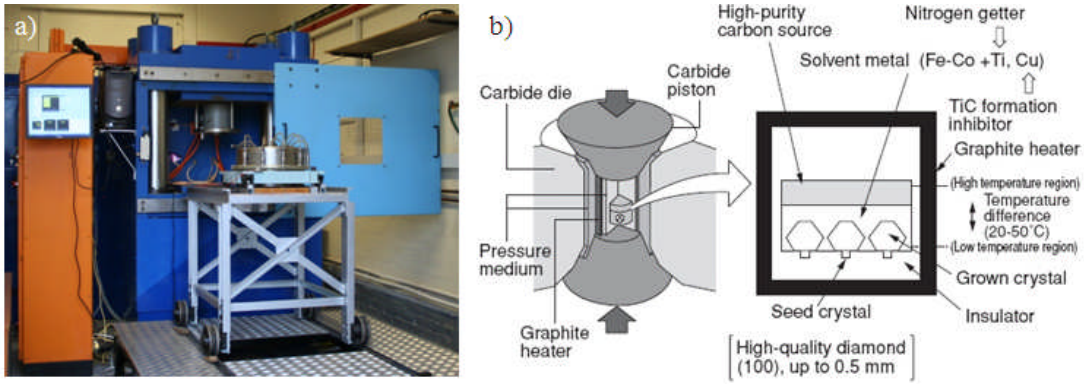

Figure 1.1. a) Photograph of the HPHT press used by the Warwick Diamond Research Group, constructed by Element Six Ltd and donated by the Diamond Trading Company Research Centre, Maidenhead. b) Schematic of a HPHT press.[9]

The press shown in Figure 1.1a can reach temperatures of ~3000 °C and operate at hydrostatic pressures up to ~1 million atm. Diamonds grown using the HPHT method are usually in the range nanometres to millimetres in size, which can

limit their industrial application, hence alternative growth methods, which allow more of diamonds unique properties to be exploited, have been explored.[2]

In 1962, Eversole[10] discovered that diamond could be deposited on a substrate using a hydrocarbon or carboxyl containing gas via CVD, at low temperatures and pressure where diamond is metastable with respect to graphite. This process however only produced low yields of diamond. Angus *et al.* later found that the use of atomic hydrogen lead to reduced graphitic carbon deposition therefore higher growth rates of diamond.[11] Extensive research has now been performed using CVD to grow larger quantities of diamond material.

CVD is a chemical process that produces high purity solid materials. It is used to make ultra-thin films in the semiconductor industry in addition to the growth of synthetic diamonds.[12-14]Typically, the substrate (wafer) is exposed to at least one volatile precursor which decomposes and/or reacts on the substrate surface to generate the required product. The CVD process can deposit materials in many forms including, sc, polycrystalline and amorphous carbon morphologies.[15-17] The growth of diamond via CVD has been subject to extensive global research,[18] and there are numerous reviews summarising efforts towards improving CVD diamond quality and respective growth rates.[19-25] A schematic of two different CVD reactor chambers is shown in Figure 1.2.

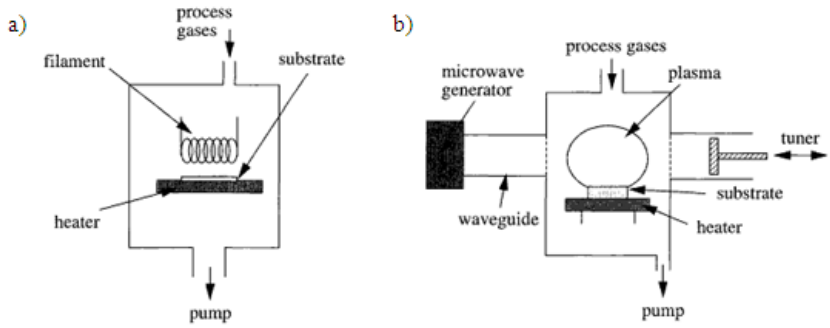

Figure 1.2. a) Schematic of a hot filament CVD reactor chamber and b) NIRIM microwave plasma CVD reactor.[2]

Several types of diamond CVD processes are regularly used, most of them involving carbon containing gases of a low percentage (0.5 - 5 %) in hydrogen. Integration of a desired dopant e.g. boron or nitrogen into diamond is performed by the introduction of this material in the gas phase e.g. diborane, boron trioxide,[26] diborane,[27] trimethyl borane,[28] tripropyl borate[28,29] and boron nitride,[28] nitrogen.[30-32]The boron doped diamond (BDD) materials characterised during this study were grown using diborane. Initiation of the gas phase can be achieved in two ways using a hot filament[33] or a microwave reactor.[34]

Hot filament CVD (HFCVD) uses a metal filament (usually Ta or W) which is heated above 2000 °C to enable chemical activation of the gas phase with the substrate heated in the range 650-900 °C. Gas pressure within the growth chamber is ~15,000-23,000 atm, resulting in planar or 3D diamond films with relatively low costs.[35] Disadvantages of this growth method include a limited number of gas combinations because oxygen and halogen containing gases aggressively destroy the metal filament.[36] Degradation of the metal filament is highly likely to result in contamination.

A more commonly used CVD method for the synthesis of diamond is microwave plasma CVD (MWCVD); here the microwave creates a discharge starting a chain reaction whereby the energy couples to gas phase electrons which then pass energy to surrounding gas molecules to create the plasma. High microwave powers up to 5 kW and high growth rates (> 10 μm per hour) can be achieved with MWCVD, also a range of gas combinations can be employed. Applying a potential to the substrate increases nucleation and subsequent growth rates.[37] When compared to HFCVD, contamination such as amorphous carbon[22] is greatly reduced hence the diamond is of higher quality. All diamond used herein was grown using MWCVD.

A highly important factor in diamond synthesis is the substrate on which growth occurs. Considerations such as pre-treatments, orientation, melting point, thermal expansion and how easily it forms carbide bonds all effect the resulting diamond quality and growth rates.[2] Diamond growth via MWCVD and HFCVD has been achieved on a variety of substrates including Si,[38,39] Cu,[40,41] W[41,42] and diamond.[43-46]

Growth of diamond via CVD is a complex chemical process which has been intensely studied[47] and has led to the discovery of several key principals.[47-50] In particular, activation of the gas phase has two functions. Energy provided to the carbon and boron gaseous species cause fragmentation of these molecules into electrons, ions and radicals.

These active species continually mix and react until hitting the surface of the substrate where they either adsorb/desorb or react with the surface. Activation breaks down hydrogen gas into atomic hydrogen which is important for several reasons: (i) Hydrogen atoms react with source gas hydrocarbon species creating radicals (e.g. CH_3•), these in turn react with the substrate surface. (ii) The diamond surface is

stabilised via bonding hydrogen atoms which can be abstracted and replaced by carbon containing species during the growth phase. (iii) Atomic hydrogen creates reactive sites on the diamond surface via the removal of hydrogen from CH sites, thereby aiding carbon lattice incorporation.(iv) atomic hydrogen is capable of etching sp and sp^2 carbon at much faster rates than sp^3, thereby removing graphitic clusters, leaving sp^3 diamond behind.[11]

Despite the complex chemical processes occurring CVD diamond growth, it is relatively insensitive to the carbon source gas,[51] such that similar results are seen when either C_2H_2 or CH_4 is used. This is because both gases suffer from degradation into the CH_3• radical, essential for diamond growth.

1.1.2 Diamond Structure, Orientations and Doping

Diamond is a cubic polymorph of carbon[52] and forms a tetrahedral bonded network[53] as shown in Figure 1.3.

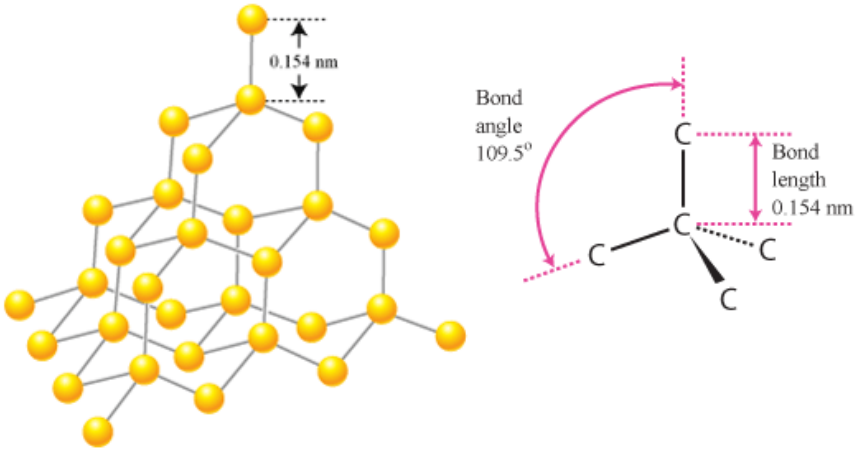

Figure 1.3. The structure of the diamond crystal lattice showing the tetrahedrally coordinated carbon atoms and bond angles.[54]

The fundamental properties of diamond can be attributed to the single σ bonds (0.154 nm) binding the carbons along the (111) orientation.[52] Figure 1.4 shows the lowest index crystallographic planes (orientations) of diamond; single crystal boron doped diamond (scBDD) characterised herein were of (100), (110) or (111) orientation.

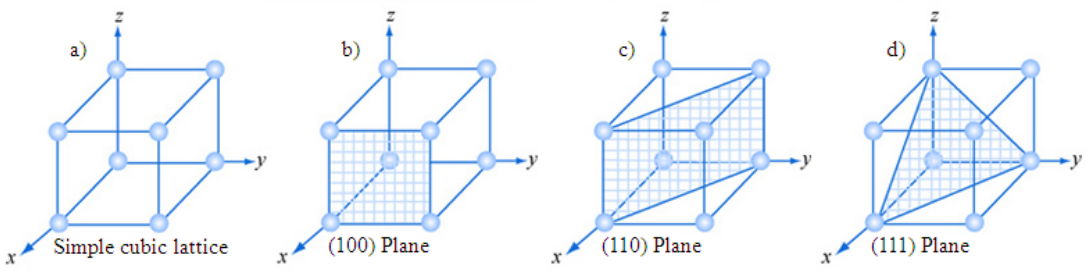

Figure 1.4. Schematic illustrations of the three lowest index crystallographic ordinations in diamond stemming from a) simple cubic lattice, b) (100), c) (110) and d) (111).[55]

Boron is readily incorporated into the diamond lattice during growth and randomly replaces carbon within the dense diamond lattice. As boron is one electron deficient compared to carbon, boron incorporation creates an acceptor level of 0.37 eV[56] above the valence band as shown in Figure 1.5. Electrons are promoted from the valence band to the acceptor level leaving behind a mobile positive charge, called holes.[57] The concentration of boron atoms ([B]) required to establish metal-like conductivity is thought to be [B] ~1 × 10^{20} cm^{-3} *i.e.* 1 boron atom per 1000 carbon atoms;[58,59] this has been achieved using trimethylboron concentrations of several thousand parts per million (ppm) in the gas phase of CVD.[60]

Natural BDD exists, however it is extremely rare[61] and usually has very low [B], typically <$10^{17}$$cm^{-3}$ hence it's use traditionally as gemstones due to the beautiful blue colour that results.

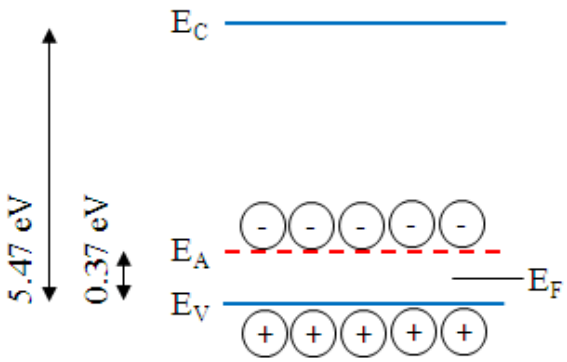

Figure 1.5. Band structure for diamond showing intrinsic bandgap of 5.47 eV and the acceptor level at 0.37 eV of p-type semiconducting diamond. Where E_C is the conduction band, E_A the acceptor level, E_F the potential of the Fermi level and E_V the valance band (not to scale).

The BDD resistivity depends on concentration of incorporated boron as shown in Figure 1.6.[59] In lowly doped diamond where [B] is $< 10^{19}$ cm^{-3}, the material is p-type semiconducting. At a sufficient [B] hopping conduction is possible as the wave functions of neighbouring boron atoms overlap such that an impurity band arise, which correlates to a reduction in the activation energy.[62,63] This is referred to as moderate doping and has demonstrated diamond resistivities of $\sim 2 \times 10^3$ Ω cm. At high enough [B] $\sim 1 \times 10^{20}$ cm^{-3}, the activation energy falls to zero and metal-like conductivity is initiated,[64] with resistivities of ≤ 0.1 Ω cm. However the exact nature of the electrical conductivity in BDD is still under investigation.[65-67]

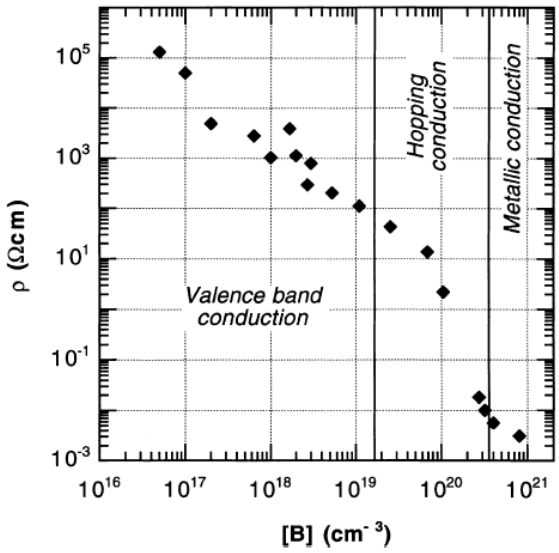

Figure 1.6. Room temperature resistivity of scBDD as a function of [B].[59]

1.1.3 Single Crystal Diamond Growth

Sc diamond growth is homoepitaxial, therefore the substrate employed for growth is either a natural[68-70] diamond or one grown using the HPHT technique,[8,71,72,73] of a specified crystal orientation. Orientations employed include (100), (110) and (111)[68,70,74] and are shown in Figure 1.4. The HPHT grown substrate is typically limited to 'defect free' material ~6 × 6 mm in size[2,75] this in turn limits the subsequent size of sc material grown.

Both HFCVD[68-70] and MWCVD[71,72,75-78] sc growth is reported in literature, less so for HFCVD for reasons already stated relating to contamination. Common sc MWCVD growth parameters utilise pressures of 0.1-0.5 atm and substrate temperatures of 800-1100°C,[71,72,75-81] leading to typical growth rates of ~1 μm/h.[74] Numerous factors affect the deposition of diamond, it is a fine balance between maintaining material quality with a reasonable growth rate. These factors include; substrate temperature,[71,76,77,78] chamber pressure,[82] methane[71, 78]/oxygen content[82]

and microwave power.[72,74,83] The addition of boron during the growth process only adds to the many factors involved when growing synthetic diamond.

The majority of MWCVD studies use (100) or (111) sc orientations, although (110) growth has been reported with HFCVD, but this generally has a rough surface with low crystalline quality.[69,74,84,85] The (100) orientation is generally considered to be of a higher crystalline quality when compared to both (110) and (111) however the growth rate is reduced.[69,70,74,84] In addition, the slower growth of (100) reduces the concentration of incorporated impurities such as boron, therefore (100) will have a lower incorporated impurity concentration when compared to both (111) and (110) scBDD.[86] The differences in growth of sc orientations can be explained by their growth mechanisms;[69] growth on the (100) and (111) proceeds via steps travelling laterally over the surface whereas direct integration of growth occurs on (110).

Ushizawa *et al.*[79] used MWCVD to simultaneously grow BDD of (100) and (111). At B:C ratios 60 ppm, (100) growth was observed and as the B:C increased to 80 ppm the (111) crystals began growing. At 200 ppm both orientations were found in equal distributions, beyond this the (111) orientation dominated. When B:C was 5500 ppm, the (111) dominated and the (100) had all but disappeared. Furthermore the [B] of these crystals were measured using secondary ion mass spectrometry (SIMS). From B:C 400 ppm upwards, there was a factor difference in the incorporated [B], where (111) contained higher [B].[79,87] The higher boron incorporation within scBDD (111) (when compared to (100)) has been reported by others[88] including Janssen *et al.*[68] suggesting (111) incorporation is at least ten times higher than (100). The trend relating to boron incorporation within scBDD films was also observed for HFCVD grown samples where it was reported that the (110) offered a higher incorporation efficiency than (100).[69]

1.1.4 Polycrystalline *vs*. Single Crystal Boron Doped Diamond Growth

While this thesis focuses on scBDD electrochemistry, the most common form of diamond electrode being used are polycrystalline in nature and are used as a comparison in this work. It is therefore important to note differences in growth between these materials, a key example being the growth substrate employed. For polycrystalline growth, Si is typically used[89] often using 4" wafers and the substrate scratched with diamond powder to initiate diamond thin film growth. As stated in 1.1.3 different crystal orientations take up boron differently, hence polycrystalline BDD (pBDD) is a heterogeneously doped material.[68,90]

Faster growing orientations ((111) and (110)) overlap with slower growing orientations. This leads to a film containing a smaller number (than the nucleation layer) of larger grains forming as shown in Figure 1.7a.[18] The pBDD surface once grown appears rough in texture as is seen in Figure 1.7b. pBDD can be grown with a range of final morphologies, microcrystalline,[91] nanocrystalline[39] and ultrananocrystalline,[39] the pBDD used herein was microcrystalline BDD.

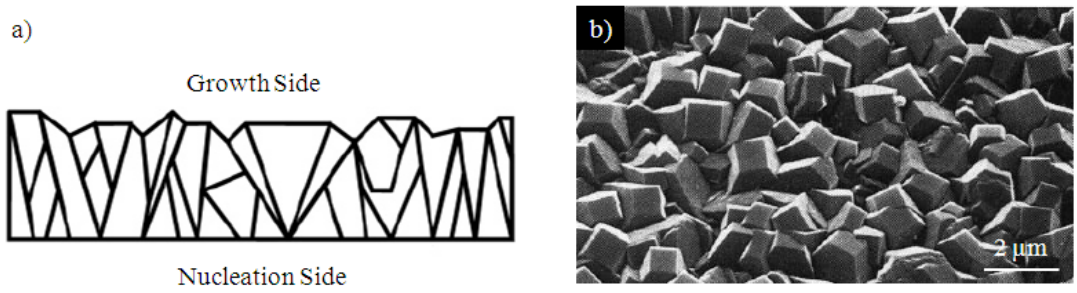

Figure 1.7. a) Schematic showing the growth of a thick polycrystalline film[92] and b) scanning electron microscopy image of as grown pBDD.[38]

1.1.5 Diamond Surfaces; Processing and Termination

In order to bring out natural diamond facets to reflect the most light, referred to as gemstones 'brilliance',[93] polishing is performed. The same applies for CVD grown material in order to give smooth surface finishes. sc material is polished using a cast iron scaife, this is a rotating cast iron disc ~0.3 m diameter and ~20 mm thick which is loaded with diamond grit (~1 to 20 μm) in pre-machined radial grooves/pores formed during the sand blasting of the cast iron.[94] Diamonds are mounted in a holder (tang) and the diamonds pressed into this surface whilst the disc rotates. The wear rate is wholly dependent on crystal orientation[95] with (100) considered softer therefore wearing faster. (110) and (111) are described as hard orientations therefore take longer to wear. Gemstone polishing requires extreme skill and takes many years of training.

A secondary influence (after boron doping) on the electrical properties of diamond is surface termination. The as grown diamond surface is hydrogen (H) terminated due to the hydrogen atmosphere present during the CVD process,[89] and as such the surface is hydrophobic. This termination is stable in air for several months, although over time (10-30 days) there is some evidence of gradual oxidation[96,97] resulting in a mixed surface termination. Polishing of BDD to achieve a smooth surface finish also removes the H-termination. The H-terminated surface can be regenerated by subjecting the material to a hydrogen plasma.

Interestingly, H-terminated BDD displays metal-like electrochemical behaviour, even at low boron doping densities ~ 7×10^{18} cm^{-3}.[98] This is thought to be due to the H-termination layer providing an additional surface conductivity and this

is why intrinsic diamond has an electrical signature, an area widely researched by Ristein[99-101] and Garrido.[102,103]

Ristein *et al.* suggested that the H-terminated intrinsic diamond (donor like) becomes susceptible to transfer doping where the holes are injected by acceptors located at the surface instead of from within the diamond lattice.[99] Tsugawa *et al.*[104] suggested the carriers are holes within an accumulation layer at the surface, supported by Ristein *et al.*[100]

At room temperature conditions, everything has a thin layer of water present on its surface, within this layer CO_2 is dissolved thereby giving H_3O^+ and HCO_3^- ions. Due to the electron negativity of H-terminated diamond surfaces these ions act as electron acceptors creating a layer of holes at the diamond surface as shown in Figure 1.8.[100]

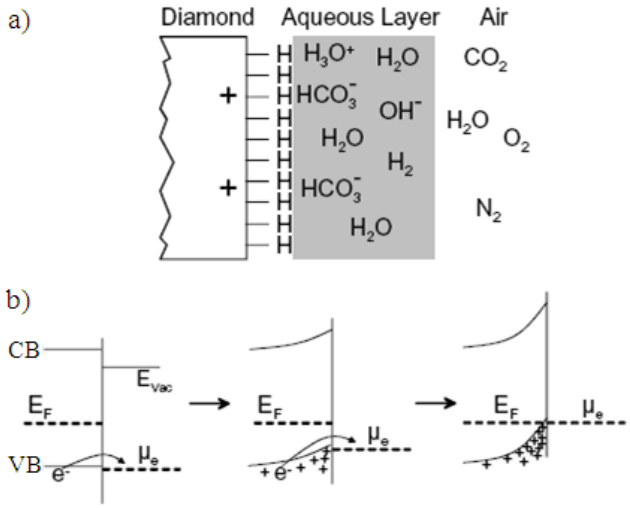

Figure 1.8 a) Schematic of H-terminated diamond surface in contact with an aqueous layer as it forms in air. b) Development of band bending during the electron transfer process at the interface between diamond and the aqueous layer. CB and VB represent the conduction and valance band respectively and E_F the Fermi level.[100]

From an electrochemical view point, oxygen (O) terminated diamond substrates offer increased stability in air, solution and under potential control. Advantageously the hydrophilic nature of the oxygenated surface is likely to facilitate electron transfer in aqueous solutions. Numerous procedures for the O-termination of diamond have been described including exposure to oxygen plasma,[39] reactions with oxygen at high temperatures,[105] photochemical oxidation,[106] anodic polarisation[107,108] and boiling in acid.[109]

Carbon itself is more electronegative than hydrogen as a surface terminating species, therefore hydrogenation of the diamond surface lowers the electron affinity[110,111](-1.3 eV) due to the polarity of the heteropolar surface bonds. Contrastly, O-termination increases the electron affinity (+1.7 eV) due to oxygen's large electronegativity (only surpassed by fluorine).[110-112] Ristein concluded that by using hydrogen or oxygen, the ionization energy and electron affinity of diamond surfaces could be varied by 3.0 eV.[99]

Additionally, the type of surface termination is able to initiate changes in the surface electronic band structure.[113] The transfer of charge carriers can be facilitated between the bulk diamond and states at the surface. This causes band bending and a space charge layer which can stretch into the bulk diamond up to several hundred nanometres. The method of diamond termination influences the resulting surface termination and the surface states, this in turn affects the band structure. The flatband potential (E_{fb}) of semiconducting H-terminated pBDD has been reported in the range 0-0.75 V *vs.* saturated calomel electrode (SCE)[105,114] whereas O-terminated semiconducting BDD is thought to lie in the range 1-4 V *vs.* SCE.[105, 115, 116]

X-ray photoelectron spectroscopy (XPS) has been employed to investigate the functional groups on diamond surfaces, typical spectra are shown in Figure 1.9 for both H and O-terminated pBDD.

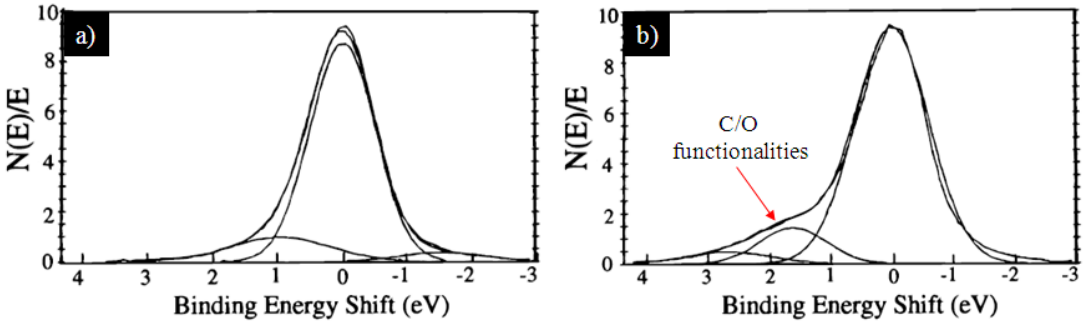

Figure 1.9. Carbon 1s XPS spectra of the same semiconducting pBDD when a) H-terminated (via hydrogen plasma treatment) and b) O-terminated (via electrochemical oxidation of 1.5 V for 10 minutes in 0.1 M KH_2PO_4).[117]

O-terminated pBDD as shown in Figure 1.9b shows carbon-oxygen functionalities, these include hydroxyl (C-OH), ether (C-O-C) and carbonyl groups (C=O).[117,118] XPS data of sc diamond suggests that (111) orientation is dominated by C-OH groups, whilst C-O-C and C=O groups are in abundance on the (100) crystal face,[45,113] as shown schematically in Figure 1.10.

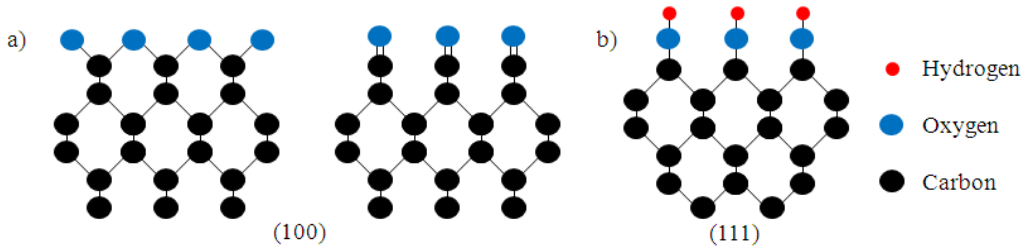

Figure 1.10 Schematic of the possible O-terminated surfaces of different orientations of diamond a) (100) and b) (111) as suggested by XPS.[45, 113,117, 118]

1.1.6 Raman Spectroscopy of Diamond Materials

Raman spectroscopy can provide details on the different carbon forms, graphitic, amorphous or diamond and is routinely employed to determine diamond quality.[119] Commonly used laser wavelengths for the analysis of diamond are of 514 nm and 633 nm, these incident beams lead to weakly inelastically scattered photons and phonons.

For intrinsic diamond, the phonon at the Brillouin zone centre is at 1332.5 cm^{-1}, which is related to sp^3 (tetrahedral) bonds found in diamond. This is also referred to as the 'zone centre peak optical phonon line' or the 'D' band and is symmetrical for intrinsic diamond. When analysing diamond material, two other key wavenumbers are 1580 cm^{-1} for graphitic carbon (the 'G' band) and 1500 cm^{-1} for amorphous carbon.[52]

As [B] increases beyond 1×10^{20} cm^{-3} a Fano resonance is observed *i.e.* asymmetry of the original zone centre phonon peak at 1332.5 cm^{-1}.[120] The peak can also decrease in energy, thereby shifting wavenumber and a distortion is easily seen by way of a peak shoulder combined with peak attenuation.[120]

Additional (wider) features on the spectra are sometimes observed as seen in Figure 1.11 when [B] is metal-like. It is thought that the disorder and intraband optical transitions are responsible for the origin of the peak at ~500 cm^{-1}.[121] The 1200 cm^{-1} broad peak is believed to be related to disorder in the diamond lattice and as the [B] increases, the lattice becomes more disordered. Generally [B]> 5×10^{21} cm^{-3} is no longer 'diamond' due to its lack of resemblance to the original intrinsic diamond lattice however the diamond phase has been reported in pBDD with[B] of at least 8×10^{21} cm^{-3}.[122] The majority of relevant research in the

field of diamond quality and the investigation of [B] have analysed synthetically grown pBDD.

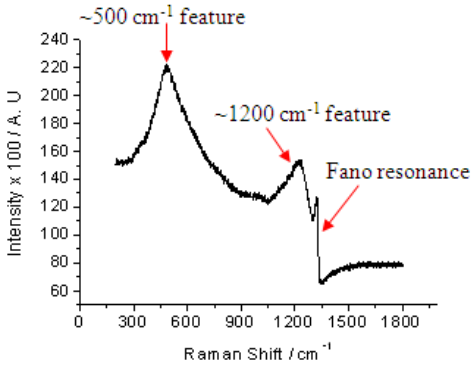

Figure 1.11. Raman spectra of scBDD excited using 633 nm laser, note the peaks at ~500 and 1200 cm^{-1}. The Fano resonance indicates the sample is heavily doped with [B] ≥ 1 × 10^{20} cm^{-3}.

Pruvost *et al.* reported the Raman characterisation (514 nm) of (001) scBDD films grown via MWCVD with [B] ~3 – 8 × 10^{20} cm^{-3}.[120] It was observed that asymmetry of the zone centre phonon peak appeared when the B:C ratio in the gas phase reached 1615 ppm shown in Figure 1.12a. At higher [B], additional graphitic bands were observed at 1350 and 1580 cm^{-1} [120] as shown in Figure 1.12b.

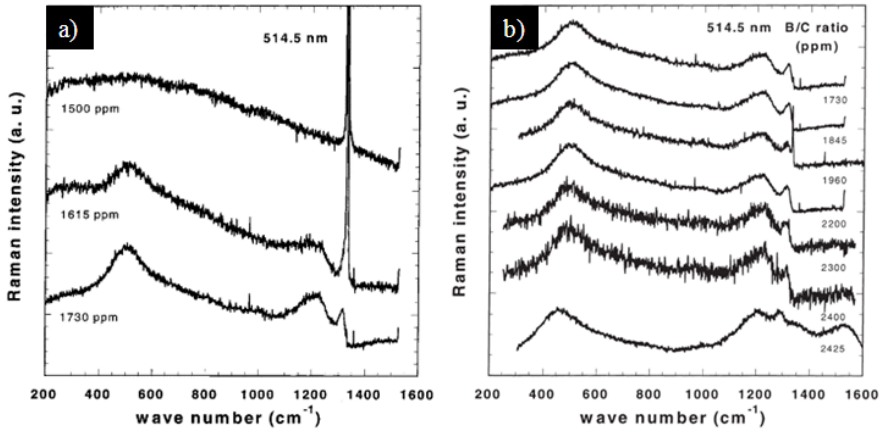

Figure 1.12 514 nm Raman spectra at room temperature of scBDD (001) films deposited using a range of B:C ratios in the MWCVD gas phase a) B:C 1500-1730 ppm and b) B:C 1730-2425 ppm.[120]

Szunerits *et al.*[123] employed Raman spectroscopy to characterise MWCVD grown pBDD ([B] 5×10^{20} cm^{-3}). The research concluded that the pBDD films contained a mixture of microcrystals with different doping levels *i.e.* metal-like and semiconducting in the range [B] high 10^{19} (lighter regions) to high 10^{20} cm^{-3}(darker regions) when analysed using scanning electron microscopy (SEM).The study also employed Raman mapping to qualitatively reveal differences in [B] across the sample, integrating line intensity of diamond (1332 cm^{-1}) and amorphous carbon (1550 cm^{-1}).

Raman mapping was also reported by Patten *et al.*[124] on MWCVD pBDD [B] ~5×10^{20} cm^{-3} where maps were constructed by integrating the area under diamond peak at 1332 cm^{-1} on a pixel by pixel basis. As [B] increases the area under the peak decreases enabling areas of high and low [B] to be identified. There are no reports of Raman mapping using scBDD samples in available literature, this technique would serve to highlight the homogeneity of scBDD samples.

1.2 ELECTROCHEMISTY OF BORON DOPED DIAMOND

1.2.1 Dynamic Electrochemistry

Dynamic electrochemistry investigates the transfer of electrons between an interface of an electrode (commonly metallic) and any chemically active redox species in solution, under non-equilibrium conditions.[125] At the interface, two types of processes can occur, non-faradaic and faradaic. A non-faradaic process can arise when a change in the solution/electrode surface causes a current to flow without facilitating charge transfer across to the electrode. The most common non-faradaic process is electrical double layer capacitance, which requires consideration when interpreting electrochemical reactions.[125,126]

A faradic current flows when a potential is applied to the electrode to promote oxidation or reduction of a redox species of interest. Consider the simple reversible one electron heterogeneous electron transfer (HET) reaction given by equation 1.1 where *n* is the number of electrons transferred and *O*, *R* the oxidised and reduced species.

$$O + ne^- \leftrightarrow R \qquad \textbf{(1.1)}$$

A schematic representation of a typical faradic electrochemical reaction at an electrode reaction can be seen in Figure 1.13. Here the interplay between HET kinetics and rates of mass transport (reactants/products) to the electrode play a role in determining the current-voltage (CV) response of the electrode.[125,127]

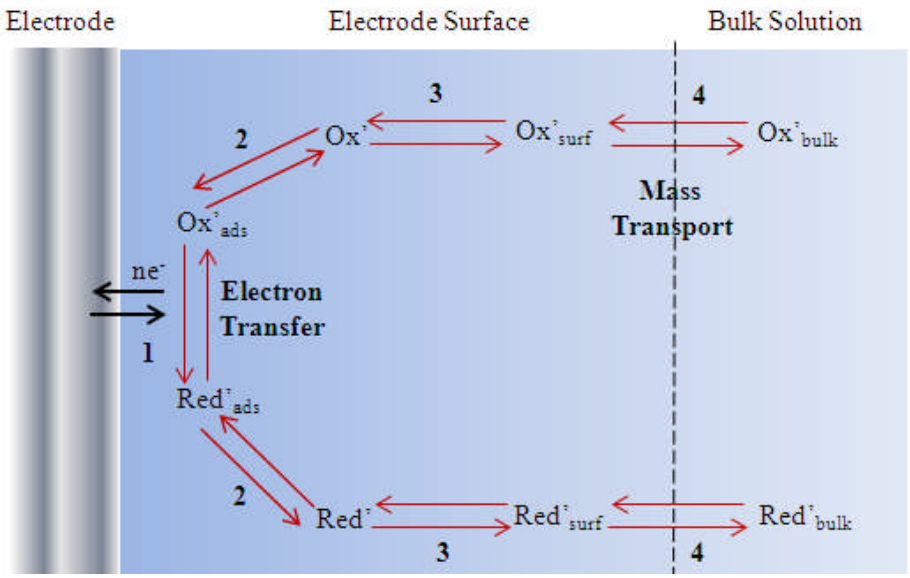

Figure 1.13. Schematic detailing the processes that potentially occur at the surface of an electrode. (1) HET across the interface; (2) adsorption/desorption surface reactions; (3) chemical reactions pre/post HET and (4) mass transport of electroactive agent from the bulk solution to/from the surface of the electrode.[125]

The rate determining step of an HET reaction is governed by the slowest step in the overall reaction scheme, which for most electrochemical systems involving fast outer sphere ET redox couples, is the rate of mass transport.[127]

Mass transport considers three factors; migration, diffusion and convection which contribute towards the movement of chemical species within a solution towards an electrode surface and can be described using the Nernst Planck equation (equation 1.2).[125]

$$J_j = -D_j \nabla c_j + c_j V - \frac{z_j F}{RT} D_j c_j \nabla \varphi \qquad \textbf{(1.2)}$$

where J_j is the flux (described as the number of moles per unit area per unit time) of species j to/from the electrode, D_j is the diffusion coefficient of species j, c_j is the concentration of species j, V is the velocity vector, z_j is the charge on species

j, F is Faraday's constant, R the gas constant, T the temperature and φ is the electrostatic potential.

Migration is the movement of ions within solution under the influence of an electric field, this aspect of mass transport can be reduced to a minimum due to the addition of an inert supporting electrolyte, usually in excess (> 100 times)[127] of the redox mediator of interest. This excess supporting electrolyte reduces ohmic drop in the solution[128]and reduces the size of the electrical double layer.

Diffusion is ascribed to the movement of species through a solution due to the difference in concentration of the active species at the electrode surface and the bulk solution. Diffusion always operates in any dynamic electrochemical process.

Convection occurs by heating, stirring, bubbling or pumping the solution.[127] Over long time frames convection can occur naturally due to concentration gradients[127] or convection can be forced specifically with the intention of increasing mass transport in the system in order to quantify HET.[127]

Butler-Volmer[125] kinetics shown in equation 1.3 are commonly used to describe HET at the electrode/solution interface.

$$k_{\mathrm{f}} = k^{0}\exp\left[-\alpha\eta F/RT\right] \qquad \textbf{(1.3)}$$

Where k_{f} describes the rate of the potential dependant forward reaction. k^{0} is the standard rate constant, α the transfer coefficient and η the overpotential.

HET processes can be described as either inner or outer sphere as shown in Figure 1.14. During outer sphere HET, the reactant and product do not strongly interact with the electrode surface, they are generally thought to be at least a solvent

layer distance away from the electrode.[125] In contrast, inner sphere redox processes involve direct interaction of the species with the electrode surface, in order to transfer electrons. Therefore special consideration must be given to the surface chemistry of the electrode in relation to the binding ligands of the redox species.[129]

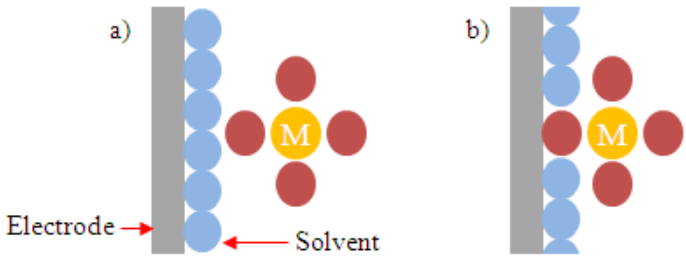

Figure 1.14. Schematic of a) outer and b) inner sphere HET reactions where the metal ion (M) is surrounded by ligands whereas in b) a ligand absorbs onto the electrode surface facilitating ET.

1.2.2 Cyclic Voltammetry (CV)

CV is a simple yet highly effective electrochemical technique employed to examine the HET characteristics of a redox species with respect to a particular electrode material. The majority of experiments control the potential of an electrode, which is in contact with the desired analyte, whilst measuring the resulting current.[125] In order to perform a voltammetric experiment, at least two electrodes are required, a working electrode (WE) to which a controlled potential is applied in order to facilitate ET between the redox species and the electrode. The other electrode (reference, RE) must have a known and constant potential in all solutions and acts to complete the circuit. Examples of REs include Ag|AgCl and SCE. When passing a large current ohmic drop problems can be encountered, hence a third

electrode is introduced, called a counter electrode (CE). The current is passed between the CE and WE, whilst the potential is applied between the WE and RE.

The potential of the WE is swept in a linear fashion from a potential (E_1) where no reaction occurs to a potential where HET occurs (E_2) and then back again. The applied potential waveform has a triangular shape as shown in Figure 1.15.

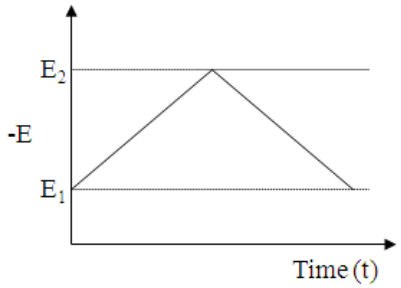

Figure 1.15. Schematic showing a triangular potential sweep during CV.

The current (i) recorded at the WE is plotted against potential (V) to produce a CV, an example is shown in Figure 1.16, recorded for the electrolysis of a redox mediator with a macro-sized electrode in a quiescent solution containing excess background electrolyte.

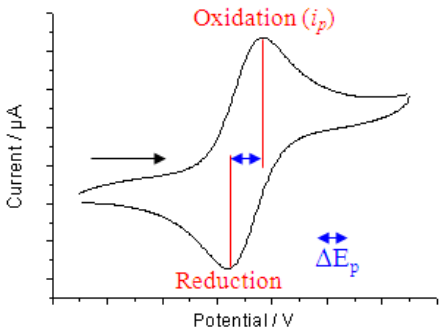

Figure 1.16. Example of a CV showing the oxidation and subsequent reduction of a redox mediator. ΔE_p is calculated from the potentials at the peak currents.

The shape of the resulting CV depends on the interplay between mass transport (typically diffusion only, under conditions where convection and migration minimised) and HET.[129] Under reversible *i.e.* diffusion-controlled conditions, a characteristic peak current, (i_p), is obtained indicative of a HET reaction controlled by linear diffusion, and is described by the Randles Sevcik equation.[127](Equation 1.4).

$$i_p = 0.4463 \left(\frac{F^3}{RT}\right)^{1/2} n^{3/2} v^{1/2} D^{1/2} A\, c^* \qquad \textbf{(1.4)}$$

Where v is the potential sweep rate (V s^{-1}), D the electroactive species diffusion coefficient (cm^2 s^{-1}), A is the electrode surface area (cm^2) and c^* the concentration of the analyte (mol cm^{-3}). The peak to peak separation (ΔE_p) for a reversible process is defined by equation 1.5.[126] For n=1,ΔE_p is ~ 59 mV when T = 298 K.

$$\Delta E_p = 2.3RT/nF \qquad \textbf{(1.5)}$$

The scan rate (ν) controls the rate of diffusional mass transport. As ν increases, for a reversible process i_p linearly increases as a function of the square root of scan rate as shown Figure 1.17.

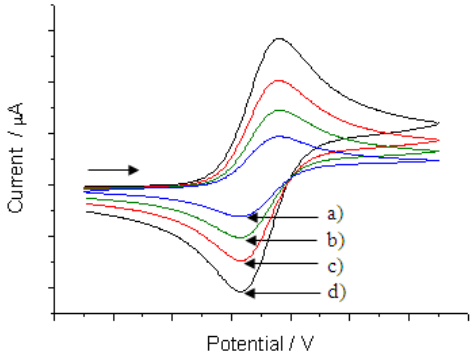

*Figure 1.17. Ideal CVs of a range of scan rates a) 20 mV s^{-1} (**blue**), b) 50 mV s^{-1} (**green**), c) 100 mV s^{-1} (**red**) and d) 200 mV s^{-1}(**black**).*

1.2.3 Electrochemistry of Boron Doped Diamond

Advances made using CVD have enabled the employment of diamond in a range of applications including; high powered lasers,[130] optical windows[131] and protective coatings.[132] For electrochemical applications conducting diamond, *i.e.* diamond doped with boron is required. This material is now commercially available in large wafers (> 15 cm diameter) at justifiable costs.[133]

The use of BDD as an electrode material has significantly increased over the last decade.[134] Initial studies suggested conducting diamond had a wide potential window in aqueous solvents,[107,135] compared to other electrodes, displayed low capacitive currents[136,137] and a resistance to fouling.[138-140] Fouling is common when employing metal electrodes. Thus BDD held great promise as a material suitable for electroanalysis.

The first reported use of diamond as an electrode material was in 1983 by Iwaki *et al.*,[141] here solution electrochemistry was undertaken using zinc ion implanted natural diamond. This material was shown to have a wider potential

window and reduced background currents when compared to glassy carbon (GC) electrodes. Further work by Vinokur *et al.*[29] verified this by comparing the electrochemical response of pBDD to Au, graphite and Pt electrodes. Extensive studies were performed by Pleskov *et al.*[142] a few years later, using semiconducting CVD grown pBDD for photo-electrochemical studies using 1 M KCl at sub-bandgap wavelengths.

BDD electrochemistry took off during the nineties pioneered by researchers such as Fujishima and Swain. Fujishima *et al.* reported on the use of HFCVD semiconducting pBDD to reduce nitrate to ammonia.[143] Swain and co-workers during this period also reported on the low background currents and low capacitance of high quality thick film pBDD ([B]~10^{20} cm^{-3}) grown via MWCVD and its suitability for electroanalysis.[114,144,145]

Typical metal electrodes e.g. Pt and Au undergo surface oxidation/reduction processes which also contribute to the electrochemical signal, as shown in Figure 1.18. These surface processes affect the background current readings and therefore can mask/interfere with the oxidation/reduction of the analyte of interest. In contrast BDD suffers from minimal surface electrolysis[29,114,144] enabling lower background currents to be recorded over a wider range,[107,143,146] essential for trace level detection. This enables the detection of electroactive species at potentials where they would normally be masked using conventional metal electrodes.[147-149]

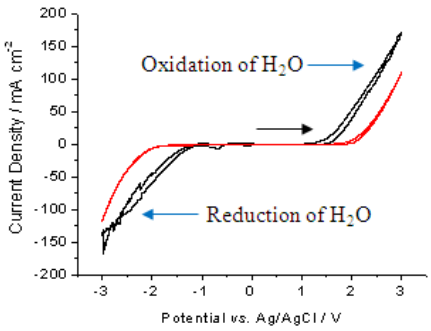

*Figure 1.18. CV showing the extended potential window of scBDD (100) (**red**) compared to a Pt electrode (**black**) in aqueous media (0.1 M KNO_3), scan rate 100 mV s^{-1}.*

BDD also has the potential to operate under harsher conditions than existing commercially available electrodes e.g. perchlorate[150] and non-aqueous media.[151] Swain investigated the susceptibility of surface corrosion on electrodes made of pBDD, GC and highly orientated pyrolytic graphite (HOPG) in an acidic fluoride media.[152]Swain concluded that after potential cycling for two hours in 0.1 M NaF and 1.0 M HNO_3, pBDD possessed a superior degree of chemical inertness and corrosion resistance. However, HOPG and GC showed surface pitting, oxidation and cavitation.[152]

The different rates of boron incorporation during pBDD growth can affect the electrochemical properties of the pBDD.[153] However provided the heterogeneous active electrode is operated under steady-state conditions, the resulting behaviour of the electrode is the same as a uniformly active electrode. When working under kinetic control, the effect of surface heterogeneity must be taken into account as this can influence the resulting electrochemical behaviour,[154-156] hence the need for scBDD material.

1.2.4 Single Crystal Boron Doped Diamond Electrochemical Studies

Over the last 15 years, BDD has been investigated for use in electrochemistry in its synthetic form.[29,114,144,157] The majority of studies have utilised pBDD due its relative ease of growth compared to scBDD. However a few limited recent studies have seen researchers investigating the properties and uses of scBDD for electrochemical research.[88,158-160]

Ramesham[161] first reported on the electrochemical response of scBDD compared to pBDD. MWCVD was employed to grow pBDD and scBDD (100). Both materials were used as grown, however the surface morphology of the pBDD was much rougher in comparison to scBDD.[161] No surface termination description was provided therefore the samples were likely to be H-terminated from the growth process. The [B] was not described.

Using 0.5 M NaCl and HCl as supporting electrolyte, similar potentials windows were reported for both pBDD and scBDD.[161] When utilised with $Fe(CN)_6^{3-/4-}$ in 0.5 M NaCl, the HET rates were described as sluggish across a range of scan rates when compared to GC electrodes. The ΔE_p decreased as the scan rate decreased attributed to either the slow HET reaction at the scBDD surface or the higher electrical resistivity of the diamond.[161] However with no information on [B] or surface termination it is difficult to draw many conclusions from the results observed.

Around the same time, Martin *et al.*[162] also compared HFCVD pBDD ([B]~10^{21} cm^{-3}) and scBDD (100) and (111) ([B] not quoted) with a redox couple. Reproducible wide potential windows were again reported for both pBDD and scBDD using 0.5 M H_2SO_4. A signal for electrolysis of the redox couple was

observed when employing the pBDD electrode, however it was absent for the scBDD electrodes, despite cycling to improve sensitivity. Furthermore it was found there was little difference in the electrochemistry observed on scBDD grown for eight and twenty four hours, using both crystal faces. The authors believed the results observed indicated the presence of non-diamond sp^2 carbon most likely at orientation boundaries,[163-167] which were thought to be electrochemically responsible for turnover of the redox species on pBDD.[161]

Pleskov and co-workers investigated the electrochemical response of scBDD publishing several studies.[88,158,160] Initially they used small (1×1×1 mm) HPHT scBDD diamonds, (O-terminated, [B] not quoted, different crystallographic orientations) and compared this to CVD as grown H-terminated pBDD films. Differences in resistivity between the scBDD electrodes were recorded. Electrochemistry was performed on the (100) scBDD orientation using $Ce^{3+/4+}$ and $Fe(CN)_6^{3-/4-}$. The $Ce^{3+/4+}$ showed moderate electrocatalytic characteristics typical of semiconducting electrodes.[160]

$Fe(CN)_6^{3-/4-}$ electrolysis showed faster HET kinetics (quasi reversible) however was still much slower than highly conducting metal-like CVD pBDD. This could be due to the differing surface termination of the pBDD. Overall they concluded that CVD pBDD and HPHT scBDD material presented electrode behaviours. The scBDD was quoted as having lower resistivities than the pBDD suggesting higher doped sc material.[160]

Pleskov *et al.*[158] grew two HPHT scBDD samples and these are shown in Figure 1.19. Details on the [B] of the different crystallographic orientations are also given in Table 1.1. Post processing of the samples resulted in O-terminated crystals.

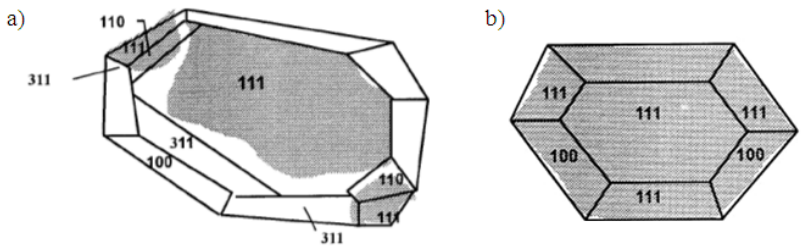

Figure 1.19. Diagram showing the single crystal orientations as described during the electrochemical research by Pleskov et al.[158] a) Crystal 168 and b) crystal 360.

Table 1.1 SIMS [B] cm^{-3} of the scBDD facets shown in Figure 1.19.[158]

Crystal 168			**Crystal 360**		
Face	**Location**	**[B] /cm^{-3}**	**Face**	**Location**	**[B] /cm^{-3}**
(111)	Central	10^{18}	**(111)**	Central	2.0×10^{19}
(111)	Lateral (right)	2.7×10^{18}	**(111)**	Rear	9.0×10^{18}
(111)	Lateral (left)	1.6×10^{19}	**(111)**	Lateral (bottom)	1.3×10^{21}
(100)		3.1×10^{18}	**(111)**	Lateral (left)	3.0×10^{20}
(311)	Left	2.0×10^{19}	**(100)**	Right	6.0×10^{21}
(311)	Right	9.5×10^{18}	**(100)**	Left	4.8×10^{21}

Using $Fe(CN)_6^{3-/4-}$ they reported the higher doped orientations offered faster HET kinetics and found all orientations to be electrochemically active. [158]

Later, Pleskov *et al.*[88] used the HFCVD method to simultaneously grow scBDD (111) (5-7 × 10^{20} cm^{-3}), (110) (1.3 × 10^{20} cm^{-3}), (100) (2-3 × 10^{19} cm^{-3}) and pBDD (5 × 10^{20} cm^{-3}) comparing their electrochemical response. All samples employed were O-terminated via boiling in concentrated perchloric acid for one hour. Using $Fe(CN)_6^{3-/4-}$ the (111), (110) and pBDD films showed quasi reversible HET whereas the (100) failed to show an oxidation or reduction peak current.

Moving onto $Ru(NH_3)_6^{3+/2+}$, this offered faster HET than with $Fe(CN)_6^{3-/4-}$ although still quasi reversible. The (100) orientation demonstrated sluggish kinetics,

however both a reduction and oxidation peak were recorded. The study concluded that HET kinetics were dependent on the [B] of samples rather than their orientation *i.e.* high [B] related to faster HET kinetics. It was also stated that HET kinetics for $Fe(CN)_6^{3-/4-}$ are hampered by surface oxidation treatments.[88]

A study by Kondo *et al.*[159] published slightly earlier than the previous work also investigated the electrochemical behaviour of scBDD grown via MWCVD ((100), (111) and pBDD). The BDD was H-terminated with the following [B]; (100) 2×10^{19} cm^{-3}, (111) 2×10^{19} cm^{-3} and pBDD typically ~1.7×10^{20} cm^{-3}. All electrodes showed similar wide potential windows. Redox mediators included $Ru(NH_3)_6^{3+/2+}$ and $Fe(CN)_6^{3-/4-}$, as reported by Pleskov[88] HET kinetics were found to be faster for the higher doped samples. The (111) scBDD film and pBDD both demonstrated similar electrochemical response, suggesting pBDD is dominated by (111).

1.2.5 Electrode Geometries and Electrochemical Cells

BDD has been used in many different formats for electrochemical studies. The simplest and most commonly used is to take the as-grown or polished surface and clamp to the bottom of a glass cell using an O-ring and employ under stationary conditions.[73,168]

Granger *et al.*[168] describes three popular ways of making an electrical connection to the diamond using the O-ring cell arrangement; scratching the rear of the Si substrate followed by coating with pencil graphite before (i) connection to a polished Al back plate or (ii) coating the area with Ag paste or (iii) running a bead of Ag paste from the top edge of the diamond film to the rear of the Si substrate should the material be freestanding.

Hutton *et al.*[169] fabricated macro sized pBDD disc electrodes insulated in glass. Laser micromachining cut out 1 mm diameter cylinders from the pBDD films, these were ohmically contacted, using Ti-carbide/Au and then sealed in glass. Polishing was employed to expose the coplanar pBDD disc thereby mimicking commercially available macrodisc electrode formats. Such electrodes have been modified with Pt nanoparticles (NPs) and used as amperometric sensors for the determination of dissolved oxygen concentration in aqueous solution.[169]

1.3 SCANNING ELECTROCHEMICAL IMAGING TECHNIQUES

High resolution electrochemical imaging can be used to probe and quantify HET across an electrode surface at microscopic or smaller spatial resolution. Such techniques are thus ideal for characterising BDD electrodes, especially when looking to identify variations in HET and correlate to material properties. In 1989, Bard *et al.*[170] first described scanning electrochemical microscopy (SECM), although the concept of using a small electrode to probe the reactivity of a larger one was not new.[171-173] SECM has now become a routinely used scanned probe technique.[174-178] SECM has been employed to study ET for both heterogeneous and homogenous reactions,[179-181] and offers high resolution imaging of the chemical reactivity or topography of a substrate, as shown in Figure 1.20.[109] Spatial resolution of SECM is limited by the tip size and minimum current that can be accurately measured. Commonly used ultra micro electrodes (UME) are disc electrodes with sizes in the range of 1-25 μm.[182-187]

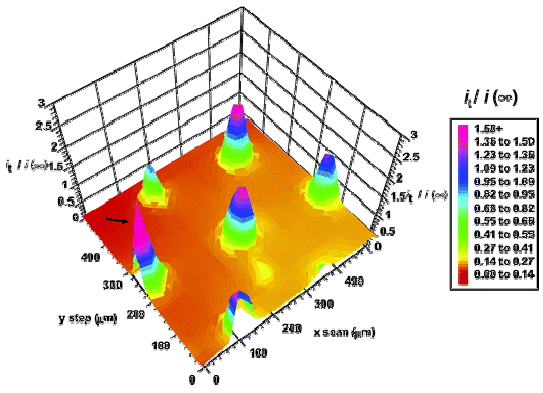

Figure 1.20. SECM substrate generation-tip collection image of the electrochemical activity of ~50 µm pBDD UME array positioned 250 µm apart.[109]

SECM is not limited to the investigation of electrode surfaces and has been used extensively to probe biological systems including neurons,[188] porous membranes,[189,190] mono-and bi-layers[191] and photosynthetic processes.[192] Alternative geometry UMEs have also been employed and include bands,[193] arrays[194,195] and rings.[196,197] Although the disc geometry is probably the format easiest to model analytically and computationally.[198,199] Many different metals have been used to produce the UME tips including Au,[200] Ag,[201] Pt,[199,202] carbon fibres[203] and superconductive ceramics.[204]

Diffusional mass transport to a disc shaped UME is much higher than that compared to a disc shaped macro electrode due to the prominence of radial diffusion resulting in an increased flux. Thus the CV response for red/ox of a redox active species is very different for macro and micro shaped disc electrode as shown in Figure 1.21.

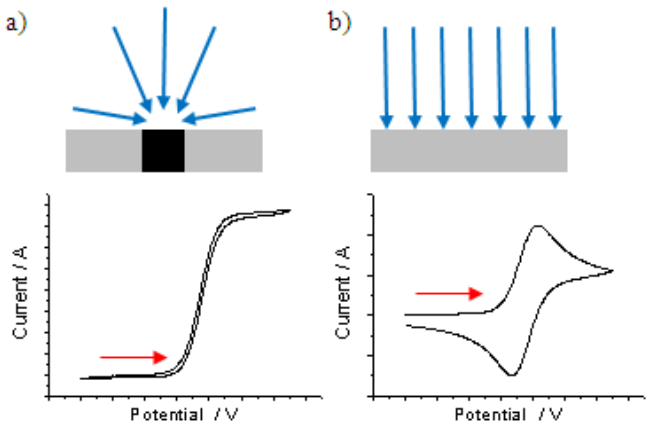

Figure 1.21. Schematic showing the diffusional behaviour to a disc electrode and therefore differing CVs (oxidation of the redox mediator) for a) UME and b) macro electrode.

For disc UMEs a unique hemispherical three dimensional diffusion profile is obtained, resulting in a time independent steady-state bulk limiting current, (i_{lim}). When a UME is operated under steady-state diffusion limited control, the i_{lim} recorded at the tip is determined using equation 1.6.[205]

$$i_{lim} = 4x\ naFDc^* \qquad \textbf{(1.6)}$$

Where a is the radius of the UME, and x is a function of RG (ratio of overall probe radius to the disk electrode radius; when RG = 10, x = 1.02),[205] the i_{lim} recorded at the UME is typically in the range 10 nA – 10pA when utilised with redox concentrations in the mM to µM range.

Traditionally SECM is performed in amperometric mode with the current at the tip monitored,[206-210] however if the substrate is (semi)conducting, this can also be connected and used as a second electrode.[109,211-215] For the majority of analysis the tip UME is held at a sufficient potential to cause diffusion controlled electrolysis of

the redox active mediator. i_{lim} is obtained via this diffusion controlled process. The UME is typically positioned within ~10 electrode radii from the substrate of interest.[170]

As the UME is brought close to a substrate, in the *z* direction, the hemispherical diffusion field of the tip starts to interact with the surface. For an insulating, redox inactive surface, the steady-state *i* decreases, as the tip-substrate separation decreases, such that *i* is less than i_{lim}. This occurs because the substrate hinders diffusion of the electroactive species to the UME tip and this is referred to as negative feedback[216] as shown in Figure 1.22a.

Conversely when the UME tip approaches a conducting substrate, the electroactive species is continually regenerated between the UME tip and the conducting substrate. This leads to an enhancement of the current recorded at the UME tip. This is referred to a positive feedback.

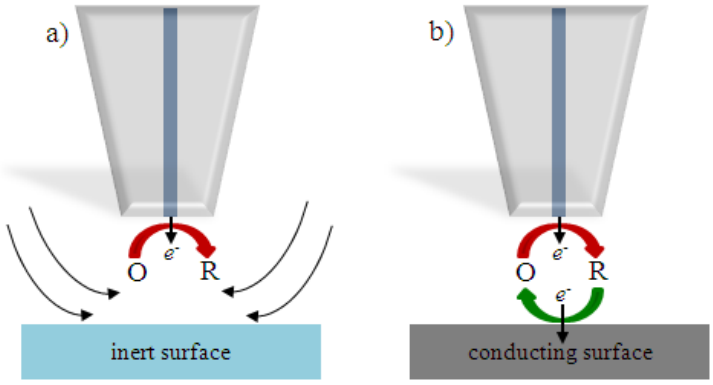

Figure 1.22 SECM feedback modes a) negative feedback caused by hindered diffusion and b) positive feedback caused by regeneration of the redox mediator.

Approach curves typically plot the *i* recorded normalised to the i_{lim} recorded in bulk solution, as a function of tip-substrate separation (*d*) as shown in Figure 1.23for negative and positive feedback representing slow (zero) ET at the substrate and diffusion controlled HET.[217]

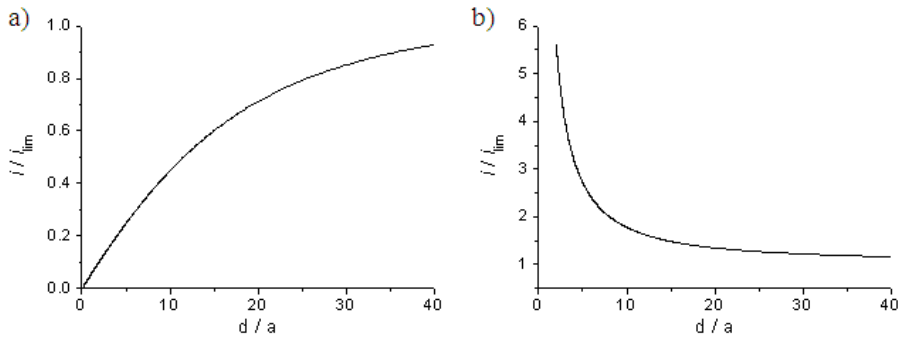

Figure 1.23. Theoretical approach curves to a) insulating substrate and b) conducting substrate showing negative and positive feedback respectively.

In negative feedback, the *i* is controlled by the *d*. For a tip scanning at a fixed height[188,218,219] *i.e.* not following the contours of the underlying substrate topography, the tip *i* varies in accordance with the change in *d*. In this way the tip *i* can be used to determine sample topography with a resolution governed by the size of the electrode.[220]

Substrate generation-tip collection (SG-TC) mode SECM requires the usually much larger (than the UME) substrate to be electrically connected. SG-TC is utilised in a four electrode electrochemical cell, where both the substrate and the UME are employed as working electrodes. The tip detects and collects the electroactive species generated at the substrate electrode as a function of *x*, *y* and *z* tip position.[171,173,221-223] The main disadvantage of SECM imaging is the challenges relating to distinguishing between topographical features and local activity of the sample. There have been several methods proposed to overcome this disadvantage including combined SECM-atomic force microscopy (AFM),[224,225] shear force SECM,[226] scanning ion conductance microscopy (SICM)-SECM[227,228] and intermittent contact SECM (IC-SECM).[219] Particular focus is given to the latter as this methodology is employed in this thesis.

1.3.1 Intermittent Contact-Scanning Electrochemical Microscopy (IC-SECM)

A recent exciting development in the field of distance control in SECM is IC-SECM.[219] Similar to tapping mode AFM[229-231] the UME tip is oscillated with a small amplitude of oscillation, typically ~70 Hz, during its approach to the substrate. Upon contact the oscillation is immediately reduced due to dampening when the tip makes contact with the substrate. This dampening is used to denote tip-substrate contact and is used as a feedback parameter enabling the tip to crucially and consistently follow the contours of the substrate topography for a forward scan by maintaining *d* separation.[219]

Hence in the forward line scan, the tip accurately tracks substrate topography and on the reverse scan the tip can be set at a user defined fixed distance, often an electrode radius away (but still tracking topography). Dampening remains fixed throughout for the scan duration, the use of a *z* bender piezoelectric positioner enables height changes to be monitored and therefore offers the possibility of plotting both topography and current.

This technique, has to-date been used to image gold bands (25 μm wide, 20 μm high) on glass,[219] visualise and quantify mass transport through dentin[232] and elucidate the HET of pBDD on an crystal facet by facet basis in SG-TC mode.[124]

1.4 AIMS AND OBJECTIVES

The majority of electrochemical investigations in the community to-date have centred around poly and nanocrystalline BDD films, due to the difficulty in reliably producing scBDD. Element Six Ltd (E6), Ascot, UK, have produced a unique sample set of MWCVD grown scBDD electrodes varying in both boron content ($0.95 \times 10^{20} - 1.2 \times 10^{21}$ cm^{-3}) and crystallographic orientations (100), (110) and (111). The samples will be critically analysed to demonstrate which scBDD orientation and growth parameters offer the most effective electrode material with a view to also elucidating HET on the crystal faces.

One of the drawbacks of many scBDD studies in the literature is the lack of information regarding material properties. Hence it is often difficult to draw reliable conclusions between differing studies. Here, a range of material characterisation techniques will be undertaken to provide in detail the material properties of the scBDD electrodes employed as discussed in Chapter 3. These include, SIMS, differential interference contrast microscopy, SEM, AFM, XPS and Raman spectroscopy. Electrochemical analysis will be undertaken using 1 mm macrodisc electrodes laser cut from the original samples. The use of a range of different redox mediators varying in concentration and HET mechanism (*i.e.* outer sphere *vs.* inner sphere) will be used to assess the scBDD electrochemical response. Furthermore surface pre-treatments will be probed assessing their influence on HET for different redox mediators.

Electrochemistry will be performed at both macro and micro-scales to investigate boron doping homogeneity. Micro-scale electrochemistry, described in Chapter 4, will be undertaken using SECM and its recent development IC-SECM.

To further investigate electrode homogeneity the electrochemical deposition of Au nanoparticles (NPs) is described in Chapter 5 using a range of potentials and time frames to fully investigate this phenomenon. Based on the results presented in Chapters 3, 4 and 5, the ideal scBDD electrode was specified and grown by E6 for further investigation, as described in Chapter 6. Finally, Chapter 7 discusses conclusions.

1.5 REFERENCES

1. S. Tolansky, *The History and Use of Diamond*, Methuen & Co Ltd, London, 1962.
2. P. W. May, *Philosophical Transactions of the Royal Society of London Series a-Mathematical Physical and Engineering Sciences*, 2000, **358**, 473-495.
3. H. M. Liu and D. S. Dandy, *Diamond chemical vapour deposition - Nucleation and early growth stages*, Noyes Publications, 1995.
4. C. Batchelor-McAuley, C. E. Banks, A. O. Simm, T. G. J. Jones and R. G. Compton, *Analyst*, 2006, **131**, 106-110.
5. R. Hazen, *The Diamond Makers*, Cambridge University Press, 1999.
6. J. Asmussen and D. K. Reinhard, *Diamond Film Handbook*, Marcel Dekker Inc., New York, 2002.
7. F. P. Bundy, *The Journal of Chemical Physics*, 1963, **38**, 618-630.
8. P. M. Martineau, M. P. Gaukroger, K. B. Guy, S. C. Lawson, D. J. Twitchen, I. Friel, J. O. Hansen, G. C. Summerton, T. P. G. Addison and R. Burns, *Journal of physics. Condensed matter : an Institute of Physics journal*, 2009, **21**, 364205.
9. http://www.diamondlab.org/80-hpht_synthesis.htm.
10. W. G. Eversole, 3030187 and 3030188, U.S.A, 1962.
11. J. C. Angus, H. A. Will and W. S. Stanko, *Journal of Applied Physics*, 1968, **39**, 2915-2922.
12. C. S. Yan, Y. K. Vohra, H. K. Mao and R. J. Hemley, *Proceedings of the National Academy of Sciences of the United States of America*, 2002, **99**, 12523-12525.
13. O. A. Williams and R. B. Jackman, *Diamond and Related Materials*, 2004, **13**, 557-560.
14. J. Asmussen, T. A. Grotjohn, T. Schuelke, M. F. Becker, M. K. Yaran, D. J. King, S. Wicklein and D. K. Reinhard, *Applied Physics Letters*, 2008, **93**.
15. A. Khodin, L. Joong-Kee, K. Chang-Sam and K. Sang-Ok, *Materials Letters*, 2009, **63**, 2552-2555.
16. Q. Yang, C. Xiao, W. Chen and A. Hirose, *Diamond and Related Materials*, 2004, **13**, 433-437.
17. Z. Huang, K. D. Harris and M. J. Brett, *Advanced Materials*, 2009, **21**, 2983-+.
18. W. A. Yarbrough and R. Messier, *Science*, 1990, **247**, 688-696.
19. D. Das and R. N. Singh, *International Materials Reviews*, 2007, **52**, 29-64.
20. V. P. Varnin, V. A. Laptev and V. G. Ralchenko, *Inorganic Materials*, 2006, **42**, S1-S18.
21. F. G. Celii and J. E. Butler, *Annual Review of Physical Chemistry*, 1991, **42**, 643-684.
22. R. S. Balmer, J. R. Brandon, S. L. Clewes, H. K. Dhillon, J. M. Dodson, I. Friel, P. N. Inglis, T. D. Madgwick, M. L. Markham, T. P. Mollart, N. Perkins, G. A. Scarsbrook, D. J. Twitchen, A. J. Whitehead, J. J. Wilman and S. M. Woollard, *Journal of physics. Condensed matter : an Institute of Physics journal*, 2009, **21**, 364221.
23. J. E. Butler, Y. A. Mankelevich, A. Cheesman, J. Ma and M. N. R. Ashfold, *Journal of Physics-Condensed Matter*, 2009, **21**.

24. C. Chen and Q. Chen, *International Journal of Modern Physics B*, 2008, **22**, 309-326.
25. P. Hess, *Journal of Applied Physics*, 2012, **111**.
26. A. Suzuki, T. A. Ivandini, K. Yoshimi, A. Fujishima, G. Oyama, T. Nakazato, N. Hattori, S. Kitazawa and Y. Einaga, *Analytical Chemistry*, 2007, **79**, 8608-8615.
27. A. N. Ndao, F. Zenia, A. Deneuville, M. Bernard and C. Levy-Clement, *Diamond and Related Materials*, 2000, **9**, 1175-1180.
28. L. F. Li, D. A. Totir, N. Vinokur, B. Miller, G. Chottiner, E. A. Evans, J. C. Angus and D. A. Scherson, *Journal of the Electrochemical Society*, 1998, **145**, L85-L88.
29. N. Vinokur, B. Miller, Y. Avyigal and R. Kalish, *Journal of the Electrochemical Society*, 1996, **143**, L238-L240.
30. L. Bergman, M. T. McClure, J. T. Glass and R. J. Nemanich, *Journal of Applied Physics*, 1994, **76**.
31. K. Okano, S. Koizumi, S. R. P. Silva and G. A. J. Amaratunga, *Nature*, 1996, **381**.
32. N. Jiang, M. Nishimura, K. Ogawa, H. Yagi, A. Hatta and T. Ito, *Diamond Films and Technology*, 1997, **7**.
33. S. Matsumoto, Y. Sato, M. Tsutsumi and N. Setaka, *Journal of Materials Science*, 1982, **17**, 3106-3112.
34. M. Kamo, Y. Sato, S. Matsumoto and N. Setaka, *Journal of Crystal Growth*, 1983, **62**, 642-644.
35. J. Herlinger, *Thin Solid Films*, 2006, **501**, 65-69.
36. M. A. Prelas, G. Popovici and L. K. Bigelow, *Handbook of industrial diamonds and diamond films*, Marcel Dekker Inc., New York, 1998.
37. S. T. Lee, Z. D. Lin and X. Jiang, *Materials Science & Engineering R-Reports*, 1999, **25**.
38. M. N. R. Ashfold, P. W. May, C. A. Rego and N. M. Everitt, *Chemical Society Reviews*, 1994, **23**, 21-30.
39. S. Wang, V. M. Swope, J. E. Butler, T. Feygelson and G. M. Swain, *Diamond and Related Materials*, 2009, **18**, 669-677.
40. M. Chandran, C. R. Kumaran, S. Vijayan, S. S. Bhattacharya and M. S. R. Rao, *Materials Express*, 2012, **2**, 115-120.
41. Y. Saito, K. Sato, S. Matuda and H. Koinuma, *Journal of Materials Science*, 1991, **26**, 2441-2444.
42. M. D. Whitfield, J. A. Savage and R. B. Jackman, *Diamond and Related Materials*, 2000, **9**, 262-268.
43. M. Kasu, K. Ueda, Y. Yamauchi, A. Tallaire and T. Makimoto, *Diamond and Related Materials*, 2007, **16**, 1010-1015.
44. C. Pietzka, A. Denisenko, L. A. Kibler, J. Scharpf, Y. Men and E. Kohn, *Diamond and Related Materials*, 2009, **18**, 816-819.
45. R. E. Thomas, R. A. Rudder and R. J. Markunas, *Journal of Vacuum Science & Technology a-Vacuum Surfaces and Films*, 1992, **10**, 2451-2457.
46. S. Ghodbane, D. Ballutaud, A. Deneuville and C. Baron, *Physica Status Solidi a-Applications and Materials Science*, 2006, **203**, 3147-3151.
47. M. N. R. Ashfold, P. W. May, J. R. Petherbridge, K. N. Rosser, J. A. Smith, Y. A. Mankelevich and N. V. Suetin, *Physical Chemistry Chemical Physics*, 2001, **3**, 3471-3485.

48. J. E. Butler and R. L. Woodin, *Philosophical Transactions of the Royal Society of London Series a-Mathematical Physical and Engineering Sciences*, 1993, **342**, 209-224.
49. J. C. Angus, A. Argoitia, R. Gat, Z. Li, M. Sunkara, L. Wang and Y. Wang, *Philosophical Transactions of the Royal Society of London Series a-Mathematical Physical and Engineering Sciences*, 1993, **342**, 195-208.
50. J. Ma, J. C. Richley, D. R. W. Davies, M. N. R. Ashfold and Y. A. Mankelevich, *Journal of Physical Chemistry A*, 2010, **114**, 10076-10089.
51. J. Ma, J. C. Richley, M. N. R. Ashfold and Y. A. Mankelevich, *Journal of Applied Physics*, 2008, **104**, 103305.
52. C. E. Nebel and J. Ristein, *Thin-Film Diamond I*, Elsevier Academic Press, 2003.
53. J. C. Angus and C. C. Hayman, *Science*, 1988, **241**, 913-921.
54. http://www.hk-phy.org/atomic_world/carbon/carbon01_e.html.
55. http://www.flickr.com/photos/mitopencourseware/3360948998/.
56. A. T. Collins, *Philosophical Transactions of the Royal Society of London. Series A: Physical and Engineering Sciences*, 1993, **342**, 233-244.
57. A. W. Bott, *Current Separations*, 1998, **17**, 87-91.
58. W. O. 03052174A2, 2003.
59. J. P. Lagrange, A. Deneuville and E. Gheeraert, *Diamond and Related Materials*, 1998, **7**, 1390-1393.
60. O. A. Williams, M. Nesladek, M. Daenen, S. Michaelson, A. Hoffman, E. Osawa, K. Haenen and R. B. Jackman, *Diamond and Related Materials*, 2008, **17**, 1080-1088.
61. R. M. Chrenko, *Physical Review B*, 1973, **7**, 4560-4567.
62. E. Gheeraert, A. Deneuville and J. Mambou, *Diamond and Related Materials*, 1998, **7**, 1509-1512.
63. A. Tajani, M. Mermoux, B. Marcus, E. Bustarret, E. Gheeraert and S. Koizumi, *Physica Status Solidi a-Applied Research*, 2003, **199**, 87-91.
64. H. Shiomi, Y. Nishibayashi and N. Fujimori, *Japanese Journal of Applied Physics Part 1-Regular Papers Short Notes & Review Papers*, 1991, **30**, 1363-1366.
65. A. W. Williams, Lightowl.Ec and A. T. Collins, *Journal of Physics Part C Solid State Physics*, 1970, **3**, 1727-&.
66. L. Boeri, J. Kortus and O. K. Andersen, *Physical Review Letters*, 2004, **93**.
67. A. Deneuville, C. Baron, S. Ghodbane and C. Agnes, *Diamond and Related Materials*, 2007, **16**, 915-920.
68. G. Janssen, W. J. P. Vanenckevort, W. Vollenberg and L. J. Giling, *Diamond and Related Materials*, 1992, **1**, 789-800.
69. E. P. Visser, G. J. Bauhuis, G. Janssen, W. Vollenberg, W. J. P. Vanenckevort and L. J. Giling, *Journal of Physics-Condensed Matter*, 1992, **4**, 7365-7376.
70. L. F. Sutcu, C. J. Chu, M. S. Thompson, R. H. Hauge, J. L. Margrave and M. P. Develyn, *Journal of Applied Physics*, 1992, **71**, 5930-5940.
71. A. Tallaire, J. Achard, F. Silva, R. S. Sussmann and A. Gicquel, *Diamond and Related Materials*, 2005, **14**, 249-254.
72. R. Ramamurti, M. Becker, T. Schuelke, T. A. Grotjohn, D. K. Reinhard and J. Asmussen, *Diamond and Related Materials*, 2009, **18**, 704-706.

73. Y. V. Pleskov, Y. E. Evstefeeva, M. D. Krotova, V. V. Elkin, V. M. Mazin, V. Y. Mishuk, V. P. Varnin and I. G. Teremetskaya, *Journal of Electroanalytical Chemistry*, 1998, **455**, 139-146.
74. T. Teraji, *physica status solidi (a)*, 2006, **203**, 3324-3357.
75. I. Friel, S. L. Clewes, H. K. Dhillon, N. Perkins, D. J. Twitchen and G. A. Scarsbrook, *Diamond and Related Materials*, 2009, **18**, 808-815.
76. Q. Liang, C.-s. Yan, Y. Meng, J. Lai, S. Krasnicki, H.-k. Mao and R. J. Hemley, *Diamond and Related Materials*, 2009, **18**, 698-703.
77. C. Findelingdufour, A. Vignes and A. Gicquel, *Diamond and Related Materials*, 1995, **4**.
78. R. Ramamurti, M. Becker, T. Schuelke, T. Grotjohn, D. Reinhard and J. Asmussen, *Diamond and Related Materials*, 2008, **17**, 1320-1323.
79. K. Ushizawa, K. Watanabe, T. Ando, I. Sakaguchi, M. Nishitani-Gamo, Y. Sato and H. Kanda, *Diamond and Related Materials*, 1998, **7**.
80. S.-G. Ri, H. Kato, M. Ogura, H. Watanabe, T. Makino, S. Yamasaki and H. Okushi, *Journal of Crystal Growth*, 2007, **299**, 235-242.
81. E. Gheeraert, A. Deneuville and J. Mambou, *Carbon*, 1999, **37**.
82. Q. Liang, C. Y. Chin, J. Lai, C.-s. Yan, Y. Meng, H.-k. Mao and R. J. Hemley, *Applied Physics Letters*, 2009, **94**, 024103.
83. R. Issaoui, J. Achard, F. Silva, A. Tallaire, A. Tardieu, A. Gicquel, M. A. Pinault and F. Jomard, *Applied Physics Letters*, 2010, **97**.
84. C. J. Chu, R. H. Hauge, J. L. Margrave and M. P. Develyn, *Applied Physics Letters*, 1992, **61**, 1393-1395.
85. C. J. Chu, M. P. Develyn, R. H. Hauge and J. L. Margrave, *Journal of Applied Physics*, 1991, **70**, 1695-1705.
86. H. Kawarada, Y. Yokota, Y. Mori, K. Nishimura and A. Hiraki, *Journal of Applied Physics*, 1990, **67**, 983-989.
87. K. Kobashi, K. Nishimura, Y. Kawate and T. Horiuchi, *Physical Review B*, 1988, **38**, 4067-4084.
88. Y. V. Pleskov, Y. E. Evstefeeva, V. P. Varnin and I. G. Teremetskaya, *Russian Journal of Electrochemistry*, 2004, **40**, 886-892.
89. Y. R. Zhang, S. Yoshihara, T. Shirakashi and T. Kyomen, *Diamond and Related Materials*, 2005, **14**, 213-219.
90. B. V. Spitsyn, L. L. Bouilov and B. V. Derjaguin, *Journal of Crystal Growth*, 1981, **52**, 219-226.
91. J. H. T. Luong, K. B. Male and J. D. Glennon, *Analyst*, 2010, **135**, 3008-3008.
92. N. R. Wilson, S. L. Clewes, M. E. Newton, P. R. Unwin and J. V. Macpherson, *The Journal of Physical Chemistry B*, 2006, **110**, 5639-5646.
93. A. A. Mol, L. S. Martins-Filho, J. D. S. da Silva and R. Rocha, *Computational Materials Science*, 2007, **38**, 727-736.
94. E. M. Wilks and J. Wilks, *Properties and Applications of Diamond*, Butterworth-Heinemann, 1991.
95. S. E. Grillo, J. E. Field and F. M. van Bouwelen, *Journal of Physics D-Applied Physics*, 2000, **33**, 985-990.
96. S. Ghodbane, D. Ballutaud, F. Omnes and C. Agnes, *Diamond and Related Materials*, 2010, **19**, 630-636.
97. G. R. Salazar-Banda, L. S. Andrade, P. A. P. Nascente, P. S. Pizani, R. C. Rocha and L. A. Avaca, *Electrochimica Acta*, 2006, **51**, 4612-4619.

98. M. N. Latto, G. Pastor-Moreno and D. J. Riley, *Electroanalysis*, 2004, **16**, 434-441.
99. J. Ristein, *Surface Science*, 2006, **600**, 3677-3689.
100. J. Ristein, M. Riedel, F. Maier, B. F. Mantel, M. Stammler and L. Ley, *Journal of Physics-Condensed Matter*, 2001, **13**, 8979-8987.
101. J. Ristein, M. Riedel and L. Ley, *Journal of the Electrochemical Society*, 2004, **151**, E315-E321.
102. J. A. Garrido, S. Nowy, A. Haertl and M. Stutzmann, *Langmuir*, 2008, **24**, 3897-3904.
103. A. Helwig, G. Mueller, J. A. Garrido and M. Eickhoff, *Sensors and Actuators B-Chemical*, 2008, **133**, 156-165.
104. K. Tsugawa, K. Kitatani, H. Noda, A. Hokazono, K. Hirose, M. Tajima and H. Kawarada, *Diamond and Related Materials*, 1999, **8**, 927-933.
105. L. Ostrovskaya, V. Perevertailo, V. Ralchenko, A. Dementjev and O. Loginova, *Diamond and Related Materials*, 2002, **11**, 845-850.
106. R. Boukherroub, X. Wallart, S. Szunerits, B. Marcus, P. Bouvier and M. Mermoux, *Electrochemistry Communications*, 2005, **7**, 937-940.
107. H. B. Martin, A. Argoitia, U. Landau, A. B. Anderson and J. C. Angus, *Journal of the Electrochemical Society*, 1996, **143**, L133-L136.
108. H. Girard, N. Simon, D. Ballutaud, M. Herlern and A. Etcheberry, *Diamond and Related Materials*, 2007, **16**, 316-325.
109. A. L. Colley, C. G. Williams, U. D'Haenens Johansson, M. E. Newton, P. R. Unwin, N. R. Wilson and J. V. Macpherson, *Analytical Chemistry*, 2006, **78**, 2539-2548.
110. F. Maier, J. Ristein and L. Ley, *Physical Review B*, 2001, **64**, art. no.-165411.
111. F. J. Himpsel, J. A. Knapp, J. A. Vanvechten and D. E. Eastman, *Physical Review B*, 1979, **20**, 624-627.
112. J. Ristein, *Applied Physics a-Materials Science & Processing*, 2006, **82**, 377-384.
113. C. E. Nebel and J. Ristein, *Thin-Film Diamond II*, Elsevier Academic Press, 2004.
114. S. Alehashem, F. Chambers, J. W. Strojek, G. M. Swain and R. Ramesham, *Analytical Chemistry*, 1995, **67**, 2812-2821.
115. H. A. Girard, N. Simon, D. Ballutaud and A. Etcheberry, *Comptes Rendus Chimie*, 2008, **11**, 1010-1015.
116. P. Actis, A. Denoyelle, R. Boukherroub and S. Szunerits, *Electrochemistry Communications*, 2008, **10**, 402-406.
117. T. N. Rao, D. A. Tryk, K. Hashimoto and A. Fujishima, *Journal of the Electrochemical Society*, 1999, **146**, 680-684.
118. J. Shirafuji, Y. Sakamoto, A. Furukawa, H. Shigeta and T. Sugino, *Diamond and Related Materials*, 1995, **4**, 984-988.
119. S. R. Sails, D. J. Gardiner, M. Bowden, J. Savage and D. Rodway, *Diamond and Related Materials*, 1996, **5**, 589-591.
120. F. Pruvost, E. Bustarret and A. Deneuville, *Diamond and Related Materials*, 2000, **9**, 295-299.
121. B. Sacepe, C. Chapelier, C. Marcenat, J. Kacmarcik, T. Klein, M. Bernard and E. Bustarret, *Physical Review Letters*, 2006, **96**.
122. M. Werner, R. Job, A. Zaitzev, W. R. Fahrner, W. Seifert, C. Johnston and P. R. Chalker, *Phys. Status Solidi A*, 1996, **154**, 385.

123. S. Szunerits, M. Mermoux, A. Crisci, B. Marcus, P. Bouvier, D. Delabouglise, J.-P. Petit, S. Janel, R. Boukherroub and L. Tay, *Journal of Physical Chemistry B*, 2006, **110**, 23888-23897.
124. H. V. Patten, K. E. Meadows, L. A. Hutton, J. G. Iacobini, D. Battistel, K. McKelvey, A. W. Colburn, M. E. Newton, J. V. Macpherson and P. R. Unwin, *Angewandte Chemie International Edition*, 2012, **51**, 7002-7006.
125. A. J. Bard and L. R. Faulkner, *Electrochemical Methods; Fundamentals and Applications*, John Wiley & Sons, **2000**.
126. C. M. A. Brett and A. M. Oliveira Brett, *Electrochemistry: Principles, Methods and Applications,*, Oxford University Press, **1996**.
127. A. C. Fisher, *Electrode Dynamics*, Oxford University Press, **2003**.
128. J. Newman and K. E. Thomas-Alyea, *Electrochemical Systems*, John Wiley & Sons, New York, 2004.
129. A. J. Bard and M. E. Stratmann, *Encyclopaedia of Electrochemistry*, Springer, **2003**.
130. H. P. Godfried, S. E. Coe, C. E. Hall, C. S. J. Pickles, R. S. Sussmann, X. Tang and W. K. L. van der Voorden, in *Conference on Advanced High-Power Lasers*, Osaka, Japan, 2000, pp. 553-563.
131. E. Woerner, C. Wild, W. Mueller-Sebert and P. Koidl, *Diamond and Related Materials*, 2001, **10**.
132. P. Ball, *New Scientist*, 1997, **153**.
133. http://www.e6.com/wps/wcm/connect/E6_Content_EN/Home.
134. A. Kraft, *International Journal of Electrochemical Science*, 2007, **2**, 355-385.
135. M. Panizza and G. Cerisola, *Electrochimica Acta*, 2005, **51**, 191-199.
136. Y. V. Pleskov, *Russian Journal of Electrochemistry*, 2002, **38**, 1275-1291.
137. T. Yano, D. A. Tryk, K. Hashimoto and A. Fujishima, *Journal of the Electrochemical Society*, 1998, **145**, 1870-1876.
138. J. S. Xu, M. C. Granger, Q. Y. Chen, J. W. Strojek, T. E. Lister and G. M. Swain, *Analytical Chemistry*, 1997, **69**, A591-A597.
139. A. G. Guell, K. E. Meadows, P. R. Unwin and J. V. Macpherson, *Physical Chemistry Chemical Physics*, 2010, **12**, 10108-10114.
140. B. V. Sarada, T. N. Rao, D. A. Tryk and A. Fujishima, *Chemistry Letters*, 1999, 1213-1214.
141. M. Iwaki, S. Sato, K. Takahashi and H. Sakairi, *Nuclear Instruments & Methods in Physics Research*, 1983, **209**, 1129-1133.
142. Y. V. Pleskov, A. Y. Sakharova, M. D. Krotova, L. L. Bouilov and B. V. Spitsyn, *Journal of Electroanalytical Chemistry*, 1987, **228**, 19-27.
143. R. Tenne, K. Patel, K. Hashimoto and A. Fujishima, *Journal of Electroanalytical Chemistry*, 1993, **347**, 409-415.
144. G. M. Swain and R. Ramesham, *Analytical Chemistry*, 1993, **65**, 345-351.
145. G. M. Swain, *Advanced Materials*, 1994, **6**, 388-392.
146. G. M. Swain, A. B. Anderson and J. C. Angus, *Mrs Bulletin*, 1998, **23**, 56-60.
147. K. B. Holt, A. J. Bard, Y. Show and G. M. Swain, *Journal of Physical Chemistry B*, 2004, **108**, 15117-15127.
148. J. Iniesta, P. A. Michaud, M. Panizza and C. Comninellis, *Electrochemistry Communications*, 2001, **3**, 346-351.
149. P. A. Michaud, M. Panizza, L. Ouattara, T. Diaco, G. Foti and C. Comninellis, *Journal of Applied Electrochemistry*, 2003, **33**, 151-154.

150. T. Ochiai, K. Arihara, C. Terashima and A. Fujishima, *Chemistry Letters*, 2006, **35**, 1018-1019.
151. M. Yoshimura, K. Honda, T. Kondo, R. Uchikado, Y. Einaga, T. N. Rao, D. A. Tryk and A. Fujishima, *Diamond and Related Materials*, 2002, **11**, 67-74.
152. G. M. Swain, *Journal of the Electrochemical Society*, 1994, **141**, 3382-3393.
153. E. Vanhove, J. de Sanoit, P. Mailley, M. A. Pinault, F. Jomard and P. Bergonzo, *Physica Status Solidi a-Applications and Materials Science*, 2009, **206**, 2063-2069.
154. J. K. Sass, *Vacuum*, 1983, **33**, 741-751.
155. A. Cięciwa, R. Wüthrich and C. Comninellis, *Electrochemistry Communications*, 2006, **8**, 375-382.
156. S. Trasatti and O. A. Petrii, *Journal of Electroanalytical Chemistry*, 1992, **327**, 353-376.
157. R. DeClements, G. M. Swain, T. Dallas, M. W. Holtz, R. D. Herrick and J. L. Stickney, *Langmuir*, 1996, **12**, 6578-6586.
158. Y. V. Pleskov, Y. E. Evstefeeva, M. D. Krotova, V. Y. Mishuk, V. A. Laptev, Y. N. Palyanov and Y. M. Borzdov, *Journal of the Electrochemical Society*, 2002, **149**, E260-E264.
159. T. Kondo, Y. Einaga, B. V. Sarada, T. N. Rao, D. A. Tryk and A. Fujishima, *Journal of the Electrochemical Society*, 2002, **149**, E179-E184.
160. Y. V. Pleskov, Y. E. Evstefeeva, M. D. Krotova and A. V. Laptev, *Electrochimica Acta*, 1999, **44**, 3361-3366.
161. R. Ramesham, *Sensors and Actuators B-Chemical*, 1998, **50**, 131-139.
162. H. B. Martin, A. Argoitia, J. C. Angus and U. Landau, *Journal of the Electrochemical Society*, 1999, **146**, 2959-2964.
163. J. Rosa, J. Pangrac, M. Vanecek, V. Vorlicek, M. Nesladek, K. Meykens, C. Quaeyhaegens and L. M. Stals, *Diamond and Related Materials*, 1998, **7**, 1048-1053.
164. J. Michler, J. Stiegler, Y. vonKaenel, P. Moeckli, W. Dorsch, D. Stenkamp and E. Blank, *Journal of Crystal Growth*, 1997, **172**, 404-415.
165. P. M. Fabis, *Thin Solid Films*, 1996, **288**, 193-197.
166. P. J. Fallon and L. M. Brown, *Diamond and Related Materials*, 1993, **2**, 1004-1011.
167. I. P. Hayward, K. J. Baldwin, D. M. Hunter, D. N. Batchelder and G. D. Pitt, *Diamond and Related Materials*, 1995, **4**, 617-621.
168. M. C. Granger, M. Witek, J. S. Xu, J. Wang, M. Hupert, A. Hanks, M. D. Koppang, J. E. Butler, G. Lucazeau, M. Mermoux, J. W. Strojek and G. M. Swain, *Analytical Chemistry*, 2000, **72**, 3793-3804.
169. L. Hutton, M. E. Newton, P. R. Unwin and J. V. Macpherson, *Analytical Chemistry*, 2009, **81**, 1023-1032.
170. J. Kwak and A. Bard, *J. Anal. Chem.*, 1989, **61**, 1221.
171. R. C. Engstrom, T. Meaney, R. Tople and R. M. Wightman, *Analytical Chemistry*, 1987, **59**, 2005-2010.
172. R. C. Engstrom, *Abstracts of Papers of the American Chemical Society*, 1986, **191**, 105-ANYL.
173. R. C. Engstrom, M. Weber, D. J. Wunder, R. Burgess and S. Winquist, *Analytical Chemistry*, 1986, **58**, 844-848.
174. M. V. Mirkin and B. R. Horrocks, *Analytica Chimica Acta*, 2000, **406**, 119-146.

175. S. Amemiya, A. J. Bard, F.-R. F. Fan, M. V. Mirkin and P. R. Unwin, in *Annual Review of Analytical Chemistry*, 2008, pp. 95-131.
176. G. Wittstock, M. Burchardt, S. E. Pust, Y. Shen and C. Zhao, *Angew. Chem., Int. Ed.*, 2007, **46**, 1584.
177. S. E. Pust, W. Maier and G. Wittstock, *Zeitschrift Fur Physikalische Chemie-International Journal of Research in Physical Chemistry & Chemical Physics*, 2008, **222**, 1463-1517.
178. P. Bertoncello, *Energy & Environmental Science*, 2010, **3**, 1620-1633.
179. S. Bollo, S. Finger, J. C. Sturm, L. J. Nunez-Vergara and J. A. Squella, *Electrochimica Acta*, 2007, **52**, 4892-4898.
180. Y. M. Bai, P. Sun, M. Q. Zhang, Z. Gao, Z. Y. Yang and Y. H. Shao, *Electrochimica Acta*, 2003, **48**, 3447-3453.
181. X. Lu, Q. Wang and X. Liu, *Analytica Chimica Acta*, 2007, **601**, 10-25.
182. C. M. Lee, J. Y. Kwak and A. J. Bard, *Proceedings of the National Academy of Sciences of the United States of America*, 1990, **87**, 1740-1743.
183. S. M. Fonseca, A. L. Barker, S. Ahmed, T. J. Kemp and P. R. Unwin, *Physical Chemistry Chemical Physics*, 2004, **6**, 5218-5224.
184. C. Amatore, F. Bonhomme, J. L. Bruneel, L. Servant and L. Thouin, *Journal of Electroanalytical Chemistry*, 2000, **484**, 1-17.
185. N. J. Gray and P. R. Unwin, *Analyst*, 2000, **125**, 889-893.
186. M. V. Mirkin, F. R. F. Fan and A. J. Bard, *Journal of Electroanalytical Chemistry*, 1992, **328**, 47-62.
187. B. B. Katemann and T. Schuhmann, *Electroanalysis*, 2002, **14**, 22-28.
188. A. Schulte, M. Nebel and W. Schuhmann, in *Annual Review of Analytical Chemistry, Vol 3*, ed. E. S. Z. R. N. Yeung, 2010, pp. 299-318.
189. E. R. Scott, H. S. White and J. B. Phipps, *Analytical Chemistry*, 1993, **65**, 1537-1545.
190. O. D. Uitto and H. S. White, *Analytical Chemistry*, 2001, **73**, 533-539.
191. M. A. Edwards, S. Martin, A. L. Whitworth, J. V. Macpherson and P. R. Unwin, *Physiological Measurement*, 2006, **27**, R63-R108.
192. M. Tsionsky, Z. G. Cardon, A. J. Bard and R. B. Jackson, *Plant Physiology*, 1997, **113**, 895-901.
193. K. R. Wehmeyer, M. R. Deakin and R. M. Wightman, *Analytical Chemistry*, 1985, **57**, 1913-1916.
194. W. P. Kang, J. L. Davidson, K. L. Soh, Y. M. Wong, D. E. Cliffel, A. B. Bonds and Ieee, in *2006 Ieee Sensors, Vols 1-3*, 2006, pp. 576-579.
195. K. Peckova and J. Barek, *Current Organic Chemistry*, 2011, **15**, 3014-3028.
196. D. R. Macfarlane and D. K. Y. Wong, *Journal of Electroanalytical Chemistry*, 1985, **185**, 197-202.
197. C. G. Zoski, *Electroanalysis*, 2002, **14**, 1041-1051.
198. A. J. Bard, J. A. Crayston, G. P. Kittlesen, T. V. Shea and M. S. Wrighton, *Analytical Chemistry*, 1986, **58**, 2321-2331.
199. T. V. Shea and A. J. Bard, *Analytical Chemistry*, 1987, **59**, 2101-2111.
200. C. Demaille, M. Brust, M. Tsionsky and A. J. Bard, *Analytical Chemistry*, 1997, **69**, 2323-2328.
201. R. J. Forster, *Chemical Society Reviews*, 1994, **23**, 289-297.
202. A. N. Correia and S. A. S. Machado, *Journal of the Brazilian Chemical Society*, 1997, **8**, 71-76.
203. F. Belal and J. L. Anderson, *Analyst*, 1985, **110**, 1493-1496.

204. J. Heinze, *Angewandte Chemie-International Edition in English*, 1993, **32**, 1268-1288.
205. S. Amemiya, N. Nioradze, P. Santhosh and M. J. Deible, *Anal. Chem.*, 2011, **83**, 5928-5935.
206. J. L. Amphlett and G. Denuault, *Journal of Physical Chemistry B*, 1998, **102**, 9946-9951.
207. N. J. Evans, M. Gonsalves, N. J. Gray, A. L. Barker, J. V. Macpherson and P. R. Unwin, *Electrochemistry Communications*, 2000, **2**, 201-206.
208. K. Schrock, A. Schulte and W. Schuhmann, *Electroanalysis*, 2005, **17**, 489-494.
209. W. Nogala, K. Szot, M. Burchardt, F. Roelfs, J. Rogalski, M. Opallo and G. Wittstock, *Analyst*, 2010, **135**, 2051-2058.
210. C. E. Jones, J. V. Macpherson, Z. H. Barber, R. E. Somekh and P. R. Unwin, *Electrochemistry Communications*, 1999, **1**, 55-60.
211. R. D. Martin and P. R. Unwin, *Analytical Chemistry*, 1998, **70**, 276-284.
212. C. M. Sanchez-Sanchez, J. Rodiriguez-Lopez and A. J. Bard, *Analytical Chemistry*, 2008, **80**, 3254-3260.
213. S. Cannan, J. Cervera, R. J. Steliaros, E. Bitziou, A. L. Whitworth and P. R. Unwin, *Physical Chemistry Chemical Physics*, 2011, **13**, 5403-5412.
214. S. Cannan, J. Zhang, F. Grunfeld and P. R. Unwin, *Langmuir*, 2004, **20**, 701-707.
215. C. G. Zoski, N. Simjee, O. Guenat and M. Koudelka-Hep, *Analytical Chemistry*, 2004, **76**, 62-72.
216. A. J. Bard, F. R. F. Fan, J. Kwak and O. Lev, *Analytical Chemistry*, 1989, **61**, 132-138.
217. A. J. Bard, F. F. Fan, D. T. Pierce, P. R. Unwin, D. O. Wipf and F. Zhou, *Science*, 1991, **254**, 68.
218. R. Wiesendanger, *Scanning Probe Microscopy and Spectroscopy; methods and its applications*, Cambridge University Press, Cambridge, UK, 1994.
219. K. McKelvey, M. A. Edwards and P. R. Unwin, *Analytical Chemistry*, 2010, **82**, 6334-6337.
220. A. J. Bard and M. V. Mirkin, *Scanning Electrochemical Microscopy*, Marcel Dekker Inc, New York, **2001**.
221. G. Wittstock, K. J. Yu, H. B. Halsall, T. H. Ridgway and W. R. Heineman, *Analytical Chemistry*, 1995, **67**, 3578-3582.
222. M. V. Mirkin, H. J. Yang and A. J. Bard, *Journal of the Electrochemical Society*, 1992, **139**, 2212-2217.
223. P. R. Unwin and A. J. Bard, *Journal of Physical Chemistry*, 1992, **96**, 5035-5045.
224. J. V. Macpherson and P. R. Unwin, *Analytical Chemistry*, 2000, **72**, 276-285.
225. M. N. Holder, C. E. Gardner, J. V. Macpherson and P. R. Unwin, *Journal of Electroanalytical Chemistry*, 2005, **585**.
226. W. Schuhmann, A. Schulte, M. Etienne, F. Turcu and I. Fritsch, *Abstracts of Papers of the American Chemical Society*, 2003, **226**.
227. C. A. Morris, C.-C. Chen and L. A. Baker, *Analyst*, 2012, **137**, 2933-2938.
228. D. J. Comstock, J. W. Elam, M. J. Pellin and M. C. Hersam, *Analytical Chemistry*, 2010, **82**, 1270-1276.
229. Q. Zhong, D. Inniss, K. Kjoller and V. B. Elings, *Surface Science*, 1993, **290**, L688-L692.

230. C. A. J. Putman, K. O. Vanderwerf, B. G. Degrooth, N. F. Vanhulst and J. Greve, *Applied Physics Letters*, 1994, **64**, 2454-2456.
231. P. Hansma, J. Cleveland, M. Radmacher, D. Walters, P. Hillner, M. Bezanilla, M. Fritz, D. Vie, H. Hansma, C. Prater, J. Massie, L. Fukunaga, J. Gurley and V. Elings, *Appl. Phys. Lett.*, 1994, **64**, 1738.
232. K. McKelvey, M. E. Snowden, M. Peruffo and P. R. Unwin, *Analytical Chemistry*, 2011, **83**, 6447-6454.

2 Materials, Instrumentation and Techniques

This section explains and defines the materials, reagents, instrumentation, apparatus and experimental techniques used during characterisation experiments described within this thesis.

2.1 MATERIALS

2.1.1 Boron Doped Diamond Samples

The BDD samples used throughout this thesis were grown and prepared by (E6) using a commercial MWCVD[1] system with methodologies developed in house for the growth of pBDD and scBDD. Although the exact method of growth is unknown, typically methane and hydrogen gases are used in the growth process at temperatures in the range 700 – 950 °C along with a boron containing gas typically diborane.

For this study the single crystal (sc) substrate used during CVD scBDD growth was a HPHT diamond of either (100) or (110) orientation, due to the homoepitaxial growth of sc material on the substrate. The growth of capping layers on scBDD formed part of a systematic study by E6 of growth conditions relating to temperatures, pressure, methane gas ratio and diborane concentration leading to the identification of optimal growth conditions for scBDD. Therefore some of the samples provided were of a scBDD bulk concentration, others with higher boron content within a capping layer, all samples discussed herein were unique.

Commercially available large (100-150 mm diameter) diamond seeded Si wafers are used by E6 for the growth of pBDD. The pBDD provided is ~500 μm thick with a surface roughness of ~1-3 nm measured by AFM.[2] The scBDD samples have been prepared with different crystallographic orientations, different dopant densities and different surface finishes. scBDD samples were provided either as scaife polished as described in section 1.1.5 or with an as grown surface (no polishing performed). Initial BDD sample details are described in Table 2.1.

Table 2.1. Showing BDD sample orientations, surface finish, sample size and sample thickness.

Sample	Orientation	Surface Finish	Sample Size / mm	Thickness / μm
HB2	(100)	**Scaife polished**	5 × 5	570
85A/B	(100)	**As grown**	3.5 × 3.5	260
05A	(110)	**As grown**	3 × 5	250
85F/G	(110)	**As grown**	3 × 4.5	460
CP09	(111)	**Scaife polished**	2 × 4.5	450
MR14	pBDD	**Lapping polished**	5 × 5	~500

2.1.2 Chemicals

All solutions were prepared using Milli-Q water (Millipore Corp.) with a resistivity of 18.2 MΩ at 25 °C followed by sonication using a Decon FS2006 sonicating bath at room temperature to ensure thorough dissolution. All solutions were used at room temperature and if stored overnight kept at + 4 °C. Chemicals used herein are detailed in Table 2.2.

Table 2.2. Chemicals, formula, purity and supplier used herein.

Chemical name	Formula	Details	Supplier
Dichlorodimethylsilane	$C_2H_6Cl_2Si$	99+%	AcrosOrganics
Ferrocenylmethyl trimethylammonium-Hexafluorophosphate	$FcTMA.PF_6$	n/a	Madein house[3]
Iron (II) sulphate	$FeSO_4$	Lab Reagent Grade	FisherChemical
Potassium chloride	KCl	99%	Sigma-Aldrich Co.
Potassium ferrocyanide (II)hydrate	$K_4Fe(CN)_6 .3H_2O$	99.99% Metals Basis	Sigma-Aldrich Co.
Potassium gold (III) chloride	$KAuCl_4$	99.995% Trace Metal Analysis	Sigma-Aldrich Co.
Potassium nitrate	KNO_3	99%	Sigma-Aldrich Co.
Potassiumhexachloro iridate (IV)	K_2IrCl_6	99.99%	Sigma-Aldrich Co.
Ruthenium (III) hexaamine	$Ru(NH_3)_6^{3+}$	99%	Sigma-Aldrich Co.
Sodium perchlorate hydrate	$NaClO_4$	99%+	Sigma-Aldrich Co.
Sulphuric acid (Acid Cleaning)	H_2SO_4	Assay 98%	BDH
Sulphuric acid (Supporting Electrolyte)	H_2SO_4	99.99%	Sigma-Aldrich Co.
Tris(bipyridine)ruthenium (II)chloride	$Ru(bpy)_3.Cl_2$	99%	Sigma-Aldrich Co.

2.2 BORON DOPED DIAMOND ELECTRODE PREPARATION

2.2.1 Acid Cleaning

All BDD utilised as an electrode material, required an initial acid clean to remove any contamination on the diamond surface. The diamond was cleaned in a concentrated H_2SO_4 solution (98%) super-saturated with KNO_3. The solution was heated until boiling, until the KNO_3 was exhausted. This was shown by the reaction gas changing colour from brown to a white (around thirty minutes). Once the cleaning solution had cooled, the sample was removed and rinsed in Milli-Q water. A second acid clean using boiling concentrated H_2SO_4 (98%) was performed for 30 minutes, once the solution was cool, the sample was removed, thoroughly rinsed in Milli-Q water and allowed to air dry laid on lint free cloth.[2] The acid clean procedure ensures the diamond surface is clean, O-terminated and hydrophilic.[4]

2.2.2 Creation of an Ohmic Contact

An effective ohmic contact is required to electrically connect to the BDD for subsequent electrical and electrochemical measurements. Using a Moorfield Minibox sputter coating instrument, the back of the BDD was coated in 10 nm Ti followed by 200 nm of Au, the samples mounted using a mask to ensure only the reverse of the material was sputtered. To generate an ohmic contact, the sputtered BDD was annealed in air at 500 °C for four hours using a Carbolite MTF 10/25/130 furnace oven and left to cool. Under these annealing conditions a Ti carbide tunnelling contact is established.[5]

2.2.3 Back Contacted Electrode Fabrication

Using silver electrodag (Agar Scientific, UK), the sputtered scBDD was ohmically contacted to sputtered Ti/Au quartz disc. Tinned copper wire was also electrically contacted to the Au surface of the quartz disc using the silver electrodag. The surround to the mounted diamond surface was then sealed in epoxy resin (Araldite, Bostick Findley, UK) leaving only the top surface of the scBDD electrode exposed for electrochemical and/or physical analysis. The resin also ensures that contact between the diamond and backing quartz disc is maintained during electrochemical measurements. This can be seen in Figure 2.1.

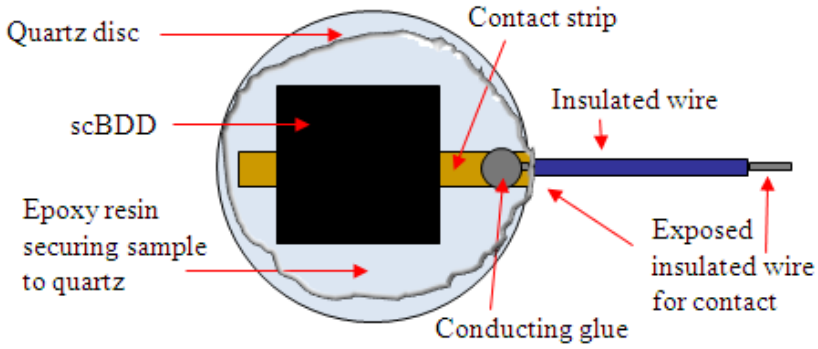

Figure 2.1. Schematic showing the fabrication of a scBDD electrode to quartz disk (not to scale).

2.2.4 Macrodisc Electrode Fabrication

To create electrodes of well defined dimensions, 1 mm diameter discs were cut from the samples provided, using a laser micromachiner (9E-355H-3-ATHI-O system, Oxford Laser).

The sputtered diamond macrodisc was sealed within an insulating borosilicate glass capillary (o.d. 2 mm, i.d. 1.16 mm, Harvard Apparatus Ltd, UK). Electrical contact was made to the back of the insulated diamond using a conducting

wire and Circuit Works Conductive Epoxy (ITW Chemtronics, USA) filling the capillary. The end of the capillary was sealed using epoxy resin to aid electrode stability, leaving the conducting electrical contact wire exposed, as shown in Figure 2.2, this method was developed by Hutton *et al.*[6]

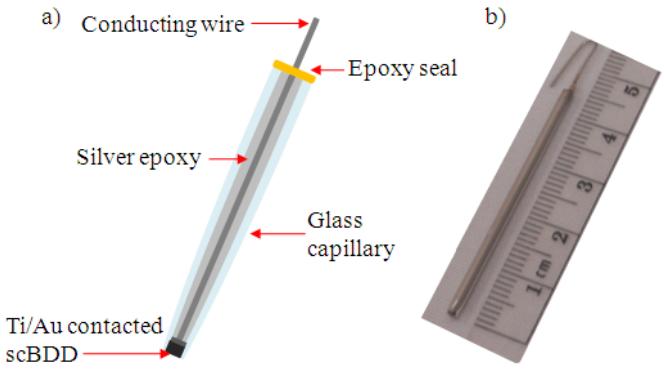

Figure 2.2. a) Schematic and b) photograph of a fabricated 1 mm diameter scBDD macrodisc electrode insulated within a glass capillary.

Careful polishing using a range of graded abrasive SiC paper (Beuhler, U.S.A) exposes only the diamond electrode surface, surrounded by the insulating glass sheath. The electrode format replicates existing commercially available electrodes,[6] geometries can be directly compared to commercially available electrodes (e.g. Au or Pt).[7]

To test how well an electrode is sealed, electrochemical cycling in 0.5 M H_2SO_4 is performed in a three electrode system as described later. If any Au is exposed within the fabric of the macrodisc electrode a characteristic Au oxide stripping peak is observed during the CV as shown in Figure 2.3. If any Au is detected, the electrode is unusable and carefully refabricated followed by subsequent testing.

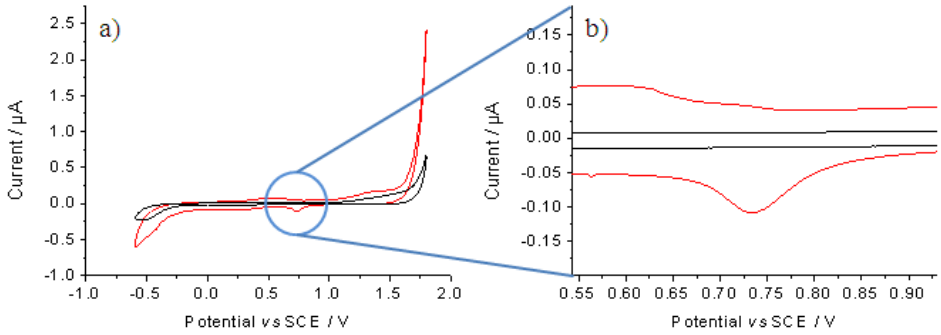

Figure 2.3. a) CV of a well-sealed (black) and poorly sealed (red) 1 mm macrodisc electrode cycled in 0.5 M H_2SO_4 using 100 mVs^{-1} scan rate. b) Increased magnification of a) clearly showing the Au oxide stripping peak of the poorly sealed electrode.

2.3 INSTRUMENTATION AND TECHNIQUES

The characterisation techniques described generally utilised the scBDD material in its original format, prepared as described previously and mounted as shown in Figure 2.1.

2.3.1 Secondary Ion Mass Spectrometry (SIMS)

In order to quantitatively determine the [B] (cm^{-3}) within the thin film scBDD samples, analysis of the samples is undertaken using SIMS.SIMS is capable of detecting all elements and their isotopes, however the disadvantage of this technique is local destruction of the surface being analysed.[8]

scBDD samples were provided post SIMS which was undertaken by Loughborough Analytical Science, Loughborough, UK. Analysis of the [B] of the bulk and capped layer samples were performed providing cap layer thickness where applicable.

2.3.2 Differential Interference Contrast Microscopy (DICM)

This technique is used to image samples which show little or no optical contrast when viewed using brightfield illumination.[9] The use of a Wollaston prism splits the polarised light beam in two. The two beams travel in slightly different directions but vibrate perpendicular to each other, this prevents the beams from recombining. The two beams hit the sample where their paths are amended due to the sample slope, thickness and refractive index.

The split beams enter a second modified Wollaston prism that allows the beams to recombine. The single beam is processed to the eyepiece where differences in colour and intensity highlights sample topography differences. In this form, DICM cannot be used to quantify heights or depths of a sample, however it can be used qualitatively to provide information on surface height heterogeneities. DICM images were taken using a Zeiss Axio Imaga.M1m with an Axio Cam 1Cc 3 using magnifications in the range 5 - 50.

2.3.3 Field Emission-Scanning Electron Microscopy (FE-SEM)

FE-SEM provides information under vacuum relating to substrate morphology by scanning a beam of electrons (typical range 1-10 nm) across a surface whilst the electron-sample interactions are analysed by selected detectors.[10] Large areas of a sample can be interrogated with FE-SEM.

Electrons are generated by means of a field emission gun and these are focussed onto the sample using electromagnetic lenses and accelerate at speeds selected by the operator which can be between 1 to 30 keV,[10] dependent on the sample under analysis. When the electrons hit the surface of the sample several

different interactions can occur, these produce secondary electrons, back scattered electrons and others as shown in Figure 2.4.

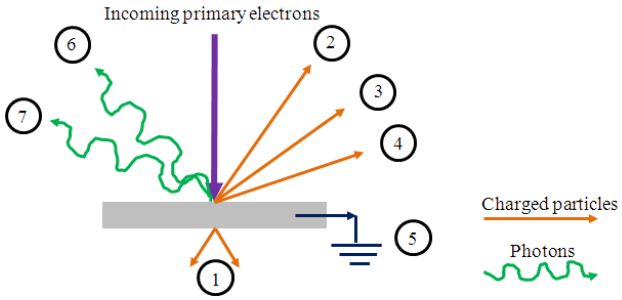

Figure 2.4. Schematic showing possible emission from a surface following electron bombardment within FE-SEM. 1; transmitted electrons, 2; secondary electrons, 3; backscattered electrons, 4; Auger electrons, 5; absorbed current, 6; X-rays and 7; cathodoluminescence.[10]

If a thick sample is under analysis, inelastic scattering occurs where energy from the incident beam is transferred to the atoms within the sample, this develops into low energy secondary electron emission, which is a function of the sample topography. This method of electron detection can be used to study uniformity, particle sizes and sample morphology and it can provide extremely high resolution images when used with the In-Lens detector.[11] When electrons are reflected by surface atoms, elastic scattering occurs, these are called backscattered electrons and have very high energy, and they are able to provide compositional information about the sample under investigation.

SEM has been routinely used to investigate pBDD for the distribution of incorporated boron, grain boundaries and grain morphology.[12] Figure 2.5a shows an example of polished pBDD from secondary electron emission where growth features are clearly evident and Figure 2.5b a backscattered electron image of the same area.[12]

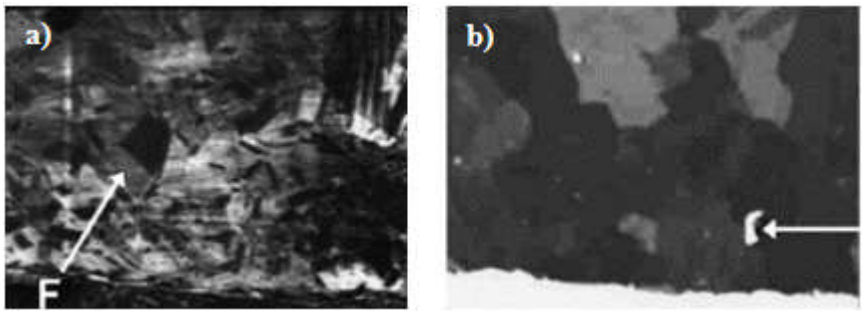

Figure 2.5. Contrasting SEM images of polished pBDD in the same areas by a) low voltage (1 keV) secondary electron emission and by b) high voltage (15 keV) backscattered electrons.[12]

The contrasts observed within Figure 2.5a are due to differing [B] within crystal orientations, therefore variation in conductivity, whereby areas of higher [B] enhance secondary electron emission leading to brighter areas. Grain clusters with identical growth directions are observed in Figure 2.5b, the contrast in this image result from the intensity of the backscattered electrons which are dependent on the crystal lattice planes with respect to the incident electron beam.[13] For homogeneous scBDD such differences as seen in Figure 2.5 would be greatly reduced if seen at all.

FE-SEM images herein were recorded using a Zeiss Supra55VP with an In-Lens detector operated typically at 2 keV with a working distance of ~5 mm, although images were also recorded using 5, 10 and 15 keV.

2.3.4 Cathodoluminescence (CL)

CL uses a beam of electrons created by an electron gun via SEM as shown in Figure 2.4. The beam of electrons impacts on luminescent material causing the material to emit a wide range of photon frequencies within the electromagnetic spectrum, commonly detecting wavelengths in the UV, visible and infra-red regions (100-900 nm).[14]

Combined SEM and CL images were recorded using a Jeol JSM-6100 SEM in conjunction with a Gatan Mono CL system comprising of a parabolic mirror, photomultiplier tube and a Peltier cooled, charged couple device as the detector, operating in pan-chromatic mode, thereby covering a wide range of wavelengths.

2.3.5 Atomic Force Microscopy (AFM)

AFM is capable of providing nanoscale topographical *x*, *y*, *z* maps of surfaces,[15] which can be performed in air or under fluid. A schematic of a typical AFM instrument is shown in Figure 2.6.

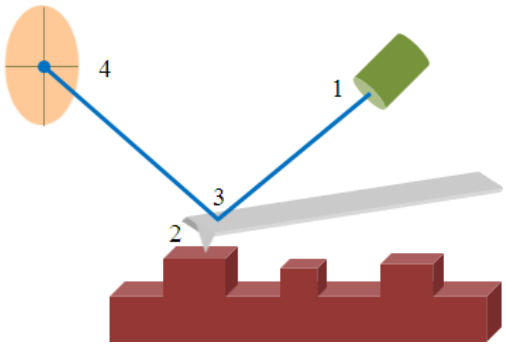

Figure 2.6. Schematic of the AFM. 1) Laser beam is shone onto the cantilever as 2) the tip scans across the surface of the sample. 3) The laser reflects off the back of the cantilever and into 4) a photodiode detector.

A laser shines onto the back of a force sensitive cantilever, close to the end, from which protrudes a sharp tip. Reflections of the laser in response to a force between tip and surface are recorded by on position sensitive photodiode. Contact mode (CM) AFM is performed by keeping the force the tip experiences constant as the tip scans over the surface,[15,16] whilst in intermittent contact or tapping mode (TM) AFM the cantilever oscillation amplitude is kept constant.[17, 18]

To investigate BDDs bare and functionalised surface topography, TM-AFM images were recorded in air using a Veeco Multimode V AFM with Nanoscope IV controller. Diamond is the hardest known substance to man and imaging diamond blunts probes tips very quickly therefore the AFM tip (RFESP Sb doped Si, Veeco Probes) was regularly replaced. For the AFM analysis of HB2 and Au NPs on a scBDD macrodisc electrode, TM using SNL tips (Bruker Probes) with Bioscope Catalyst AFM and ScanAsyst™ software was employed. Recorded images were analysed using Scanning Probe Imaging Processor (SPIP™) software, version 5.1.5 (Image Metrology) to determine NP size and density.

2.3.6 Micro Raman Spectroscopy

Raman spectroscopy is a non-destructive form of vibrational spectroscopy sensitive to symmetrical bonds.[19] In Raman microscopy, the sample is exposed to a laser (monochromatic light source). The incident photons excite the sample surface to a 'virtual' excited state, which decays to vibrational levels above/below the original state (Raman), either elastically or inelastically. Raman uses inelastic scattering[20] from the laser source. The energy difference between the incident and scattered photon is called the 'Raman shift' and is attributed to an anti-stokes shift if the photon is at a higher energy or stokes shift if at a lower energy.

Raman requires little sample preparation and employs a microscope for sample focussing ensuring the sample is in focus when the laser is in operation. The laser power intensity can be amended, thereby reducing the laser spot size hitting the sample. This allows for increased precision when necessary and is projected into the data collection and processing software. The data gathered can be used to determine

information on the sp^3 (diamond) – sp^2 (non-diamond) nature of the sample, which provides information on the quality of the scBDD.

Individual peaks in the Raman spectra can be assigned to specific bonds. A spectrum of Raman shift (essentially wavenumber with units of cm^{-1}) against Raman intensity is plotted and Raman spectroscopy can determine between types of carbon, looking at for example sp^3 (tetrahedral) bonds found in diamond (1332.5 cm^{-1}) and planar sp^2 bonds (~1550 cm^{-1}) found in graphitic carbon as shown in Figure 2.7.

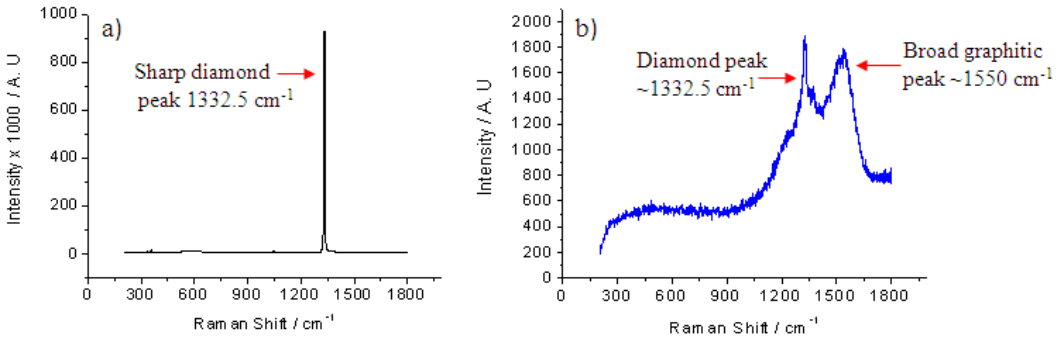

Figure 2.7. Raman spectra using 514nm laser source showing a) the characteristic diamond peak (1332.5 cm^{-1}) of intrinsic diamond (laser spot size 3 µm). b) A poor quality pBDD sample showing diamond and graphitic carbon (~1550 cm^{-1}) peaks (laser spot size 6 µm).

For high quality intrinsic diamond material, a symmetrical peak at 1332.5 $cm^{-1}$is expected as seen in Figure 2.7a, referred to as the 'zone centre peak optical phonon line'. When BDD is analysed using Raman, the zone centre phonon peak shifts downwards slightly and the area under the peak decreases. The peak, if the sample contains enough boron, will become asymmetrical and distorted, this is known as Fano resonance.[21] Fano resonance is attributed to the introduction of boron at such concentrations into the crystal lattice that the onset of metal-like conductivity is thought to occur, typically at concentrations $\geq 1 \times 10^{20}$ atoms cm^{-3}.[22] An example of Fano resonance is seen in Figure 2.8.

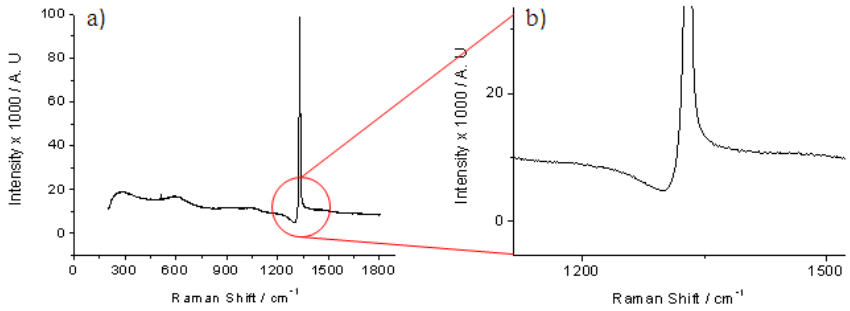

Figure 2.8. Raman spectra demonstrating a) Fano resonance on scBDD therefore suggesting [B] ≥ 1 × 10^{20} cm^{-3}. b) Increased magnification of a), clearly showing peak asymmetry. Spectra recorded using 514 nm laser, spot size 6 µm.

To provide information on the quality of the scBDD grown and qualitatively assess the amount of boron in the material, Raman measurements were performed at room temperature using a Renishaw invia reflex microscope equipped with an automatic sample stage in conjunction with a514 nm Ar^{+}(output ~6 mW) or 633 nm He-Ne laser (output 17 mW). For nine point surface mapping of the scBDD samples, ten accumulations of 60 s duration at 100 % laser power were undertaken. For highly defected samples, Raman was used to line scan across an area of the surface containing a defect and four accumulations of 10 s each were recorded.

On selected samples maps (100-200 μm^2) were performed at room temperatures using a Renishaw invia reflex microscope equipped with an *x*, *y* automatic sample stage in conjunction with a 514 nm $Argon^{+}$ laser (output ~6 mW) with a Peltier-cooled CCD detector. The spectrometer was equipped with an 1800 line / mm diffraction grating. Mapping parameters were sample dependent generally with single accumulations of < 3 s and laser power ranging from 1-100 %. The area under the peak or peak intensity ~1332 cm^{-1} was extracted using Wire 3.0 software and plotted as a function of *x*, *y* position. The spot size was 1-6 µm in

diameter, the spot intensity was greater in the centre. Raman spectra were recorded every 2 or 3 μm over the wavenumber range 1300-1400 cm^{-1}.

2.4 ELECTROCHEMICAL INSTRUMENTATION AND TECHNIQUES

2.4.1 Double Layer Capacitance Measurements (C_{meas})

C_{meas} of the BDD fabricated as 1 mm macrodisc electrodes (section 2.2.4) were undertaken using a bipotentiostat (CHI760C Electrochemical Workstations, CH Instruments Inc, USA). Using a fresh solution of 0.1 M KNO_3, the potential was swept from 0 V in the positive direction to 0.1 V and reversed in the negative direction back through 0 V sweeping back in the positive direction upon reaching -0.1 V, finishing at 0 V, six sweeps were recorded consecutively at a potential scan rate of 100 mV s^{-1}, with respect to SCE.

2.4.2 Cyclic Voltammetry (CV)

CV experiments were recorded using a bipotentiostat (CHI760C Electrochemical Workstations, CH Instruments Inc, USA) typically the following electrodes were employed; BDD (WE), Ag|AgCl (CH Instruments Inc, USA) or SCE (BAS Inc, Japan) as the RE and a coiled Pt wire (CE).For some experiments, 3 mm diameter GC electrode, Au and Pt electrode (2 mm diameter electrodes) were employed as the WE, as shown in Figure 2.9. All CV experiments were performed within a Faraday cage to reduce any background electrical noise and the room

temperature was recorded at 21 ± 1 °C controlled by air conditioning. CVs were typically recorded over a wide range of experimental scan rates (10-1000 mV s^{-1}) with different redox species at a range of concentrations.

Prior to use, all electrodes were manually mechanically polished using alumina slurry (50 nm particles) (Buehler, Germany)on a micro-cloth polishing pad (Buehler, Germany), followed by rinsing with Milli-Q water. This was repeated using a slurry free micro-cloth polishing pad saturated with Milli-Q water to ensure a clean electrode surface prior to any CV being undertaken.

The scBDD samples were formatted as macrodisc electrodes for CV, the fabrication has been previously described in section 2.2.4. Figure 2.9 shows a fabricated BDD electrode along with commercially available electrodes also used during this study. During CV experiments a single WE was dipped into redox mediator solution along with the C and RE as shown in Figure 2.10.

Figure 2.9. Image showing a pBDD (1 mm), Pt (2 mm), Au (2 mm) and GC (3 mm) electrodes used throughout this study. Image courtesy of Jon Newland.

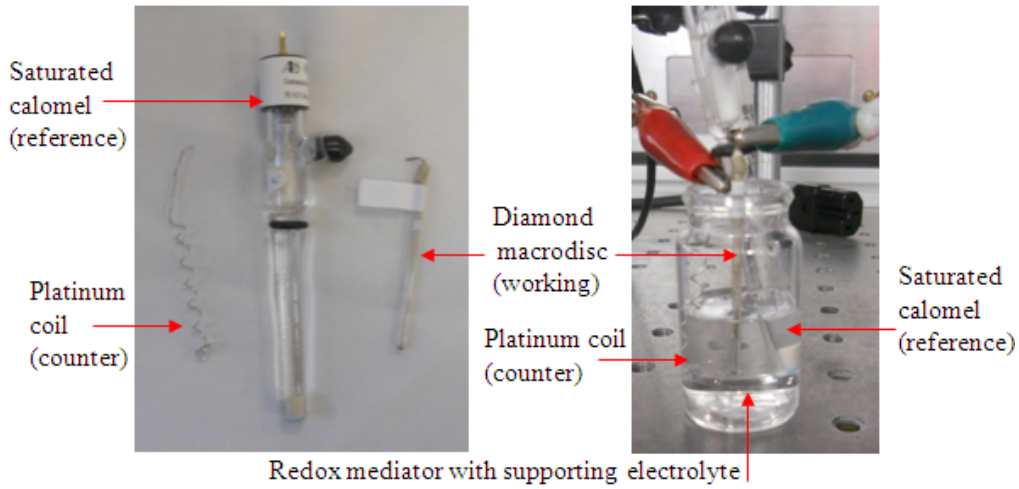

Figure 2.10. Image showing the electrodes used in CV and experimental set up for CV experiments.

2.4.3 Ultra Micro Electrode (UME) Fabrication

25 and 10 µm UMEs were fabricated in-house using standard techniques,[23] a schematic is shown in Figure 2.11.

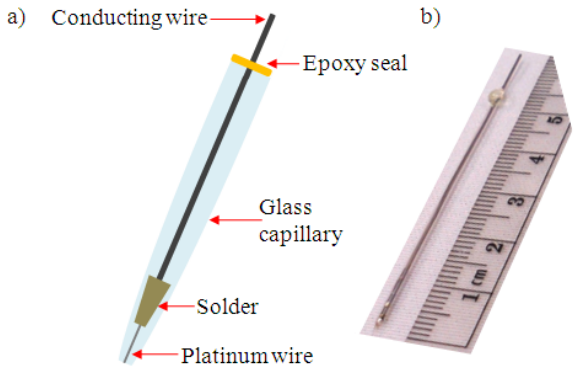

Figure 2.11. a) Schematic and b) photograph of a UME fabricated in-house.

Briefly, borosilicate capillaries (o.d. 1.0 mm, i.d. 0.58 mm, Intracel Ltd, UK) were heat pulled (Narishige, Japan, Model PB-7) into two separate capillaries, which were sealed at the pulled end using the hottest part of a Bunsen flame. A small piece

of 25 or 10 µm Pt wire (Goodfellow Cambridge Ltd) was inserted into the sealed capillary end. The sealed end of the capillary containing the Pt wire was carefully positioned within the coiled heat source of the puller. A vacuum is applied and left for ~15 minutes to allow for full evacuation of air within the capillary, this is to prevent air bubbles when partially heat sealing the wire within the capillary, some Pt wire is left unsealed in-order to make an electrical connection.

Optical microscopy is used to check for any air bubbles before the insertion of a solder piece followed by a protruding length of tinned copper wire. An external heat source is applied to the capillary, melting the piece of solder, thereby connecting the Pt wire to the tinned copper wire. Optical microscopy confirms a visual electrical connection and the open end of the UME is sealed with epoxy resin to aid stability.

Electrochemical testing of the UME is performed once the Pt wire has been exposed by a polishing process. UMEs require careful polishing (coning) to expose the glass sealed Pt wire and also to ensure a round even glass sheath. Coning was achieved using a range of graded SiC abrasive paper (Beuhler, Germany), before final polishing using a homemade polishing wheel set up using a 0.1 µm polishing pad (Buehler, Germany). The UME must be flat therefore polishing of the tip is performed coplanar to a flat surface, this is confirmed using optical microscopy.

2.4.4 Constant Height-Scanning Electrochemical Microscopy (CH-SECM)

Within a Faraday cage to prevent interference via electrical noise, the sample was mounted as shown in Figure 2.1 within a Teflon cell and the UME coarsely positioned overhead vertically using *x, y, z* stepper motors (PI M-112 1DG). Followed by precise positioning using *x* and *y* piezoelectric positioners

(nanocube PI P-625-2CD) with a maximum travel of 400 µm in both the *x* and *y* directions, the UME was approached to the surface using a *z* piezoelectric positioner (max travel 100 µm, PI P-621 ZCD), controlled by a bespoke computer programme written in LabVIEW (LabVIEW 9.0, National Instruments (NI)).

CH-SECM utilised 1 mM $FcTMA^+$ in 0.1 M KNO_3, employed in conjunction with coiled Pt wire (CE) and Ag|AgCl (RE). CVs and amperometric current-time (*i*-*t*) curves (used in SG-TC mode) were performed using a bipotentiostat (CHI760C, CH Instruments, USA). The scBDD substrate driven at 100 mV s^{-1} and the 25 µm UME at 20 mV s^{-1} independently during CVs, these were repeated prior to and after any scans being performed to ensure no adverse effects of the redox mediator were interfering with the resulting electrochemical behaviour of the scBDD or the UME.

Scan sizes were typically 200 × 200 µm. CH-SECM was performed in raster formation, starting at 0, 0 in *x* and *y* before travelling in the *x* direction. Data points were recorded every ~10 µm and current data was recorded from the forward scan. The potentials (*E*) selected for SG-TC measurements on scBDD were chosen based on initial CVs recorded in order to establish the half wave potential ($E_{½}$). The substrate was held at potentials either > or < $E_{½}$.

2.4.5 Approach Curves

Initial CVs determined the UME i_{lim} (typically 0.5 V) such that the oxidation of $FcTMA^+$ to $FcTMA^{2+}$ would be under diffusion limited control. Approach curves were performed whilst applying the i_{lim} to the UME tip, the tip approach (using *z* piezoelectric positioner) was stopped manually when the tip touched the substrate, this could be determined from a sharp increase in current recorded at the tip because the experimental apparatus arrangement causes a short circuit. The current at this

point was noted and used to aid subsequent approach curves. In all cases, post approach curve and pre scan initiation, the tip was retracted 5 µm and fixed at this distance from the substrate for the scan duration.

2.4.6 Intermittent Contact -Scanning Electrochemical Microscopy (IC-SECM)

10 µm UMEs were fabricated in-house as described in 2.4.3, a schematic is shown in Figure 2.11. Situated within a Faraday cage to reduce external electrical noise, the 10 µm Pt UME (RG < 10) was oscillated (section4.1.2) using an AC Generator (TG100 Low Distortion) combined with a *z* bender piezoelectric positioner (PI E651 1-channel) controlled through a data acquisition (DAQ) break out board (NI BNC-2110). To avoid electrical noise from mains electricity (multiples of 50 Hz), tip oscillation was performed at 70 Hz, generally leading to tip dampening of ~5 % calculated from the initial approach curves.

For IC-SECM imaging studies scBDD samples were initially fabricated as shown in Figure 2.1. Experience in SECM led to the insulation of the majority of the scBDD samples with epoxy resin followed by nail varnish to prevent epoxy leaching. This leaves a small window of diamond material exposed to the imaging technique. The sample was mounted and UME positioned as described above (2.4.4). Figure 2.12 shows an image of the laboratory apparatus set up for SG-TC mode.

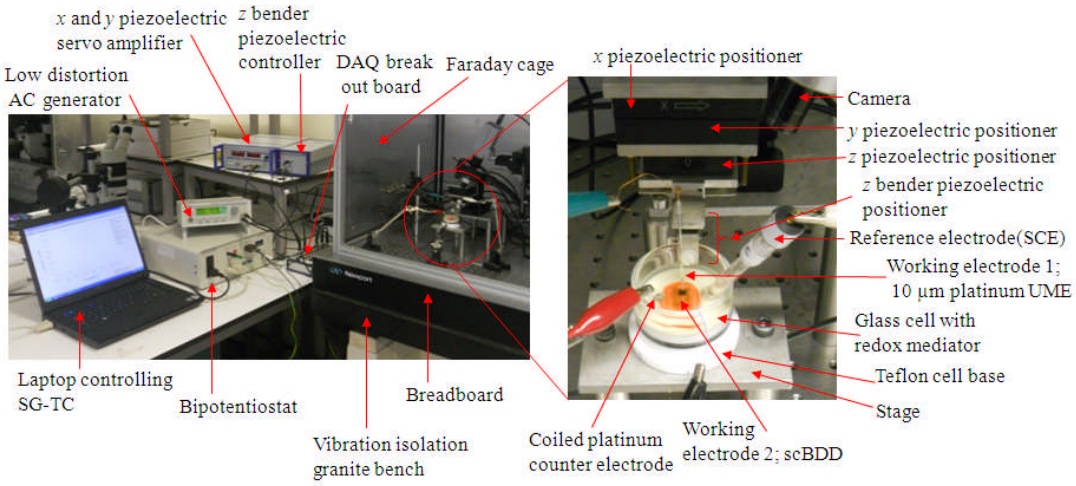

Figure 2.12. Image of IC-SECM apparatus and electronic components.

Redox mediators of 1 mM $Ru(NH_3)_6^{3+}$ in 0.1 M KNO_3 and 1 mM $FcTMA^+$ in 0.1 M KNO_3, were employed in conjunction with a coiled Pt wire (CE) and SCE (RE). CVs, amperometric *i-t* curves used in SG-TC mode and the *E* selected have been described previously (2.4.4).

Typical scan sizes were 200 × 200 µm with 0.25 µm sub steps. Data points recorded every ~10 µm and data was recorded from the forward scan (current), *z* piezoelectric positioner height (µm), reverse scan (current) and reverse *z* piezoelectric positioner height (µm).

2.4.7 Finite Element Modelling (FEM)

In order to quantify 1 mm macrodisc and UME currents observed, FEM was undertaken simulating a theoretical current response as a function of k^0 using Butler-Volmer kinetics.[24] This was performed in house using a commercial FEM package; COMSOL Multiphysics 3.5a or 4.2a (COMSOL AB, Sweden) with a Matlab

Interface (Release 2010a) (Mathworks Inc., Cambridge, UK). Specifications provided in sections 3.2.6 and 4.1.3.

2.4.8 Deposition of Gold Nanoparticles using Microcapillary Electrochemistry (MCEM)

The MCEM technique is utilised herein to electrochemically deposit metal NPs on scBDD acting as the WE. Borosilicate capillaries (o.d. 1.0 mm, i.d. 0.58 mm, Intracel Ltd, UK) were pulled to defined point using a laser pipette puller (Model P-2000, Sutter Instruments Laser Puller, U.S.A). These were polished flat using a homebuilt polishing wheel arrangement where the capillary was held vertical with respect to the polishing disk (0.5 µm polishing pad, Buehler, Germany). Typically, capillaries with internal diameters ~ 50 to 70 µm were used measured using an optical microscope to verify the inner dimensions and to check for the absence of cracks/residual glass threads from the laser pull or the polishing wheel as shown in Figure 2.13.

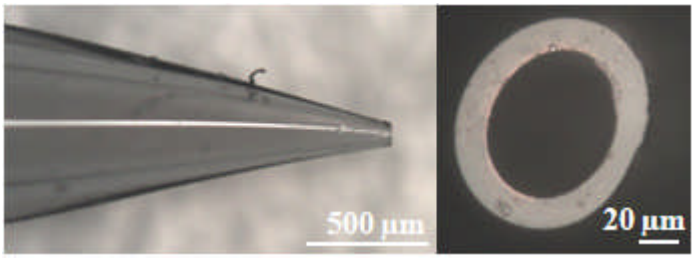

Figure 2.13. Images of a polished laser pulled micro capillary used during the deposition of NPs. Actual internal diameter 60 ×68 µm.

Prior to electrolyte filling, the capillary was connected to a low pressure Ar gas flow and dipped into *dimethyldichlorosilane* (Acros Organics) for 120 s to silanise the tip outer walls. The capillary was then dried in air whilst maintaining

Argas flow for a further 60 s, to prevent residual silane solution entering the capillary. Silanisation of the external capillary wall prevents electrolyte solution spreadingout of the end of the capillary.

The experimental set up is shown in Figure 2.14. The back contacted scBDD electrode, as shown in Figure 2.1 was mounted on a Teflon cell base with a protruding stage. A glass cell with a 30 mm diameter optical window was fitted to the cell base.A camera (PixeLINK, Edmund Optics, UK) was employed to help position the capillary on the electrode surface as shown in Figure 2.14. The cell was saturated with a small volume of aqueous saturated KCl, used to prevent evaporation of the redox mediator from within the cell environment. When in operation the capillary housed a quasi RE which was a 50 µm diameter Ag wire with a thick coating of AgCl.

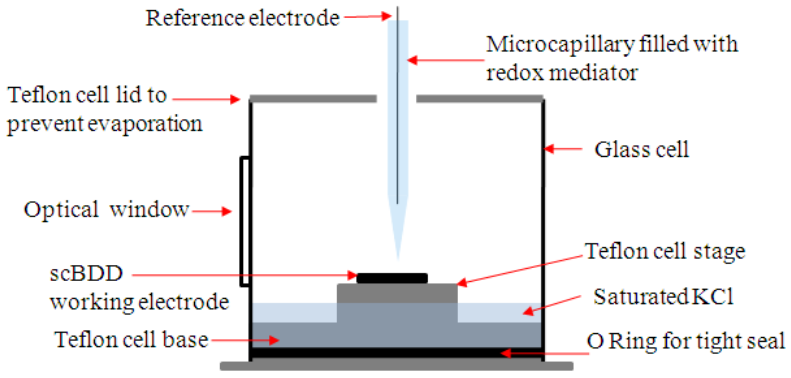

Figure 2.14. Schematic of the apparatus used during MCEM for the deposition of Au NPs (not to scale).

Using a fine syringe (Microfil 34 Gauge, World Precision Instruments, USA) the capillary was filled with 1 mM $KAuCl_4$ in 0.1 M $NaClO_4$. The quasi Ag|AgCl RE was inserted into the capillary. The capillary was mounted and manually controlled by Newport (New Jersey, U.S.A) *x*, *y*, *z* micro positioners. Using the

camera, the capillary was carefully approached to the surface of the WE such that only the meniscus of the capillary touched the electrode surface as shown in Figure 2.15.

CVs were performed using a scan rate of 100 mV s^{-1}. From initial CVs, deposition potentials (V_{dep}) were selected for further analysis using single step chronoamperometry relating to the initiation and subsequent growth of the NPs.

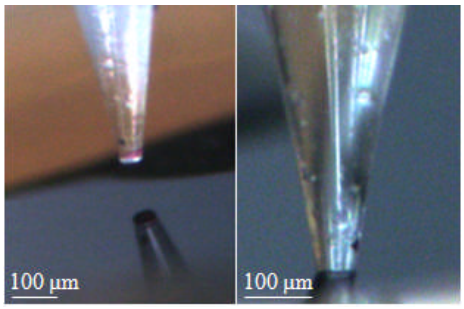

Figure 2.15. a) Micro capillary approach to scBDD surface, the reflection is clearly visible and used to guide the approach. b) The contact of the solution meniscus to the substrate such the capillary walls do not touch the surface.

2.4.9 Deposition of Gold Nanoparticles employing a Boron Doped Diamond Macrodisc Electrode

scBDD macrodisc electrodes were placed into a solution of 1 mM $KAuCl_4$ in 0.1 M $NaClO_4$,. Due to the size of the WE,a three electrode set up using a Pt coiled wire (CE) and Ag|AgCl RE as shown in Figure 2.10, was employed. Deposition potentials were selected from CVs, recorded at a scan speed of 100 mV s^{-1} as described above.

2.5 REFERENCES

1. I. Friel, S. L. Clewes, H. K. Dhillon, N. Perkins, D. J. Twitchen and G. A. Scarsbrook, *Diamond and Related Materials*, 2009, **18**, 808-815.
2. N. R. Wilson, S. L. Clewes, M. E. Newton, P. R. Unwin and J. V. Macpherson, *The Journal of Physical Chemistry B*, 2006, **110**, 5639-5646.
3. I. Dumitrescu, P. R. Unwin, N. R. Wilson and J. V. Macpherson, *Analytical Chemistry*, 2008, **80**, 3598-3605.
4. A. L. Colley, C. G. Williams, U. D'Haenens Johansson, M. E. Newton, P. R. Unwin, N. R. Wilson and J. V. Macpherson, *Analytical Chemistry*, 2006, **78**, 2539-2548.
5. T. Tachibana, B. E. Williams and J. T. Glass, *Physical Review B*, 1992, **45**, 11975-11981.
6. L. Hutton, M. E. Newton, P. R. Unwin and J. V. Macpherson, *Analytical Chemistry*, 2009, **81**, 1023-1032.
7. http://www.chinstruments.com/accessories.shtml.
8. A. Adriaens and M. G. Dowsett, *Applied Surface Science*, 2006, **252**, 7096-7101.
9. D. Murphy, *Differential Interference Contrast (DIC) microscopy and modulation contrast microscopy; Fundamentals of light microscopy and digital imaging.*, Wiley-Liss, **2001**.
10. I. M. Watt, *The Principles and Practice of Electron Microscopy.*, Cambridge University Press, **1997**.
11. P. R. Thornton, *Scanning Electron Microscopy: applications to materials and device science.*, Chapman & Hall, London, 1968.
12. J. W. Steeds, A. E. Mora, S. J. Charles, D. J. F. Evans and J. E. Butler, *Materials Chemistry and Physics*, 2003, **81**, 281-285.
13. E. M. Schulson, *Journal of Materials Science*, 1977, **12**, 1071-1087.
14. D. Briggs and M. P. Seah, *Practical Surface Analysis: by Auger and x-ray photoelectron spectroscopy.*, Wiley, New York, 1983.
15. C. F. Quate, *Surface Science*, 1994, **299**, 980-995.
16. G. Binnig, C. F. Quate and C. Gerber, *Physical Review Letters*, 1986, **56**, 930-933.
17. F. Moreno-Herrero, J. Colchero, J. Gómez-Herrero and A. M. Baró, *Physical Review E*, 2004, **69**, 031915.
18. J. P. Aime, R. Boisgard, L. Nony and G. Couturier, *The Journal of Chemical Physics*, 2001, **114**, 4945-4954.
19. S.-N. Yuen, S.-M. Choi, D. L. Phillips and C.-Y. Ma, *Food Chemistry*, 2009, **114**, 1091-1098.
20. D. A. Long, *Raman Spectroscopy*, McGraw-Hill, New York, 1977.
21. J. P. Lagrange, A. Deneuville and E. Gheeraert, *Diamond and Related Materials*, 1998, **7**, 1390-1393.
22. E. Gheeraert, P. Gonon, A. Deneuville, L. Abello and G. Lucazeau, *Diamond and Related Materials*, 1993, **2**, 742-745.
23. R. M. Wightmann and D. O. Wipf, *Electroanalytical Chemistry*, Marcel Dekker, New York, 1989.
24. A. J. Bard and L. R. Faulkner, *Electrochemical Methods; Fundamentals and Applications*, John Wiley & Sons, **2000**.

3 Physical & Electrochemical Characterisation of Single Crystal Boron Doped Diamond

ABSTRACT

In this chapter, the scBDD electrodes are comprehensively characterised using a range of experimental techniques including; secondary ions mass spectrometry (SIMS), differential interference contrast microscopy (DICM), field emission-scanning electron microscopy (FE-SEM), cathodoluminescence (CL), atomic force microscopy (AFM) and Raman spectroscopy which probe both the bulk or the surface features of the samples. Electrochemistry was undertaken employing the scBDD in a macrodisc electrode format with a variety of outer sphere redox mediators, covering a wide potential range. This was complemented by the use of finite element modelling (FEM) to determine electron transfer (ET) kinetic rates. Inner sphere redox mediators were also investigated along with the effect of electrode pre-treatment by using anodic or cathodic polarisation.

3.1 PHYSICAL CHARACTERISATION OF SINGLE CRYSTAL BORON DOPED DIAMOND

3.1.1 Secondary Ions Mass Spectrometry (SIMS)

SIMS results are detailed in Table 3.1 for the different scBDD materials employed, which vary in [B], number of layers *i.e.* (bulk versus capped) and crystal orientation.

Table 3.1. Showing the bulk and capped layer [B] (cm^{-3}) and cap layer thickness as determined by SIMS of BDD samples.

Sample	Orientation	Bulk [B] / cm^{-3}	Cap layer [B] / cm^{-3}	Cap thickness / nm
HB2	(100)	1.5×10^{20}	n/a	n/a
85A/B	(100)	1.0×10^{19}	1.2×10^{21}	65
05A	(110)	1.1×10^{20}	n/a	n/a
85F/G	(110)	$0.8\text{-}1 \times 10^{20}$	n/a	n/a
CP09	(111)	0.95×10^{20}	n/a	n/a
MR14	pBDD	$\sim 3 \times 10^{20}$	n/a	n/a

As SIMS is a destructive technique[1] a 200 × 200 μm etched pit is visible in the materials post analysis, using optical microscopy. After SIMS, acid cleaning as described in section 2.2.1 was used to remove any graphitic carbon resulting from the analysis, leaving the sample surface clean and oxygen terminated.[2]

3.1.2 Differential Interference Contrast Microscopy (DICM)

The samples were provided with an as grown or scaife polished surface finish (Table 2.1) and were initially assessed using DICM. Figure 3.1 shows a DICM image of the scaife polished HB2 sample. The sample topography is clearly heterogeneous with polycrystalline like defects present. These were inherent

throughout the whole sample, after examining the reverse of the sample where several much smaller nucleation sites could be seen. This suggests that the defects were present from the start of growth and may even have been present on the HPHT growth substrate.

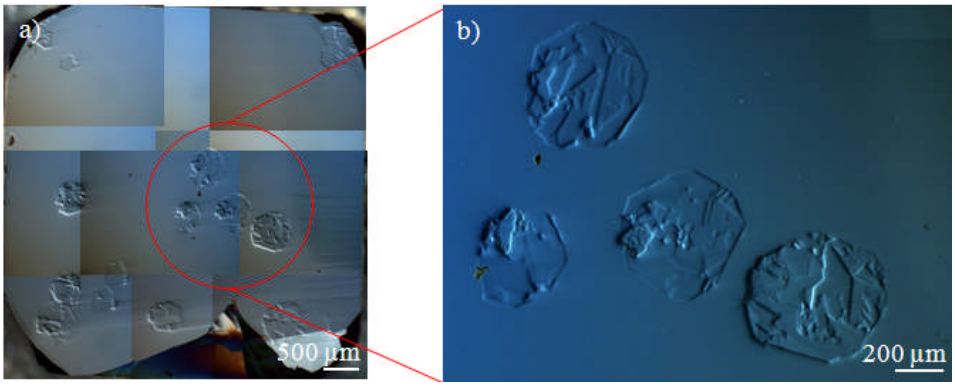

Figure 3.1. a) DICM image of bulk (100) HB2 showing pBDD like defects and polishing lines and b) increased DICM magnification. The defect at the top of b) is further analysed.

DICM suggests a well-polished flat surface for HB2, confirmed also by AFM (Table 3.2). Using DICM at higher resolution (Figure 3.1b) the surface does not appear to show significant height changes, except in the region of the polycrystalline defects. Capped 85A (100) was provided as grown, the initial bulk growth substrate was scaife polished (< 5 nm) prior to the overgrowth of the cap layer. The upper surface of this sample is as grown and no surface features of any kind were observed using DICM, on either sample 85A or B, suggesting topographically a homogeneous substrate. 85B was fabricated into a macrodisc electrode format,[3] and the sister sample, 85A remained as received.

DICM images of the (110) scBDD are shown in Figure 3.2 and Figure 3.3. Figure 3.2 shows the bulk sample 05A, this sample was provided as grown and height differences are indicated by the colour differences across the sample. It

appears the sample is bowed as seen in Figure 3.2a. Some small surface features are apparent (flecks) as shown in Figure 3.2b and are randomly distributed across the sample. This technique it is not possible to say if they contain differing concentrations of boron. These features do not extend the depth of the crystal.

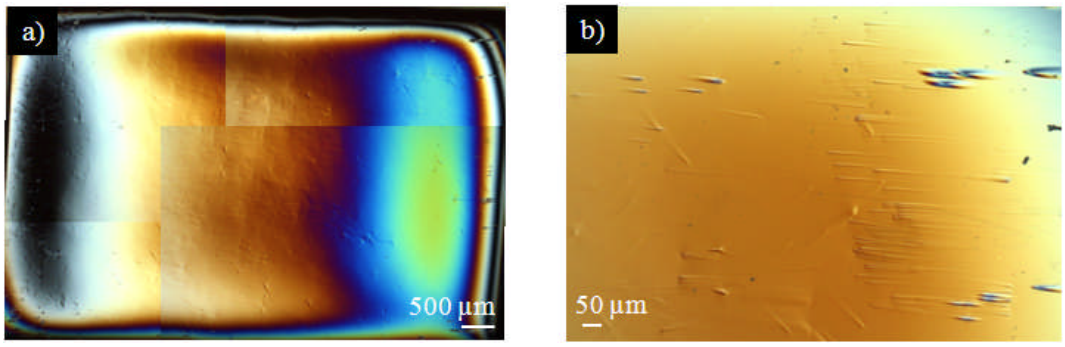

Figure 3.2. a) DICM image of bulk (110) 05A showing a bowed sample. b) Increased magnification highlighting the random orientated surface features (flecks).

Figure 3.3a shows the DICM image of the as grown (110) scBDD, 85F. Figure 3.3b-d are of the sister scBDD (110) sample, 85G. Both samples were subject to a second growth run to produce a thin capping layer of high [B], akin to 85A (100). However, SIMS analysis determined that as the [B] was uniform with depth, the capping layer had failed to grow, therefore 85F/G are treated herein as bulk samples.

Figure 3.3a also shows a bowing of 85F/G where the colour changes suggest that the sample slope is more prevalent than 05A. 85F/G also contains fleck like features, but at considerably higher density in the corners and edges of the material. The flecks also appear slightly larger on 85F/G. As with 05A, DICM is unable to confirm if these flecks contain differing [B].

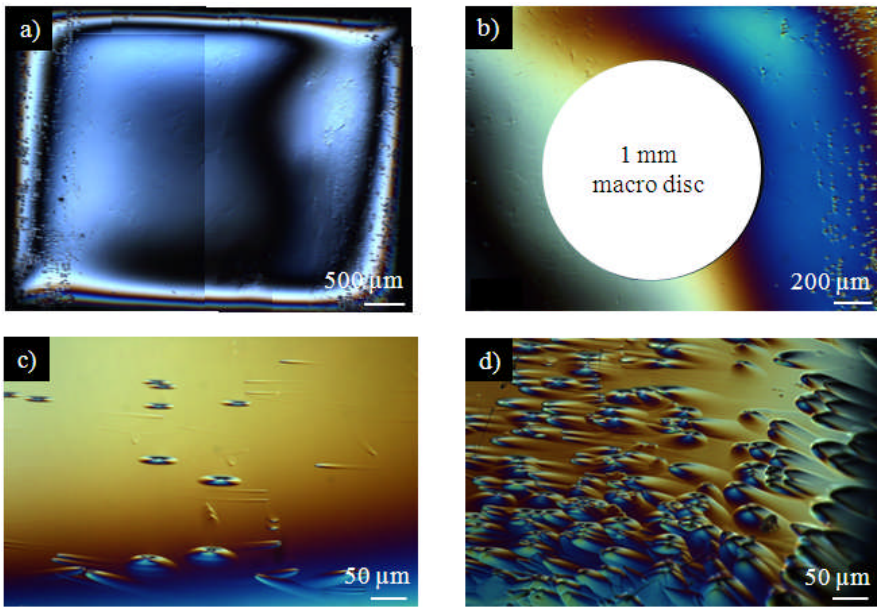

Figure 3.3. a) DICM image of bulk (110) scBDD 85F, b) DICM image of bulk (110) scBDD 85G with a 1 mm macrodisc piece laser cut out. c) Features of 85G and d) peripheral features of 85G both suggesting some localised height differences.

It is useful to note that sample 85F/G is nearly twice as thick as 05A *i.e.* was grown for significantly longer. Also the failure of the cap layer growth, meant the sample was exposed to hydrogen plasma during the failed growth attempt, which causes substrate etching and may have induced the additional surface damage.

Further studies were carried out on 05A and 85G which were processed in the format of a 1 mm macrodisc electrode (Figure 3.3b of 85G).

The (111) sample (CP09) surface was produced by careful polishing of an original piece of (110). The (110) original film thickness dictated how much of the sample could be polished to the (111) direction, as the schematic in Figure 3.4 shows.

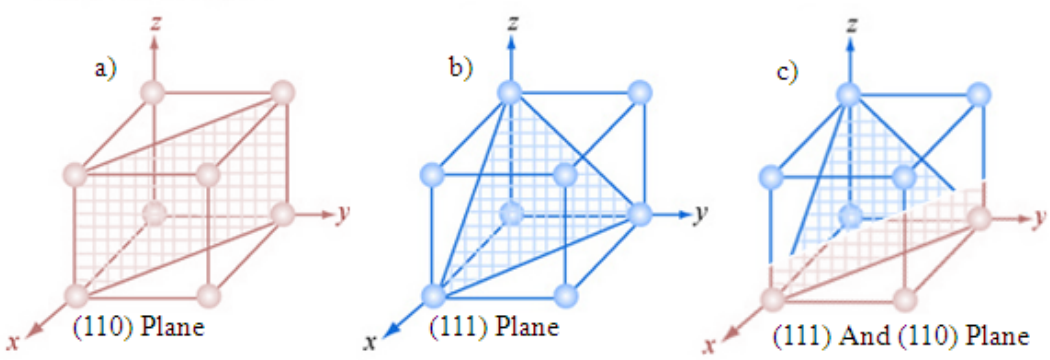

Figure 3.4. Schematic of a) (110) plane, b) (111) plane and c) combination of both (111) top two thirds and (110) bottom third of the sample.

Figure 3.5 shows the DICM image of the (111) orientated sample CP09. The top two thirds of the sample are well polished along the (111) orientation; however the bottom third represents the original (110) orientation. White light interferometery measured the angle between the two orientations at 40º whereas literature reports the angle between the (111) and (110) orientations as 35.3º.[4-7] A 1 mm macrodisc electrode was cut from this sample as shown in Figure 3.5.

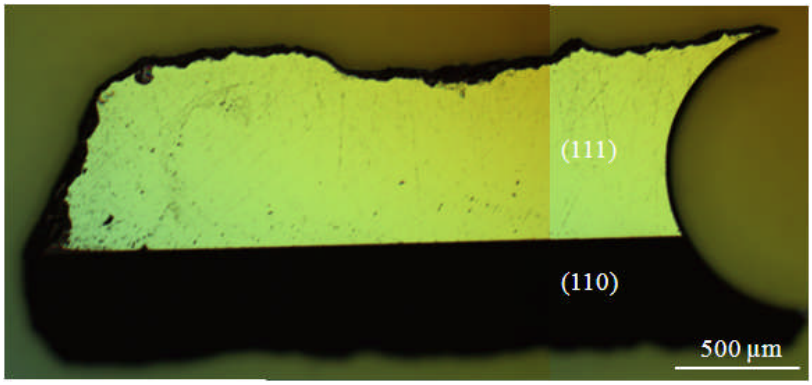

Figure 3.5. DICM image of CP09, bulk (111) scBDD.

3.1.3 Field Emission-Scanning Electron Microscopy (FE-SEM)

Figure 3.6a shows a DICM image of a pBDD-like defect within HB2 and Figure 3.6b, the respective In-Lens FE-SEM image. The contrast in Figure 3.6b is due to differing [B] between the non-defect and polycrystalline defect area. No such contrast was observed in the non defect areas.

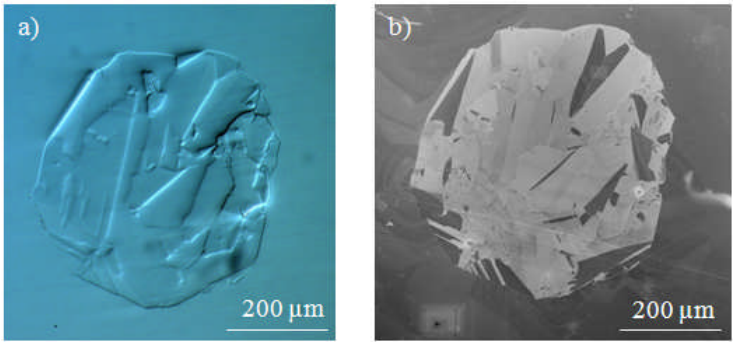

Figure 3.6. a) DICM image of a polycrystalline like defect within scBDD HB2 and b) corresponding In-Lens FE-SEM image.

The capped (100) sample 85A did not show any features under FE-SEM, further suggesting sample homogeneity. FE-SEM imaging of 85G (110) is shown in Figure 3.7.

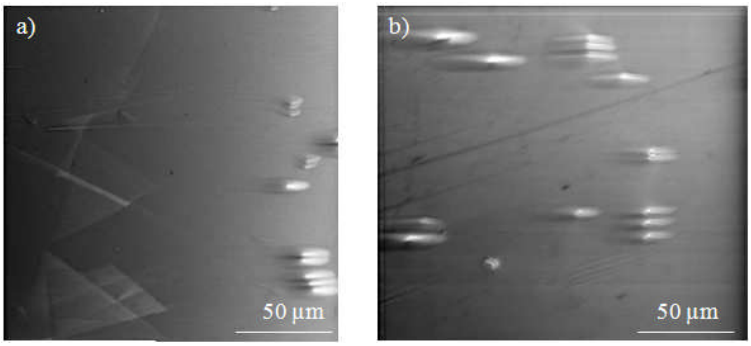

Figure 3.7. Secondary electron FE-SEM images showing areas of interest on scBDD 85G (110) a) bottom edge of the sample and b) right hand side of the sample.

FE-SEM highlights the surface flecks along with scratch lines. Some contrast is observed, as indicated by the white regions of the flecks which indicate a change in [B] compared to surrounding areas.

The two different orientated surfaces in CP09 are shown in Figure 3.8. It is not possible to identify differences in [B] between the planes as both surfaces are not in focus.

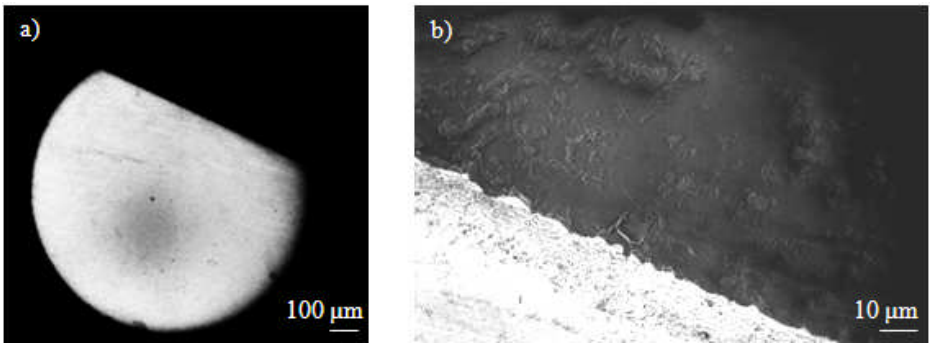

Figure 3.8. a) In-Lens FE-SEM image of scBDD CP09 (111) and b) the (110) section.

3.1.4 Atomic Force Microscopy (AFM)

For each sample, triplicate tapping mode (TM) AFM images (typically 5 × 5 µm) were performed in air to determine the surface roughness.[8, 9] Table 3.2 shows the relative mean square (RMS) value which calculates the best fit of all height points over the sample area.

Table 3.2. Showing sample name, orientation, surface finish and RMS measured by TM-AFM.

Sample	Orientation	Surface Finish	RMS / nm (n=3)
HB2 non-defect	(100)	**Scaife polished**	0.52 ± 0.02
85A/B	(100)	**As grown**	1.55 ± 0.85
05A	(110)	**As grown**	1.33 ± 0.13
85F/G	(110)	**As grown**	0.91 ± 0.01
CP09	(111)	**Scaife polished**	3.01 ± 1.60
MR14	pBDD	**Lapped**	1-3 nm[10]

Figure 3.9a shows the defect free area of HB2, polishing lines are evident as a direct result of the scaife polish. Figure 3.9b is much larger (50 × 50 µm) in order to image an area of a defect within HB2. The cross section suggests the height variation associated with the defect shown in Figure 3.6b is ± 7 nm. Figure 3.9c is of the as grown capped sample 85A.

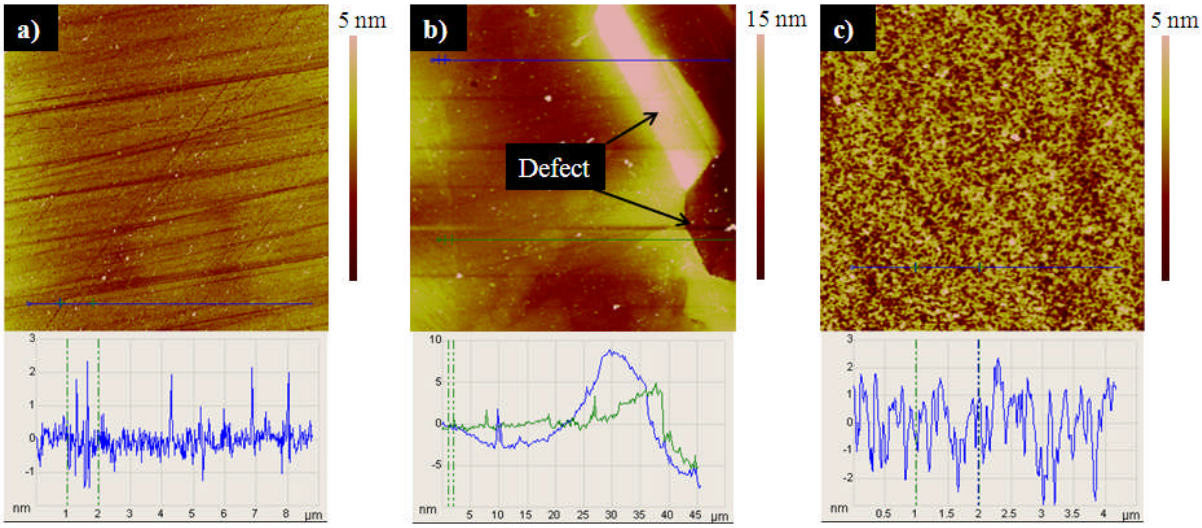

Figure 3.9. TM-AFM images and respective cross sections showing surface roughness of a) HB2 (non-defect) (10 × 10 µm), b) HB2 (defect area) (50 × 50 µm) and c) 85A (5 ×5 µm).

Figure 3.10 shows TM-AFM images of both as grown (110) samples (05A and 85G) in areas away from the flecks, as well as the scaife polished CP09 (on the

(111) surface only). Figure 3.10c of the CP09 (111) sample shows polishing lines, which is expected.

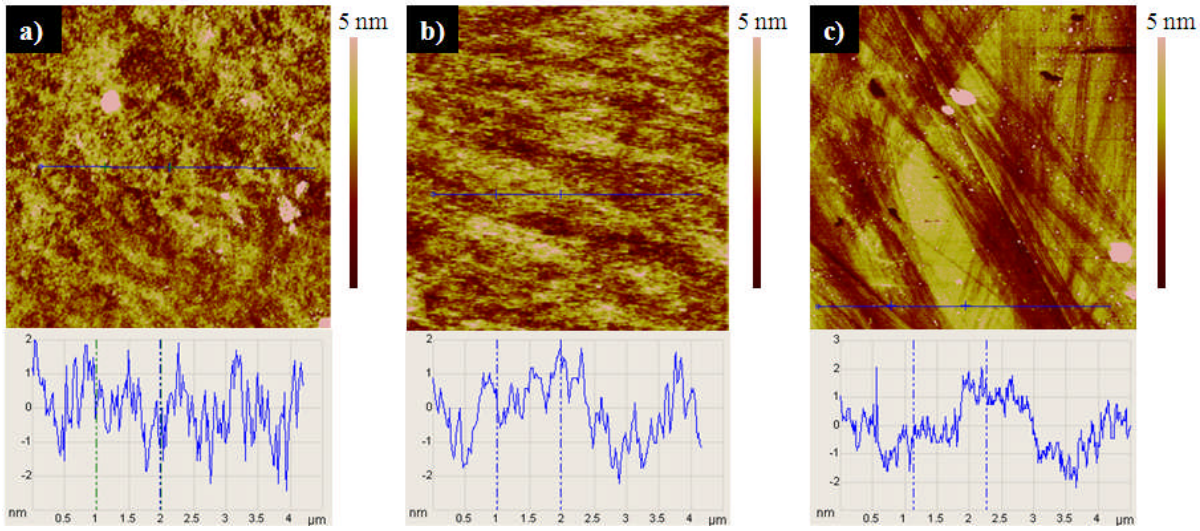

Figure 3.10. 5 × 5 µm TM-AFM images with a single respective cross section showing surface roughness of a) 05A (110), b) 85G (110) and c) CP09 (111).

3.1.5 Micro Raman Spectroscopy

In order to assess scBDD diamond quality, Raman spectroscopy was performed, to identify the sp^3 *vs.* sp^2 characteristics of the scBDD material as discussed in sections 1.1.6 and 2.3.6.

Initially Raman spectroscopy was performed using the 514 nm laser to investigate crystalline sample quality. Figure 3.11 – Figure 3.13 show typical scBDD Raman spectra on the different samples.

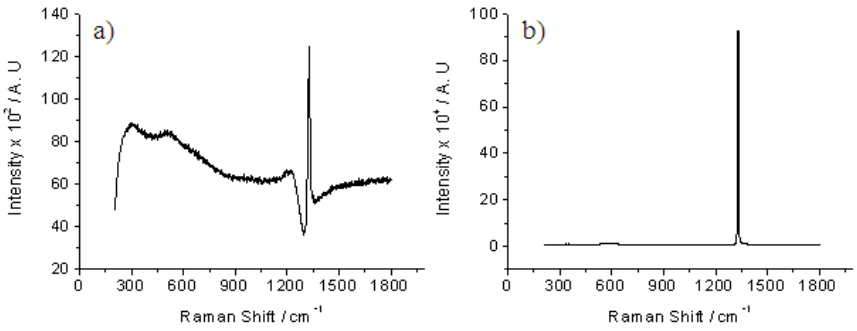

Figure 3.11. Raman spectra of a) bulk HB2 in non defected region and b) capped 85A. Recorded using 514 nm laser, spot size ~6 µm.

Figure 3.11a shows a large Fano resonance ~1332 cm^{-1} for sample HB2 recorded in a non-defected area, suggesting the sample contains [B] ≥ 10^{20} cm^{-3} and can therefore be considered metal-like. No sp^2 carbon is detected which would appear at ~1550 cm^{-1}; further Raman analysis in the polycrystalline like defect area is described below.

Figure 3.11b whilst showing a very clean spectra does not show a Fano resonance, even though the cap layer contains [B] at ≥ 1 x 10^{20}, however as the cap layer is only 65 nm thick, and the laser penetrates ~1 µm the spectra observed is dominated by [B] from the bulk layer where [B] 1 × 10^{19} cm^{-3} as determined by SIMS.

Figure 3.12 shows an overlaid plot (offset 40 % in *y*) of typical Raman spectra recorded on the three (110) samples *i.e.* (05A, 85F and 85G). All three materials show similar spectra, *i.e.* the absence of sp^2 carbon and the presence of a Fano resonance.

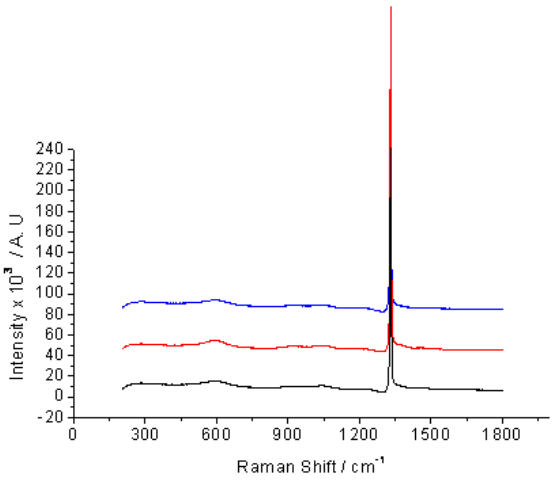

*Figure 3.12. Raman spectra of the (110) samples 05A (**black**), 85F (**blue**) and its sister sample 85G (**red**). Recorded using 514 nm laser, ~6 µm spot size.*

Initial Raman spectra recorded on the two different surfaces of sample CP09 are shown in Figure 3.13 (overlaid, without offset). Both spectra show a Fano resonance and the absence of sp^2 carbon. The smaller area (110) shows a taller peak with a more obvious Fano resonance than the highly polished (111) area of the sample. The spectra initially might suggest the (110) area contains a higher [B], however this surface is rough in comparison to the (111) surface, therefore the former would provide significantly increased luminescence and scattering.

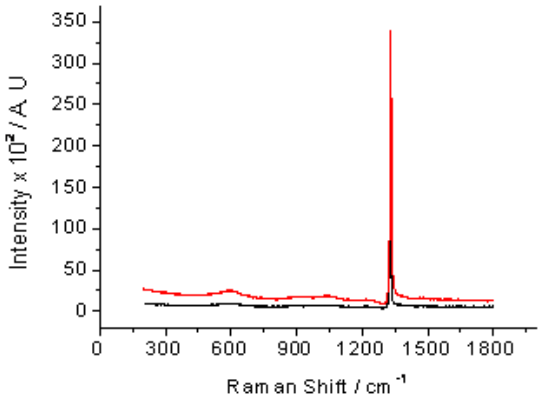

*Figure 3.13. Overlaid Raman spectra of the scBDD sample CP09, highly polished area in **black** of (111) orientation and the (110) section of the sample in **red**, recorded using a 514 nm laser, ~6 µm spot size.*

With the exception of the capped sample 85A, which given the laser penetration depth, could not be analysed effectively using Raman, all scBDD sample proved to be of high quality. No sp^2 peaks were detected for any of the samples and the zone centre phonon peak (~1332 cm^{-1}) was observed with a Fano resonance suggesting high [B], supporting SIMS data.

For further analysis of the HB2 defects, the 633 nm laser was employed because it resonantly enhances non-diamond like carbon covalently bonded material,[11] *i.e.* boron. Figure 3.14 shows two spectra, selected from many taken across the defect are, across a non-defect area overlaid with a defected area. Clear differences can be seen and whilst both peaks have a Fano resonance, the defected area spectra, in the wavenumber region 1300 – 1340 cm^{-3} (sp^3) shows a more asymmetric peak of lower peak height and smaller integrated area under the peak, than the defect free area, suggesting higher [B].[12-14]

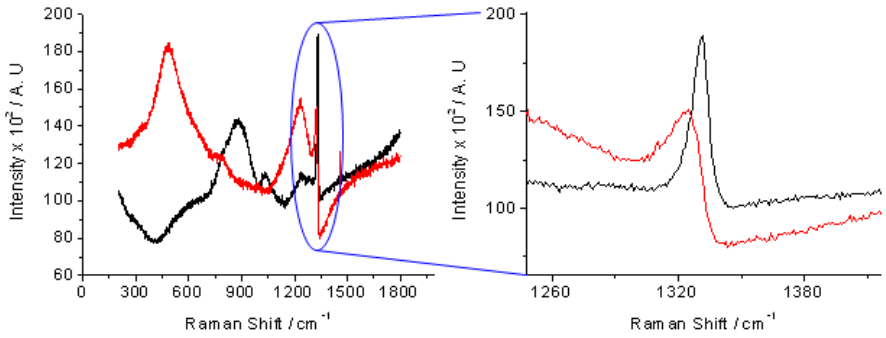

*Figure 3.14. Overlaid Raman spectra of HB2, the **black** spectra is taken in a non-defect area and the **red** spectra within a defected area, an increased magnification is shown of the Fano resonance, using 633 nm laser, spot size ~6 µm.*

To assess sample homogeneity from a Raman perspective, areas for investigation were randomly selected from across the sample, avoiding the edges for focussing reasons. Figure 3.15 shows nine spectra, overlaid with an offset of 40 % in the *y* axis, for each of the three (110) samples, in defect free areas.

The Raman spectra all show very similar features, a sharp peak at ~1332 cm^{-1} with a Fano resonance and a peak ~900 cm^{-1}, no sp^2 carbon is detected ~1550 cm^{-1} suggesting high quality single crystal material. The zone centre phonon peak between all three samples are similar in height which could suggest similar [B] as confirmed by SIMS, Table 3.1.

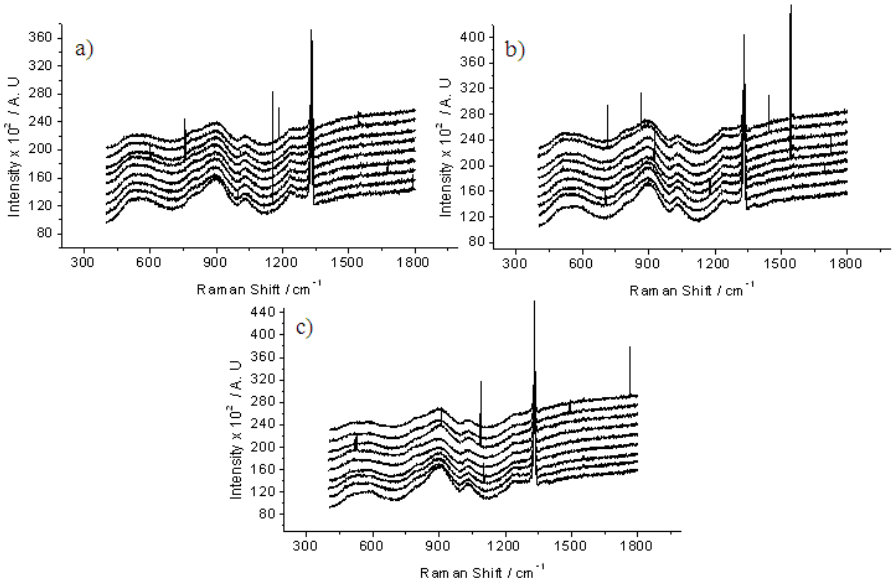

Figure 3.15. Random nine point Raman mapping spectra of scBDD (110) a) 05A, b) 85F and its sister sample c) 85G showing the zone centre phonon peak at 1332.5 cm^{-1} with a Fano resonance suggesting metal-like conductivity. Using 633 nm laser, spot size ~6 µm.

For more detailed information on the homogeneity of [B], Raman mapping was performed in raster mode. Maps were obtained in a central area of each sample. The resulting maps show the Raman peak of diamond at ~1332 cm^{-1}, integrated with respect to peak area or intensity, as a function of *x, y* position. As discussed in section 1.1.6 incorporated boron distorts the 1332 cm^{-1} peak with a Fano resonance and attenuation (see Figure 1.1 and 2.8), this effect increases as [B] increases.

The 514 nm laser was employed for all samples subject to Raman mapping (output ~6 mW) and full details of instrumental conditions used for each sample are shown in Table 3.3.

Table 3.3. Showing sample name, laser power, laser spot size, scan step size and scan size used for Raman mapping with 514 nm laser.

Sample	Laser Power	Spot size / µm	Step size / µm	Scan size/ µm
HB2(100)	50 %	**6**	2	200 × 200
85B(100)	1 %	**1**	3	200 × 200
05A(110)	5 %	**3**	3	200 × 200
85G(110)	5 %	**3**	3	100 × 100
CP09(111)	5 %	**3**	3	200 × 200

Figure 3.16 shows the area of HB2 which was mapped using Raman, spectra of selected areas are shown demonstrating the differences in Raman peak height and shape in a non-defect (Figure 3.16b) and a defected area (Figure 3.16c and d). The spectra between the areas are markedly different such that peak area fitting was not compatible with the two different spectral types. Therefore peak intensity was used as shown in Figure 3.16e.

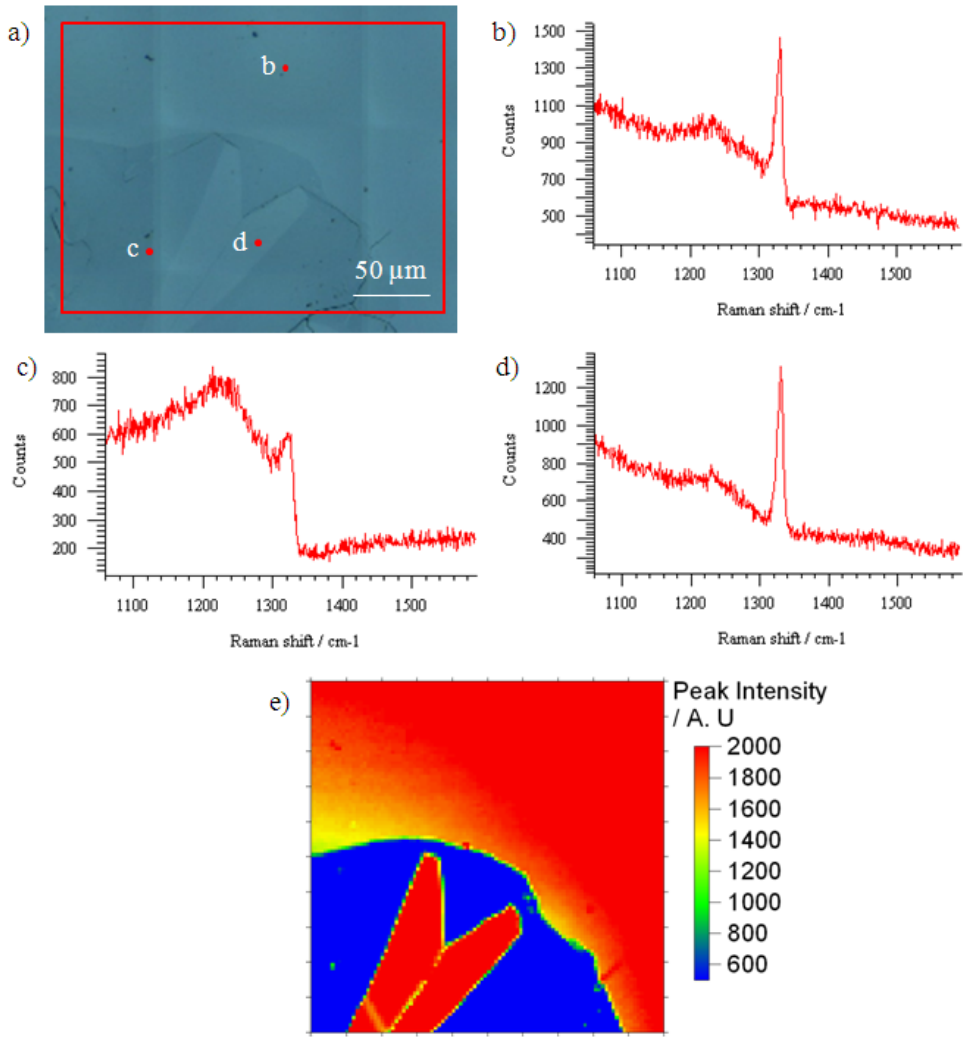

Figure 3.16. a) Optical image of HB2 (100) showing the boundaries of the 200 × 200 µm Raman map. b), c) and d) Raman spectra at selected points highlighted in a). e) Raman map shows the peak intensity ~1332 cm^{-1} as a function of spot location using 514 nm laser, spot size 6 µm.

Figure 3.16e clearly shows there are two areas of similar peak intensity (surrounding the defect and the arrow feature). The peak intensity is greatly reduced within certain areas of the defect as the increased [B] attenuates and broadens the diamond peak. These results support the FE-SEM images (Figure 3.6) suggesting differing [B] in this area. Figure 3.17shows Raman mapping of 85 B. The optical image suggests the sample is sloped, which is reflected in the Raman map. To verify

this was a sample mounting issue, Figure 3. 17f shows the same area but with the substrate rotated by 90°.

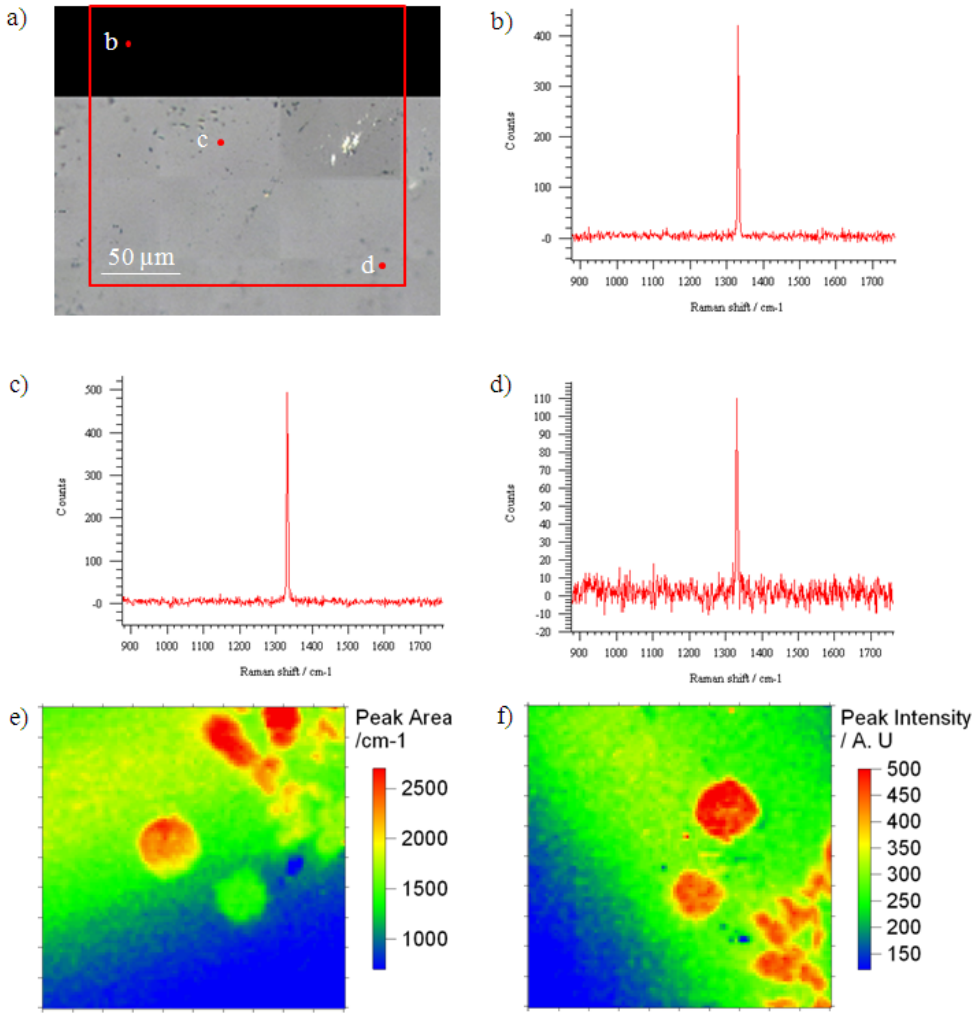

Figure 3.17. a) Optical image of 85B (100) showing the boundaries of the 200 × 200 µm Raman map (even if where no optical image was taken). b), c) and d) Raman spectra at selected points highlighted in a). e) Raman map showing the integrated peak area ~1332 cm^{-1} as a function of spot location and f)Raman map performed at 90° to the original map showing the measured peak intensity ~1332 cm^{-1}. Both maps performed using 514 nm laser, spot size 1 µm.

Despite the presence of the sample gradient, Figure 3.17e and f show features which are not visible in the optical image (Figure 3.17a). As the laser penetrates

~1 µm into the surface it is thought the Raman is now mapping defects which are present in the underlying substrate.

A Raman map of the bulk (110) sample 05A is shown in Figure 3.18, the lack of any features suggest the central region of this sample is homogeneous with respect to [B].

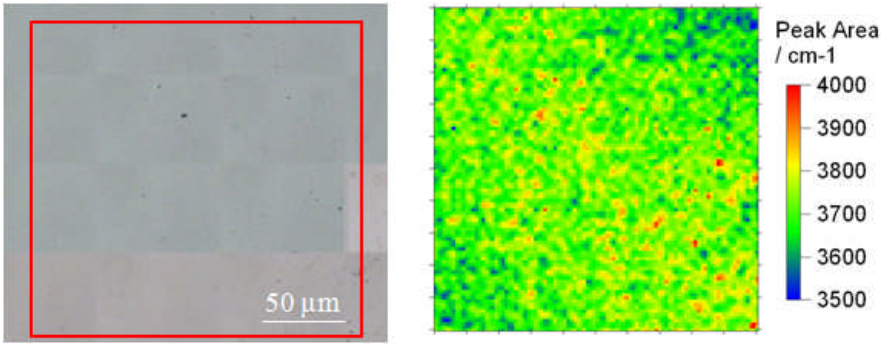

Figure 3.18. Optical image of 05A (110) showing the boundaries of the 200 × 200 µm Raman map. The Raman map shows the integrated peak area ~1332 cm^{-1} as a function of spot location using 514 nm laser, spot size 3 µm.

Sample 85G (110) has a higher concentration of fleck like features at the sample edges and corners (seen in Figure 3.3), of typical size 10 × 25 µm therefore a Raman map incorporating these features was recorded as shown in Figure 3.19. The map was plotted using both peak area and peak intensity, which correlate.

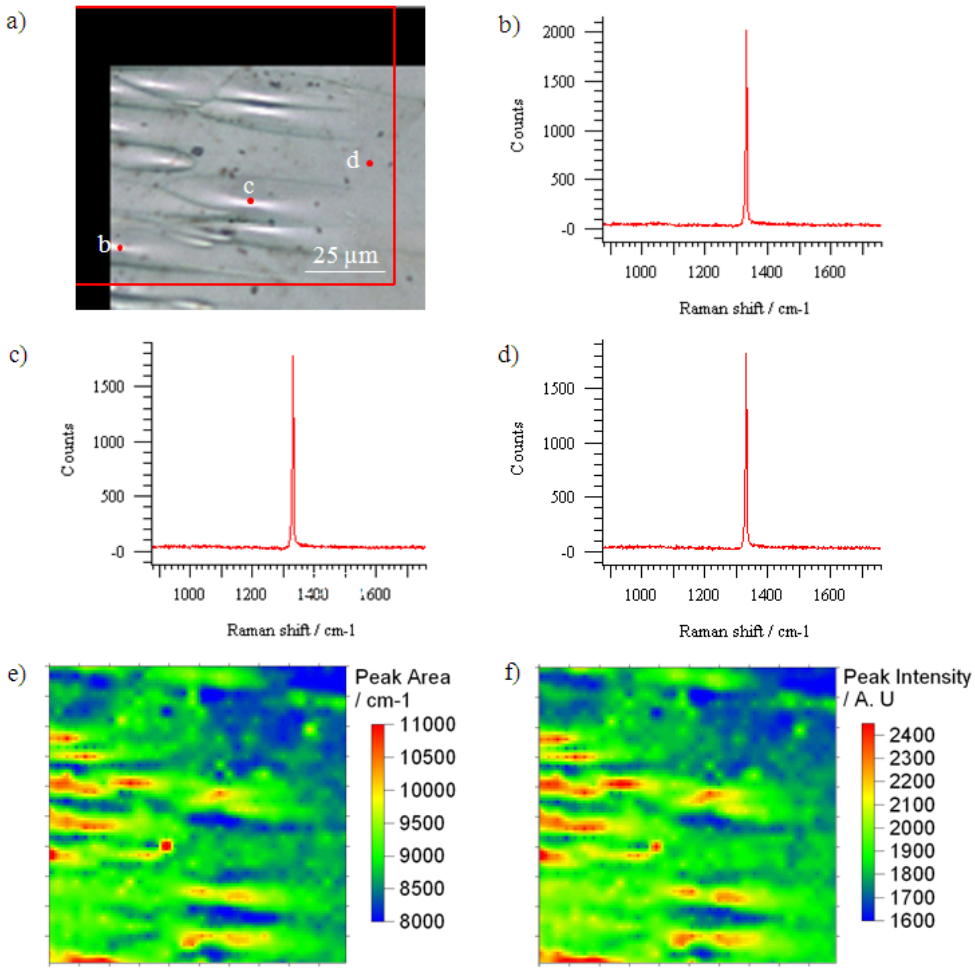

Figure 3.19. a) Optical image of 85G (110) showing the boundaries of the 100 × 100 µm Raman map (even if where no optical image was taken). b), c) and d) Raman spectra at selected points highlighted in a). e) Raman map showing the integrated peak area ~1332 cm-1 as a function of spot location using 514 nm laser, spot size 3 µm). f) Raman map plotted as peak intensity correlating peak area and peak intensity data.

Sample CP09 (111) was subject to Raman mapping and is shown in Figure 3.20, where the sample appears homogeneously doped apart from in the area of possible polishing lines.

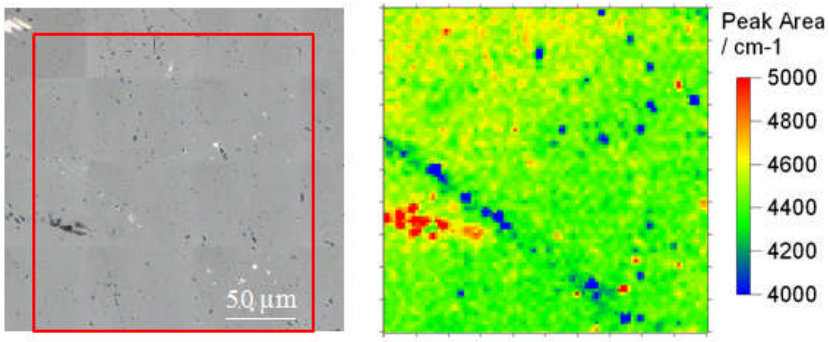

Figure 3.20. a) Optical image of CP09 (111) showing the boundaries of the 200 × 200 µm Raman map. The Raman map shows the integrated peak area ~1332 cm^{-1} as a function of spot location using 514 nm laser, spot size 3 µm.

3.1.6 Cathodoluminescence (CL)

CL was employed to locate the 'defects' within the bulk (100) 85B sample highlighted by Raman mapping. Initial analysis indicated crystal-shape like defects, when operating at 15 keV as shown in Figure 3.21a. The shape of the defects indicates single crystal shaped defects as opposed to the polycrystalline defects observed in (100) HB2.

As the penetration depth of the CL electron beam is strongly dependant on the operating voltage, by varying this parameter it is possible to depth profile the defect and provide an assessment on whether the defect is solely in the underlying bulk layer, which we believe from Raman mapping, or has propagated through to the top layer.[15, 16]

Using equation 3.1,[15] the penetration depth of the emitted electrons were calculated. These calculations and model predictions are based on the density of diamond being 3.51 g cm^{-3}.[17]

$$\rho R = \frac{2.76 \times 10^{-11} A_w E_0^{5/3}}{Z^{8/9}} \qquad \textbf{(3.1)}$$

Where ρR is mass-range (using density (g cm^{-3})), A_w is atomic weight, E_0incident energy and Z atomic number. Figure 3.21a-d shows simultaneously recorded SEM (left) and CL (right) images of an area of the sample containing defects recorded at operating voltages of a) 15 keV, b) 10 keV, c) 5 keV and d) 4 keV. Using equation 3.1 this corresponds to penetration depths of a) 1.8 μm; b) 0.9 μm; c) 0.3 μm and d) 0.2 μm.

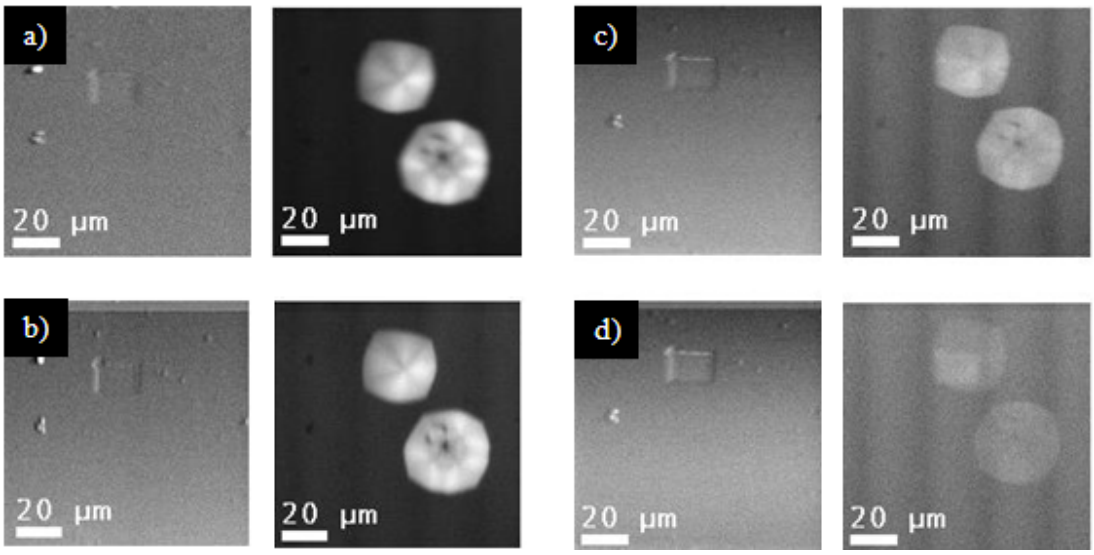

Figure 3.21. Corresponding SEM and CL images of scBDD 85B (100) where the CL image was recorded using an accelerator voltage of a) 15 keV, b) 10 keV, c) 5 keV and d) 4 keV.

As the operating voltage is reduced it can be clearly seen that the defect becomes less and less focussed indicating strongly that these defects lie in the bulk material and are not part of the cap layer. Similar responses were observed for all the defects identified with the 1 mm area investigated suggesting that the cap layer is free from single crystal growth defects.

Findeling-Dufour *et al.*[18] suggest MWCVD intrinsic sc (100) orientations are commonly studded with particles and pyramidal hillocks showing crystallites at their tops. Optical images shown by Ramamutri *et al.*[19] of MWCVD scBDD (100) also carry the pyramidal hillock description and do indeed look similar to those features observed using CL with scBDD (100) 85B.

3.2 ELECTROCHEMICAL CHARACTERISATION OF SINGLE CRYSTAL BORON DOPED DIAMOND

3.2.1 Double Layer Capacitance Measurements (C_{meas})

Macrodisc electrodes (described in 2.2.4) were fabricated for electrochemical investigation of the scBDD materials. All samples are O-terminated (section 2.2.1) and CVs were initially recorded in background electrolyte only (0.1 M KNO_3, pH 7.2), in order to determine the double layer capacitance (C_{meas}).

The current was measured at 0 V, *vs*. SCE, on both the forward and reverse sweeps and C_{meas} was calculated using equation 3.2.[20]

$$C = [(\frac{i_f + i_b}{2})/v]/A \qquad \textbf{(3.2)}$$

where C represents C_{meas} (values typically μF cm^{-2}), i_f and i_b, the i (amps) recorded at 0 V during the forward and backward sweeps, an example of a C_{meas} CV is shown in Figure 3.22.

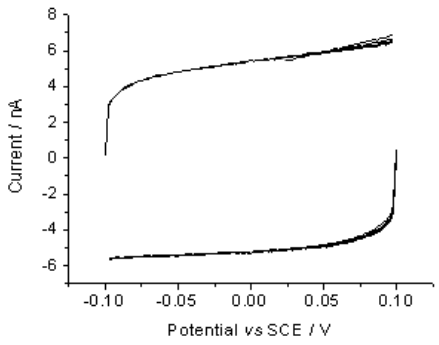

Figure 3.22. CV response using 1 mm scBDD macrodisc electrode (85B) in 0.1 M KNO_3, scan rate 100 mV s^{-1}.

The calculated C_{meas} values (n=3) and respective [B] are shown in Table 3.4.

Table 3.4. Table showing 1 mm macrodisc BDD sample orientation, C_{meas} values and [B] compared with commercial electrodes.

Sample	C_{meas}/ µF cm^{-2} (n=3)	[B] / cm^{-3}
HB2(100)	**5.98 ± 0.15**	1.5×10^{20}
85B (100)	**6.21 ± 0.08**	1.0×10^{21}
05A(110)	**4.64 ± 0.03**	1.06×10^{20}
85G(110)	**9.60 ± 0.20**	$0.8\text{-}1 \times 10^{20}$
CP09 (111)	**7.61 ± 0.18**	0.95×10^{20}
MR14 pBDD	**8.58 ± 0.70**	$\sim 3 \times 10^{20}$
GC	**77.9 ± 1.0**	n/a
Au	**36.8 ± 2.6**	n/a
Pt	**88.7 ± 1.5**	n/a

Compared to other electrode types, metal-like scBDD has lower C_{meas} values which is likely to result from the lower density of states, a reduction in the number of ionisable groups, and also the inability of the surface to undergo direct oxidation/reduction processes as is the case for a metal.

Interestingly, there appears to be no significant difference in measured capacitance between the (100) samples despite an order of magnitude difference in

[B]. For the (110) samples, even though the [B] is similar, the capacitance for 05A is approximately half that of 85G and is shown in Figure 3.23. The only difference being that 85G was subject to an additional hydrogen plasma treatment during failed growth of the capping layer. It is important to note the C_{meas} for (111), is associated not just with the (111) sample orientation but also (110), see above.

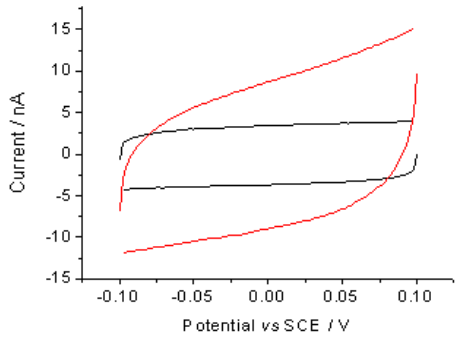

*Figure 3.23. CV response using 1 mm macrodisc electrodes in 0.1 M KNO_3 swept at 100 mV s^{-1}, scBDD (110) 05A (**black**) and 85G (**red**) highlighting differences in their capacitance behaviour.*

3.2.2 Potential Windows in Background Electrolyte (0.1 M KNO_3)

CVs over the potential range -3 to +3 V were performed in 0.1 M KNO_3 (background electrolyte) at 100 mV s^{-1}, for the scBDD 1 mm macrodisc electrodes and Au, Pt and GC macrodisc electrodes, as shown in Table 3.5 and

Figure 3.24.

Table 3.5. Mean tabulated values of potential limits for BDD and commercial electrodes measured using 0.1 M KNO_3, swept between -3 and +3 V at 100 mV s^{-1}, values recorded at 0.3 mA. Values measured from original CVs (n=3).

Sample	Potential Window Voltage Range (V)	Negative Potential Limit / V	Positive Potential Limit / V
HB2(100)	**4.82** ± 0.11	-2.37 ± 0.14	2.51 ± 0.03
85B (100)	**4.68** ± 0.08	-2.26 ± 0.07	2.42 ± 0.02
05A(110)	**4.74** ± 0.17	-2.32 ± 0.16	2.41 ± 0.02
85G(110)	**5.02** ± 0.03	-2.56 ± 0.02	2.40 ± 0.01
CP09 (111)	**4.84** ± 0.07	-2.42 ± 0.05	2.42 ± 0.02
MR14 pBDD	**4.64** ± 0.14	-2.26 ± 0.12	2.36 ± 0.02
GC	**3.10** ± 0.23	-1.16 ± 0.25	1.94 ± 0.11
Au	**2.51** ± 0.18	-0.41 ± 0.70	1.78 ± 0.01
Pt	**1.48** ± 0.32	-0.20 ± 0.08	1.29 ± 0.41

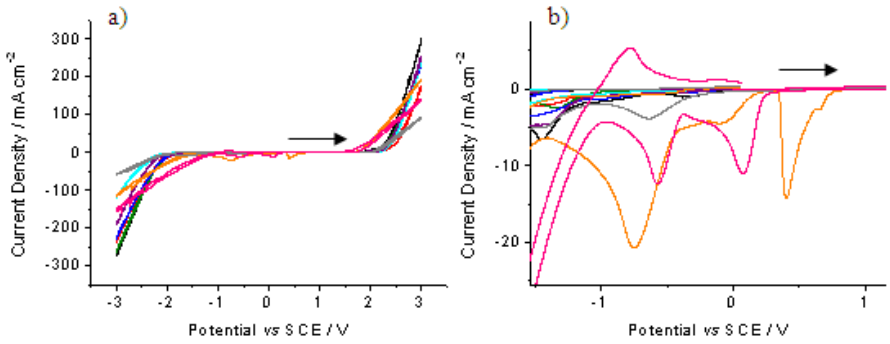

*Figure 3.24. CVs in 0.1 M KNO_3 in the potential window a) -3 to +3 V and b) increased magnification where (**black**) pBDD, (**red**) HB2 (100), (**green**) 85B (100), (**blue**) 05A (110), (**cyan**) 85G (110), (**purple**) CP09 (111), Au (**orange**), GC (**grey**) and Pt (**pink**), all electrode areas factored into the y axis. Scan rate 100 mV s^{-1}.*

The extended potential window is clearly visible for all BDD electrodes between -2 and 2 V. The electrochemical process of water decomposition defines the range of the potential window, at cathodic and anodic extremes hydrogen and oxygen evolution occurs. These two reactions are known to follow complex mechanisms involving intermediates adsorbed onto the electrode surface.[21, 22] The

activity of the electrode is a function of its surface structure and outer electron arrangement, e.g. for Pt, the intermediates of water electrolysis can chemisorb via partially filled d-orbitals which initiates effective electrolysis.[21]

Figure 3.24 shows for scBDD electrodes, the decomposition of water occurs at high overpotentials suggesting these reactions are likely to be inhibited at the scBDD surface. Breaking or rearrangement of these bonds in order to form intermediates is a likely hindering factor during the oxygen and hydrogen evolution reactions.

Similarly oxygen reduction is notably absent on the CVs employing scBDD electrodes but is clearly seen on the Pt and Au electrodes at ~0 V and -0.5 V respectively *vs.* SCE as shown in Figure 3.24b. During oxygen reduction, dioxygen molecules bind directly to the electrode surface and this is facilitated by d-orbitals and/or quinone groups.[23, 24] Given the scBDD is O-terminated, the electrode surface is pre saturated with stable oxygen functional groups therefore strongly hindering further oxygen adsorption leading to oxygen reduction being kinetically hindered on BDD surfaces.[25-28] The wide potential window also indicates a distinct lack of any non-diamond carbon, which acts to reduce the size of the potential window[29-31] or other contaminants from the electrode fabrication process e.g. exposed Au from the contact, or graphitic carbon produced during laser micromachining of the BDD cylinders.[3, 32, 33]

3.2.3 Cyclic Voltammetry at Single Crystal Boron Doped Diamond Macro Electrodes with Outer Sphere Redox Mediators

PBDD is a well-known and well reported electrode material.[25,34-43] pBDD is available commercially and has also been used extensively by many different research groups.[34, 44-47]

Preliminary CVs, over a wide range of scan rates, were performed with a range of fast ET, outer sphere redox mediators at differing concentrations and compared to the electrochemical performance of metal-like pBDD. The CVs were analysed in terms of peak to peak separations (ΔE_p) and compared with that predicted by equation 1.5 (59 mV for a metal electrode where n=1) and peak currents (i_p) using Randles Sevcik (equation 1.4). Table 3.6 details the redox mediator's respective diffusion coefficients (D) and their formal potential ($E°´$).

Table 3.6. Outer sphere redox mediators used herein detailing diffusion coefficient and respective formal potentials.

Redox Mediator	D / cm^2 s^{-1}	$E°´$ / V
$FcTMA^{+/2+}$	6.0×10^{-6} [48]	0.42[49](*vs.* Ag|AgCl)
$IrCl_6^{2-/3-}$	8.2×10^{-6} [50]	0.87[51] (*vs*. NHE)
$Ru(NH_3)_6^{3+/2+}$	8.8×10^{-6} [52]	0.10[53] (*vs*. NHE)

All electrodes were O-terminated and prior to CV analysis, polished using alumina slurry and a micro cloth polishing pad as described in section 2.4.2. CVs and a corresponding data table for all BDD electrodes, using a range of scan rates (20-1000 mV s^{-1}) and varying concentrations of $FcTMA^+$, are shown in Figure 3.25 and Table 3.7.

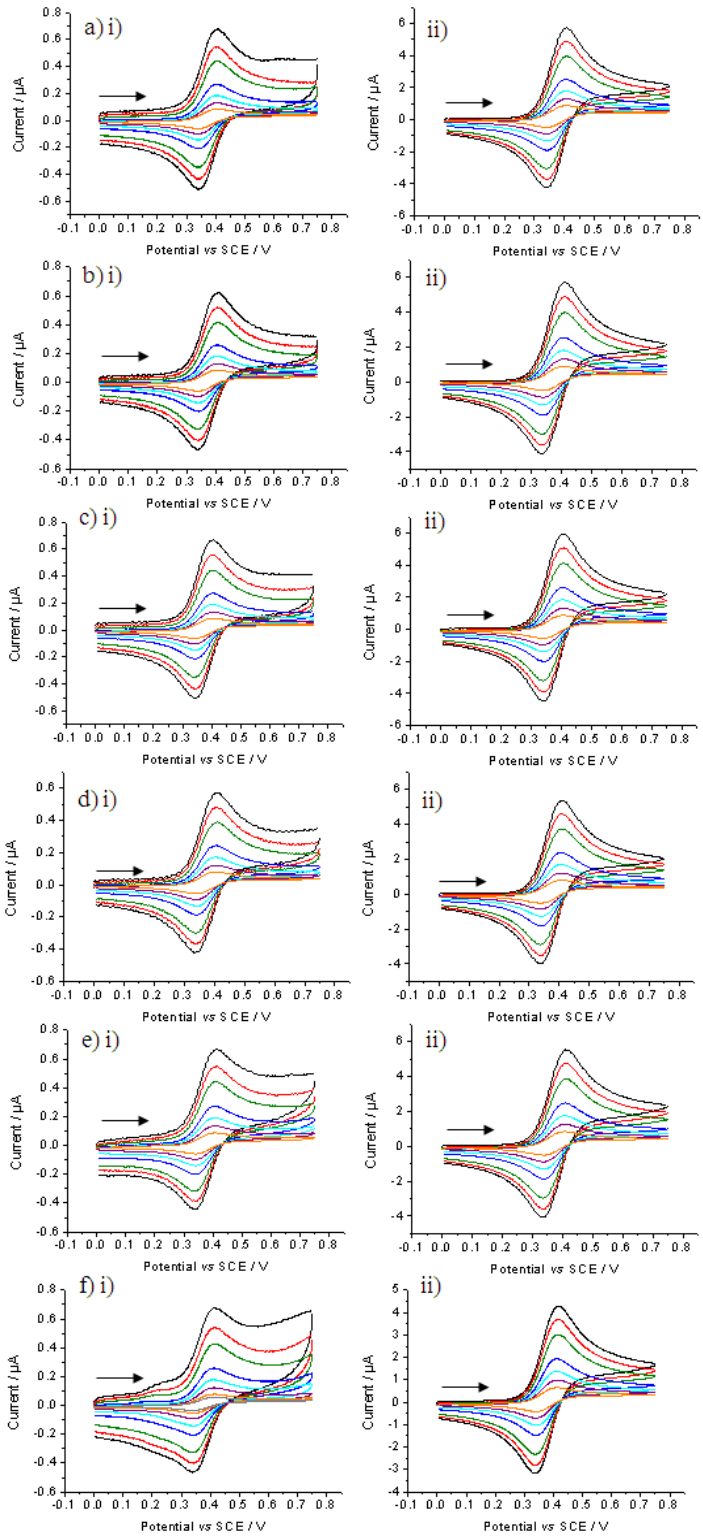

Figure 3.25. CV recorded using a range of scan rates showing the oxidation of i) 0.1 mM $FcTMA^+$ in 0.1 M $KNO_3$and ii) 1 mM $FcTMA^+$ in 0.1 M KNO_3 for 1 mm macrodisc; a) pBDD, b)HB2 (100), c) 85B (100), d) 05A (110), e) 85G (110) and f) CP09 (111). The following colour key for scan rates applies; ***20 mV s^{-1}***, ***50 mV s^{-1}***, ***100 mV s^{-1}***, ***200 mV s^{-1}***, ***500 mV s^{-1}***, ***750 mV s^{-1}*** *and* ***1000 mV s^{-1}***.

Table 3.7. Theoretical oxidation i_p using a range of scan rates and varying concentrations of $FcTMA^+$ compared to experimental i_p and ΔE_p values for 1 mm macrodisc BDD electrodes.

0.1 mM		pBDD		HB2 (100)		85B (100)		05A (110)		85G (110)		CP09 (111)	
Scan rate / mV s^{-1}	Theory i_p / µA	i_p / µA	ΔEp / mV	i_p / µA	ΔEp / mV	i_p / µA	ΔEp / mV	i_p / µA	ΔEp / mV	i_p / µA	ΔEp / mV	i_p / µA	ΔEp / mV
20	0.07	0.08	66	0.08	66	0.09	66	0.08	66	0.08	69	0.08	71
50	0.12	0.13	66	0.13	68	0.13	66	0.12	66	0.12	69	0.12	71
100	0.16	0.18	64	0.18	67	0.19	63	0.17	65	0.17	67	0.17	71
200	0.23	0.25	62	0.25	66	0.26	57	0.24	69	0.24	66	0.23	73
500	0.37	0.39	73	0.39	69	0.41	60	0.37	72	0.38	78	0.36	77
750	0.45	0.49	69	0.48	68	0.50	56	0.45	72	0.46	75	0.42	71
1000	0.52	0.59	64	0.57	67	0.61	60	0.53	66	0.57	72	0.44	76
1 mM		pBDD		HB2 (100)		85B (100)		05A (110)		85G (110)		CP09 (111)	
Scan rate / mV s^{-1}	Theory i_p / µA	i_p / µA	ΔEp / mV	i_p / µA	ΔEp / mV	i_p / µA	ΔEp / mV	i_p / µA	ΔEp / mV	i_p / µA	ΔEp / mV	i_p / µA	ΔEp / mV
20	0.73	0.84	69	0.86	69	0.87	69	0.80	69	0.83	72	0.66	70
50	1.16	1.30	69	1.32	69	1.34	69	1.24	72	1.27	75	1.01	73
100	1.64	1.82	64	1.84	69	1.80	63	1.74	66	1.78	67	1.40	67
200	2.31	2.54	66	2.58	69	2.64	66	2.43	69	2.49	69	1.95	70
500	3.66	3.97	69	3.98	75	4.14	69	3.67	75	3.84	75	3.00	78
750	4.48	4.84	63	4.85	72	5.05	63	4.58	69	4.66	75	3.62	77
1000	5.17	5.59	66	5.57	78	5.84	66	5.29	72	5.35	78	4.14	79

The pBDD electrode shows CV behaviour close to reversible at both 0.1 and 1 m M (ΔE_p 62-73 mV). Heavily doped 85B offers the fastest ΔE_p values (56-69 mV) which is not unexpected given its proposed homogeneous nature and high [B]. Samples HB2 (100), 05A (110 and 85 G (110) all show fairly reversible behaviour at both concentrations between scan rates 20-200 mV s^{-1}. However at faster scan rates the samples are slightly less reversible. In general the i_p values recorded were close to theoretical values for all BDD samples except CP09.

The electrode CP09 contained both (111) and (110) orientations, therefore direct comparisons to other samples are unable to be made. At both concentrations, the $\Delta E_p$is noticeably higher at all scan rates (67-79 mV). This may be due to its

heterogeneity or a lack of charge carriers at the surface reducing facile electron transfer due to its borderline metal-like [B]. Up to 750 mV $s^{-1}$the i_p was close to theoretical values for 0.1 mM. At 1 mM, beyond 100 mVs^{-1}, i_p was lower than theoretical values thereby suggesting a lower [B] or an increasing effect of the heterogeneous surface on reaction kinetics from both (111) and (110).

To further investigate the electrochemical response of BDD, another well known outer sphere redox mediator was utilised, $IrCl_6^{2-/3-}$ at two differing concentrations; 0.1 mM and 1 mM. CVs and corresponding data table for all BDD electrodes, using a range of scan rates (20-1000 mV s^{-1}) are shown in Table 3.8 and Figure 3.26.

Table 3.8. Theoretical oxidation i_p using a range of scan rates and varying concentrations of$IrCl_6^{2-}$ compared to experimental i_p and ΔE_p values for 1 mm macrodisc BDD electrodes.

0.1 mM		pBDD		HB2 (100)		85B (100)		05A (110)		85G (110)		CP09 (111)	
Scan rate / mV s^{-1}	Theory i_p / µA	i_p / µA	ΔEp / mV	i_p / µA	ΔEp / mV	i_p / µA	ΔEp / mV	i_p / µA	ΔEp / mV	i_p / µA	ΔEp / mV	i_p / µA	ΔEp / mV
20	0.09	0.08	59	0.08	59	0.08	62	0.07	63	0.07	62	0.07	70
50	0.14	0.12	62	0.12	62	0.12	62	0.11	63	0.11	62	0.11	71
100	0.19	0.17	61	0.17	62	0.17	62	0.16	62	0.14	62	0.16	67
200	0.27	0.24	62	0.23	59	0.24	62	0.23	60	0.20	59	0.21	66
500	0.43	0.38	59	0.36	65	0.39	64	0.37	63	0.33	65	0.40	79
750	0.52	0.46	59	0.44	59	0.48	59	0.45	58	0.42	57	0.41	66
1000	0.60	0.53	59	0.51	59	0.56	62	0.51	60	0.50	58	0.47	73
1 mM		pBDD		HB2 (100)		85B (100)		05A (110)		85G (110)		CP09 (111)	
Scan rate / mV s^{-1}	Theory i_p / µA	i_p / µA	ΔEp / mV	i_p / µA	ΔEp / mV	i_p / µA	ΔEp / mV	i_p / µA	ΔEp / mV	i_p / µA	ΔEp / mV	i_p / µA	ΔEp / mV
20	0.85	0.88	69	0.84	62	0.92	68	0.87	71	0.85	70	0.78	71
50	1.35	1.33	70	1.28	62	1.39	68	1.30	71	1.28	70	1.17	72
100	1.91	1.84	63	1.76	65	1.93	62	1.80	66	1.78	69	1.59	68
200	2.67	2.55	64	2.42	63	2.68	67	2.49	67	2.46	66	2.17	73
500	4.27	3.91	69	3.68	68	4.12	69	3.80	70	3.78	69	3.28	78
750	5.23	4.74	69	4.44	65	4.99	68	4.58	68	4.59	64	3.92	77
1000	6.04	5.45	71	5.06	68	5.73	68	5.28	69	5.24	64	4.44	79

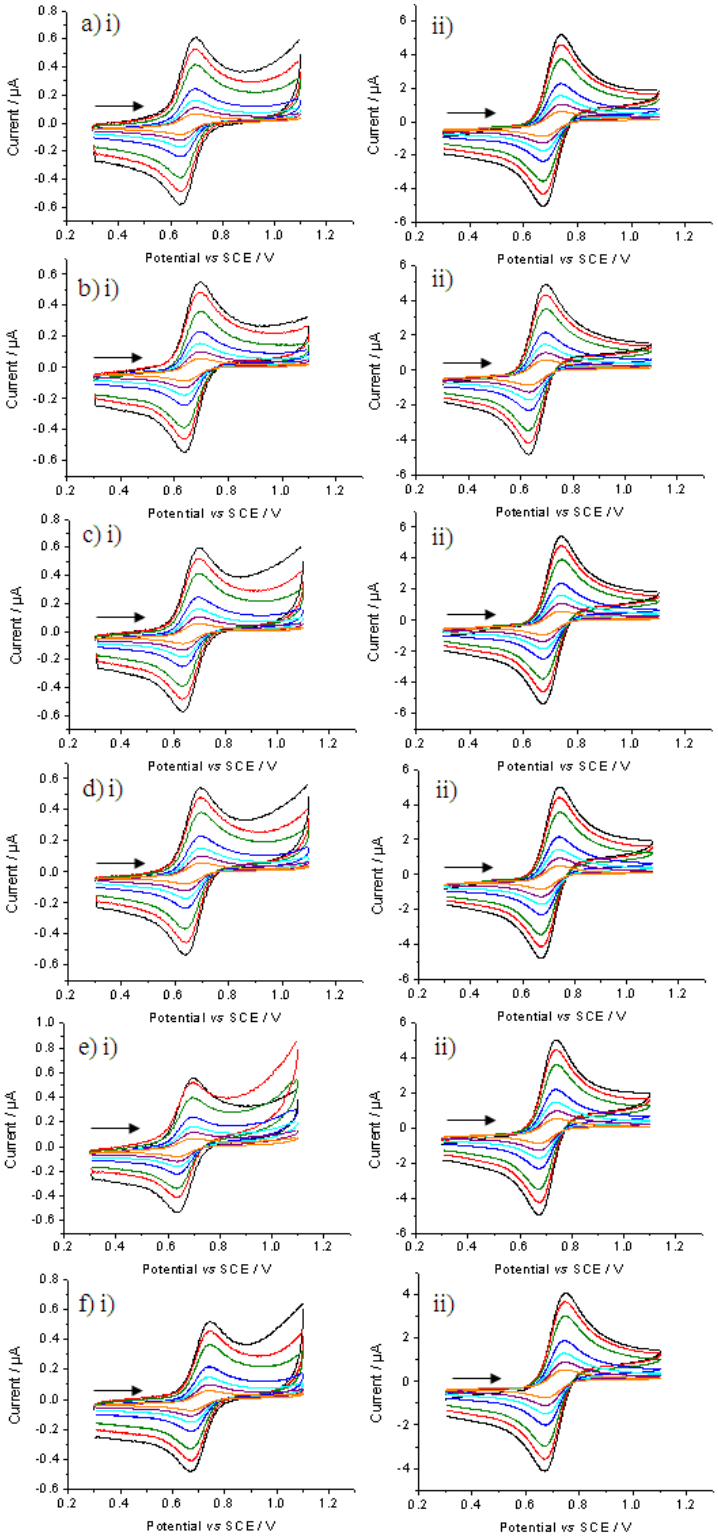

Figure 3.26. CV recorded using a range of scan rates showing the oxidation of i) 0.1 mM $IrCl_6^{2-}$ in 0.1 M $KNO_3$and ii) 1 mM $IrCl_6^{2-}$ in 0.1 M KNO_3 for 1 mm macrodisc; a) pBDD, b)HB2 (100), c) 85B (100), d) 05A (110), e) 85G (110) and f) CP09 (111). The following colour key for scan rates applies; ***20 mV s^{-1}****,* ***50 mV s^{-1}****,* ***100 mV s^{-1}****,* ***200 mV s^{-1}****,* ***500 mV s^{-1}****,* ***750 mV s^{-1}*** *and* ***1000 mV s^{-1}****.*

With the exception of CP09, all BDD electrodes are offering fairly reversible ΔE_p values at both concentrations, more so than during the oxidation of $FcTMA^+$ especially at faster scan rates. All i_p values were close to predicted theoretical values, with 85B (highest [B]) excelling.

CP09 (111) ΔE_p range of 66-79 mV is similar to that observed when using FcTMA+. Experimental i_p values were slightly below calculated values, this was also seen with $FcTMA^+$.

Electrochemically, $FcTMA^+$ and $IrCl_6^{2-}$ are similar as both are oxidised at positive potentials. Unfortunately due to solubility limitations the two redox mediators could not be used at high concentration (10 mM).

$Ru(NH_3)_6^{3+}$ is another well-known fast electron transfer outer sphere redox mediator. However the E$^{o\prime}$ of $Ru(NH_3)_6^{3+}$ [53] positions it just within the band gap of p-type BDD semiconducting diamond[10] as shown in Figure 3.27. Hence this couple is likely to be most sensitive to the differing electrical properties ([B]) of scBDD especially for [B] $\leq 1 \times 10^{20}$ cm^{-3}. Existing studies have shown close to reversible electrochemical behaviour for $Ru(NH_3)_6^{3+}$ reduction at H-terminated BDD (1×10^{19} cm^{-3}) *i.e.* with [B] below the metal-like threshold.[54,55] However, this was attributed to the presence of additional surface carriers due to sp^2 carbon or directly from the H-termination of the surface.[56]

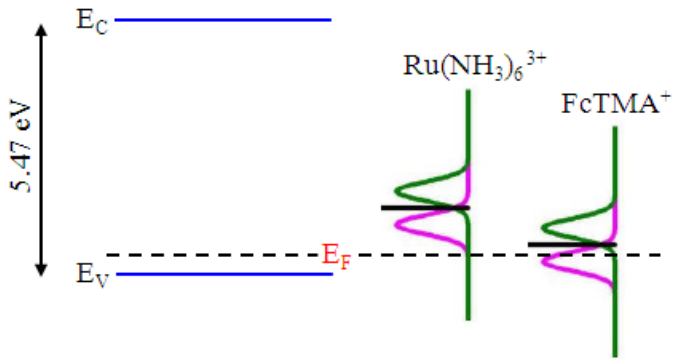

Figure 3.27. Band diagram showing the differences in redox potential for $Ru(NH_3)_6^{3+}$ *and* $FcTMA^+$ *(not to scale).*

BDD electrodes were employed using a range of scan rates (10 – 1000 mV s^{-1}) and three different concentrations of $Ru(NH_3)_6^{3+}$; 0.1, 1 and 10 mM. CVs and corresponding data table are shown in Figure 3.28 and Table 3.9.

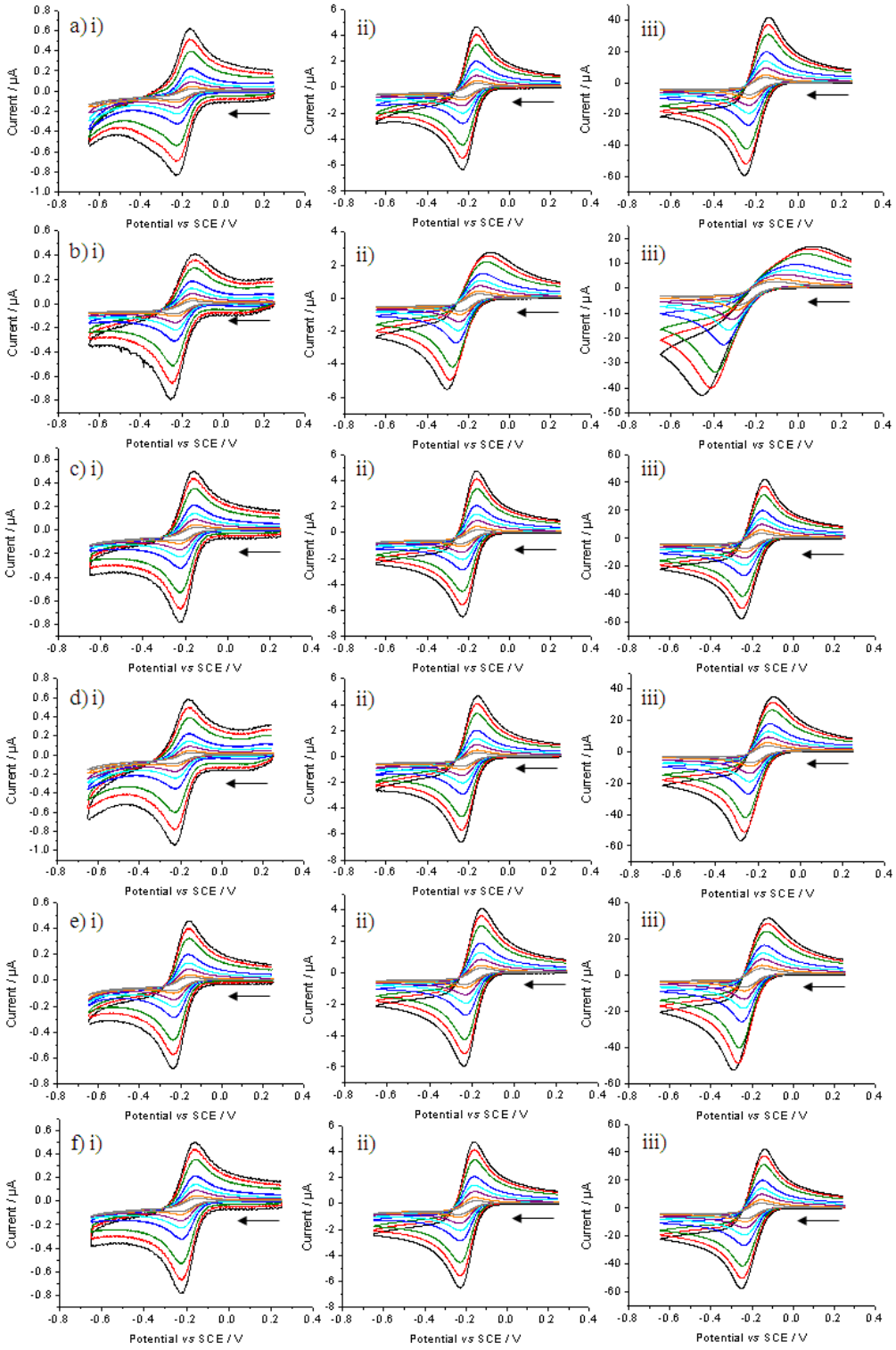

Figure 3.28. CV recorded using a range of scan rates showing the reduction of i) 0.1 mM $Ru(NH_3)_6^{3+}$ in 0.1 M KNO_3, ii) 1 mM $Ru(NH_3)_6^{3-}$ in 0.1 M KNO_3 and iii) 10 mM $Ru(NH_3)_6^{3-}$ in 0.1 M $KNO_3$for 1 mm macrodisc; a) pBDD, b)HB2 (100), c) 85B (100), d) 05A (110),e) 85G (110) and f) CP09 (111). The following colour key for scan rates applies; ***10 mV s^{-1}***, ***20 mV s^{-1}***, ***50 mV s^{-1}***, ***100 mV s^{-1}***, ***200 mV s^{-1}***, ***500 mV s^{-1}***, ***750 mV s^{-1}*** *and* ***1000 mV s^{-1}***.

Table 3.9. Theoretical reduction i_p using a range of scan rates and varying concentrations of $Ru(NH_3)_6^{3+}$ compared to experimental i_p and ΔE_p values for 1 mm macrodisc BDD electrodes.

0.1 mM		pBDD		HB2 (100)		85B (100)		05A (110)		85G (110)		CP09 (111)	
Scan rate / mV s^{-1}	Theory i_p / µA	i_p / µA	ΔEp / mV	i_p / µA	ΔEp / mV	i_p / µA	ΔEp / mV	i_p / µA	ΔEp / mV	i_p / µA	ΔEp / mV	i_p / µA	ΔEp / mV
10	-0.06	-0.08	90	-0.08	92	-0.08	93	-0.08	90	-0.08	85	-0.07	94
20	-0.09	-0.10	77	-0.10	81	-0.11	78	-0.11	77	-0.10	75	-0.09	84
50	-0.14	-0.15	74	-0.16	81	-0.16	72	-0.16	76	-0.15	71	-0.12	77
100	-0.20	-0.24	65	-0.22	83	-0.20	64	-0.22	67	-0.20	67	-0.17	72
200	-0.28	-0.31	69	-0.30	87	-0.32	65	-0.32	66	-0.28	68	-0.22	76
500	-0.43	-0.49	74	-0.46	105	-0.50	72	-0.50	75	-0.45	79	-0.33	86
750	-0.54	-0.61	65	-0.59	114	-0.62	69	-0.65	65	-0.55	79	-0.42	86
1000	-0.63	-0.71	69	-0.70	120	-0.71	69	-0.77	68	-0.64	72	-0.51	79
1 mM		pBDD		HB2 (100)		85B (100)		05A (110)		85G (110)		CP09 (111)	
Scan rate / mV s^{-1}	Theory i_p / µA	i_p / µA	ΔEp / mV	i_p / µA	ΔEp / mV	i_p / µA	ΔEp / mV	i_p / µA	ΔEp / mV	i_p / µA	ΔEp / mV	i_p / µA	ΔEp / mV
10	-0.63	-0.76	79	-0.77	95	-0.84	87	-0.76	79	-0.74	80	-0.62	83
20	-0.88	-0.98	71	-0.98	94	-1.05	79	-0.99	72	-0.96	76	-0.80	79
50	-1.40	-1.46	71	-1.45	104	-1.53	68	-1.48	73	-1.42	72	-1.18	80
100	-1.98	-2.02	64	-1.98	110	-2.10	67	-2.06	67	-1.98	68	-1.62	74
200	-2.80	-2.82	69	-2.71	129	-2.92	66	-2.90	68	-2.75	73	-2.23	81
500	-4.43	-4.43	69	-4.05	164	-4.54	68	-4.58	86	-4.27	82	-3.35	95
750	-5.40	-5.40	68	-4.70	189	-5.53	65	-5.57	75	-5.16	80	-3.87	116
1000	-6.21	-6.26	68	-5.10	209	-6.39	66	-6.41	83	-5.90	83	-4.29	136
10 mM		pBDD		HB2 (100)		85B (100)		05A (110)		85G (110)		CP09 (111)	
Scan rate / mV s^{-1}	Theory i_p / µA	i_p / µA	ΔEp / mV	i_p / µA	ΔEp / mV	i_p / µA	ΔEp / mV	i_p / µA	ΔEp / mV	i_p / µA	ΔEp / mV	i_p / µA	ΔEp / mV
10	-6.26	-7.52	74	-6.47	162	-7.29	79	-6.90	80	-6.67	80	-5.70	84
20	-8.83	-9.75	74	-8.31	189	-9.61	80	-9.30	81	-8.93	83	-7.52	84
50	-14.0	-14.4	80	-11.6	236	-14.3	84	-14.0	89	-13.5	92	-11.1	90
100	-19.8	-19.9	82	-14.9	136	-19.6	84	-19.5	91	-18.7	97	-15.3	94
200	-28.0	-27.6	85	-18.9	198	-27.0	89	-27.1	104	-25.9	109	-20.9	104
500	-44.3	-42.6	101	-24.2	359	-41.3	106	-41.7	125	-39.7	134	-31.3	130
750	-54.2	-51.7	106	-24.7	412	-49.7	108	-50.4	134	-47.6	142	-37.3	142
1000	-62.6	-58.1	115	-42.9	454	-56.4	116	-54.5	155	-49.7	168	-35.4	190

When using the redox couple $Ru(NH_3)_6^{3+/2+}$ for all BDD electrodes the response at low and medium concentrations is close to reversible, but slightly less so than for the more positive formal redox potential species, $FcTMA^{+/2+}$ and $IrCl_6^{2-/3-}$.

pBDD, (100) 85B, (110) 05A and (110) 85G all show a better electrochemical response in terms of reversibility. At the highest concentration all electrode materials start to show significant deviations away from reversible behaviour especially at the higher scan rates. This is especially true of heterogeneous (111) CP09 and more so of bulk (100) HB2.

One potential explanation for the difference in behaviour with this redox couple compared with $FcTMA^+$ and $IrCl_6^{2-}$ is the fact that the electrode is being held at a potential where there will be a depletion of charge carriers which is exacerbated for $[B] \leq 1 \times 10^{20}$ cm^{-3} *i.e.* where BDD moves into the p-type semiconducting region, moreover, the lower the [B] the higher the intrinsic resistance of the BDD. Comparing HB2 and 85A which differs by an order of magnitude in [B], with the latter firmly in the metal-like conductivity region it is no surprise the latter electrode behaves far more ideally than the former, even when challenged to pass very high currents.

3.2.4 Macro Electrochemistry of Complex Redox Mediators

The wide aqueous potential window of BDD can be exploited to investigate the electrochemical activity of $Ru(bpy)_3^{2+/3+}$. BDD advantageous wide potential window (~4 V, Table 3.5) suggests it is likely to facilitate the reduction of the first bipyridine (bpy) ligand π^* system to $[Ru^{II}(bpy)(bpy)(bpy^-)]$ in aqueous solution which occurs at ~ -1.3 V.

Both metal and pBDD electrodes are capable of detecting the oxidation/reduction of the central metal ion of $Ru(bpy)_3^{2+/3+}$ in aqueous solution as seen in Figure 3.29. $Ru(bpy)_3^{2+/3+}$; $E°'$ = 1.24 V (*vs.* NHE),[51] D = 4.80×10^{-6} cm^2 s^{-1}.[57] This is near reversible for pBDD (61 mV) and less

reversible for Pt at 76 mV. The larger ΔE_p for Pt could be attributed to the formation of PtO_2on the electrode surface at the positive potentials swept to, which in turn may retard ET. Pt electrodes also suffer from higher background currents as demonstrated in Figure 3.24 and therefore have a significantly reduced potential window when compared to BDD electrodes, resulting in the early onset of water oxidation/reduction when employed with aqueous solutions.

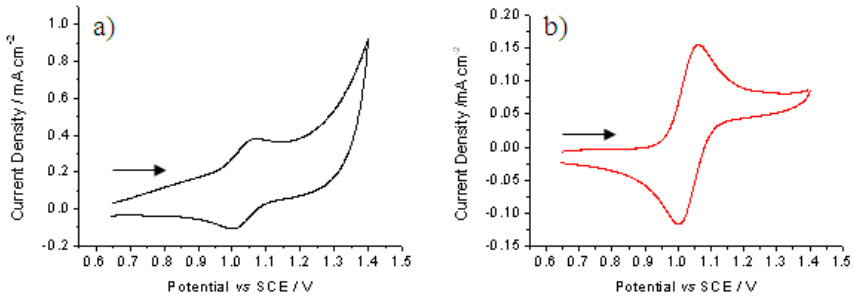

Figure 3.29. CVs in aerated 1 mM $Ru(bpy)_3^{2+/3+}$ in 0.1 M KNO_3 showing the oxidation/reduction of $Ru^{2+/3+}$ using a) Pt electrode and b) pBDD both using a scan rate of 100 mV s^{-1}.

When employing a Pt electrode, the reduction of the bpy ligand in aqueous solution is masked by the onset of water electrolysis in the negative potential window, therefore electrochemical analysis of the ligand is not possible as seen in Figure 3.30a and b. Therefore for Pt electrodes, in order to visualise the oxidation/reduction of the ligand, acetonitrile[58-60] is commonly used as the electrochemical solvent for analysis of this redox mediator. Whereby within this solvent , potentials of -1.28, -1.47 and -1.71 V have been reported , successively more negative for each of the three ligands undergoing a redox process.[61] This redox mediator is utilised in photo catalytic applications due to its range of excited states.[58]

Figure 3.30c shows the oxidation/reduction processes for the central metal ion followed by the irreversible reduction/oxidation of the first bpy ligand of $Ru(bpy)_3^{2+/3+}$ with pBDD due to low background currents and wide potential window, performed in an aqueous solvent.

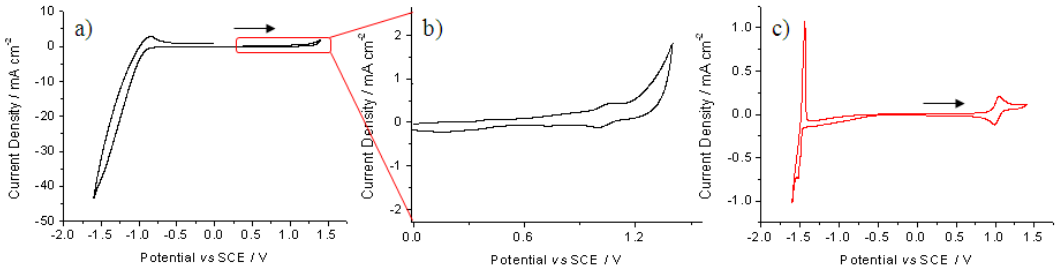

Figure 3.30. CVs in aerated 1 mM $Ru(bpy)_3^{2+/3+}$ in 0.1 M KNO_3showing multiple oxidation/reduction reactions using a) Pt electrode with an increased magnification shown in b) and c) pBDD. Scan rate 100 mV s^{-1}.

The reduction peak observed ~-1.5 V is likely to be that of the first ligand, slightly shifted due the different solvent utilised to that reported in literature. Utilisation of a heterogeneous pBDD electrode in aqueous solution suggests that homogeneous scBDD may also perform well with $Ru(bpy)_3^{2+/3+}$ and this is shown in Figure 3.31for scBDD HB2 and 85B, both (100).

The utilisation of a heterogeneous pBDD electrode in aqueous solution suggests that homogeneous scBDD may also perform well with $Ru(bpy)_3^{2+/3+}$and this is shown in Figure 3.31for scBDD HB2 and 85B, both (100).

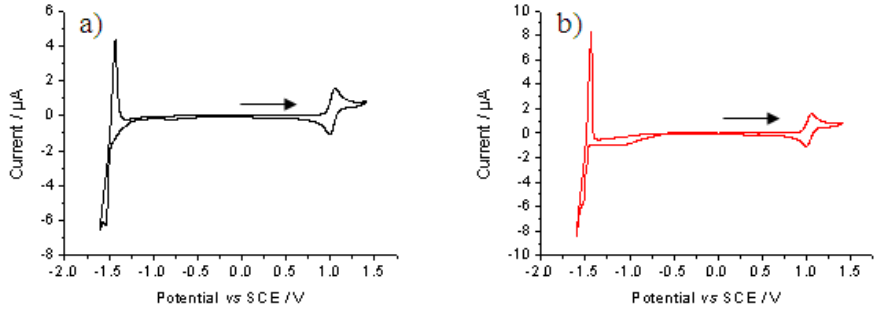

Figure 3.31. CVs in aerated 1 mM $Ru(bpy)_3^{2+/3+}$ with 0.1 M KNO_3at scan rate of 100 mV s^{-1},showing multipl oxidation/reduction reactions using a) HB2 and b) 85B.

There is little difference in the electrochemical behaviour between the pBDD and (100) scBDD electrodes clearly showing the oxidation/reduction of the $Ru^{2+/3+}$ ion, followed by the irreversible reduction/oxidation of the first bpy ligand. The irreversible nature of the reduction/oxidation of the first bpy ligand could be attributed to the possible onset of the potential window on BDD, however the currents recorded are still very small. The CVs for the (110) and (111) samples employing $Ru(bpy)_3^{2+/3+}$ are shown in Figure 3.32.

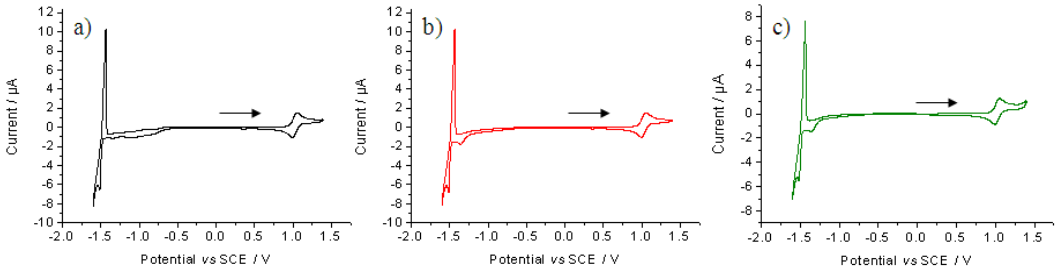

Figure 3.32. CVs in aerated 1 mM $Ru(bpy)_3^{2+/3+}$ with 0.1 M KNO_3at a scan rate of 100 mV s^{-1},showing multiple oxidation/reduction reactions using a) 05A (110), b) 85G (110) and c) CP09 (111).

With the exception of (110) 05A scBDD where at ~0.5 V the onset of the reduction of the ligand or aqueous solution is noticeable. All other BDD electrochemical responses are similar suggesting that $Ru(bpy)_3^{2+/3}$ can be considered

an outer sphere redox mediator. The possible onset of the aqueous solvent window of BDD suggests further work using a non-aqueous solvent such as acetonitrile would be beneficial to fully understand this complex redox mediator. BDD would be a suitable electrode material for further investigation employing non-aqueous solutions for photocatalytic applications.[62]

3.2.5 Single Crystal Boron Doped Diamond Electrode Pre-treatment and its Effects

Outer sphere redox mediators are insensitive to the specific functional groups of an O-terminated BDD sample, in contrast to inner sphere redox mediators,[20,54,63-66] as shown in Figure 1.14. Inner sphere redox mediators must approach and bind to the substrate to facilitate electron transfer between the electrode and redox mediator, thus inner sphere redox mediators are very sensitive to surface termination.[20, 65]

PBDD is heterogeneous with multiple crystallographic orientations and a range of O-terminated functional groups. This has been demonstrated via XPS.[67] In contrast, scBDD of a specific orientation would therefore be expected to have a reduced selection of oxygen containing functional groups across the surface (depending on surface treatment).

Comprehensive research of ($Fe(CN_6)^{3-/4-}$) on traditional electrodes such as GC[65, 68] showed complex electrochemical responses dependant on the electrode material combined with surface chemical state/functionalities, redox species concentration and supporting electrolyte. Using highly doped pBDD ([B] > 1×10^{20} cm^{-3}) Granger and Swain,[54] Szunerits *et al.*[69, 70] and Marken *et al.*[71] suggested faster ET kinetics for $Fe(CN_6)^{3-/4-}$ with H-terminated material.[54, 69-71]

Several studies have also reported that post anodic treatment of pBDD electrodes leads to an increase in the rate of ET for $Fe(CN_6)^{3-/4-}$, and a corresponding decrease in ΔE_p from 200 to 90 mV.[72, 73] Thus in general it is believed the surface termination of BDD strongly affects the ET kinetics of $Fe(CN_6)^{3-/4-}$. It has been suggested that the negative charges on the oxygen functional groups present on the surface repel negatively charged redox species.[64]Alternatively, it was proposed that oxygen functional groups are able to function as site blockers therefore hindering ET.[54, 73]

A classic inner sphere redox couple is $Fe^{3+/2+}$ and using GC (sp^2) electrodes, results have shown that the ET kinetics are convincingly effected by the electrode surface, specifically when oxides are present.[74] Severe anodic treatments have demonstrated the reduction in reversibility of the$Fe^{2+/3+}$ redox mediator when compared to H-terminated electrodes.[75] Thus leading to the same conclusion as with $Fe(CN_6)^{3-/4-}$that oxygen containing functional groups have an effect on the ET kinetics of inner sphere redox mediators. As suggested for GC electrodes,[65, 76] it is believed carbonyl groups facilitate ET for electrochemical reactions of $Fe^{2+/3+}$.

Thus the aim here was to study, on scBDD electrodes of defined crystallographic orientation and chemical functionality, the effect of surface chemistry on the ET kinetics of $Fe(CN_6)^{3-/4-}$and $Fe^{3+/2+}$and compare with the electrochemical performance of pBDD. All electrodes were prepared as described in 2.4.2 prior to the pre-treatment process. Two pre-treatments were undertaken in 0.5 M H_2SO_4, either anodic polarisation (+3 V *vs*. Ag|AgCl for 60 s) or cathodic polarisation (-3 V *vs*. Ag|AgCl, for 60 s). The electrodes were rinsed with Milli-Q water and dried in air before CV was performed.

Figure 3.33 shows the CV response of BDD electrodes with selected pre-treatments using (i) 1 mM $Fe(CN_6)^{3-/4-}$ in 0.1 M KNO_3 where $E°'$ = 0.36 V (*vs.* NHE)[51] and (ii) 1 mM $Fe^{2+/3+}$ in 0.1 M H_2SO_4 where $E°'$ = 0.77 V (*vs.* NHE).[51]

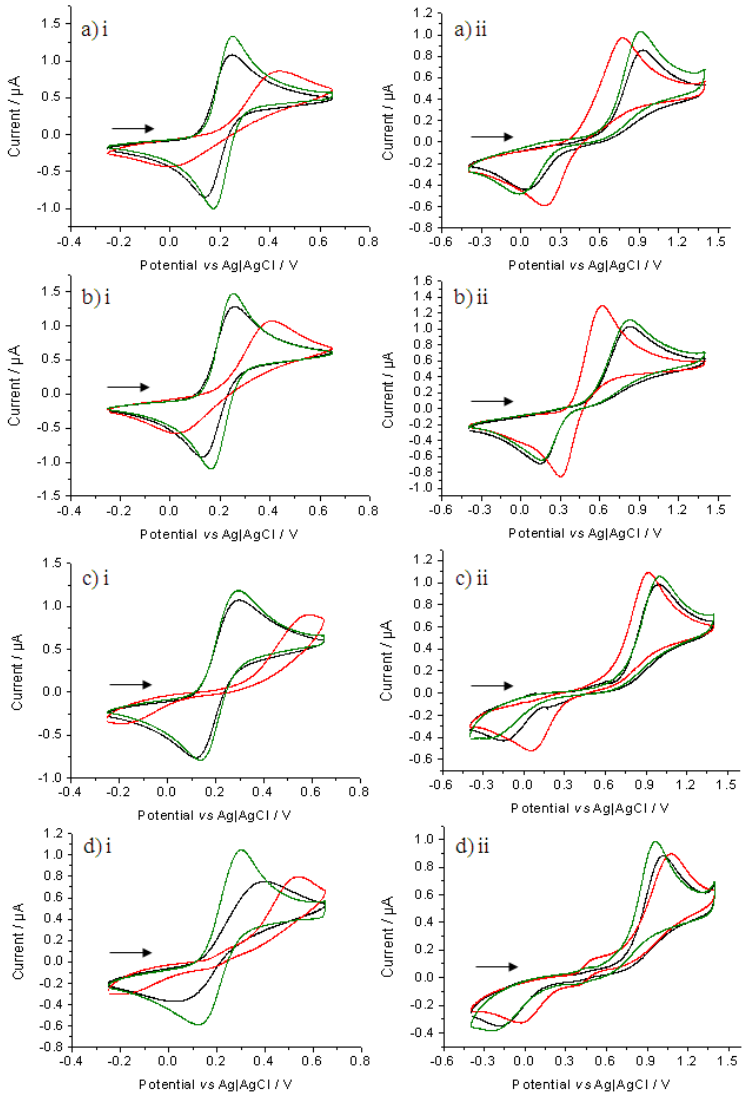

Figure 3.33. CVs showing the response of selected pre-treatment's on a) pBDD, b) 85B (100), c) 85G (110) and d) CP09 (111) when used with inner sphere redox mediator i)1 mM $Fe(CN_6)^{3-/4-}$ in 0.1 M KNO_3 and ii) 1 mM $Fe^{2+/3+}$ in 0.1 M H_2SO_4. In all cases colours are represented as ***alumina polish****,* ***anodic polarisation*** *(****+3 V for 60 sec****) and* ***cathodic polarisation*** *(****-3 V for 60 sec****).Scan rate of 100 mV* s^{-1}.

Figure 3.33 clearly demonstrates the changes in CV response resulting from electrode surface pre-treatment for both redox mediators, this is further confirmed referring to the data in Table 3.10

*Table 3.10. Extracted i_p and ΔE_p values from the CVs of Figure 3.33 from three different sample pre-treatments (**alumina polish**, **anodic polarisation**(**+3 V for 60 s**) and **cathodic polarisation** (**-3 V for 60 s**) using inner sphere redox mediators 1 mM $Fe(CN_6)^{3-/4-}$ in 0.1 M KNO_3 followed by 1 mM $Fe^{2+/3+}$ in 0.1 M H_2SO_4.*

Sample	Pre-Treatment	1 mM $Fe(CN)_6^{3-}$		1 mM Fe^{2+}	
		i_p/ µA	ΔE_p / mV	i_p/ µA	ΔE_p / mV
MR14 pBDD	**Alumina Polish**	**1.08**	108	**0.86**	899
	+3 V, 60 sec	**0.86**	431	**0.94**	589
	-3 V, 60 sec	**1.33**	78	**1.03**	890
85B (100)	**Alumina Polish**	**1.27**	127	**1.03**	681
	+3 V, 60 sec	**1.07**	378	**1.29**	310
	-3 V, 60 sec	**1.45**	90	**1.11**	671
85G (110)	**Alumina Polish**	**1.06**	176	**0.99**	1133
	+3 V, 60 sec	**0.87**	763	**1.09**	912
	-3 V, 60 sec	**1.18**	158	**1.05**	969
CP09 (111)	**Alumina Polish**	**0.76**	362	**0.88**	1198
	+3 V, 60 sec	**0.79**	704	**0.89**	1011
	-3 V, 60 sec	**1.05**	174	**0.98**	1184

Starting with $Fe(CN_6)^{3-/4-}$, pBDD being heterogeneous will have multiple orientations, therefore a variety of different oxygen containing functional groups on the surface. The use of alumina slurry and anodic polarisation offer faster ET kinetics than anodic polarisation suggesting the oxygen functional groups (known to be mixed for alumina polished) do not hinder the reaction. Cathodic polarisation introduces preferred surface termination thereby aiding the ET for $Fe(CN)_6^{3-}$ however anodic polarisation appears to enhance the ET kinetics observed for Fe^{2+},

thereby suggesting oxygen containing functional groups rearrangement as a direct result of the polarisation treatment.

When 85B (100) was subject to cathodic polarisation, as seen before with pBDD, the ET kinetics for $Fe(CN)_6^{3-}$ were faster, anodic polarisation enhanced the ET kinetics for Fe^{2+}. This proposed homogeneous sample offered much faster ΔE_p values (by ~ 200 mV) which was the most (quasi) reversible of all electrodes employed.

The (110) sample continued to follow suit relating to $Fe(CN)_6^{3-}$ whereby cathodic polarisation led to faster ET kinetics, however this was much slower than pBDD and 85B. There was little change to the sluggish ET kinetics when employed with Fe^{2+},suggesting anodic polarisation did not encourage the rearrangement of functional groups to those appearing to facilitate ET.

The (111) sample which is heterogeneous in nature demonstrated the slowest kinetics (ΔE_p > 1000 mV) with Fe^{2+}, again with very little change when anodic polarisation was applied. ET kinetics with $Fe(CN)_6^{3-}$ were faster when cathodic polarisation was performed, although this was still quasi reversible. The use of anodic polarisation doubled ΔE_p from 362 mV when alumina polished to 704 mV when anodically polarised and used with $Fe(CN)_6^{3-}$ suggesting this pre-treatment blocks the surface for this heterogeneous electrode.

Upon a final alumina slurry polish, the ET kinetics observed were similar to the original CVs from Figure 3.33. This suggests electrode pre-treatment is not permanent (although longevity testing was not performed) and alumina slurry polishing is able to return the electrode to its initial state of mixed O-terminating functional groups.

3.2.6 Finite Element Modelling (FEM)

FEM is capable of simulating CVs for different ET rate constants for a given scan rate (in this case 100 mV s^{-1}). As the scBDD is proposed to be homogeneous, in the simplest case the whole surface can be considered uniformly active. Butler-Volmer kinetics can be used to simulate a *CV* response as a function of standard rate constant (k^0) using a transfer coefficient α=0.5 which is reasonable for outer sphere redox mediators.[77]

Butler-Volmer[20] kinetics were used to describe the ET kinetics at the scBDD electrode/solution interface as shown Figure 3.34 and Figure 3.35 describing how a potential range applied to the electrode affect its kinetics which consequently influences the measured current and rate of ET. ET kinetics determines the rate that the electrode can reduce or oxidise a species such that faster ET kinetics will produce higher currents and by comparison slower ET kinetics, reduced currents.

Modelling was undertaken using a commercial FEM package; COMSOL Multiphysics 4.2a (COMSOL AB, Sweden) with a Matlab Interface (Release 2011a) (Mathworks Inc., Cambridge, UK). A valid approximation of the experimental system was built using 52,247 triangular mesh points per simulation with the highest concentration of mesh points at the scBDD electrode and reducing in number until the bulk boundaries. Four simple one electron outer sphere redox mediator reactions were considered which mimicked the experimental set up of linear diffusion to the electrode surface. One of the reactions is described in equation 3.3.

$$FcTMA^{+} + e^{-} \underset{\boldsymbol{k_f}}{\overset{\boldsymbol{k_b}}{\rightleftharpoons}} FcTMA^{2+} \qquad \textbf{(3.3)}$$

Where k_b and k_f are the respective rate constants for the oxidation and reduction of the reactive species. For the reaction above, the simulation solved a time dependent diffusion equation described in equation 3.4.

$$\frac{\partial c_j}{\partial t} = D_j\left(\frac{\partial c_j}{\partial r^2} + \frac{1}{r}\frac{\partial c_j}{\partial r} + \frac{\partial^2 c_j}{\partial z^2}\right) \qquad \textbf{(3.4)}$$

Where c_j (mol cm^{-3}) and D_j (cm^2 s^{-1}) represent the concentration and diffusion coefficient of active species j (FcTMA$^+$ in this example), r is radial direction from the macrodisc centre and z the coordinate in the directions normal to the centre of the macrodisc. For simplification, D_j was assumed to be identical for both the oxidation and reduction states of the redox mediator, to allow each simulation to be formulated with only one species. (Table 3.6 and page 111 for Ru(bpy)$_3^{2+}$).

The model assumes there are no convection or migration effects therefore the Nernst Planck relationship (equation 1.2) can be simplified to consider only the diffusion component shown in equation 3.5.

$$J_j = -D_j \nabla c_j \qquad \textbf{(3.5)}$$

Equation 3.6 describes the reaction rate as it progresses over time considering the diffusion transport between the redox species and its solvent giving flux across the model boundaries.

$$Rj = \frac{\partial cj}{\partial t} + \nabla . -(Dj\nabla cj) \qquad \textbf{(3.6)}$$

Where R_j is the reaction rate, ∂c_j the accumulation/consumption of redox species over time and $D_j \nabla c_j$is the flux across model boundaries. The boundary conditions used within the FEM[78] to determine the theoretical current response at the scBDD electrode by solving equation 3.4 and 3.5 are visualised in Figure 3.34 and described in Table 3.11.

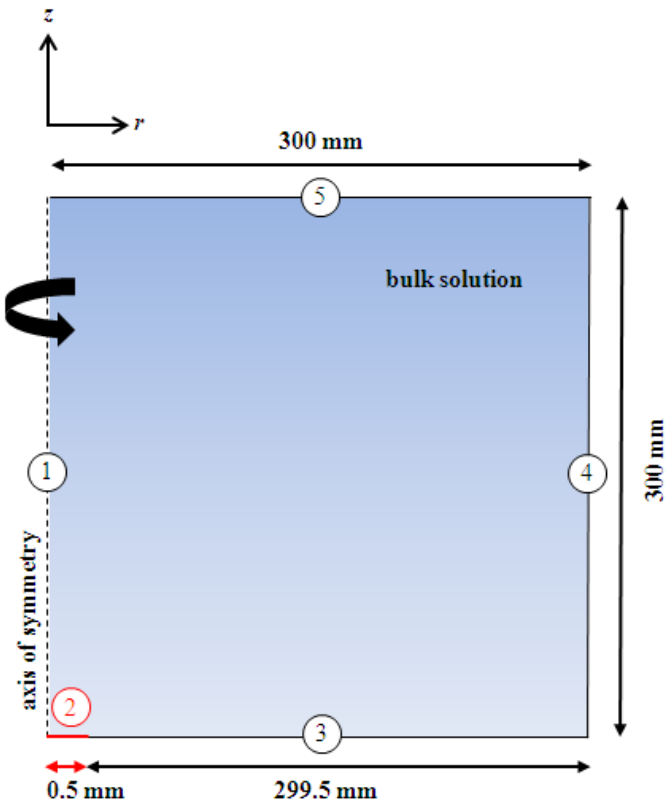

Figure 3.34. 2D simulation domain for the 1 mm macrodisc electrode dipped into a redox mediator and electrochemistry undertaken (not to scale).

Table 3.11. Summary of the boundary conditions used for the simulation of the 1 mm macrodisc electrode.

Label	Boundary Type	Coordinates (*r*, *z*)	Equation
1	Axis of symmetry	0, 0	$0 = \nabla c . \underline{n}$
2	scBDD Electrode	0, 0 to 0, 0.5	$N_{oj} = -n . N_j$ and $N_{oj} = k_b . (c_b - c) - k_f . c$
3	Bulk Solution	0, 0.5 to 0.5, 300	$0 = -n . N_j$
4	Bulk Solution	300,300	$c_j = c_b$
5	Bulk Solution	300, 300 to 0, 300	$c_j = c_b$

Where c represents the initial concentration of the redox mediator and $\underline{n}$ represents the inward-pointing unit normal vector and N_{oj} represents overall flux. Model boundaries were selected at 300 mm, which is reasonable for linear diffusion at a 1 mm diameter electrode. Figure 3.35 demonstrates the model working over time, highlighting changes in the concentration of $FcTMA^+$ at the start, mid-way point and end of the CV.

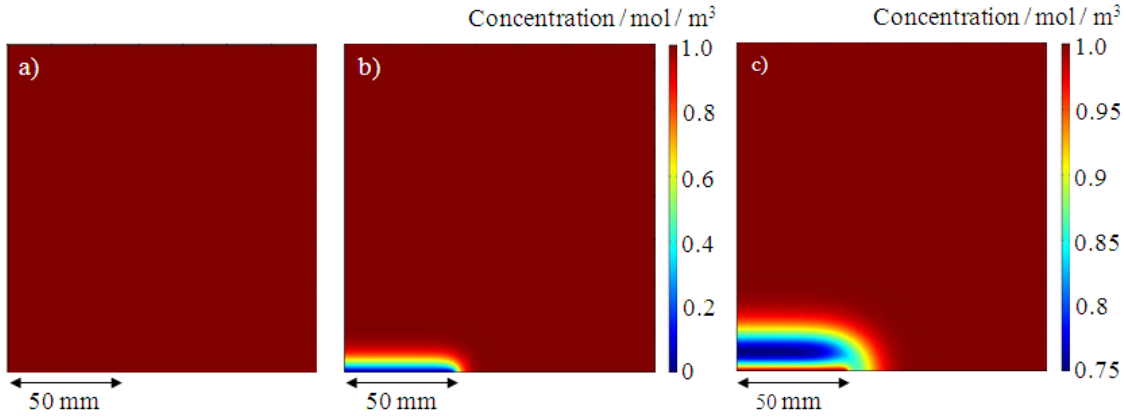

Figure 3.35. a) Simulated electrode response to the oxidation of 1 mM $FcTMA^+$ at 0 s, b) at 7 s (half way point) and c) at 15 s (completion). Scan rate 100 mV s^{-1}.

Simulations were undertaken using a wide range of k^0at a single scan speed for a range of concentrations and redox mediators appropriate to the experiments undertaken. Model data was plotted generating a sigmoidal plot of log(k^0) *vs.* ΔE_p for

each experiment performed. A Boltzmann function was fitted to the data to provide an analytical expression for ΔE_p as a function of k^0. Finally, the experimental ΔE_p was used to determine the k^0 for reactions, results of which already quoted herein.

3.2.7 Finite Element Modelling (FEM) Results

Table 3.12 shows k^0 values for three different oxidation reactions at differing concentrations and a reduction reaction across a wider range of concentrations, experimental results of which have already been described within this chapter.

Table 3.12. FEM of k^0 values for selected oxidation and reduction reactions using experimental ΔE_p values, quoted herein with the exception of Ru(bpy)$^{2+}$.

	Oxidation, k^0 / cm s^{-1}						**Reduction, k^0 / cm s^{-1}**		
Redox Mediator	**FcTMA$^+$**		**IrCl$_6^{2-}$**		**Ru(bpy)$^{2+}$**		**Ru(NH$_3$)$_6^{3+}$**		
Concentration / mM	**0.1**	**1**	**0.1**	**1**	**0.1**	**1**	**0.1**	**1**	**10**
pBDD	0.12	0.16	0.13	0.12	0.05	0.04	0.05	0.06	0.013
HB2 (100)	0.04	0.03	0.04	0.12	0.06	0.06	0.01	0.01	0.003
85B (100)	0.09	0.08	0.16	0.16	0.19	0.19	0.05	0.05	0.012
05A (110)	0.05	0.04	0.04	0.04	0.04	0.06	0.04	0.04	0.008
85G (110)	0.05	0.05	0.06	0.04	0.03	0.05	0.05	0.04	0.007
CP09 (111)	0.02	0.03	0.05	0.03	0.05	0.05	0.03	0.02	0.007

The majority of samples offered ET rates close to each other for the 0.1 and 1 mM solution. If k^0 values were similar between differing concentrations of the same redox mediator this would suggest the electrode is behaving independently of concentration and this was observed for HB2, 05A, 85G and CP09 for oxidation reactions (with the exception of HB2 with 0.1 mM $IrCl_6^{2-}$which is a suspected outlier). Furthermore these samples all have reported similar [B].

Faster ET kinetics were noted for pBDD and 85B with $FcTMA^+$ and $IrCl_6^{2-}$. 85B also offered the fastest ET rates for $Ru(bpy)^{2+}$, which is not unexpected due it the higher [B].

The employment of 10 mM $Ru(NH_3)_6^{3+}$proved challenging for all BDD electrodes. ET rates were much slower than for the lower concentrations of the same mediator. This suggests the finite number of charge carriers within BDD was a contributing factor to the sluggish ET rates due to the high concentration utilised. Both pBDD and 85B provided the fastest k^0 values whereas HB2 the lowest. Both (110) and the (111) all of similar [B] offered similar ET rates lying at the centre of this range.

3.2.8 Delamination of the Cap Layer from 1 mm Macrodisc 85B (100)

Over time a change in the electrochemical response of the 1 mm macrodisc 85B (100) was observed. This was observed in differing redox mediators ($Ru(NH_3)_6^{3+}$ and $FcTMA^+$) and at differing concentrations (0.1-10 mM) as seen in Figure 3.36.

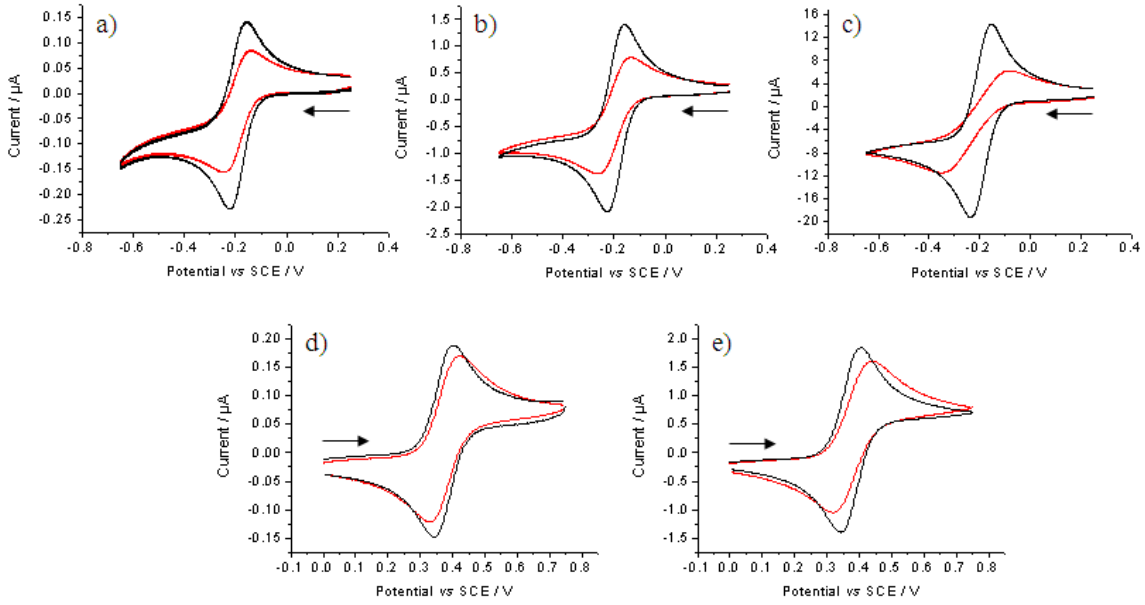

*Figure 3.36. CVs of the 1 mm macrodisc 85B (100) comparing the original 85B (**black**) behaviour to that of a well used 85B (**red**) subject to numerous abrasive treatments during cleaning and fabrication into a macrodisc electrode. a) 0.1 mM $Ru(NH_3)_6^{3+}$, b) 1 mM $Ru(NH_3)_6^{3+}$, c) 10 mM $Ru(NH_3)_6^{3+}$, d) 0.1 mM $FcTMA^+$ and e) 1 mM $FcTMA^+$. For all CVs the supporting electrolyte was 0.1 M KNO_3 ,scan rate 100 mV s^{-1}.*

This particular sample was the most heavily doped and had been subject to numerous acid cleans and electrode refabrications.

C_{meas} (n=3) gave 3.50 ± 0.08µF cm^{-2}, much lower than the original value of 6.21 ± 0.08 µF cm^{-2}(Table 3.4). These results combined with the CVs suggest a change in the material properties of this sample.

DICM microscopy showed surface heterogeneities, noticeably height differences as shown in Figure 3.37, which were investigated further using AFM.

Figure 3.37. DICM image of 85B.1 macrodisc electrode.

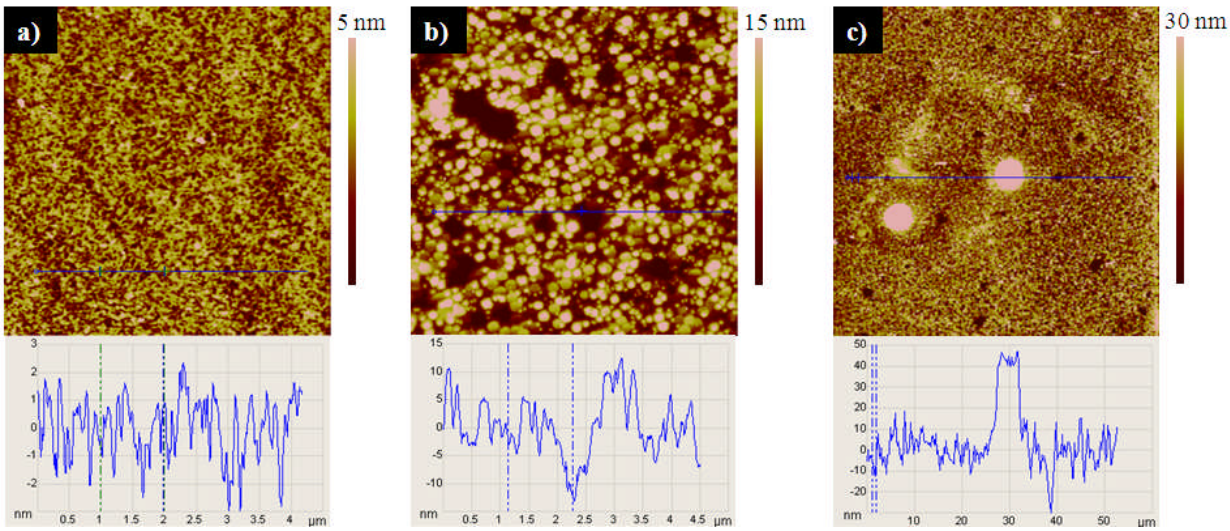

Figure 3.38. TM-AFM images of a) 85A (100) (5 × 5 µm), b) 85B macrodisc (5 × 5 µm) and c) 50 × 50 µm image of 85B macrodisc and their respective cross sections showing surface roughness.

Figure 3.38a shows the original surface of as grown 85A, the sister sample to 85B. 85A was retained whole and therefore subject to reduced handling and fabrication into macrodisc electrodes. Figure 3.38b shows a 5 × 5 µm image clearly showing a very different surface to Figure 3.38a, suggesting that 85B has suffered damage over time. The very differing nature of the surface would suggest that the

cap layer has delaminated and the larger scale image of Figure 3.38c and its cross section confirm this by the change in height across the surface.

To further support the delamination theory, In-Lens FE-SEM was performed and is shown in Figure 3.39. This shows many white spots on the surface with one much darker circular area. This darker circular area is similar in shape to the features seen in Figure 3.38.

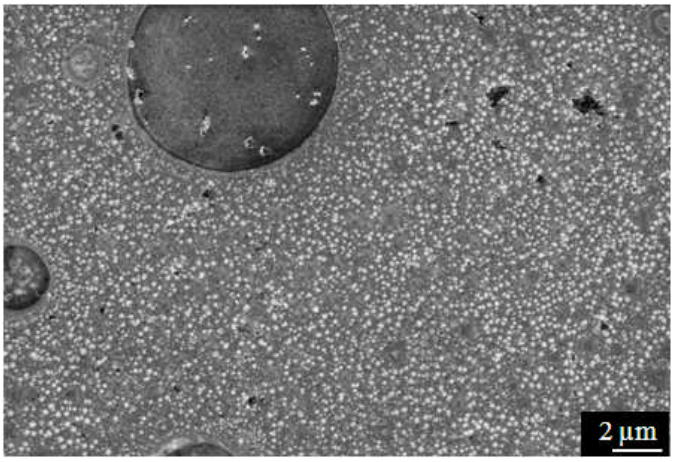

Figure 3.39. In-Lens FE-SEM image of 85B.

Szunerits [79]*et al* used a combination of Raman and SEM to suggest that pBDD films contained differing dopant levels. Particularly, the lighter regions of a pBDD SEM image correlated to lower [B] (high 10^{19} cm^{-3}) and the darker regions of the SEM image to higher [B] of 10^{20} cm^{-3} when combined with Raman spectroscopy. The same principle relating to lighter/darker regions of SEM images can be applied to scBDD and its [B].

The lighter 'white spots' of the image are likely to demonstrate they are of the lower [B] (1 x 10^{19} cm^{-3}) bulk layer. The capping layer of [B] 1 x 10^{21} cm^{-3} would therefore be expected to be of a darker colour should any areas of the cap layer remain on the sample. The dark feature correlates in shape to those observed

under AFM (Figure 3.38c), further supporting the delamination theory. Such that due to fabrication and numerous harsh treatments only a little of the original capping layer remains.

3.3 CONCLUSIONS

A selection of scBDD samples of differing orientations, [B] and surface finishes have been characterised by physical and electrochemical methods. SIMS has provided [B] suggesting a range across the sample provided, this difference in [B] is has the most influence on electrochemical reduction reactions when in the flat band region of BDD. Metals have infinite number of charge carriers so that this reaction would be reversible, however BDD is limited by the amount of [B]. Therefore lower [B] would result in slower ET kinetics, this indeed was the case across a wide range of concentrations (10-0.1 mM) with HB2 offering the slowest ET rates.

Electrochemically, all samples performed well when compared to pBDD for oxidation reactions and several redox mediators were employed. Complex electron processes were visualised in aqueous solution utilising the wide potential window of BDD. The electrochemical response of pre-treated electrodes using inner sphere redox mediators was performed, anodic potentials appearing to promote the oxidation of Fe^{2+} and cathodic potentials promoting the oxidation of $Fe(CN_6)^{3-}$.

DICM and spectroscopy suggested that HB2 contained polycrystalline like defects in certain areas. 85A/B did not show any surface defects but CL suggested some crystalline material of lower [B] within the bulk semiconducting layer, these do not appear to be present at the surface. 05A and 85F/G of (110) orientation were as grown and DICM highlighted the surface was slightly tilted as a result of sample growth coupled with some fleck like surface features Surface roughness was < 5 nm for all samples, polished or as grown.

Raman microscopy demonstrated all samples were of high diamond quality with no sp^2 carbon detected. For sample 85A/B the laser penetrated through the

capping layer (65 nm) and was therefore probing the semiconducting bulk of a lower [B] (1×10^{19} cm^{-3}). This resulted in a lack of Fano resonance which is generally observed when [B] is > 1×10^{20} cm^{-3}.[80] For all other samples analysed using this technique, a Fano resonace was detected. Thus supporting SIMS data that these samples under investigation were above the metal-like conductivity threshold of [B] ~ 1×10^{20} cm^{-3}.[80]

Raman mapping was performed and demonstrated that the polycrystalline like defect of HB2 did contain differing [B]. Raman probed the bulk layer of 85B suggesting the presence of some ‘pyramidal hillock’ defects within the bulk layer, this was also detected using CL. 05A (110) gave a fairly homogeneous map taken from the central area of the sample.

A Raman map of 85G (110) taken incorporating fleck like features was unable to determine these flecks contain higher [B], because the difference in height of the sample would provide a slightly differing Raman response. Finally CP09 (111) suggested a fairly homogeneous substrate, some features (a scratch) on the surface not removed during an acid clean, were highlighted on the optical image and corresponding Raman map. The (110) section of CP09 was not analysed due to focussing issues.

Cumulative evidence from DICM, TM-AFM, FE-SEM and macro electrochemical analysis suggested that over time, thin scBDD layers (~65 nm) when subject to harsh fabrication treatment such as acid cleaning and abrasive treatments can delaminate, thus rendering macrodisc 85B unfit for purpose.

3.4 REFERENCES

1. A. Adriaens and M. G. Dowsett, *Applied Surface Science*, 2006, **252**, 7096-7101.
2. A. L. Colley, C. G. Williams, U. D'Haenens Johansson, M. E. Newton, P. R. Unwin, N. R. Wilson and J. V. Macpherson, *Analytical Chemistry*, 2006, **78**, 2539-2548.
3. L. Hutton, M. E. Newton, P. R. Unwin and J. V. Macpherson, *Analytical Chemistry*, 2009, **81**, 1023-1032.
4. http://www.cleanroom.byu.edu/EW_orientation.phtml.
5. J. K. Barton, A. A. Vertegel, E. W. Bohannan and J. A. Switzer, *Chemistry of Materials*, 2001, **13**, 952-959.
6. T. W. Mercer, J. N. Russell Jr and P. E. Pehrsson, *Surface Science*, 1997, **392**, L21-L26.
7. D. S. Yoon, C. J. Kim, J. S. Lee, W. J. Lee and K. No, *Journal of Materials Research*, 1994, **9**, 420-425.
8. C. F. Quate, *Surface Science*, 1994, **299**, 980-995.
9. G. Binnig, C. F. Quate and C. Gerber, *Physical Review Letters*, 1986, **56**, 930-933.
10. N. R. Wilson, S. L. Clewes, M. E. Newton, P. R. Unwin and J. V. Macpherson, *The Journal of Physical Chemistry B*, 2006, **110**, 5639-5646.
11. S. R. Sails, D. J. Gardiner, M. Bowden, J. Savage and D. Rodway, *Diamond and Related Materials*, 1996, **5**, 589-591.
12. G. Janssen, W. J. P. Vanenckevort, W. Vollenberg and L. J. Giling, *Diamond and Related Materials*, 1992, **1**, 789-800.
13. Y. V. Pleskov, Y. E. Evstefeeva, V. P. Varnin and I. G. Teremetskaya, *Russian Journal of Electrochemistry*, 2004, **40**, 886-892.
14. B. V. Spitsyn, L. L. Bouilov and B. V. Derjaguin, *Journal of Crystal Growth*, 1981, **52**, 219-226.
15. K. Kanaya and S. Okayama, *Journal of Physics D: Applied Physics*, 1972, **5**, 43.
16. D. J. Marshall, *Cathodoluminescence of Geological Materials*, Academic Division of Unwin Hyman Ltd, 1988.
17. O. G. a. G. L. a. C. Reynaud, *The Astrophysical Journal Letters*, 1999, **521**, L133.
18. C. Findelingdufour, A. Vignes and A. Gicquel, *Diamond and Related Materials*, 1995, **4**.
19. R. Ramamurti, M. Becker, T. Schuelke, T. Grotjohn, D. Reinhard and J. Asmussen, *Diamond and Related Materials*, 2008, **17**, 1320-1323.
20. A. J. Bard and L. R. Faulkner, *Electrochemical Methods; Fundamentals and Applications*, John Wiley & Sons, **2000**.
21. A. Damjanovic, A. Dey and J. O. M. Bockris, *Electrochimica Acta*, 1966, **11**, 791-814.
22. A. N. Correia and S. A. S. Machado, *Electrochimica Acta*, 1998, **43**, 367-373.
23. E. Yeager, *Electrochimica Acta*, 1984, **29**, 1527-1537.
24. E. Yeager, *Journal of Molecular Catalysis*, 1986, **38**, 5-25.

25. G. Sine, I. Duo, B. El Roustom, G. Foti and C. Comninellis, *Journal of Applied Electrochemistry*, 2006, **36**, 847-862.
26. C. Batchelor-McAuley, I. B. Dimov, L. Aldous and R. G. Compton, *Proceedings of the National Academy of Sciences*, 2011, **108**, 19891-19895.
27. P. A. Michaud, E. Mahe, W. Haenni, A. Perret and C. Comninellis, *Electrochemical and Solid State Letters*, 2000, **3**, 77-79.
28. S. Szunerits and R. Boukherroub, *Journal of Solid State Electrochemistry*, 2008, **12**, 1205-1218.
29. H. B. Martin, A. Argoitia, U. Landau, A. B. Anderson and J. C. Angus, *Journal of the Electrochemical Society*, 1996, **143**, L133-L136.
30. T. Yano, E. Popa, D. A. Tryk, K. Hashimoto and A. Fujishima, *Journal of the Electrochemical Society*, 1999, **146**, 1081-1087.
31. J. A. Bennett, J. A. Wang, Y. Show and G. M. Swain, *J. Electrochem. Soc.*, 2004, **151**, E306.
32. E. Mahe, D. Devilliers and C. Comninellis, *Electrochimica Acta*, 2005, **50**, 2263-2277.
33. S. Ferro, M. Dal Colle and A. De Battisti, *Carbon*, 2005, **43**, 1191-1203.
34. A. Kraft, *International Journal of Electrochemical Science*, 2007, **2**, 355-385.
35. J. Lee and S. M. Park, *Analytica Chimica Acta*, 2005, **545**, 27-32.
36. M. Panizza and G. Cerisola, *Electrochimica Acta*, 2005, **51**, 191-199.
37. C. A. Martinez-Huitle, E. V. dos Santos, D. M. de Araujo and M. Panizza, *Journal of Electroanalytical Chemistry*, 2012, **674**, 103-107.
38. S. Fierro, N. Mitani, C. Comninellis and Y. Einaga, *Physical Chemistry Chemical Physics*, 2011, **13**, 16795-16799.
39. L. Svorc, J. Sochr, P. Tomcik, M. Rievaj and D. Bustin, *Electrochimica Acta*, 2012, **68**, 227-234.
40. E. O. Faria, A. C. Viera Lopes Junior, D. E. Pires Souto, F. R. Figueiredo Leite, F. S. Damos, R. d. C. Silva Luz, A. S. dos Santos, D. L. Franco and W. T. Pio dos Santos, *Electroanalysis*, 2012, **24**, 1141-1146.
41. K. E. Toghill and R. G. Compton, *Electroanalysis*, 2010, **22**, 1947-1956.
42. L. Hliwa, M. Azzi, A. Bennani, N. Saib, S. Maximovitch and F. Dalard, *Journal of New Materials for Electrochemical Systems*, 2010, **13**, 141-146.
43. J. H. T. Luong, K. B. Male and J. D. Glennon, *Analyst*, 2010, **135**, 3008-3008.
44. J. H. T. Luong, K. B. Male and J. D. Glennon, *Analyst*, 2009, **134**, 1965-1979.
45. R. G. Compton, J. S. Foord and F. Marken, *Electroanalysis*, 2003, **15**, 1349-1363.
46. A. Deneuville and E. Gheeraert, *Vide-Science Technique Et Applications*, 2001, **56**.
47. J. C. Angus, H. B. Martin, U. Landau, Y. E. Evstefeeva, B. Miller and N. Vinokur, *New Diamond and Frontier Carbon Technology*, 1999, **9**, 175-187.
48. P. Bertoncello, I. Ciani, F. Li and P. R. Unwin, *Langmuir*, 2006, **22**, 10380-10388.
49. Y. Narui, D. M. Ceres, J. Chen, K. P. Giapis and C. P. Collier, *Journal of Physical Chemistry C*, 2009, **113**, 6815-6820.
50. S. Petrovic, *The Chemical Educator*, 2000, **5**, 231-235.

51. P. Vanysek, *Handbook of Chemistry and Physics; Electrochemical Series*, CRC Press LLC, 1999.
52. J. V. Macpherson, D. O'Hare, P. R. Unwin and C. P. Winlove, *Biophysical journal*, 1997, **73**, 2771-2781.
53. C. M. A. Brett and A. M. Oliveira Brett, *Electrochemistry: Principles, Methods and Applications,*, Oxford University Press, **1996**.
54. M. C. Granger and G. M. Swain, *Journal of the Electrochemical Society*, 1999, **146**, 4551-4558.
55. M. C. Granger, M. Witek, J. S. Xu, J. Wang, M. Hupert, A. Hanks, M. D. Koppang, J. E. Butler, G. Lucazeau, M. Mermoux, J. W. Strojek and G. M. Swain, *Analytical Chemistry*, 2000, **72**, 3793-3804.
56. F. B. Liu, J. D. Wang, B. Liu, X. M. Li and D. R. Chen, *Diamond and Related Materials*, 2007, **16**, 454-460.
57. A. L. Barker, J. V. Macpherson, C. J. Slevin and P. R. Unwin, *The Journal of Physical Chemistry B*, 1998, **102**, 1586-1598.
58. D. P. Rillema, G. Allen, T. J. Meyer and D. Conrad, *Inorganic Chemistry*, 1983, **22**, 1617-1622.
59. M. Al-Noaimi and M. A. AlDamen, *Inorganica Chimica Acta*, 2012, **387**, 45-51.
60. S.-N. Ding, W. Zhu, D. Shan, N. Wan, Y.-M. Sun and S. Cosnier, *Electroanalysis*, 2011, **23**, 1306-1310.
61. H. Li, W.-j. Mei, Z. Xu, D.-w. Pang, L.-n. Ji and Z.-h. Lin, *Journal of Electroanalytical Chemistry*, 2007, **600**, 243-250.
62. D. P. Rillema, W. J. Dressick and T. J. Meyer, *Journal of the Chemical Society-Chemical Communications*, 1980.
63. A. J. Bard, *Journal of the American Chemical Society*, 2010, **132**, 7559-7567.
64. I. Yagi, H. Notsu, T. Kondo, D. A. Tryk and A. Fujishima, *Journal of Electroanalytical Chemistry*, 1999, **473**, 173-178.
65. P. H. Chen, M. A. Fryling and R. L. McCreery, *Analytical Chemistry*, 1995, **67**, 3115-3122.
66. D. Y. Kim, J. Wang, J. Yang, H. W. Kim and G. M. Swain, *Journal of Physical Chemistry C*, 2011, **115**, 10026-10032.
67. S. Ghodbane, D. Ballutaud, F. Omnes and C. Agnes, *Diamond and Related Materials*, 2010, **19**, 630-636.
68. S. Ranganathan, T. C. Kuo and R. L. McCreery, *Analytical Chemistry*, 1999, **71**, 3574-3580.
69. P. Actis, A. Denoyelle, R. Boukherroub and S. Szunerits, *Electrochemistry Communications*, 2008, **10**, 402-406.
70. R. Boukherroub, X. Wallart, S. Szunerits, B. Marcus, P. Bouvier and M. Mermoux, *Electrochemistry Communications*, 2005, **7**, 937-940.
71. F. Marken, C. A. Paddon and D. Asogan, *Electrochemistry Communications*, 2002, **4**, 62-66.
72. C. H. Goeting, F. Marken, A. Gutierrez-Sosa, R. G. Compton and J. S. Foord, *New Diamond and Frontier Carbon Technology*, 1999, **9**, 207-228.
73. J. P. McEvoy and J. S. Foord, *Electrochimica Acta*, 2005, **50**, 2933-2941.
74. I. F. Hu, D. H. Karweik and T. Kuwana, *Journal of Electroanalytical Chemistry*, 1985, **188**, 59-72.
75. S. Ferro and A. De Battisti, *Electrochimica Acta*, 2002, **47**, 1641-1649.

76. A. E. Fischer, Y. Show and G. M. Swain, *Analytical Chemistry*, 2004, **76**, 2553-2560.
77. M. V. Mirkin and A. J. Bard, *Analytical Chemistry*, 1992, **64**, 2293-2302.
78. D. S. Burnett, *Finite Element Analysis; from concept to applications*, Addison-Wesley, **1987**.
79. S. Szunerits, M. Mermoux, A. Crisci, B. Marcus, P. Bouvier, D. Delabouglise, J.-P. Petit, S. Janel, R. Boukherroub and L. Tay, *Journal of Physical Chemistry B*, 2006, **110**, 23888-23897.
80. J. P. Lagrange, A. Deneuville and E. Gheeraert, *Diamond and Related Materials*, 1998, **7**, 1390-1393.

4 Electrochemical Imaging of Single Crystal Boron Doped Diamond

ABSTRACT

Electrochemical imaging of scBDD was performed using constant height-scanning electrochemical microscopy (CH-SECM) and intermittent contact (IC)SECM.[1, 2] Differing redox mediators to were employed to challenge the scBDD at both positive ($FcTMA^+$) and negative ($Ru(NH_3)_6^{3+}$) applied potentials.

Whilst applying increasing driving potentials to scBDD during CH-SECM, sequential increases in currents were observed. The images shown herein suggest a gradient of current changes across the substrate, this was attributed to a sample mounting issue rather than differences in [B] across the sample, and this drawback was overcome utilising IC-SECM. The experimental apparatus allows the tip to self regulate the tip-substrate separation after initial optimisation via oscillation normal to the substrate.

Finite element modelling (FEM) was employed to determine electron transfer(ET) kinetics of each redox mediator for each sample. In all instances standard rate constant (k^0) values for $FcTMA^+$ were faster than those for $Ru(NH_3)_6^{3+}$, the highest containing [B] sample naturally offering much faster ET kinetics than those samples with [B] a factor less. Three scBDD samples with similar [B] (all borderline metal-like ~1×10^{20} cm^{-3}) all demonstrated similar k^0 values when imaged using $FcTMA^+$. The k^0 values were all much reduced for $Ru(NH_3)_6^{3+}$ however this ranged from ~2-5 times lower.

4.1 IMAGING TECHNIQUES

4.1.1 Constant Height Scanning Electrochemical Microscopy (CH-SECM)

Numerous solid-liquid interfacial ET processes are naturally heterogeneous,[3,4]therefore high resolution electrochemical imaging techniques are required to measure localised surface reactivity with high spatial resolution.[5-10] To date the most commonly used electrochemical imaging technique is SECM, first described by Bard *et al.* in 1989.[6] SECM has multiple applications including, for example, the analysis of single crystal dissolution[11-13] gas transport across a liquid monolayer interface,[14-16]live cellular activity[17-19] and the transport of electroactive species through porous membranes.[20-22] The spatial resolution of the technique is dependent on the size of the probe used.[23]

During SECM, the typical diameter of disc UMEs are 0.1-25 µm. Disc UMEs are characterised by their RG value, where RG = r_g/ a (r_g is the radius of the glass sheath plus the electrode) as shown in Figure 4.1. The UME is positioned using precise piezoelectric positioners and the tip, during imaging, is scanned close to the surface of interest in the x, and y directions.

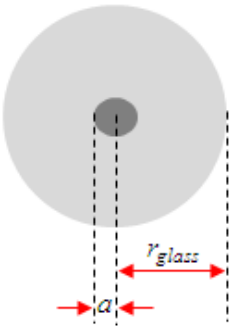

Figure 4.1. Schematic of a UME tip where r_g is the radius of glass sheath plus the electrode and a is the radius of the electrode.

The response at the tip (most often current (*i*)) is measured as a function of the tip position, and can be directly correlated quantitatively with surface reactivity provided mass transport in the system is known accurately.

CH-SECM measurements are commonly performed in amperometric mode where the tip is employed as the WE within a standard electrochemical cell having a CE and RE. If the substrate of interest is conducting then it can also be connected as a second WE. In SECM the UME or substrate typically is held at a potential (*E*) causing diffusion controlled electrolysis of the redox mediator of interest. Under these conditions SECM can be used to extract one or more of the following parameters; surface conductivity,[24,25] surface heterogeneity[24] and ET kinetics at the substrate.[24,25]

CH-SECM has been used to map spatial variations in the ET characteristics of pBDD electrodes.[24-30] For example, Figure 4.2 shows CH-SECM maps of pBDD ([B] 5×10^{20} cm^{-3}) recorded in substrate generation-tip collection (SG-TC) mode, whereby the tip is biased at a potential to collect electroactive species generated at the substrate electrode at a diffusion controlled rate.

Using $Ru(NH_3)_6^{3+}$as the redox couple the pBDD was subject to different driving *E*, the 25μm diameter tip was held at 3 μm above the substrate. Results indicated the whole substrate was electrochemically active as shown in Figure 4.2, however some regions were more active than others. These results were qualitatively correlated to conducting AFM and FE-SEM images.[24] The tips employed in these studies were not of a suitable size, or the tip-substrate separation (*d*) small enough, to resolve the electrochemical activity of individual grains.

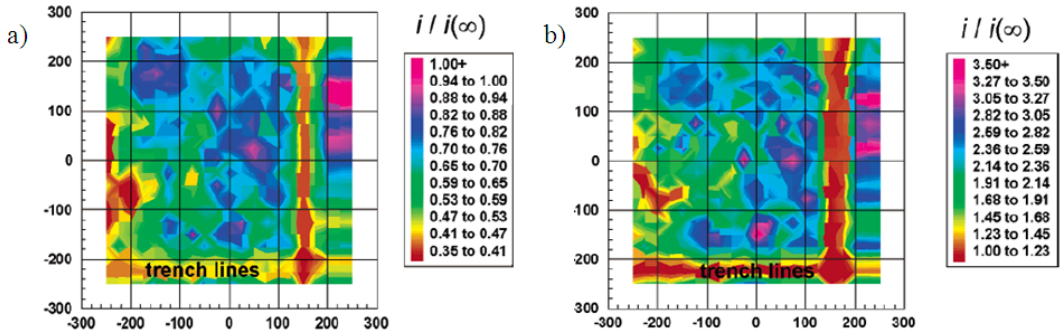

Figure 4.2. 500 × 500 µm SECM SG-TC scans for the collection of $Ru(NH_3)_6^{2+}$ electrogenerated at the surface of pBDD. The substrate was held at a) E=−0.23 V and b) E=−0.3 V. The tip was held at E=0.0 V to detect the $Ru(NH_3)_6^{2+}$. Tip currents have been normalized with respect to the steady-state current, i (∞), for the reduction of $Ru(NH_3)_6^{3+}$ in bulk solution.[24]

A recent study by Patten *et al.*[31] successfully resolved the electrochemical activity of pBDD ([B] 5 × 10^{20} cm^{-3}) using IC-SECM with two differing redox mediators ($Ru(NH_3)_6^{3+}$ and $FcTMA^+$). Higher and lower doped facets were determined and these were corroborated using FE-SEM and Raman mapping as shown in Figure 4.3

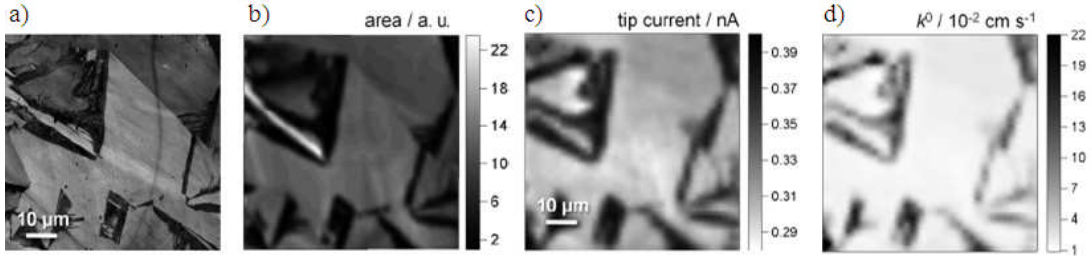

Figure 4.3. 70 × 70 µm images of pBDD obtained using a) In-Lens FE-SEM b) integration of the 1332 cm^{-1} as a function of spot location using 514 nm Raman. c) IC-SECM SG-TC scans of 2 µm Pt UME collecting $FcTMA^{2+}$ electrogenerated at the surface of pBDD when η = 0.045 V, d = 1.03 µm. d) Calculated k^0 values from currents recorded in c), using FEM.[31]

The employment of FEM demonstrated that on metal-like pBDD, k^0 directly correlated with the local [B], which in turn correlates with the LDOS.[31]Areas of

higher [B] in a pBDD sample offered ET rates of 0.097 cm s^{-1} for $FcTMA^+$ and 0.033 cm s^{-1} for $Ru(NH_3)_6^{3+}$ where as lower [B] demonstrated ET rates of 0.022 cm $s^{-1}$for $FcTMA^+$ and 0.007 cm s^{-1} for $Ru(NH_3)_6^{3+}$.

The aim of the work described below is to use CH-SECM and related techniques to map the ET activity of the surface of the different scBDD samples and relate back to material characterisation data, detailed in Chapter 3.

Initial CV of the substrate the redox solution of interest enables the $E_{½}$ to be determined. CV response of sample 85A (100) (exposed surface area~ 3 × 3 mm) and a 25 µm Pt UME in a solution containing 1 mM $FcTMA^+$ in 0.1 M $KNO_3$are shown in Figure 4.4a and b respectively. Experimentally recorded tip currents, during feedback imaging or approach curves measurements are normalised with respect to i_{lim} *i.e.* i/i_{lim}.

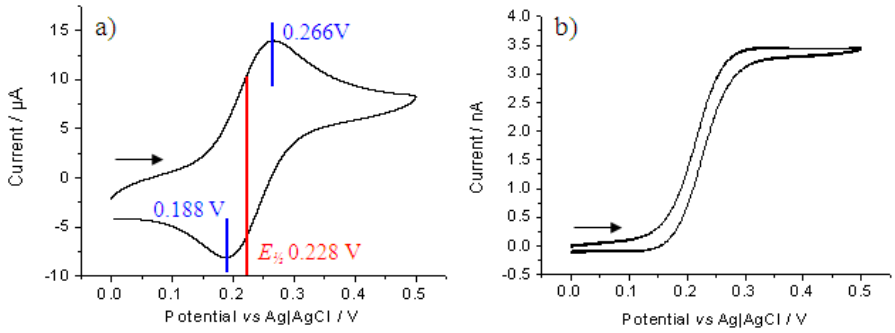

Figure 4.4. a) CV of 85A (100) showing the oxidation/ reduction of 1 mM $FcTMA^+$, scan rate 100 mV s^{-1}. b) CV of 25 µm Pt UME (RG=10) showing the oxidation of 1 mM $FcTMA^+$, scan rate 20 mV s^{-1}.

The UME tip i_{lim} shown in Figure 4.4b was measured at 3.40 nA, this is slightly higher than the calculated 2.89 nA using equation 1.6, assuming a = 12.5 µm. Equation 1.6 therefore suggests a radius of 14.7 µm.

During imaging the substrate electrode (E_s) was held at a defined overpotential, η (V), calculated using equation 4.1.

$$\eta = E - E_{½} \qquad \textbf{(4.1)}$$

Figure 4.5 shows a typical approach curve for a 25 µm tip biased (E_t) at 0.5 V *vs.* Ag|AgCl, approaching the unbiased 85A (100) electrode in a solution containing 1 mM $FcTMA^+$ in 0.1 M KNO_3.

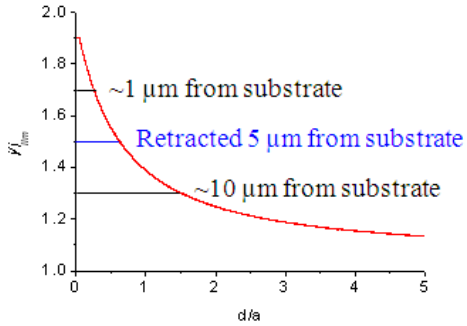

Figure 4.5. Approach curve of 25 µm Pt UME (RG=10) to 85A, applying E_t 0.5 V whilst E_s unbiased vs. Ag|AgCl.

The approach curve shown in Figure 4.5 does not show diffusion-controlled positive feedback (section 1.3). The tip current increases as the unbiased substrate is approached indicating finite ET kinetics.[17] The current plateaus at the closest tip-substrate separation (d) suggesting tip contact with the surface. However, in order to extract out quantitative information on the ET kinetics it would be necessary to know the exact d.

For spatial information on ET kinetics, SECM imaging was undertaken. Upon the tip making contact with the substrate (Figure 4.5), the tip was retracted

5 µm (annotated on Figure 4.5). For sensitive imaging, the defined distance between the tip and substrate is commonly a radius of the tip or less.[17]

The scan was performed in raster mode starting from the bottom left hand corner finishing in the top right hand corner. Using 1 mM $FcTMA^+$ in 0.1 M KNO_3, an initial scan in feedback mode (diffusion controlled rate) was performed (E_t 0.5 V, E_s unbiased *vs.* Ag|AgCl), followed by SG-TC scans at the following; E_t 0 V (fixed for every scan), and η= -0.078 V, -0.028 V, 0.022 V and 0.122 V respectively. The scans are shown in Figure 4.6.

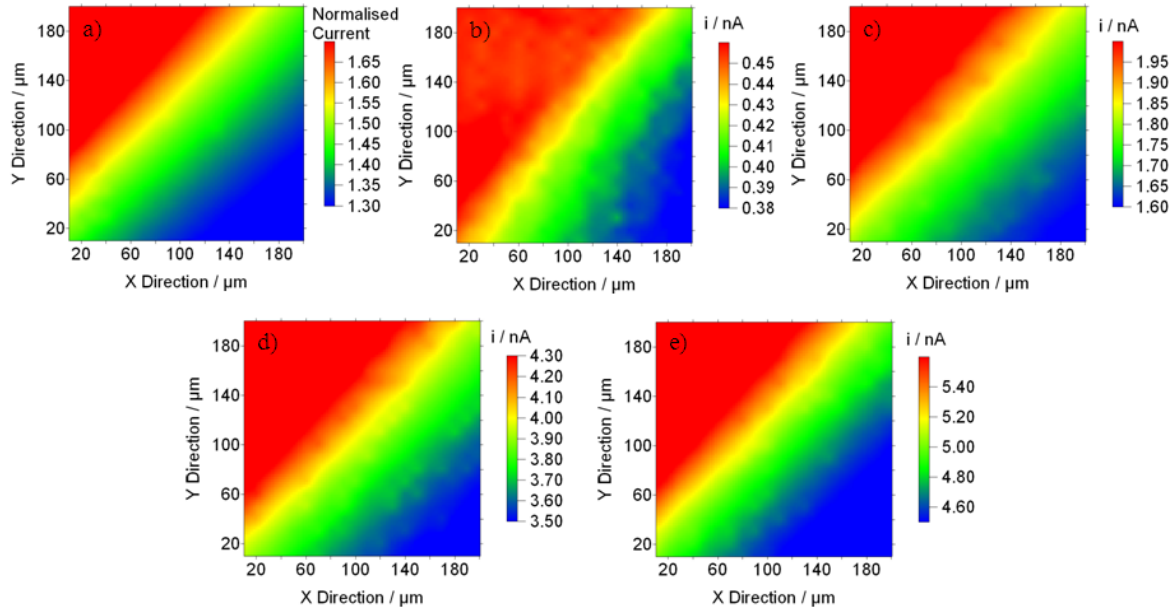

Figure 4.6. CH-SECM scans performed in 1 mM $FcTMA^+$ in 0.1 M KNO_3 using 25 µm Pt UME, RG=10 and d = 5 µm from 85A (100). a) Scan performed in feedback mode, E_t 0.5 V, substrate unbiased. The following were performed in SG-TC mode where E_t 0 V and b) η = -0.078 V, c) η = -0.028 V, d) η = 0.022 V and e) η = 0.122 V increasingly driving the reaction.

The normalised currents recorded in Figure 4.6a are similar to those recorded during the initial approach curve as shown in Figure 4.5. As η is increased Figure

4.6b-e show an expected increase in the tip collection current as the rate of ET transfer at the substrate electrode is increased.

A key observation is the sequential decrease in tip currents seen in all scans, from the top left hand corner to the bottom right hand corner. The decrease in current can be due to two factors, (i) the rate of ET across the substrate is not uniform due to heterogeneities in [B] or (ii), the *d* is changing during the course of the scan.

As there is a systematic decrease in tip current it is highly likely that the sample is not perfectly aligned perpendicular to the tip, such there is a systematic increase in *d* as the tip scans down from top to bottom, shown schematically in Figure 4.7. The approach curve (Figure 4.5) for the feedback scan (Figure 4.6a) is annotated showing the range of currents recorded, suggesting the *d* changes from ~1 to 10 µm over the scan duration, again demonstrating the limitations of CH-SECM imaging without feedback control. This was confirmed using high resolution optical microscopy.

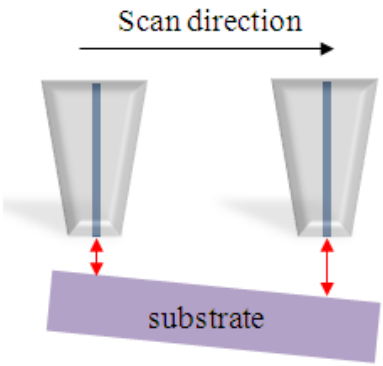

Figure 4.7. Schematic of a misaligned substrate and tip during CH-SECM, a higher current would be recorded the closer the tip is to the substrate as observed in Figure 4.6.

Although the capped (100) sample surface was provided as grown, the underlying bulk substrate was polished prior to cap overgrowth. Post processing

scaife polishing is unlikely to be truly coplanar and homoepitaxial growth would result in the final as grown material also being non coplanar.

The (110) sample was also provided as grown and even at the lowest magnification DICM clearly indicated height differences across the surface. Given the limitations of CH-SECM and the importance of maintaining a fixed *d*, neither the (110) nor (111) sample were analysed further using CH-SECM.

4.1.2 Intermittent Contact-SECM (IC-SECM)

IC-SECM[2] was recently developed at Warwick, a photograph of the experimental set up is shown in Figure 2.12.In this imaging technique the UME is oscillated normal to the substrate surface. When the tip comes into contact with the substrate the oscillation of the tip is dampened, as shown in Figure 4.8, which is detected and used to denote the point of *d* contact unambiguously.

The tip can then be retracted a set distance from the surface for electrochemical imaging under constant distance conditions. In practice the tip scans one line across the substrate determining the *d* contact position and tracking the topography of the substrate and then on the reverse scan traces the topography of the surface at a set *d* whilst recording the tip current.[2] For experiments described below employing a 10 µm diameter UME, reverse scan *d* was kept fixed at 5 µm.

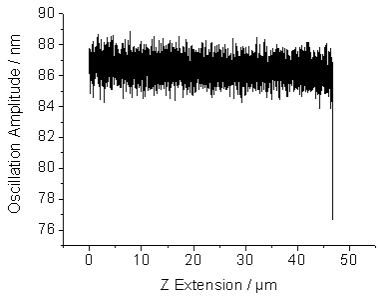

Figure 4.8. Graphic showing the initial free oscillation signal (frequency 70 Hz) followed by dampening as the 10 µm UME tip approaches a scBDD substrate.

As stated above, a perfect coplanar alignment between the tip and substrate is practically impossible to achieve, it is likely the edge of the glass sheath surrounding the Pt UME touches the surface first, (shown in Figure 4.9) and it is this interaction which defines *d* contact. This is actually preferred as perfect coplanar alignment with a conducting substrate would result in a short circuit current.

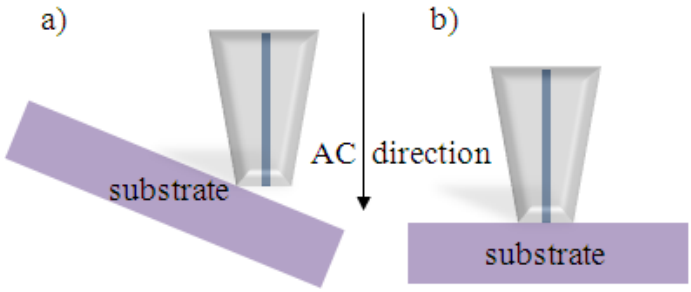

Figure 4.9. a) Schematic showing realistic substrate and tip alignment during SECM and b) perfect coplanar alignment which would result in a short circuit if employing a conducting substrate.

Initial approach curves to the scBDD substrate were performed at E_t = 0.5 V for $FcTMA^+$ *vs.* SCE or E_t-0.3 V *vs.* SCE for $Ru(NH_3)_6^{3+}$ (diffusion controlled rate for the respective oxidation/reduction of the redox mediator) with E_s unbiased. Piezoelectric positioners are highly sensitive but suffer from minimal drift when at

50 % of their extension (*i.e.* 50 µm for this particular *z* bender piezoelectric positioner). For this reason, it was important to optimise the *z* bender piezoelectric positioner via initial approach curves to the substrate of interest. Dual data recording of both current and oscillation amplitude were undertaken during initial approach curves without any oscillation set point, therefore a manual stop of the tip approach was used. Subsequent approach curves undertaken as part of the scan programme were performed using a predetermined dampening set point and *z* bender piezoelectric positioner optimisation. For both redox mediators all SG-TC scans E_t 0 V and E_s was held at a range of different η values.

IC-SECM was carried out on four samples; HB2 (known polycrystalline like defects) of (100) orientation, 85A (100), 85F (110) which has an uneven surface and the highly polished section of CP09 (111) with two differing redox mediators. The aim was to elucidate the ET kinetics of both an oxidising and a reducing electrochemical reaction at scBDD electrodes.

4.1.3 Finite Element Modelling (FEM) of IC-SECM Data

To quantify SECM tip currents, FEM simulations were employed to simulate the theoretical current response as a function of k^0 using Butler-Volmer[32] kinetics and a transfer coefficient α = 0.5 which is reasonable for outer sphere redox mediators.[33] Modelling was undertaken using a commercial FEM package; COMSOL Multiphysics 3.5a (COMSOL AB, Sweden) with a Matlab Interface (Release 2010a) (Mathworks Inc., Cambridge, UK).

Using 100,000 triangular mesh points per simulation with the highest concentration of mesh points at the scBDD and UME boundaries, two simple one

electron outer sphere redox mediator reactions were considered mimicking the experimental set up. One of the reactions is described in equation 4.2.

$$Ru(NH_3)_6{}^{3+} + e^- \underset{\boldsymbol{k_b}}{\overset{\boldsymbol{k_f}}{\rightleftharpoons}} Ru(NH_3)_6{}^{2+} \qquad \textbf{(4.2)}$$

The simulation solved a time dependent diffusion equation described in equation 4.3, ($Ru(NH_3)_6^{3+}$ in this example). *D* values are quoted in Table 3.6.

$$\frac{\partial c_j}{\partial t} = D_j\left(\frac{\partial c_j}{\partial r^2} + \frac{1}{r}\frac{\partial c_j}{\partial r} + \frac{\partial^2 c_j}{\partial z^2}\right) \qquad \textbf{(4.3)}$$

The boundary conditions used within the FEM[34] to determine the theoretical current response at the UME using SG-TC by solving equation 4.2 are described in and visualized using Figure 4.10a. Figure 4.10b shows an example of the steady-state concentration profile of $Ru(NH_3)_6^{3+}$ when SG-TC mode is applied, the scBDD substrate is held at η = -0.063 V meaning the reduction of $Ru(NH_3)_6^{3+}$ to $Ru(NH_3)_6^{2+}$ which is subsequently collected at the UME Pt tip at a diffusion-controlled rate.

Table 4.1. Summary of the boundary conditions used for the simulation of the Pt UME tip current in the SG-TC mode.

Label	Boundary Type	Coordinates	Equation
1	Axis of symmetry	$r = 0$ $0 \leq z \leq h$	$0 = \nabla c.\underline{n}$
2	Pt UME tip	$0 \leq r \leq a$ $z = d$	$c = c^*$
3	UME glass sheath	$a \leq r \leq a \times \mathrm{RG}$ $z = d$ and $r = a \times \mathrm{RG}$ $d \leq z \leq h$	$0 = \nabla c.\underline{n}$
4	scBDD substrate	$0 \leq r \leq l$ $z = 0$	$D\frac{\partial c}{\partial z} = k_{\mathrm{b}}(c^* - c) - k_{\mathrm{f}}c$ for $\mathrm{Ru(NH_3)_6^{3+}}$ $D\frac{\partial c}{\partial z} = k_{\mathrm{f}}(c^* - c) - k_{\mathrm{b}}c$ for $\mathrm{FcTMA^+}$
5	Bulk solution	$a \times \mathrm{RG} \leq r \leq l$ $z = h$	$c = c^*$

As seen in Figure 4.10, *h* and *l* represent the height and width parameters of the simulation (both 250 µm each) and it is reasonable to suggest planar diffusion at these distances.

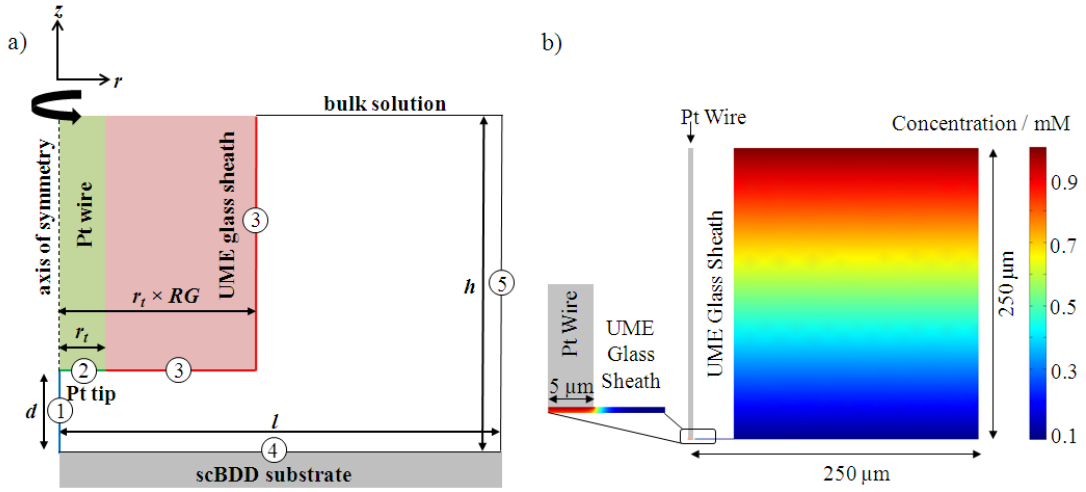

Figure 4.10. 2D simulation domain for the SG-TC setup (not to scale). The measured d value is used in the simulation. a) r_t for the Pt UME is set to match that determined experimentally. The RG value is defined for each simulation. ii) Simulated steady-state diffusion-limited concentration profile of 1 mM $Ru(NH_3)_6^{3+}$ in the SG-TC mode with the overpotential, η = -0.063 V and k^0 0.01 cm s^{-1} at scBDD surface. The inset shows the concentration profile at the Pt UME in more detail.

Prior to each IC-SECM scan, the observed i_{lim} was recorded and using equation 1.6 the specific *D* of each solution determined. Similarly *d* was determined from IC-SECM approach curves to an insulating substrate as previously described.

Butler-Volmer[32] kinetics were used to describe the ET kinetics at the scBDD electrode/solution interface as shown in equation 1.3and describes how the *E* applied to the electrode affects ET kinetics which consequently influences the measured current. ET kinetics determines the rate that the electrode can reduce or oxidise a species such that faster ET kinetics will produce higher currents and by comparison slower ET kinetics; reduced currents. Should the *E* be increased to extreme levels such η is large, the current at the electrode may become limited by mass transfer to the electrode.

A range of simulations was undertaken varying k^0 and the respective i_{lim} at UME tip, this was plotted generating a sigmoidal plot of log(k^0) *vs.* i_{lim} for each experiment performed shown in Figure 4.11. A Boltzmann function is fitted to the data to provide an analytical expression for i_{lim} as function of k^0 enabling current maps recorded using IC-SECM to be converted to k^0 maps.

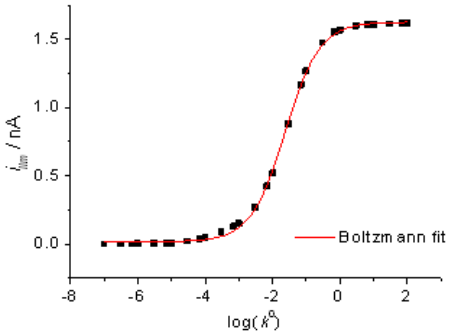

Figure 4.11. Plot of simulated Pt UME tip i_{lim}vs. log (k^0) for k^0 values in the range 1 x 10^{-8} – 1 cm s^{-1}.

The experimental IC-SECM scan data was re-plotted expressing i_{lim} in terms of k^0 in the *x* and *y* direction, and enabling visualisation of the rate of intrinsic ET across the scBDD electrodes.

4.1.4 IC-SECM Current and k^0 Maps of Single Crystal Boron Doped Diamond using $FcTMA^+$

HB2 (100) IC-SECM Maps

Corresponding SG-TC IC-SECM current and k^0 maps of the HB2 (100) with a range of applied η are shown in Figure 4.12a-c.The UME was carefully positioned in the area of the defect as shown in the FE-SEM image in Figure 4.12d. All scans

detailed herein were performed in raster formation starting in the bottom left hand corner, finishing in the top right hand corner.

The IC-SECM tip current images show a clear difference between the non-defect area and the defect. The non-defected area appears to show a homogeneous current response which differs from that seen at the defect. The shape of the current image in the defected area agrees well with the topographical features identified using FE-SEM (Figure 4.12d). As η is increased there is a noted increase in the experimentally recorded tip current in all areas of the scan, as expected due to an increase in k_f (Equation 4.2).

The current images in (i) are converted to k^0 maps as described in section 4.1.3 and shown in Figure 4.12a-c) ii), k^0, as expected, is independent of the applied η and ranged from ~0.01 cm s^{-1} (in the non-defect areas) to ~0.035 cm s^{-1} (in the defected area). As such the employment of Butler-Volmer[32] kinetics is appropriate for the sample.

Raman mapping across this region corroborate this (Figure 4.12e) clearly showing differences in [B]. Raman mapping spatial resolution can be related back to the laser spot size (6 μm) in this instance, therefore similar to the 10 μm tip size utilised in IC-SECM. The defect free area contains [B] at > 10^{20} due to the Fano resonance. However in the defect area Raman indicates [B] increases (due to increasing peak width and attenuation) in line with the IC-SECM images. It has not been possible to determine the precise [B] via SIMS in the defected areas due to their heterogeneous nature and sample positioning within the SIMS chamber.

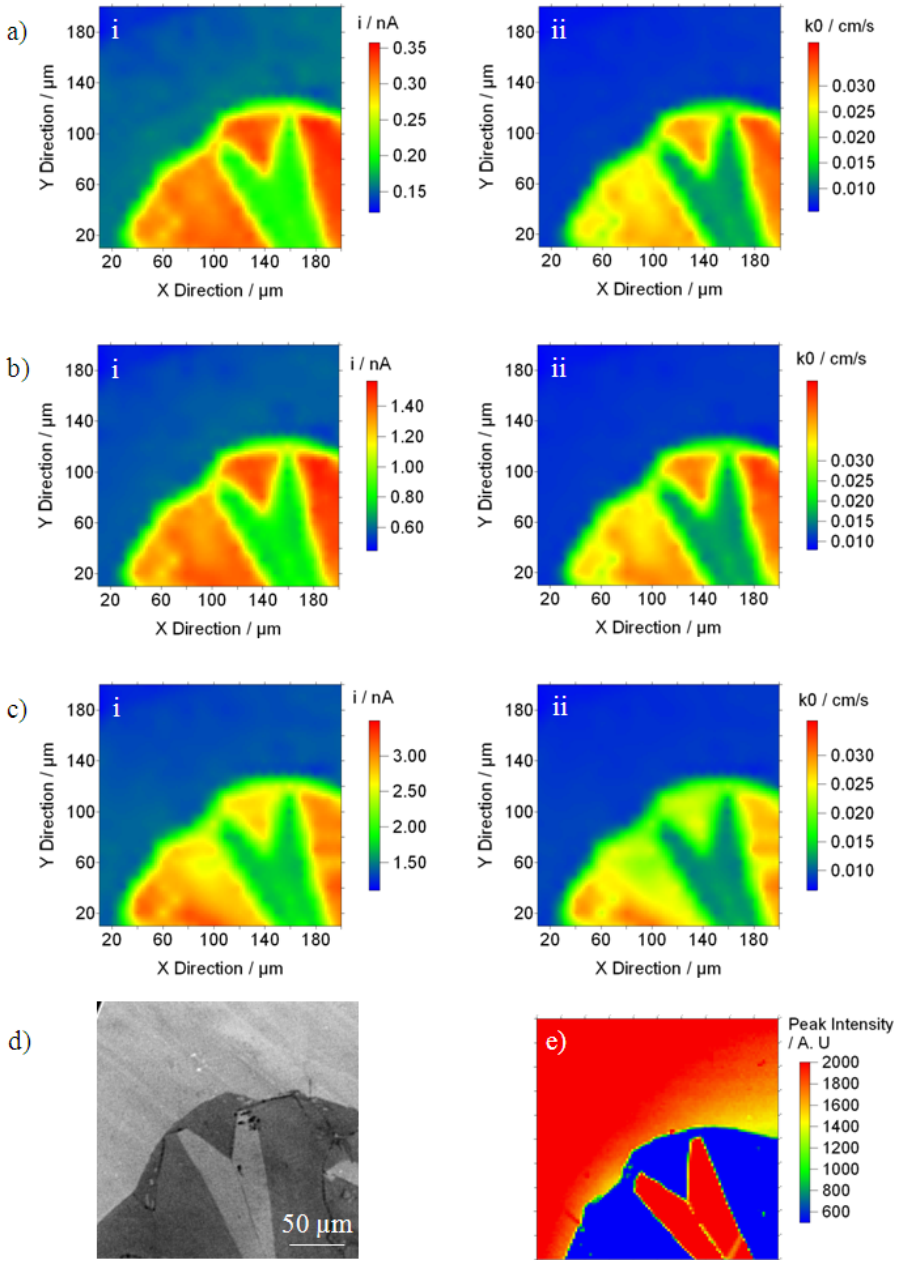

Figure 4.12. IC-SECM SG-TC mode images of HB2 (100) using 10 µm Pt UME (RG=5) for the collection of 1 mM FcTMA^{2+} electrogenerated at the surface where for a) i) η = -0.076, b) i) η = -0.026 and c) i) η = 0.02 where d = 0.54 µm. a-c) ii) corresponding k^0 maps. d) In-Lens FE-SEM image of HB2 e) 200× 200 µm Raman map of the defect plotted as a function of 1332 cm^{-1} peak intensity (514 nm laser with 6 µm spot size.

The scans in Figure 4.12 were performed simultaneously in the same area such that a definitive threshold could be identified between the defect and non-defect

area on each scan. Table 4.2 describes the threshold applied to each k^0 scan, the mean k^0 of the values within each threshold at each η applied and its relative percentage of the 400 data points recorded.

Table 4.2. Threshold k^0 values for various η relating to the IC-SECM scans shown in Figure 4.12 separating the non-defect and defect area of HB2.

	HB2 Non-defect Area			**HB2 Defect Area**		
η / V	**k^0 / cm s^{-1}**	**Mean k^0 / cm s^{-1}**	**%**	**k^0 / cm s^{-1}**	**Mean k^0 / cm s^{-1}**	**%**
-0.076	< 0.022	0.009 ± 0.003	74 %	>0.0221	0.028 ± 0.003	16 %
-0.026	<0.025	0.012 ± 0.003	72 %	>0.0251	0.036 ± 0.005	18 %
0.024	<0.020	0.010 ± 0.003	74 %	>0.0201	0.025 ± 0.003	16 %

When split into defect and non-defect areas, the k^0 values are all within error of each other with a similar distribution of the 400 data points recorded, Thus demonstrating IC-SECM combined with FEM is able to provide reproducible k^0 values for scBDD.

The k^0 maps thus suggest the non-defect area of the sample where lower k^0 values were recorded, have incorporated less boron compared to the defected area which exhibits higher k^0 values, by a factor of 3. This k^0 difference was also seen by Patten *et al.*[31] when using IC-SECM with pBDD, the similarity in k^0 results suggest differences in [B] of the same order.

85A (100) IC-SECM Maps

Corresponding SG-TC IC-SECM current and k^0 map of 85A (100) with a heavily doped capped layer are shown in Figure 4.13.

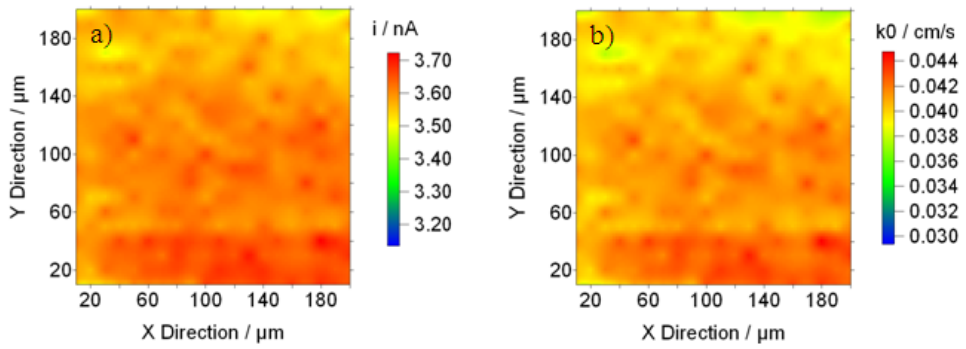

Figure 4.13. a) IC-SECM SG-TC image of 85A (100) for the collection of 1 mM $FcTMA^{2+}$ electrochemically generated at the surface when η = 0.028 V. Using 10 µm Pt UME, RG=7, d=0.68 µm. b) Corresponding k^0 map.

Note in stark contrast to the data presented in Figure 4.6 where there was no positional feedback implemented during SECM scanning, there is now no significant gradient in the tip current response as the tip scans over the surface. The absence of any gradient on these scans suggest that the gradual current decrease previously observed using CH-SECM can most definitely be attributed to a slope on the substrate.

The k^0 values shown in Figure 4.13b obtained from the experimental current data, suggest a fairly uniform ET rate. These values are higher than those recorded for HB2 (non-defect area), this is expected given that 85A contains a higher average [B] than HB2.[31] The k^0 values for 85A are also slightly higher than those in the defected area of HB2 which is known to have a higher [B] than the non-defect area.

85F (100) IC-SECM Maps

Corresponding SG-TC IC-SECM current and k^0 map of 85F (110) are shown in Figure 4.14. 85F has marginally lower [B] than the (100) samples and is close to the metal-like threshold.[35]

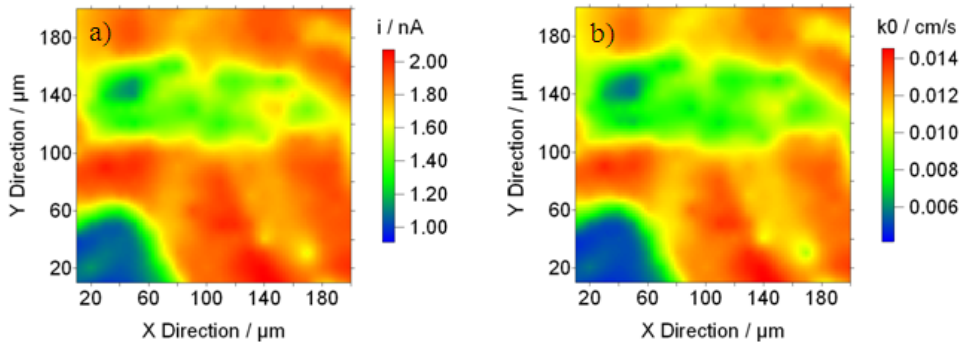

Figure 4.14. a) IC-SECM SG-TC image of 85F (110) for the collection of 1 mM $FcTMA^{2+}$ electrochemically generated at the surface when η = 0.024 V. Using 10 µm Pt UME, RG=7, d= 0.75 µm. b) Corresponding k^0 map.

The IC-SECM map was performed on the centre of the sample where the fleck like defects were not abundant and no definitive defects were imaged. Some change in current and therefore k^0 is observed, however this change is very small. k^0values are similar to those of HB2 (in the defect free area) which is not unexpected given the reported [B] via SIMS.

CP09 (111) IC-SECM Maps

Corresponding SG-TC IC-SECM current and k^0 map of CP09 (111) are shown in Figure 4.15 (specifically the highly polished (111) area of the sample).

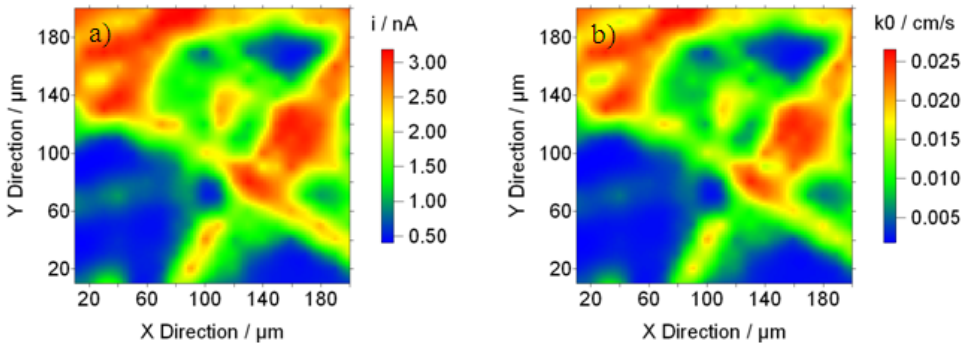

Figure 4.15. a) IC-SECM SG-TC image of CP09 (111) for the collection of 1 mM $FcTMA^{2+}$ electrochemically generated at the surface when η = 0.026 V. Using 10 µm Pt UME, RG=7, d= 0.39 µm. b) Corresponding k^0 map.

Sample CP09 was scaife polished from an original (110) sample such that some differences in [B] might be observed during this technique. A range of currents and k^0 values were observed, (i 0.5-3.0 nA and k^0 0.001-0.025). Table 4.3 combines the mean k^0 values for all samples analysed for similar η applied.

Table 4.3. Comparison of current and k^0 values recorded using IC-SECM in SG-TC mode for selected scBDD samples using 1 mM $FcTMA^+$ in 0.1 M KNO_3.

Sample	[B] / cm^{-3}	Mean k^0 / cm s^{-1}
HB2 non-defect	1.5×10^{20}	0.010 ± 0.003
HB2 defect	n/a	0.025 ± 0.003
85A	1.0×10^{21}	0.041 ± 0.001
85F	$0.8\text{-}1 \times 10^{20}$	0.011 ± 0.002
CP09	0.95×10^{20}	0.011 ± 0.007

Using k^0 values (n=400), Table 4.3 shows that HB2 (non-defect), 85F and CP09, all with similar [B], have similar ET rates. The heavily doped 85A offers the fastest ET rates. The HB2 defect k^0 values are lower than those of 85A, however these k^0 values are double those of lower [B] suggesting the [B] of HB2 defect lies in the range > 1.0×10^{20} but < 1.0×10^{21} cm^{-3}.

4.1.5 IC-SECM Current and k^0 Maps of Single Crystal Boron Doped Diamond using $Ru(NH_3)_6^{3+}$

To further investigate and challenge ET kinetics of the scBDD electrodes, a redox mediator with a more negative standard potential was employed; $Ru(NH_3)_6^{3+}$, thereby investigating ET kinetics at positive and negative redox potentials. The use of this redox mediator would highlight non-metal-like electrode behaviour on the

micro scale, this is relevant for sample 85F and CP09 because their respective [B] content is close to the metal-like threshold.[35]

HB2 (100) IC-SECM Maps

Corresponding SG-TC IC-SECM current and k^0 map of HB2 (100) are shown in Figure 4.16.

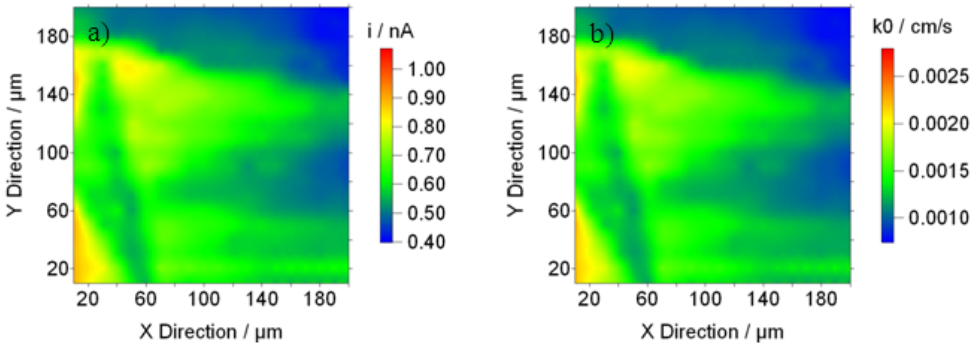

Figure 4.16. a) IC-SECM SG-TC image of HB2 (100) for the collection of 1 mM $Ru(NH_3)_6^{2+}$ electrochemically generated at the surface when η = -0.054 V. Using 10 µm Pt UME, RG=7, d= 0.54 µm. b) Corresponding k^0 map.

Figure 4.16 shows a slightly different area of the same defect shown in Figure 4.12, as performing the scan in the same area as for Figure 4.12, was challenging. The electrochemical image is not as clear defined as Figure 4.12, however it is still possible to locate the position of the defect and defect free areas. Using the whole image (rather than thresholding approach taken with $FcTMA^+$), the overall mean k^0 values (n= 400) was 0.0013 ± 0.0003 cm s^{-1} which is a factor lower than k^0 values recorded when using $FcTMA^+$.

85A (100) IC-SECM Maps

Corresponding SG-TC IC-SECM current and k^0 map of 85A (100) are shown in Figure 4.17.

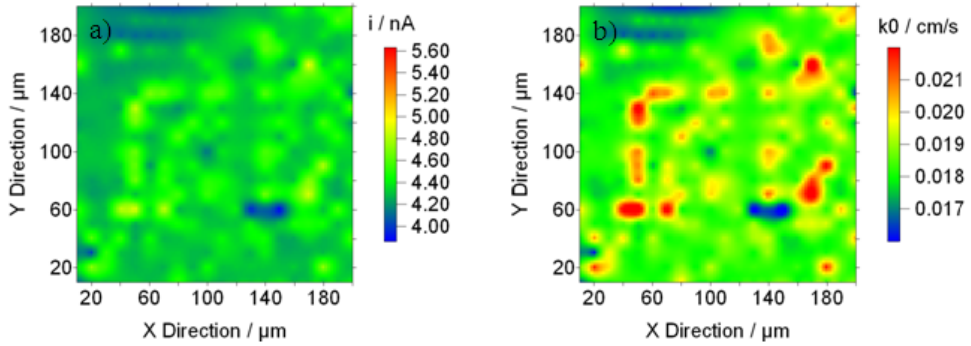

Figure 4.17. a) IC-SECM SG-TC image of 85A (100) for the collection of 1 mM $Ru(NH_3)_6^{2+}$ electrochemically generated at the surface when η = -0.054 V. Using 10 µm Pt UME, RG=7, d= 0.77 µm. b) Corresponding k^0 map.

The k^0 values shown in Figure 4.17b obtained from the experimental current data, suggest a homogeneous ET rate. These values are higher than those recorded for HB2 which given the factor difference in [B] is not unexpected. The k^0 values $Ru(NH_3)_6^{3+}$ are about half that of $FcTMA^+$.

85F (110) IC-SECM Maps

Corresponding SG-TC IC-SECM current and k^0 map of 85F (110) are shown in Figure 4.18.

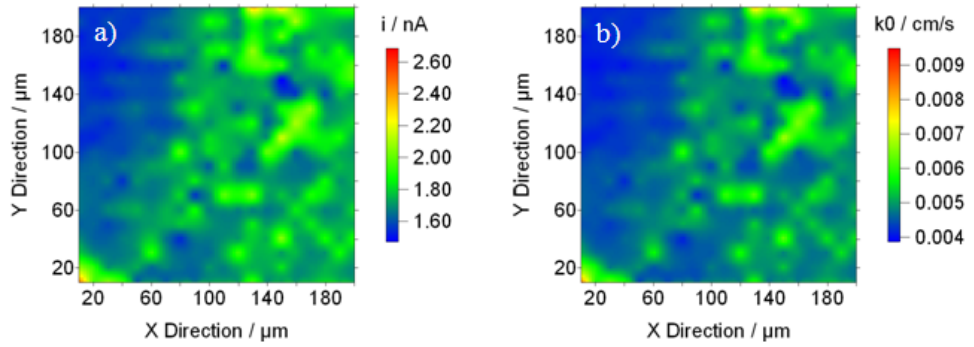

Figure 4.18. a) IC-SECM SG-TC image of 85F (110) for the collection of 1 mM $Ru(NH_3)_6^{2+}$ electrochemically generated at the surface when η = -0.052 V. Using 10 µm Pt UME, RG=7, d=0.77 µm. b) Corresponding k^0 map.

As before, this image was taken in the centre of the sample thereby avoiding most of the fleck like features. Minimal changes in current (~0.4 nA) and therefore k^0 values were recorded. Lower currents would be expected for this sample, lying on the border of metal-like [B].[35] The mean k^0 values for $Ru(NH_3)_6^{3+}$ were half those of $FcTMA^+$ following the trend of 85A (n=400).

CP09 (111) IC-SECM Maps

Corresponding SG-TC IC-SECM current and k^0 map of CP09 are shown in Figure 4.19, again imaging only the highly polished (111) area.

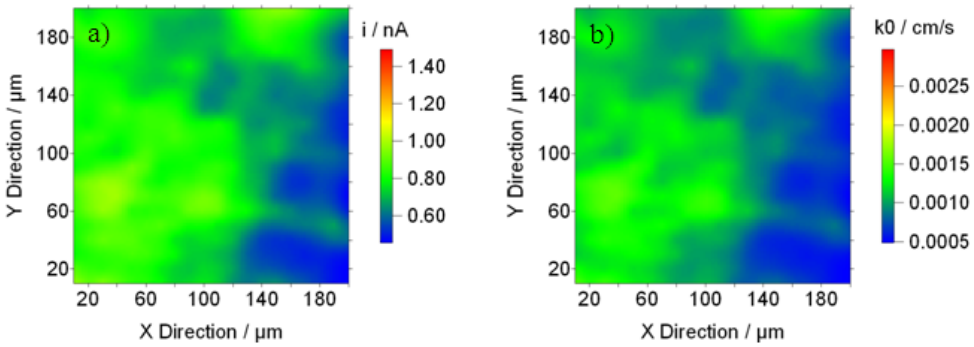

Figure 4.19. a) IC-SECM SG-TC image of CP09 (111) for the collection of 1 mM $Ru(NH_3)_6^{2+}$ electrochemically generated at the surface when η = -0.065 V. Using 10 µm Pt UME, RG=7, d=1.02 µm. b) Corresponding k^0 map.

Whilst some differences in current and k^0 are observed, these are minimal and on a similar scale to those seen for 85F. Due to the post processing nature of this sample, homogeneity is unlikely. CP09 is also lies on the borderline of metal-like [B] and the k^0 values for $Ru(NH_3)_6^{3+}$ are a factor lower than those of $FcTMA^+$, thereby continuing to follow suit. Table 4.4 summarises the k^0 values for $Ru(NH_3)_6^{3+}$.

Table 4.4. k^0 values recorded using IC-SECM in SG-TC mode for selected scBDD samples using 1 mM $Ru(NH_3)_6^{3+}$ in 0.1 M KNO_3.

Sample	[B] / cm^{-3}	Mean k^0/ cm s^{-1}
HB2 whole image	1.5×10^{20}	0.0013 ± 0.0003
85A	1.0×10^{21}	0.019 ± 0.0010
85F	$0.8\text{-}1 \times 10^{20}$	0.005 ± 0.0005
CP09	0.95×10^{20}	0.001 ± 0.0002

The ET rates determined herein are all lower than those reported for pBDD,[31] however in all cases, the $FcTMA^+ k^0$ values were higher than those of $Ru(NH_3)_6^{3+}$. Reasons behind these differences relates to ferrocenes higher self-exchange mechanism[36, 37] With the exception of 85A (100) ([B] 1×10^{21} cm^{-3}), all samples were close to the metal-like threshold[35] of BDD, as suggested by Patten *et al.*[31] the LDOS for these samples will play a crucial role dominating mass transport.

4.2 CONCLUSIONS

A range of scBDD samples orientations were electrochemically imaged using SG-TC IC-SECM with two differing mediators (oxidation and reduction reaction) and a range of η. The use of outer sphere redox mediators challenged the [B] rather than the scBDD orientation, as such the samples close to the metal-like threshold[35] (HB2 (non-defect), 85G and CP09) offered lower ET rates than the heavily doped 85A with [B] 1×10^{21} cm^{-3}.

Specifically k^0 using $FcTMA^+$ with sample HB2 (non-defect), 85G and CP09 were 0.010 ± 0.003, 0.011 ± 0.002 and 0.011 ± 0.007 cm s^{-1} whereas 85A 0.041± 0.001 cm s^{-1}. Employing $Ru(NH_3)_6^{3+}$ with sample HB2 (whole image), 85G and CP09 were 0.0013 ± 0.0003, 0.005 ± 0.0005 and 0.001 ± 0.0002 cm s^{-1} whereas 85A 0.019± 0.001 cm s^{-1}, showing a decrease when used with a redox mediator whose potential lies in the band gap.

The three samples with [B] close to the metal-like threshold are most likely to suffer from charge depletion effects; therefore this decrease is not unexpected. 85A being heavily doped should not suffer from charge depletion effects and the decrease in k^0 values between redox mediators can be attributed to the higher self-exchange mechanism of ferrocenes.[36,37]

A defect on HB2 (100) were clearly mapped using $FcTMA^+$, less so with $Ru(NH_3)_6^{3+}$, distinct differences in ET kinetics were recorded for $FcTMA^+$ further supporting FE-SEM and Raman mapping conclusions of differing [B], *i.e.* higher [B] in the defected area than the non-defected area. k^0 values recorded suggest it lies in the range $>1 \times 10^{20}$ to $<1 \times 10^{21}$ cm^{-3}.

4.3 REFERENCES

1. K. McKelvey, M. E. Snowden, M. Peruffo and P. R. Unwin, *Analytical Chemistry*, 2011, **83**, 6447-6454.
2. K. McKelvey, M. A. Edwards and P. R. Unwin, *Analytical Chemistry*, 2010, **82**, 6334-6337.
3. A. J. Bard, M. V. Mirkin, P. R. Unwin and D. O. Wipf, *The Journal of Physical Chemistry*, 1992, **96**, 1861-1868.
4. C. J. Slevin, J. V. Macpherson and P. R. Unwin, *The Journal of Physical Chemistry B*, 1997, **101**, 10851-10859.
5. A. J. Bard, F. R. F. Fan, D. T. Pierce, P. R. Unwin, D. O. Wipf and F. M. Zhou, *Science*, 1991, **254**, 68-74.
6. A. J. Bard, F. R. F. Fan, J. Kwak and O. Lev, *Analytical Chemistry*, 1989, **61**, 132-138.
7. A. J. Bard, P. R. Unwin, D. O. Wipf and F. M. Zhou, *Scanning Electrochemical Microscopy*, 1992.
8. A. J. Bard, G. Denuault, C. Lee, D. Mandler and D. O. Wipf, *Accounts of Chemical Research*, 1990, **23**, 357-363.
9. M. V. Mirkin, *Analytical Chemistry*, 1996, **68**, A177-A182.
10. P. R. Unwin and J. V. Macpherson, *Chemistry & Industry*, 1995, 874-&.
11. P. R. Unwin and J. V. Macpherson, *Chemical Society Reviews*, 1995, **24**, 109-119.
12. J. V. Macpherson and P. R. Unwin, *The Journal of Physical Chemistry*, 1995, **99**, 14824-14831.
13. J. V. Macpherson and P. R. Unwin, *The Journal of Physical Chemistry*, 1994, **98**, 11764-11770.
14. C. J. Slevin, S. Ryley, D. J. Walton and P. R. Unwin, *Langmuir*, 1998, **14**, 5331-5334.
15. J. Zhang and P. R. Unwin, *Langmuir*, 2002, **18**, 1218-1224.
16. J. Zhang, A. L. Barker, D. Mandler and P. R. Unwin, *Journal of the American Chemical Society*, 2003, **125**, 9312-9313.
17. J. Kwak and A. J. Bard, *Analytical Chemistry*, 1989, **61**, 1221-1227.
18. S. Amemiya, J. Guo, H. Xiong and D. A. Gross, *Analytical and Bioanalytical Chemistry*, 2006, **386**, 458-471.
19. A. J. Bard, X. Li and W. Zhan, *Biosensors & Bioelectronics*, 2006, **22**, 461-472.
20. E. R. Scott, H. S. White and J. B. Phipps, *Analytical Chemistry*, 1993, **65**, 1537-1545.
21. E. R. Scott, H. S. White and J. B. Phipps, *Journal of Membrane Science*, 1991, **58**, 71-87.
22. B. D. Bath, R. D. Lee, H. S. White and E. R. Scott, *Analytical Chemistry*, 1998, **70**, 1047-1058.
23. A. J. Bard and M. V. Mirkin, *Scanning Electrochemical Microscopy*, Marcel Dekker Inc, New York, 2001.
24. N. R. Wilson, S. L. Clewes, M. E. Newton, P. R. Unwin and J. V. Macpherson, *The Journal of Physical Chemistry B*, 2006, **110**, 5639-5646.

25. A. L. Colley, C. G. Williams, U. D'Haenens Johansson, M. E. Newton, P. R. Unwin, N. R. Wilson and J. V. Macpherson, *Analytical Chemistry*, 2006, **78**, 2539-2548.
26. K. B. Holt, A. J. Bard, Y. Show and G. M. Swain, *Journal of Physical Chemistry B*, 2004, **108**, 15117-15127.
27. A. K. Neufeld and A. P. O'Mullane, *Journal of Solid State Electrochemistry*, 2006, **10**, 808-816.
28. S. H. Wang and G. M. Swain, *Journal of Physical Chemistry C*, 2007, **111**, 3986-3995.
29. J. Chane-Tune, J. P. Petit, S. Szunerits, P. Bouvier, D. Delabouglise, B. Marcus and M. Mermoux, *Chemphyschem*, 2006, **7**, 89-93.
30. S. Szunerits, M. Mermoux, A. Crisci, B. Marcus, P. Bouvier, D. Delabouglise, J.-P. Petit, S. Janel, R. Boukherroub and L. Tay, *Journal of Physical Chemistry B*, 2006, **110**, 23888-23897.
31. H. V. Patten, K. E. Meadows, L. A. Hutton, J. G. Iacobini, D. Battistel, K. McKelvey, A. W. Colburn, M. E. Newton, J. V. Macpherson and P. R. Unwin, *Angewandte Chemie International Edition*, 2012, **51**, 7002-7006.
32. A. J. Bard and L. R. Faulkner, *Electrochemical Methods; Fundamentals and Applications*, John Wiley & Sons, **2000**.
33. M. V. Mirkin and A. J. Bard, *Analytical Chemistry*, 1992, **64**, 2293-2302.
34. D. S. Burnett, *Finite Element Analysis; from concept to applications*, Addison-Wesley, **1987**.
35. J. P. Lagrange, A. Deneuville and E. Gheeraert, *Diamond and Related Materials*, 1998, **7**, 1390-1393.
36. P. J. Smolenaers and J. K. Beattie, *Inorganic Chemistry*, 1986, **25**, 2259-2262.
37. G. M. Brown and N. Sutin, *Journal of the American Chemical Society*, 1979, **101**, 883-892.

5 Gold Nanoparticle Deposition onto Single Crystal Boron Doped Diamond

ABSTRACT

Current-time (*i-t*) transients were recorded using the microcapillary electrochemical method (MCEM), where using a fine capillary (internal diameter <60 μm) filled with 1 mM $KAuCl_4$ in 0.1 M $NaClO_4$ is positioned such that the capillary meniscus makes contact with the scBDD substrate. Using the *i-t* transients recorded and Scharifker and Hills theoretical model of progressive and instantaneous nucleation, lead to the conclusion of Au nanoparticles (NPs) growing via the progressive method at the driving potentials selected on scBDD (100). Due to heterogeneities on the surface of the (110) sample, theoretical plotting could not be undertaken.

The use of AFM imaging and FE-SEM on the (100) orientation leads to the conclusion that the sample provided is homogeneous. The electrodeposition of Au onto the (110) sample highlighted areas of preferential NP deposition via both AFM and FE-SEM, which was thought to have been as a result of damage caused to the surface during the failed growth of a higher doped thin cap layer. Despite identical sample preparation and using the same capillary, the onset of Au deposition occurred (~350 mV) later on the (110) sample, which can be attributed to the heterogeneous nature of the (110) sample such that a range of kinetic processes were occurring over a wider potential when compared to the homogeneous (100) sample.

5.1 ELECTROCHEMICAL DEPOSITION OF METALS

Understanding the mechanism of deposition of metallic NPs or structures electrodeposited onto carbon substrates is a diverse field of research, utilising many different surfaces including HOPG,[1-3] GC,[1, 4-6] carbon nanotubes (CNTs) (either singly[7-9] or networks[10-12]) and more recently graphene.[13-15] Electrodeposition enables the deposition of NPs with controlled characteristics such as size and morphology. The main advantage of this technique is the direct adhesion of the NPs to the substrate.

5.1.1 Boron Doped Diamond Utilised as an Electrocatalytic Support Material

BDD is a very interesting electrode material that can be functionalised via electrodeposition. BDD is electrochemically inert towards the vast majority of electrocatalytic reactions, so serves only as a low background current and conducting support structure for the electrodeposited metallic nanostructures. Thus the electrochemical signature is due only to the electrocatalytic process of interest.

The majority of research utilising the functionalisation of BDD has been achieved with pBDD. There is a small amount of previous literature where scBDD was employed, discussed later.

The first instance of as grown pBDD being used as a substrate for electrodeposition of metallic nanostructures was reported by Awada *et al.*[16] in 1995. It was demonstrated that Pt and Pb NPs could be deposited (using CV) onto MWCVD pBDD ([B] ~5×10^{19} cm^{-3}) using a conventional three electrode glass cell arrangement.[16]

Pt NPs were deposited onto films of MWCVD pBDD ([B] $>10^{20}$ cm^{-3}) by Gonzalez-Gonzalez *et al.*[17] using CV where it was found the NPs selectively deposited onto the (111) orientation. Furthermore, the NPs location was affected by the CV scan rate. At higher scan rates the NP size was dependent on the orientation, smoother (110) orientations had a smaller number of NPs with a larger diameter.[17]

Metal coated electrodes have been used for the detection of many different analytes in solution and microelectrode arrays offer increased sensitivity and lower detection limits than traditional macro electrodes.[18-21]

Ag was deposited onto a BDD microdisc array (E6 Ltd) from solution at a potential (V_{dep}) of -0.2 V *vs.* Ag|AgCl for 60 s[22] shown in Figure 5.1.

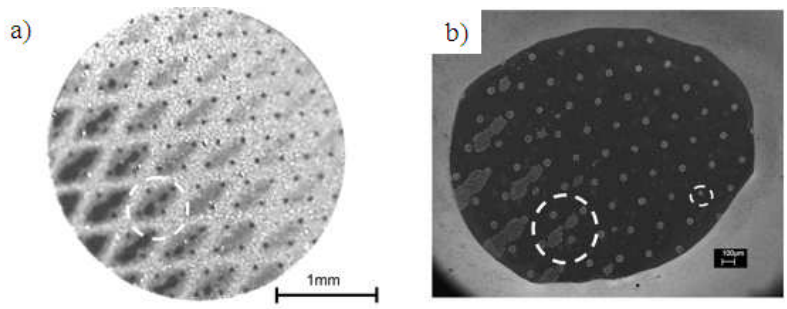

Figure 5.1. a) Photoluminescence image (inverted) of the ~78 micro disk BDD array and b) FE-SEM image of the same BDD array after the electrodeposition of Ag from 1 mM $AgNO_3$ in 0.2 M KNO_3 solution, V_{dep} = -0.2 V vs. Ag|AgCl applied for 60 s.[22]

Two of the pBDD micro discs within the array are shown in Figure 5.2, where a) and c) show the conventional SEM images of two different discs and b) and d) the corresponding In-Lens image (inverted) which allows for simultaneous imaging of the orientation structures and the Ag NP morphology.

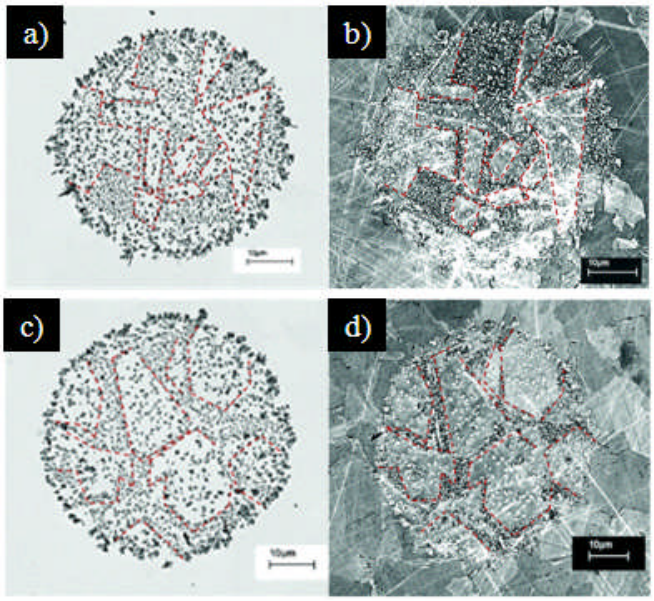

Figure 5.2. a) Secondary electron FE-SEM image of an electrode from the ~78 pBDD disc array and b) In-Lens FE-SEM image of the same BDD disc. c) and d) show a differing disc within the array using the same imaging techniques. The red dashed lines on the images highlight differing orientations.[22]

As discussed previously, In-Lens FE-SEM colour contrast suggests areas of higher or lower conductivity (in this instance [B]), therefore the lighter areas are thought to be less conducting. The images clearly show Ag depositing differently on differing regions of conductivity. On less conducting areas Ag appears to form more disperse larger agglomerates compared with the more conducting areas.[22]

Hutton *et al.*[23] used 1 mm disc MWCVD pBDD ([B] ~5 × 10^{20} cm^{-3}) electrodes modified with Pt NPs to investigate this substrates potential as an oxygen sensor. It was found that by increasing the negative driving potential (V_{dep}) for Pt electrodeposition the differences in nucleation morphology between orientations was much less.[23] Although no preference was observed for orientation boundaries; the higher doped regions of the material promoted the nucleation of smaller NPs with a higher density, also confirmed by FE-SEM and AFM.[23]

The employment of high negative V_{dep} (-1.5 V) for the electrodeposition of Pb NPs onto MWCVD pBDD ([B] ~5 × 10^{20} cm^{-3}) was reported. Whereby this negative driving potential resulted in uniform NP nucleation between differently doped orientations of pBDD.[24]

Batchelor-McAuley *et al.*[25] compared a MWCVD pBDD (Windsor Scientific, UK) 3 mm macrodisc with a MWCVD pBDD ([B]> × 10^{20} cm^{-3}) microdisc array electrode[26] (362 micro discs of 25 µm diameter each separated by 250 µm) using Pd NPs for the detection of hydrazine. Both substrates subject to the same V_{dep} = 0 V and deposition time (t_{dep}).

In both cases a random distribution of Pd NPs was supported. AFM showed that the macro and all the microdiscs were well covered with NP. For the microdisc array electrode, AFM images revealed larger NPs at the edges of the microdiscs, attributed to the higher flux of metal species in solution at the edges of the electrode.[25]

Szunerits and Boukherroub[27] deposited Pd and Au NPs onto H-terminated MWCVD pBDD (~10^{20} [B] cm^{-3}) and reported on their use for the oxygen reduction reaction in basic media. CVs show the use of high driving potentials for Au and Pd, thereby providing a homogeneous distribution of both Au and Pd NPs across the pBDD surface.[27]

To date, the only reported research using scBDD as the substrate for metal NP deposition was published in 2010 by Denisenko *et al.*[28] however the NP deposition was performed by sputtering rather than electrodeposition techniques. Using O-terminated scBDD substrates of (100) differing in [B] from 0.8 × 10^{20} to 1 × 10^{21} cm^{-3}, were subject to sputtering of Au resulting in either a 1 or 3 nm thick

layer. Subsequent annealing produced isolated Au NPs ~15 nm in size for the 1 nm thick layer and ~50 nm for the 3 nm layer determined using SEM. The electrochemical activity of the scBDD electrode decorated with Au NPs correlated well to theoretical predictions with respect to NP size and respective[B].[28]

5.1.2 Electronucleation and Growth Theories

Theories relating to nucleation and growth of NPs via electrodeposition, generally presume a homogeneously active substrate. In the case of pBDD electrodes, unless extreme V_{dep} are employed this is clearly not the case, and the recorded *i-t* response averages over the surface area considered.

The original nucleation and growth model is described by Johnson-Mehl-Avrami-Kolomogorov theory.[29-34] However, the most widely acknowledged method to model nucleation and growth of metallic NPs from *i-t* transients was established by Scharifker and Hills (SH Model),[35] from which many other models have now developed.[36-38]

There are two limiting forms of nucleation behaviour firstly, instantaneous nucleation is where the number of nuclei remains constant, growing in size with t_{dep}. Instantaneous nucleation tends to occur when the nucleation stage of phase transition is short compared to the growth phase or when there are a low number of active site on the substrate.[39] Note the concept of whether a growth process can be truly instantaneous has been debated in the literature.[40-45] The second form of nucleation is progressive nucleation where the number and size of NPs growing on the surface changes with t_{dep}. Both cases are illustrated schematically in Figure 5.3.

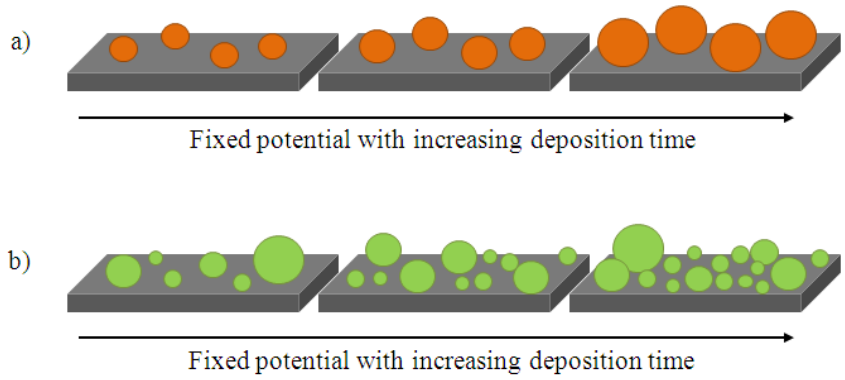

Figure 5.3. Schematic showing a) instantaneous nucleation where the same number of NP nucleate regardless of t_{dep}, over time the fixed number of nuclei increase in size. b) Progressive nucleation where the number and size of NPs changes over t_{dep}.

Equation 5.1 and 5.2 expresses the SH model, *i* as a function of *t* for limiting cases of instantaneous and progressive nucleation.[35]

$$\left(\frac{i}{i_m}\right)^2_{inst.} = 1.9542\left(\frac{t_m}{t}\right)\left\{1-exp\left[-1.2564\left(\frac{t}{t_m}\right)\right]\right\}^2 \quad \textbf{(5.1)}$$

$$\left(\frac{i}{i_m}\right)^2_{progr.} = 1.2254\left(\frac{t_m}{t}\right)\left\{1-exp\left[-2.3367\left(\frac{t}{t_m}\right)^2\right]\right\}^2 \quad \textbf{(5.2)}$$

Data is typically plotted in dimensionless coordinates $(i/i_m)^2 vs. t/t_m$ where i_m and t_m represent the maximum peak current of the *i-t* transient with the relevant time. Theoretical nucleation theories are as shown in Figure 5.4.

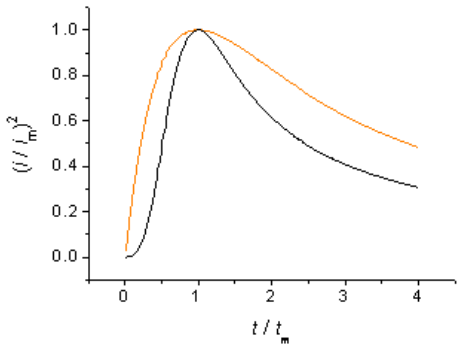

*Figure 5.4. The SH model of theoretical nucleation via instantaneous (**orange**) and progressive (**black**) pathways.*[35]

The SH model has proven to be a good descriptor, in the past, for metal nucleation on carbon and semiconductor electrodes.[46-49] Krumm *et al.*[46] investigated the electrodeposition of Tl, Cd and Cu NPs onto semiconducting Si (111) substrates. Their experimental data plotted against the SH model demonstrated progressive nucleation of the three differing metallic NPs.

The nucleation mechanism of Au NPs onto a GC substrate was evaluated.[47] The interpretation of *i-t* curves showed that at more positive electrode potentials the NPs corresponded to progressive nucleation with diffusion controlled growth. Conversely at more negative electrode potentials nucleation occurred instantaneously when fitted to the SH model.[47]

Lu *et al.*[50] investigated deposition η, supporting electrolyte, anion additives and concentration of the deposition solution in relation to a HOPG substrate. The use of Cl^- inhibits Pt deposition due to its adsorption onto the substrate therefore blocking reduction sites, whilst $[SO_3]^{2-}$ and $[ClO_3]^-$ somewhat promote Pt reduction.

The electrodeposition of Pt NPs at low η when fitted using the SH model[35] demonstrated progressive nucleation, upon increasing η significantly, instantaneous

nucleation was observed when fitted theoretically. The addition of $[ClO_3]^-$ improves the instantaneous nucleation theoretical fit, whereas the addition of $[SO_3]^{2-}$ induced very small changes. Concluding the optimum conditions of growing Pt NPs on HOPG involved acidified Pt solution and high cathodic η.[50]

Bennett and Swain[51] investigated nucleation type of Pt NPs on microcrystalline and ultrananocrystalline pBDD using electrodeposition. *i-t* curves measured at fixed V_{dep} were compared to the SH model,[35] at shorter deposition timeframes (t_{dep}) instantaneous nucleation was noted with low η (< 700 mV) for both types of pBDD substrate. As higher η were applied there was a transition to progressive nucleation.

The study suggests there appears to be a fairly constant nucleation site density at low η. New nucleation sites develop over time with higher η, this was linked to heterogeneities in LDOS as a result of variation in local boron and hydrogen concentrations rather than any physiochemical properties. A shift to progressive nucleation as η is increased is consistent with an increased LDOS at increasingly negative η.[51]

5.1.3 Aims of Gold Nanoparticle Deposition using Single Crystal Boron Doped Diamond Substrates

The electrodeposition of Au NPs on scBDD was considered important because of their catalytic involvement in several key electrochemical processes including oxygen[27] and hydrogen peroxide reduction,[52] oxidation of hydrazine[53] and glucose oxidation.[54]

In this chapter, we investigate the nucleation behaviour of Au NPs on scBDD, specifically (100) and (110) facets (fully characterised in Chapter 3), using the microcapillary electrochemical method (MCEM). This has previously been shown to be an extremely useful method for investigating the electrodeposition characteristics of metal NPs on single walled nanotube networks.[7,8] Given the following attributes: the ability to position the capillary at numerous locations on the surface with high precision, thereby allowing for rapid multiple depositions across the substrate. This method also allows for selective patterning of the substrate using metal NPs.

The aim of this research was to compliment and confirm whether the surface of the scBDD samples were of a homogeneous construction as potentially demonstrated by characterisation discussed in Chapter 3. Furthermore, the electrodeposition onto a potentially homogeneous surface would elucidate NP nucleation and growth mechanisms via data interpretation and the SH model.

5.2 ELECTRODEPOSITION USING GOLD CHLORIDE

5.2.1 Cyclic Voltammetry (CV) using Gold Chloride

The scBDD was prepared for deposition post electrode fabrication (Figure 2.1) by alumina slurry polishing and cycling in 0.5 M H_2SO_4 (1.8 to -0.6 V *vs.* SCE) thereby ensuring the surface was clean and free of any Au (discussed in section 2.2.4 and 2.4.2) from the sample preparation process.

The experimental set up is described in Chapter 2, section 2.4.8. Initially CVs were recorded over the potential range -1.0 – 1.2 V, *vs.* quasi Ag|AgCl RE, in order to select suitable V_{dep} for the electrodeposition of Au NPs as shown in Figure 5.5. The supporting electrolyte $NaClO_4$, in preference to a chloride salt was selected, as the $[ClO_4]^-$ is far more inert than Cl^-, which competes for active sites on substrates during metal deposition.[50]

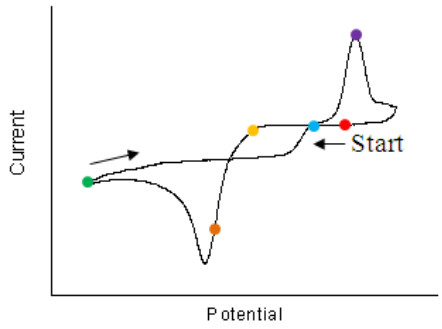

Figure 5.5. CV vs. quasi Ag|AgCl of 1 mM $KAuCl_4$ in 0.1 M $NaClO_4$ using a micro capillary (50 × 60 µm) with a scan rate 100 mV s^{-1}. Highlighted areas of interest are discussed below.

The **red** spot indicates where the CV starts from, progressing in the negative direction to the **yellow** spot where Au^{3+} is reduced to Au under kinetic control, thereby creating nuclei on the electrode surface. Driving the V_{dep} more negatively (**orange**) results in an increasing Au deposition η. As the V_{dep} sweeps even further negative (**green**), the presence of Au on the surface of BDD means that the Au can electrocatalyse the reduction of oxygen (BDD does not support oxygen reduction) and the current begins to increase again ca. -1.0 V.

On the return sweep, Au^{3+} is further reduced from solution to Au and at the cross over point (**blue**), the deposited NPs begin to grow in size. The peak observed

at ~0.8 V (**purple**) is due most likely to the surface oxidation of Au, although we cannot rule out contributions from the electrodissolution of the Au itself.

Figure 5.6 shows FE-SEM images, at different resolutions, recorded after the scBDD surface had been subject to a CV sweep as described, followed by rinsing with Milli-Q water and dried in air.

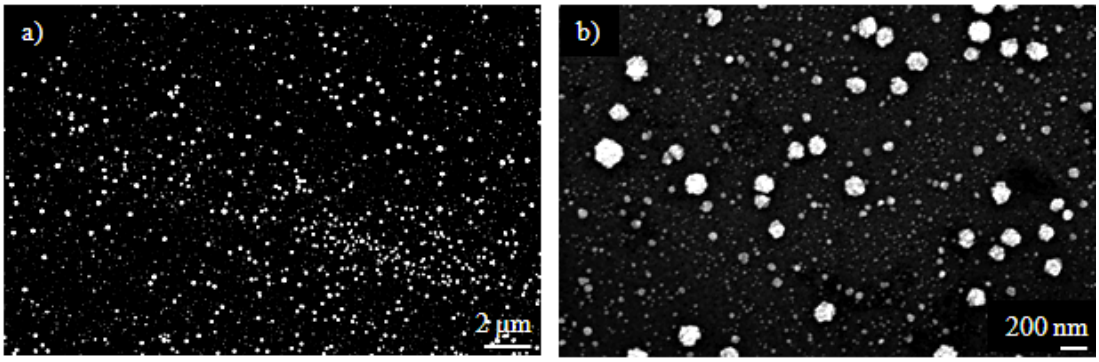

Figure 5.6. In-Lens FE-SEM images of 85A (100) after Au NP electrodeposition during a CV sweep (deposition and subsequent AuO stripping from Au NPs) using 1 mM $KAuCl_4$ in 0.1 M $NaClO_4$. a) ×5 magnification and b) ×25 magnification.

It is clear that there is a range of Au NP sizes on the surface of the scBDD after CV electrodeposition and AuO stripping. However, although FE-SEM is very useful for providing information on Au NP number densities over large areas it is not able to provide truly quantitative information on Au NP sizes due to charging effects of the NPs and substrate within the chamber. FE-SEM data reported herein is used quasi quantitatively to demonstrate nucleation trends, thereby supporting *i-t* transients.

Figure 5.7a shows a TM-AFM image of the scBDD surface after CV electrodeposition. The surface is clearly dominated by a very high density of small NPs, and a much smaller number of larger particles. TM-AFM can be used

quantitatively to provide information on Au NP heights although there maybe tip convolution effects in the *x, y* direction.

TM-AFM images such as those shown in Figure 5.7a and FE-SEM images such as those in Figure 5.6 were quantitatively analysed. Figure 5.7b shows the related histogram demonstrating the relatively low number of much larger NPs.

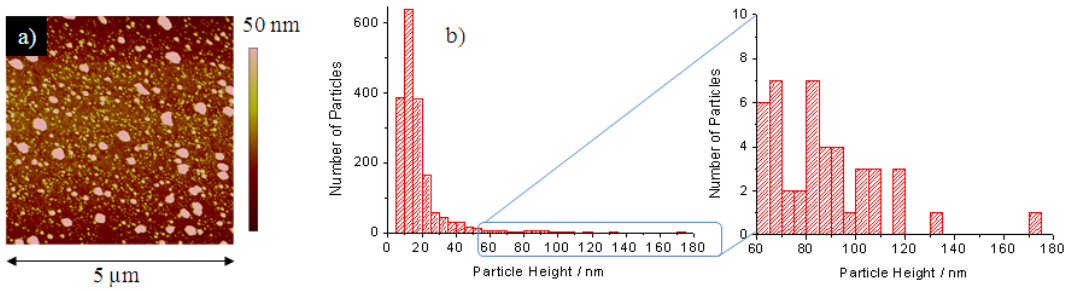

Figure 5.7. a) 5 × 5 µm TM-AFM image of deposited Au NPs after CV sweep and b) histogram analysis of deposited NPs onto 85A (100).

NP analysis from different areas of the sample (including Figure 5.7) gave a NP distribution of 63 ± 17 μm^{-2} and an average NP height of 19.7 ± 14.0 nm (n=5). The AFM and FE-SEM images suggest the whole scBDD surface is active towards Au deposition, with no preferential nucleation as expected for a homogeneous sample. This is in contrast to what has been observed previously with pBDD.[16,20,23, 55,56]

5.2.2 Chronoamperometry (Electrodeposition of Gold Nanoparticles)

In order to provide more detailed information on the nucleation behaviour, chronoamperometric measurements were carried out where the potential of the WE (scBDD) is stepped, from a V_{dep} where there are no redox processes occurring

(determined from Figure 5.5), to different Au deposition V_{deps}. The resulting current (*i*) was then monitored as a function of time (*t*) as shown in Figure 5. 8

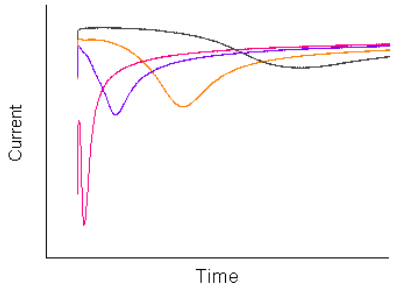

Figure 5.8. Representative i-t transients showing a range of applied V_{dep} onto scBDD for identical times.

Figure 5.8 shows the peaks all decrease in current as the NPs deposit onto the electrode surface, here diffusion fields are isolated. As time continues NP diffusion fields on the electrode start overlapping and the current increases again as more NP are reduced from the metal salt solution onto the electrode substrate or onto existing electrodeposited NPs.

As the V_{dep} is increased (from **grey**-low V_{dep} through to a high V_{dep}-**pink**) the current peak response shifts to shorter times, as expected with an increase in the nucleation driving force.

5.3 ELECTRODEPOSITION ON SINGLE CRYSTAL BORON DOPED DIAMOND

5.3.1 Gold Nanoparticle Deposition Utilising (100) Single Crystal Boron Doped Diamond with AFM and FE-SEM

Careful positioning of the capillary (50 × 60 µm internal diameter) led to well separated deposition spots as shown in Figure 5.9.

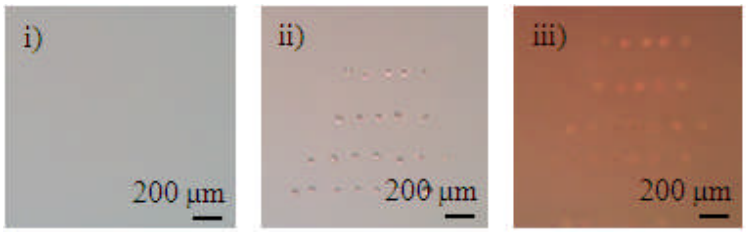

Figure 5.9. Optical microscopy (×5 magnification) images showing 85A (100), i) pre Au NP deposition, ii) post Au NP deposition and iii) post washing with Milli-Q water prior to AFM.

Figure 5.10a shows a CV using (100) scBDD as the substrate, using 1 mM $KAuCl_4$ in 0.1 M $NaClO_4$. From this the following V_{dep} were selected for *i-t* study: 0.1, 0, -0.05 and -0.2 V all at t_{dep}= 10 s. Figure 5.10b shows the earlier deposition behaviour, there was no significant change in current beyond 5 s.

In order to emphasise the short time behaviour, Figure 5.10c shows the logarithmic t_{dep}. Finally Figure 5.10d uses equations 5.1 and 5.2 to plot the expected responses for instantaneous (**orange**) and progressive (**black**) nucleation and compares this to experimental data.

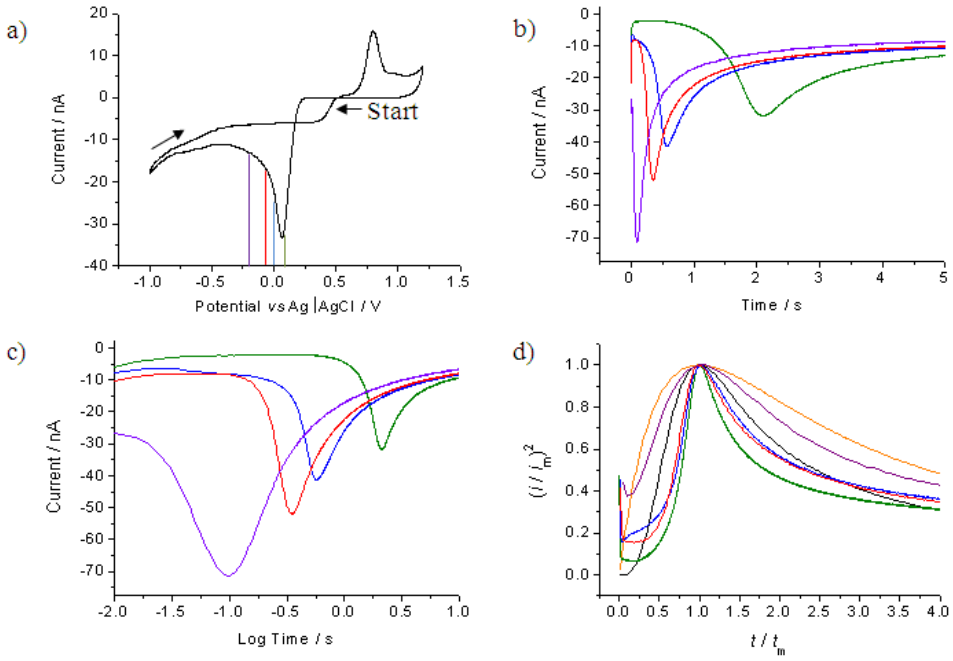

*Figure 5.10. a) Typical CV vs. quasi Ag|AgCl for the electrodeposition of Au onto the 85A (100) using 50 × 60 µm capillary filled with 1 mM $KAuCl_4$ in 0.1 M $NaClO_4$ using scan rate 100 mV s^{-1}. b) i-t transients where t_{dep} = 10 s and V_{deps} = 0.1 V (**green**), 0 V (**blue**), -0.05 V (**red**) and -0.2 V (**purple**) there were no changes in currents beyond 5 s. c) Logarithmic time plot of the same i-t transients and d) dimensionless plots of the data from b) plotted with theoretical curves of instantaneous nucleation (**orange**) and progressive nucleation (**black**) as originally described by the SH model.*

The V_{dep} of 0.1, 0 and -0.05 V as shown in Figure 5.10d all closely follow the theoretical plot shape of progressive nucleation, whereas at the highest V_{dep} (-0.2 V) falls in-between the theoretical fit of both progressive and instantaneous nucleation giving an inconclusive result.

For information on NP sizes, analysis was performed using AFM. Examples of TM-AFM images taken within the MCEM deposition spots are shown in Figure 5.11 with respective histograms. Challenges with AFM imaging led to analysis of

the sample using FE-SEM which enabled full visualisation of the whole deposition spot at much higher resolution as shown in Figure 5.12.

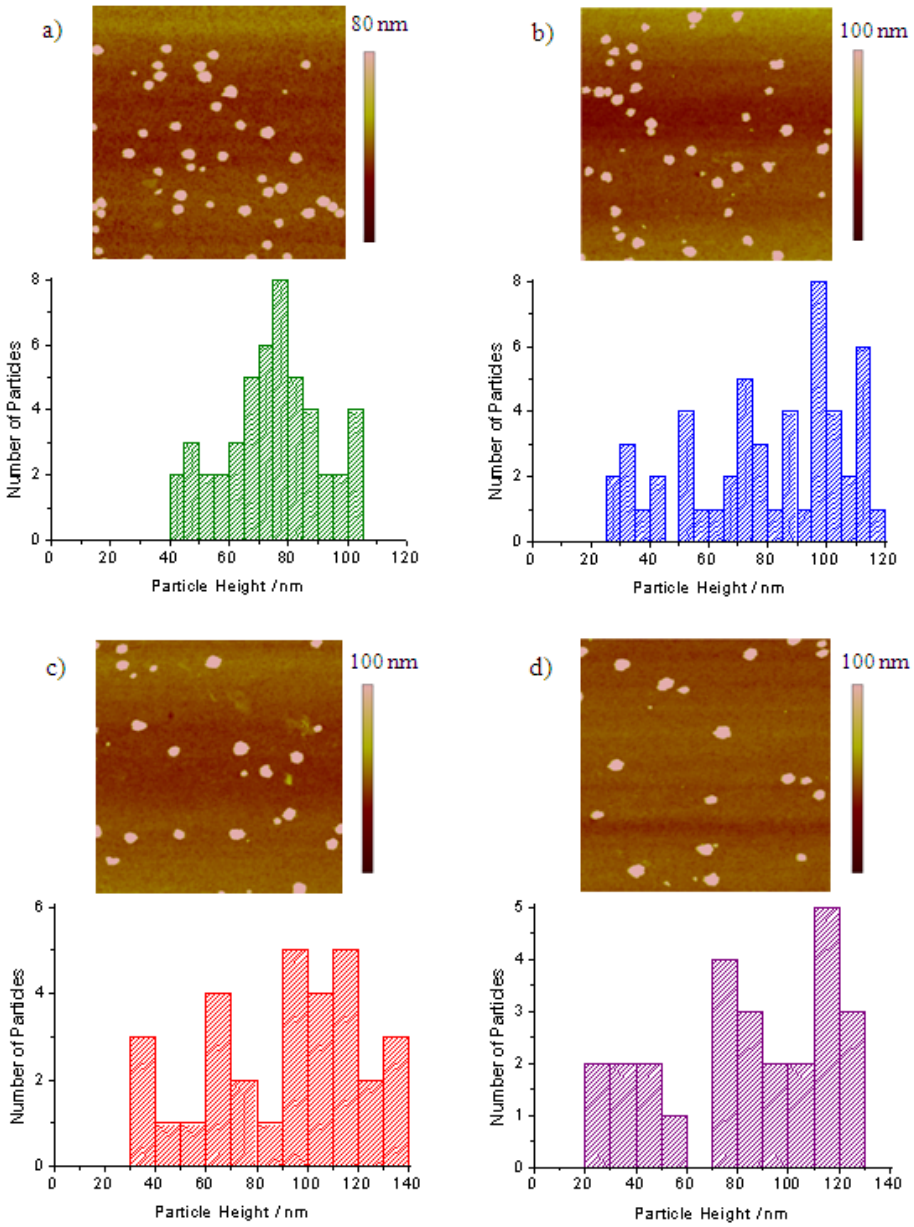

Figure 5.11. TM-AFM images (5 × 5 µm) and NP analysed histograms of t_{dep} = 10 s of Au NPs V_{dep} = a) 0.1 V, b) 0 V, c) -0.05 V and d) -0.2 V on 85A (100).

NP analysis for the above AFM images (n=1) combined with larger scale FE-SEM images (n=3) (as seen in Figure 5.12a) provided NP distributions and heights/widths as shown in Table 5.1.

Table 5.1. NP analysis for the TM-AFM images (n=1) from Figure 5.11 and FE-SEM images (n=3).

Potential / V	**NP Distribution/ µm^{-2}**		**NP Height / nm**	**NP Width / nm**
Technique	**AFM**	**FE-SEM**	**AFM**	**FE-SEM**
0.1	**2**	**0.59 ±0.09**	**74.7 ± 16.1**	**84.5 ± 29.8**
0	**2**	**1.22 ± 0.07**	**80.0 ± 26.5**	**56.8 ± 21.1**
-0.05	**1**	**1.43 ± 0.13**	**91.0 ± 31.9**	**48.6 ± 22.1**
-0.2	**1**	**2.11 ± 0.25**	**84.4 ± 33.3**	**38.3 ± 16.3**

Clearly the AFM and FE-SEM NP analysis shows differing trends. The AFM shows a low distribution of NPs per µm^{-2} leading to the inability to identify a real trend. This might suggest the instantaneous nucleation theory given the low number of particles counted. However this could also be attributed to the small surface area analysed, a limitation of the technique when compared to FE-SEM. The larger scale FE-SEM NP distribution data shows an increasing statistical trend which would be expected with progressive nucleation.

The AFM data would suggest the instantaneous nucleation mechanism is operating at all V_{dep} given the lack of any significant change in NP height. This correlates with the NP distribution data but does not correlate with the *i-t* curves which suggest a progressive nucleation of NPs.

The trends observed from FE-SEM NP width show a regular decrease in particle width as the deposition potential is increasingly applied coupled with an increase in NP distribution, thereby both width and distribution of NPs following the

progressive nucleation theorem. The capability of FE-SEM to image large scale areas at various magnifications has offered qualitative support to the *i-t* curves of this experiment.

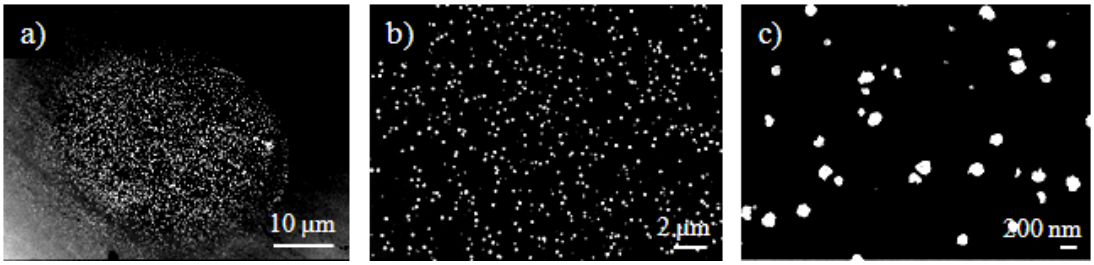

Figure 5.12. FE-SEM images of a t_{dep} = 10 s of Au NPs on 85A (100) at V_{dep} = 0 V, a) whole deposition spot, b) centre of the deposition spot ×5 magnification and c)centre of the deposition at ×25 magnification.

Both AFM and FE-SEM failed to highlight any heterogeneities relating to Au NP deposition on the surface of the (100) scBDD either on the specific V_{dep} or the CVs, thereby supporting its proposed homogeneous nature.

5.3.2 Gold Nanoparticle Deposition Utilising (110) Single Crystal Boron Doped Diamond with AFM and FE-SEM

The (110) scBDD sample was prepared in exactly the same way as the (100) sample to ensure continuity. Results reported herein for the (110) sample were for a range of V_{dep} and t_{dep}, due to surface features of the sample which allowed for easier visualisation of the deposition spots.

A CV with fresh solution was performed prior to each systematic series of depositions an example is shown in Figure 5.13a. Figure 5.13b shows a typical series of *i-t* transients at different spots on the surface for the same V_{dep} (-0.1 V) but for t_{dep} = 0.5, 2 and 10 s. Even though these depositions were performed using the same

capillary and in succession, the *i-t* curves do not overlay, as would be expected for a homogenously active surface, the data indicates that the surface of this scBDD material is not truly homogeneous.

Figure 5.13c shows the short time behaviour by plotting *i* versus log *t*. Given it was not possible to achieve overlay data on this surface the *i-t* transients were not analysed in terms of SH theory.

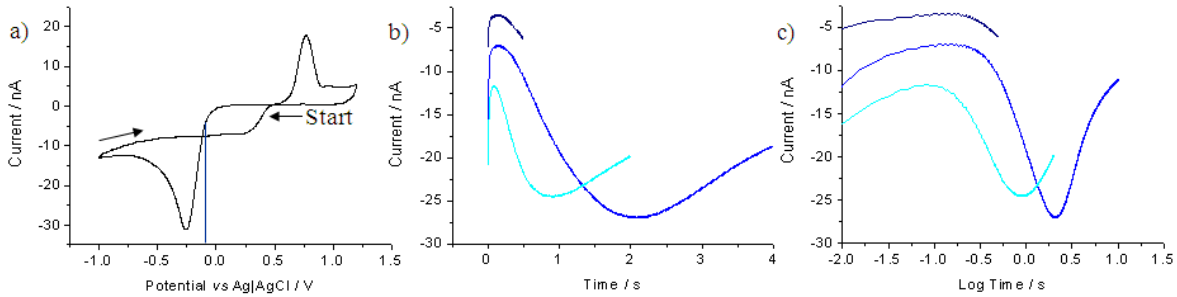

*Figure 5.13. a) Typical CV vs. quasi Ag|AgCl, for the electrodeposition of Au NPs onto 85F (110) using 50 × 60 µm capillary filled with 1 mM $KAuCl_4$ in 0.1 M $NaClO_4$ using scan rate 100 mV s^{-1}. b) i-t transients at V_{dep} = -0.1 V for t_{dep} = 0.5 s (**navy**), 2 s (**cyan**) and 10 s (**blue**). c) Logarithmic time plot of the same i-t transients.*

The Au nucleation morphologies resulting from the *i-t* transients shown in Figure 5.13b were imaged using AFM followed by NP analysis, as shown in Figure 5.14. The images clearly show that as t_{dep} increases the dominant effect appears to be the particles increasing in size, as outlined in Table 5.2.

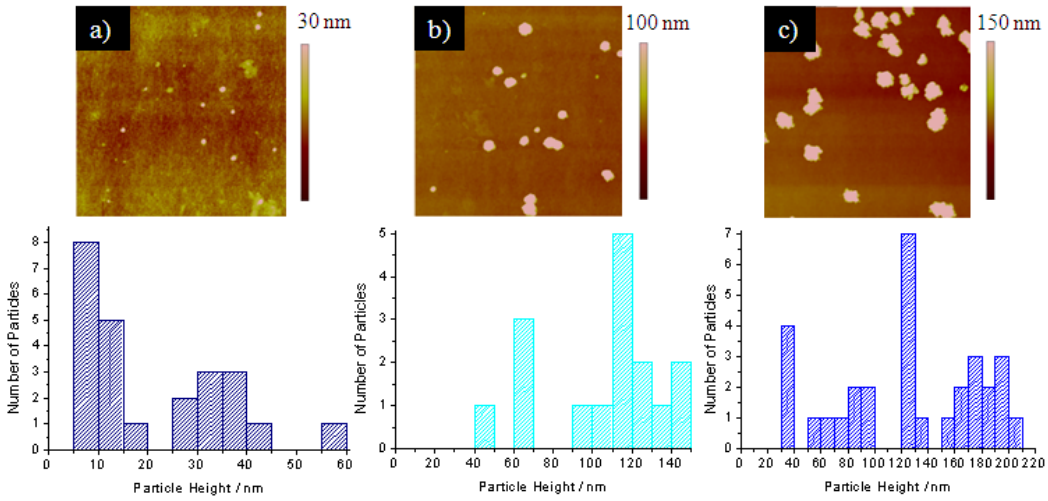

Figure 5.14. TM-AFM images (5 × 5 µm) and NP analysed histograms of the AFM images of V_{dep}= -0.1 V for t_{dep} = a) 0.5 s, b) 2 s and c) 10 s on 85F (110).

NP analysis of Figure 5.14 provides NP heights, widths and distributions as shown in Table 5.2.

Table 5.2. NP analysis for the TM-AFM images (n=1) from Figure 5.14 and FE-SEM images (n=3).

Time / s	**NP Distribution / µm^{-2}**		**NP Height / nm**	**NP Width / nm**
Technique	**AFM**	**FE-SEM**	**AFM**	**FE-SEM**
0.5	**1**	**n/a**	**20.78 ± 14.4**	**n/a**
2	**1**	**4.40 ± 0.6**	**104.66 ± 30.2**	**56.3 ± 27.0**
10	**1**	**20.7 ± 1.5**	**125.76 ± 53.1**	**59.1 ± 34.0**

As AFM only gives information on a small area of the sample, subsequent FE-SEM imaging was carried out to obtain more representative data and also to provide information on deposition homogeneity. No Au NPs were detected (only salt crystals) during FE-SEM for V_{dep} = -0.1 V and t_{dep} = 0.5 s. Figure 5.15 shows an

inverted FE-SEM image taken from the centre of the Au electrodeposition spot for V_{dep} = -0.1 V and t_{dep} = 10 s.

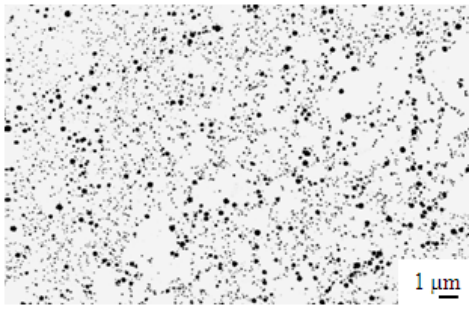

Figure 5.15. Inverted FE-SEM image (×5 magnification) from the centre of the V_{dep}=-0.1 V and t_{dep} = 10 s on 85F (110).

Figure 5.15 clearly shows a range of NP sizes, which appears to agree with the AFM image (Figure 5.14c), which denotes that particles of heights in the range 40 – 200 nm are visible. Interestingly, there also appears to be areas of the surface which do not support deposition (white zones). It is at the longest t_{dep} that the largest range of NP sizes is observed.

The AFM and FE-SEM NP analysis shown in Table 5.2 offer contrasting results relating both to NP height/width and distribution, the AFM data support an instantaneous nucleation mechanism for both NP distribution and height whereas the FE-SEM weakly suggest progressive nucleation.

At long t_{dep} times, Ostwald ripening may be a contributing factor, where larger NP clusters grow by consuming smaller NPs, as shown schematically in Figure 5.16.[7] Typically Ostwald ripening is a slow process,[57] sometimes taking days[58] although this phenomena has also been observed on shorter timescales.[7,59,60]

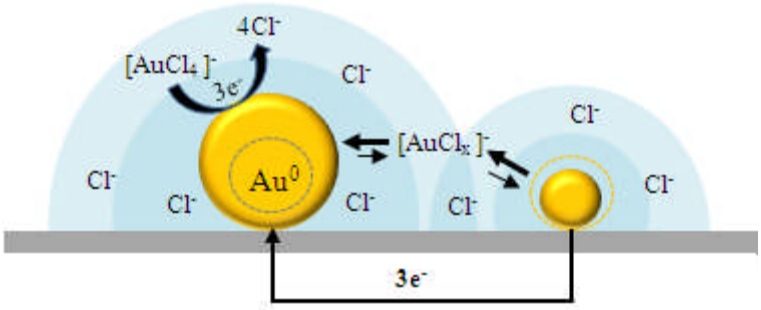

Figure 5.16. Electrochemically induced Ostwald ripening of Au NPs occurring due to overlapping diffusion fields, leading to the consumption of smaller particles leading to the growth of much larger NP aggregates.[7]

Further Au electrodepositions were carried out under fixed conditions where t_{dep} = 2 s, with V_{dep} = 0, -0.1, -0.2 and -0.3 V as shown on the CV in Figure 5.17a.

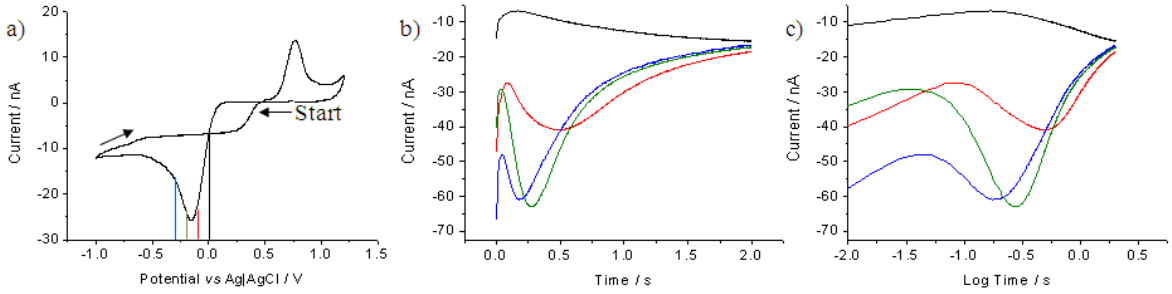

*Figure 5.17. a) Typical CV vs. quasi Ag|AgCl, for the electrodeposition of Au NPs onto 85F (110) using 50 × 60 µm capillary filled with 1 mM $KAuCl_4$ in 0.1 M $NaClO_4$. scan rate 100 mV s^{-1}. b) t_{dep} = 2 s and V_{dep}= 0 V (**black**), -0.1 V (**red**), -0.2 V (**green**) and -0.3 V (**blue**). c) Logarithmic time plot of the same i-t transients.*

The *i-t* transients shown in Figure 5.17b, qualitatively indicate that as V_{dep} is increased then the nucleation peak moves to shorter times. However, the *i-t* behaviour does not follow the expected trend where increasing V_{dep} results in an increase in the size of the nucleation peak, as well as a move to shorter times, as clearly shown for the recorded *i-t* behaviour on the (100) surface (Figure 5.10b). The

short time behaviour is emphasised in Figure 5.17c, again highlighting differences in early nucleation between the range of V_{dep}.

AFM images and histograms denoting NP density and size (Table 5.3), for the range of V_{dep} employed to record the data shown in Figure 5.17b for a t_{dep} = 2 s are shown in Figure 5.18.

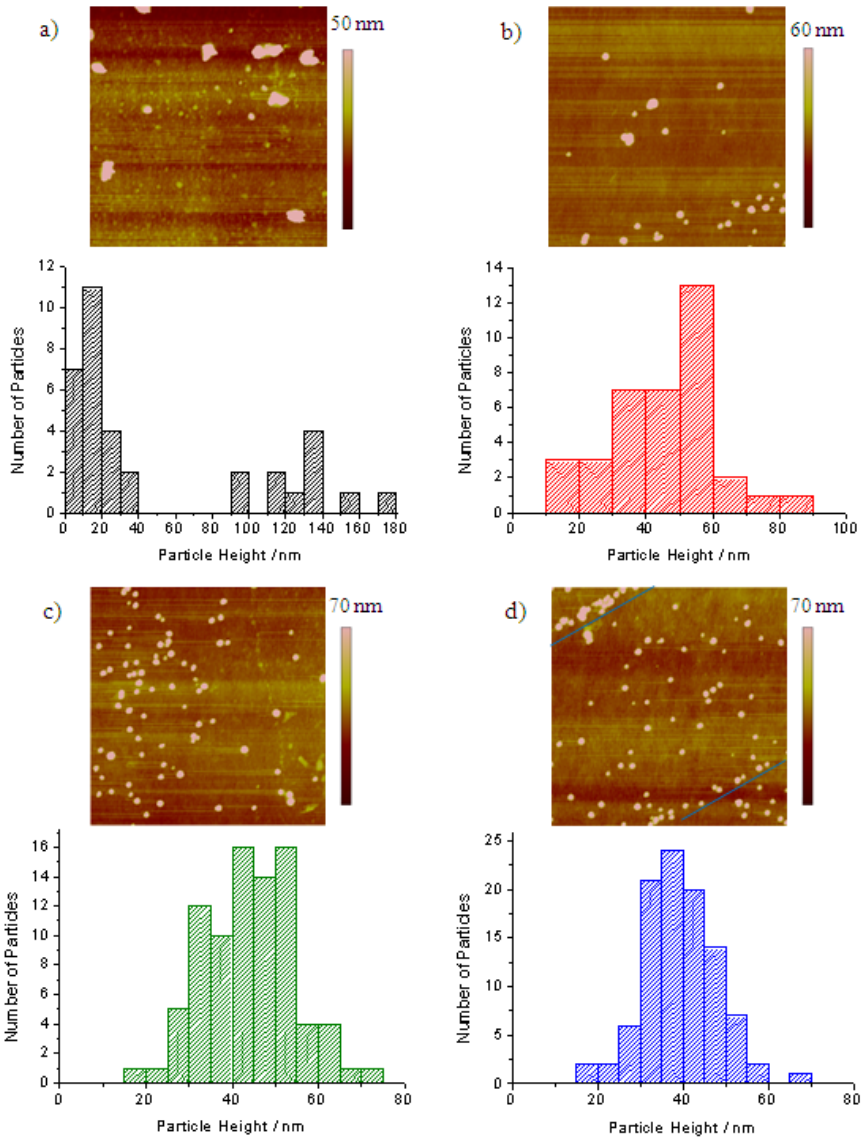

Figure 5.18. TM-AFM images (5 × 5 µm) and analysed histograms of t_{dep} = 2 s Au NP at V_{dep} = a) 0 V, b) -0.1 V, c) -0.2 V and d) -0.3 V on 85F (110).

Table 5.3. NP analysis of the TM-AFM images (n=1) in Figure 5.18 and FE-SEM images (n=3).

Potential / V	NP Distribution / µm^{-2}		NP Height / nm	NP Width / nm
Technique	AFM	FE-SEM	AFM	FE-SEM
0	1	3.3 ± 0.2	54.9 ± 50.5	30.3 ± 22.7
-0.1	2	18.0 ± 8.0	45.4 ± 16.1	74.8 ± 23.8
-0.2	3	22.3 ± 5.1	43.9 ± 10.5	82.2 ± 18.7
-0.3	4	25.6 ± 6.6	39.2 ± 8.50	93.4 ± 12.3

In general the AFM NP data shown in Table 5.3indicates that as the V_{dep} increases the number density increases and the NPs get smaller, whereas NP width and distribution via FE-SEM indicate an increase in particle density and width. However it is clear from the AFM images that Au NP nucleation appears more heterogeneous in nature on the surface than homogeneous. For example, in the AFM image in Figure 5.18d two clear lines of Au NPs are apparent which both run in the same direction (highlighted with blue lines).

To explore further where the (110) surface was heterogeneous towards Au electrodeposition, depositions using longer t_{dep} followed by AFM and FE-SEM were performed. Thus enabling larger areas to be viewed as shown in Figure 5.19.

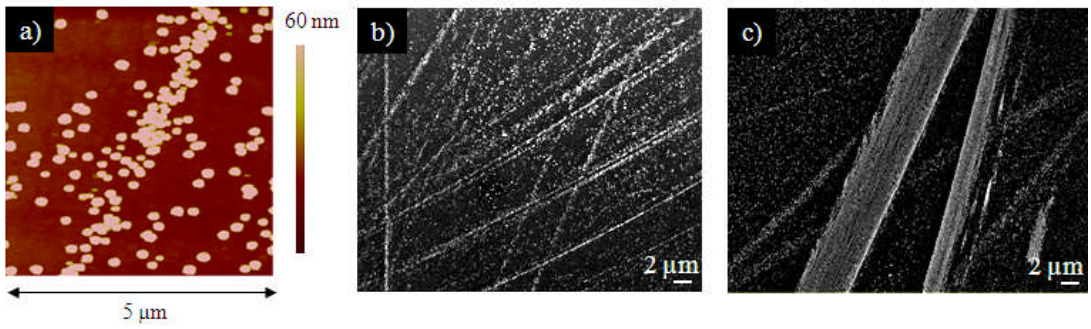

Figure 5.19. Preferential deposition of Au NPs seen on 85F (110) by a) TM-AFM (5 × 5 µm) (V_{dep} = -0.3 V, t_{dep} = 10 s), b) FE-SEM (V_{dep} = -0.3 V, t_{dep} = 10 s and c) FE-SEM (V_{dep} = -0.5 V, t_{dep} = 2 s).

Both the AFM and FE-SEM images reveal a clear preferential deposition of Au structures on the surface of (110), which appear to run along lines on the surface. Literature suggests a hydrogen plasma treatment can be used to smooth a diamond surface, although this is only reported for the (100) and (111) orientations.[61-63]

Specifically Küttel *et al.*[64]reported on the smoothing of naturally doped (100) from 2 nm_{rms} to 0.8 nm_{rms} and the (111) orientation from 7 nm_{rms} to 1 nm_{rms} using a hydrogen plasma at 870 °C and 0.04 atm.

Koslowski *et al.*[65] reported that whilst the use of hydrogen plasma treatment does indeed smooth a (100) diamond surface, this method in fact leads to scratches with depths of up to 40 nm. The research describes a 'brick wall' pattern running along the (110) direction post hydrogen plasma exposure for 3 minutes under typical CVD growth conditions when used with heavily doped scBDD ([B] ~10^{21} cm^{-3}).[65]

When the scBDD was exposed for a further 5 minutes, the surface roughness was further increased to 20-40 nm_{rms} and the sample exhibited a regular pattern with characteristics of 60 nm width, 250 nm length and 160 nm heights running along the (110) direction.

Koslowski *et al.* proposed two different mechanisms, the first an analogy to surface roughening occurring on strained SiGe/Si,[66-68] due to the similar patterns observed. In this instance the underlying roughening mechanism is explained in terms of (i) strain within the surface and (ii) material transport across the surface. The pattern observed by Koslowski on SiGe/Si is similar to that observed on the (100) diamond

Considering the differing reports in literature, there are two feasible explanations for the Au NP exposed lines across the surface; (i) these are as a result

of abrasion of the surface by the hydrogen plasma as a direct result of the failed cap layer growth, the striations may therefore be of a rougher texture which could be encouraging NP deposition. (ii) Whilst the cap layer growth failed (according to two SIMS measurements), it is possible that some cap layer growth occurred, thereby creating areas of a higher [B] when compared to the original bulk layer, although this was not observed under FE-SEM.

These regions of potentially higher [B] within the crystal lattice would support increased NP deposition over the bulk layer which is of a lower [B]. The lines across the surface whilst linear, do not appear to be solely of one direction nor are they of uniform thickness, such that the direction in which they run is unable to be determined.

DICM initially showed surface features for this sample, however these were not striations as highlighted by Au NP deposition. At the time this was the sole (110) sample under investigation utilising electrodeposition and analysis by large scale FE-SEM did not show any defects akin to the (100) bulk sample HB2. CV undertaken at the macro scale appeared to show reversibility given the whole electrode area (1 mm disc) and similar behaviour to that of the (100) samples and pBDD when using outer sphere one electron redox mediators.

Figure 5.20 shows typical CVs for Au electrodeposition on scBDD (110) and (100) using the same 50 × 60 μm capillary. The onset potential for Au nucleation was always found to be more positive on the (100) surface than the (110) surface.

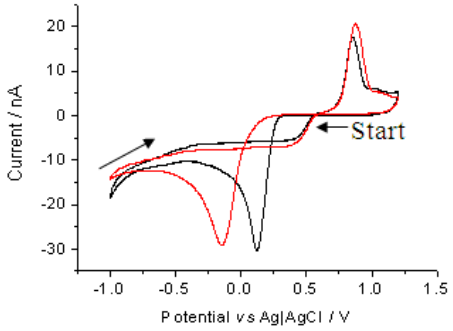

*Figure 5.20. Comparison of (100)(**black**) and (110) (**red**) scBDD orientations showing a typical CV vs. quasi Ag|AgCl for the electrodeposition of Au NPs using 50 × 60 µm capillary filled with 1 mM $KAuCl_4$ in 0.1 M $NaClO_4$. Scan rate 100 mV s^{-1}.*

The difference in maximum deposition potential could be caused by several reasons; (i) surface wetting by the capillary meniscus or (ii) surface heterogeneities. The Au oxide stripping peak in Figure 5.20 for both orientations overlay therefore occurs at the same potential, indicating the stripping is likely to be an AuO stripping process rather than Au stripping directly from the surface where a potential dependant stripping peak might also be expected as for nucleation. This explanation therefore lends support to the alternative explanation which relates to how Au actually deposits onto each substrate.

As Figure 5.19 clearly shows, there are areas of preferential deposition, therefore demonstrating the surface is in fact heterogeneous and that this is likely due to sparse sporadic growth of the cap layer over the bulk layer. A heterogeneous substrate would result in a range of kinetic processes occurring, akin to pBDD,[22, 69] therefore a difference in the deposition peak would be expected if compared to a kinetically homogeneous substrate.

5.4 CONCLUSIONS

The MCEM deposition of Au NPs has been investigated on both (100) and the (110) scBDD using a range of t_{dep} and V_{dep} selected from initial CVs. The deposited NPs were characterised using TM-AFM and FE-SEM, the images analysed using SPIP™ therefore elucidating NP distribution , heights and widths.

The (100) substrate has no surface features therefore t_{dep} was fixed at 10 s to allow for easier visualisation, *i-t* curves were performed at V_{dep} 0.1, 0, -0.05 and -0.2 V, this data was fitted using the SH model suggesting progressive nucleation for all but the V_{dep} -0.2 V which proved inconclusive. The limited AFM performed suggested instantaneous nucleation whereas the much larger scale FE-SEM supported the *i-t* curve plot using the SH model suggesting progressive nucleation.

The (110) substrate is not homogeneous therefore was not plotted using the SH model, however this enabled V_{dep} and t_{dep} to be varied because surface features allowed for easier visualisation of the Au NP deposition spots. TM-AFM images provided a wide range of NP sizes whereas FE-SEM highlighted areas of non-deposited scBDD. Both sets of NP data proved inconclusive with respect to a nucleation theory.

With t_{dep} fixed and V_{dep} varied, NP analysed TM-AFM and FE-SEM images both suggested the progressive nucleation although not fitted to the SH model due to its heterogeneous nature, a decrease in NP height and width with increasing NP distribution was clearly seen. AFM highlighted areas of preferential deposition, further supported by FE-SEM whereby these areas had a much higher NP density with smaller NPs.

The homogeneous nature of the (100) sample led to the earlier onset of NP deposition as shown in CVs compared to the later and wider onset for the (110) substrate which can be explained due to a range of kinetic processing occurring across its inhomogeneous surface when a fixed V_{dep} is applied.

5.5 REFERENCES

1. M. S. El-Deab, T. Sotomura and T. Ohsaka, *Journal of the Electrochemical Society*, 2005, **152**, C730-C737.
2. C. R. Bradbury, L. Kuster and D. J. Fermin, *Journal of Electroanalytical Chemistry*, 2010, **646**, 114-123.
3. G. F. Ndlovu, W. D. Roos, Z. M. Wang, J. K. Asante, M. G. Mashapa, C. J. Jafta, B. W. Mwakikunga and K. T. Hillie, *Nanoscale research letters*, 2012, **7**, 173.
4. A. Kishi and M. Umeda, *Applied Surface Science*, 2009, **255**, 9154-9158.
5. M. Oyama, S.-y. Yamaguchi and J. Zhang, *Analytical Sciences*, 2009, **25**, 249-253.
6. M. Wei, Y. Zhou, J. Zhi, D. Fu, Y. Einaga, A. Fujishima, X. Wang and Z. Gu, *Electroanalysis*, 2008, **20**, 137-143.
7. P. V. Dudin, P. R. Unwin and J. V. Macpherson, *Journal of Physical Chemistry C*, 2010, **114**, 13241-13248.
8. T. M. Day, P. R. Unwin and J. V. Macpherson, *Nano Letters*, 2007, **7**, 51-57.
9. I. Perez, B. L. Corso, V. R. Khalap and P. G. Collins, *Electrochemistry Communications*, 2011, **13**, 590-592.
10. P. V. Dudin, P. R. Unwin and J. V. Macpherson, *Physical Chemistry Chemical Physics*, 2011, **13**, 17146-17152.
11. I. Dumitrescu, P. R. Unwin, N. R. Wilson and J. V. Macpherson, *Analytical Chemistry*, 2008, **80**, 3598-3605.
12. U. Schlecht, K. Balasubramanian, M. Burghard and K. Kern, *Applied Surface Science*, 2007, **253**, 8394-8397.
13. L. E. G. Armas, G. T. Landi, M. F. G. Huila, A. Champi, M. Pojar, A. C. Seabra, A. D. Santos, K. Araki and H. E. Toma, *Diamond and Related Materials*, 2012, **23**, 18-22.
14. S. Mayavan, J.-B. Sim and S.-M. Choi, *Journal of Materials Chemistry*, 2012, **22**, 6953-6958.
15. R. Bajpai, S. Roy, N. Kulshrestha, J. Rafiee, N. Koratkar and D. S. Misra, *Nanoscale*, 2012, **4**, 926-930.
16. H. Awada, J. W. Strojek and G. M. Swain, *Journal of the Electrochemical Society*, 1995, **142**, L42-L45.
17. I. González-González, E. o. R. Fachini, M. A. Scibioh, D. A. Tryk, M. Tague, H. c. D. Abruña and C. R. Cabrera, *Langmuir*, 2009, **25**, 10329-10336.
18. D. W. M. Arrigan, *Analyst*, 2004, **129**, 1157-1165.
19. A. Berduque, G. Herzog, Y. E. Watson, D. W. M. Arrigan, J. C. Moutet, O. Reynes, G. Royal and E. Saint-Aman, *Electroanalysis*, 2005, **17**, 392-399.
20. A. O. Simm, X. B. Ji, C. E. Banks, M. E. Hyde and R. G. Compton, *Chemphyschem*, 2006, **7**, 704-709.
21. A. O. Simm, C. E. Banks, S. Ward-Jones, T. J. Davies, N. S. Lawrence, T. G. J. Jones, L. Jiang and R. G. Compton, *Analyst*, 2005, **130**, 1303-1311.
22. A. L. Colley, C. G. Williams, U. D'Haenens Johansson, M. E. Newton, P. R. Unwin, N. R. Wilson and J. V. Macpherson, *Analytical Chemistry*, 2006, **78**, 2539-2548.

23. L. Hutton, M. E. Newton, P. R. Unwin and J. V. Macpherson, *Analytical Chemistry*, 2009, **81**, 1023-1032.
24. L. A. Hutton, M. E. Newton, P. R. Unwin and J. V. Macpherson, *Analytical Chemistry*, 2011, **83**, 735-745.
25. C. Batchelor-McAuley, C. E. Banks, A. O. Simm, T. G. J. Jones and R. G. Compton, *Analyst*, 2006, **131**, 106-110.
26. M. Pagels, C. E. Hall, N. S. Lawrence, A. Meredith, T. G. J. Jones, H. P. Godfried, C. S. J. Pickles, J. Wilman, C. E. Banks, R. G. Compton and L. Jiang, *Analytical Chemistry*, 2005, **77**, 3705-3708.
27. S. Szunerits and R. Boukherroub, *Comptes Rendus Chimie*, 2008, **11**, 1004-1009.
28. A. Denisenko, C. Pietzka, L. A. Kibler and E. Kohn, *Journal of the Electrochemical Society*, 2010, **157**, H342-H348.
29. F. Canac, *Comptes Rendus Academie des Sciences*, 1933, **196**, 51.
30. A. N. Kolmogoroff, *Bull. Acad. Sci. U.S.S.R/Sci. Mat. Nat.*, 1937, **3**, 355.
31. M. Avrami, *The Journal of Chemical Physics*, 1939, **7**, 1103-1112.
32. M. Avrami, *The Journal of Chemical Physics*, 1940, **8**, 212-224.
33. M. Avrami, *The Journal of Chemical Physics*, 1941, **9**, 177-184.
34. W. A. Johnson and R. F. Mehl, *Transactions of the American Institute of Mining and Metallurgical Engineers*, 1939, **135**, 416-442.
35. B. Scharifker and G. Hills, *Electrochimica Acta*, 1983, **28**, 879-889.
36. M. V. Mirkin and A. P. Nilov, *Journal of Electroanalytical Chemistry*, 1990, **283**, 35-51.
37. L. Heerman and A. Tarallo, *Journal of Electroanalytical Chemistry*, 1999, **470**, 70-76.
38. J. Farjas and P. Roura, *Acta Materialia*, 2006, **54**, 5573-5579.
39. A. Milchev, *Electrochimica Acta*, 1997, **42**, 1533-1536.
40. R. L. Deutscher and S. Fletcher, *Journal of Electroanalytical Chemistry*, 1988, **239**, 17-54.
41. M. Y. Abyaneh, *Journal of Electroanalytical Chemistry*, 2002, **530**, 96-104.
42. M. Y. Abyaneh and M. Fleischmann, *Journal of Electroanalytical Chemistry*, 2002, **530**, 89-95.
43. M. Y. Abyaneh, *Journal of Electroanalytical Chemistry*, 2002, **530**, 82-88.
44. S. Fletcher, *Journal of Electroanalytical Chemistry*, 2002, **530**, 119-122.
45. S. Fletcher, *Journal of Electroanalytical Chemistry*, 2002, **530**, 105-107.
46. R. Krumm, B. Guel, C. Schmitz and G. Staikov, *Electrochimica Acta*, 2000, **45**, 3255-3262.
47. L. Komsiyska and G. Staikov, *Electrochimica Acta*, 2008, **54**, 168-172.
48. D. Grujicic and B. Pesic, *Electrochimica Acta*, 2002, **47**, 2901-2912.
49. A. B. Soto, E. M. Arce, M. PalomarPardave and I. Gonzalez, *Electrochimica Acta*, 1996, **41**, 2647-2655.
50. G. J. Lu and G. Zangari, *Journal of Physical Chemistry B*, 2005, **109**, 7998-8007.
51. J. A. Bennett and G. M. Swain, *Journal of The Electrochemical Society*, 2010, **157**, F89-F95.
52. M. S. El-Deab and T. Ohsaka, *Electrochemistry Communications*, 2002, **4**, 288-292.

53. B. Alvarez-Ruiz, R. Gomez, J. M. Orts and J. M. Feliu, *Journal of the Electrochemical Society*, 2002, **149**, D35-D45.
54. M. Tominaga, T. Shimazoe, M. Nagashima and I. Taniguchi, *Electrochemistry Communications*, 2005, **7**, 189-193.
55. T. Kondo, K. Hirata, T. Kawai and M. Yuasa, *Diamond and Related Materials*, 2011, **20**, 1171-1178.
56. T. Kondo, S. Aoshima, K. Hirata, K. Honda, Y. Einaga, A. Fujishima and T. Kawait, *Langmuir*, 2008, **24**, 7545-7548.
57. M. Di Vece, D. Grandjean, M. J. Van Bael, C. P. Romero, X. Wang, S. Decoster, A. Vantomme and P. Lievens, *Physical review letters*, 2008, **100**, 236105.
58. K. Heinemann and H. Poppa, *Thin Solid Films*, 1976, **33**, 237-251.
59. J. D. Porter and T. O. Robinson, *Journal of Physical Chemistry*, 1993, **97**, 6696-6709.
60. P. L. Redmond, A. J. Hallock and L. E. Brus, *Nano Letters*, 2005, **5**, 131-135.
61. C. Nutzenadel, O. M. Kuttel, L. Diederich, E. MaillardSchaller, O. Groning and L. Schlapbach, *Surface Science*, 1996, **369**, L111-L116.
62. R. E. Rawles, S. F. Komarov, R. Gat, W. G. Morris, J. B. Hudson and M. P. Develyn, *Diamond and Related Materials*, 1997, **6**, 791-795.
63. A. Gaisinskaya, R. Edrei, A. Hoffman and Y. Feldheim, *Diamond and Related Materials*, 2009, **18**, 1466-1473.
64. O. M. Kuttel, L. Diederich, E. Schaller, O. Carnal and L. Schlapbach, *Surface Science*, 1995, **337**, L812-L818.
65. B. Koslowski, S. Strobel, M. J. Wenig, R. Martschat and P. Ziemann, *Diamond and Related Materials*, 1998, **7**, 322-326.
66. A. G. Cullis, *Mrs Bulletin*, 1996, **21**, 21-26.
67. D. E. Jesson, K. M. Chen and S. J. Pennycook, *Mrs Bulletin*, 1996, **21**, 31-37.
68. C. Roland, *Mrs Bulletin*, 1996, **21**, 27-30.
69. H. V. Patten, K. E. Meadows, L. A. Hutton, J. G. Iacobini, D. Battistel, K. McKelvey, A. W. Colburn, M. E. Newton, J. V. Macpherson and P. R. Unwin, *Angewandte Chemie International Edition*, 2012, **51**, 7002-7006.

6 Characterisation of Recent Single Crystal Boron Doped Diamond

ABSTRACT

ScBDD (100) samples were grown based on feedback from the characterisation data presented reported in Chapter 3, 4 and 5. Two sample types were provided (i) as grown with a thicker capping layer (400 and 1200 nm) doped at [B] ~6 × 10^{20} cm^{-3} and (ii) scaife polished bulk scBDD heavily doped with [B] 1.2 × $10^{21}$$cm^{-3}$.

Physical and electrochemical characterisation was undertaken as described in Chapters 3-5. Electrodeposition measurements were carried out only on the heavily doped bulk sample employing both the macro electrode approach and the MCEM Finally electrochemical imaging using carried out using IC-SECM on both samples.

Thorough analysis and comparison to the 85A (100) capped (65 nm) sample led to the conclusion that scBDD grown as a bulk material offers increased stability as an electrode over capped layer samples. Bulk samples of [B] 1.2 × 10^{20} cm^{-3} were found to display the most superior electrochemical properties of all single crystal electrodes investigated including; reversible ET for outer sphere redox mediators, faster ET kinetics when subject to pre-treatment and used in conjunction with inner sphere redox mediators. Finally Au NP deposition and IC-SECM elucidated to a homogeneous substrate.

6.1 PHYSICAL CHARACTERISATION OF (100) SAMPLES

6.1.1 Secondary Ion Mass Spectrometry (SIMS)

(100) scBDD samples were grown by E6 for analysis in-order to demonstrate their potential suitability as an electrode material. Initial sample details and SIMS results are shown in Table 6.1.

Table 6.1. Showing the bulk and capped layer of (100) scBDD; surface finish, sample size, thickness, [B](cm^{-3}) and cap layer thickness determined by SIMS.

Sample	Surface Finish	Size / mm	Thickness / µm	Bulk [B] / cm^{-3}	Cap Layer [B] / cm^{-3}	Cap Thickness / nm
20-01	**As grown**	3.8 × 3.8	525	2×10^{19}	6×10^{20}	400
23-01	**As grown**	3.8 × 3.8	300	2×10^{19}	7×10^{20}	1200
34-0X	**Scaife polished**	3.1 × 3.1	200	1.2×10^{21}	n/a	n/a

The capped samples contain sufficient [B] to be well into the metal-like conductivity region.[1] The thicker cap layers will help determine if thicker capped layers are just as effective as the bulk material. Bulk sample 34-0X, along with 85A/B (discussed in Chapter 3) contains the highest [B].

6.1.2 Differential Interference Contrast Microscopy (DICM)

Optical imaging using DICM did not show any discernible surface features (nm surface height differences[2, 3]) or defects as seen previously in Figures 3.1, 3.2 and 3.3. All samples appeared flat under DICM although scaife polishing lines were evident across all four 34-0X samples, as seen in Figure 6.1. Laser processing for macrodisc electrode formation avoided the regions containing structural cracks.

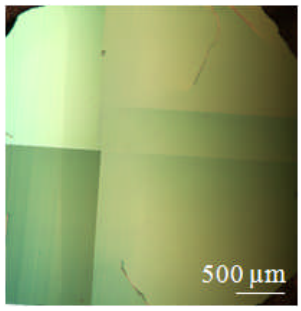

Figure 6.1. DICM image of bulk 34-0X (100).

6.1.3 Field Emission-Scanning Electron Microscopy (FE-SEM)

Little contrast was observed for the capped sample 20-01 suggesting this is of homogeneous [B]. Furthermore, no features or contrast were observed for the 23-01 sample with a thicker and slightly higher [B] cap layer. The cracks in the 34-0X sample were observed under FE-SEM as seen in Figure 6.2. Other than polishing lines there were no other surface features nor were there any differences in contrast across the surface suggesting a homogeneously doped substrate.[4, 5]

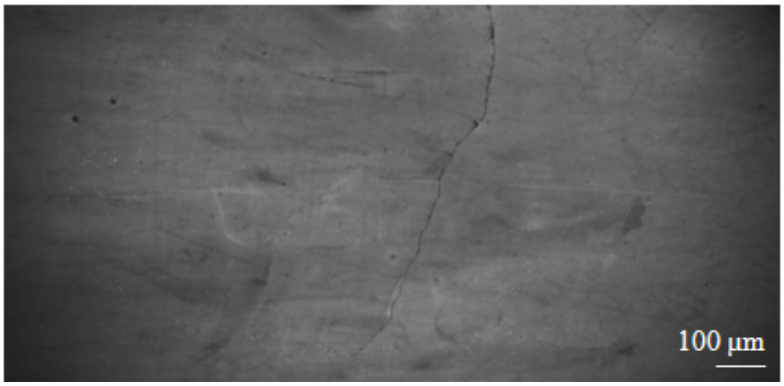

Figure 6.2. In-Lens FE-SEM image of 34-0X (100).

6.1.4 Atomic Force Microscopy (AFM)

Triplicate TM-AFM was performed in air to determine surface roughness of samples.[6, 7] Table 6.2 shows the RMS value which determines the best fit of all height points over the sample area. Figure 6.3 shows TM-AFM images and their respective cross sections.

Table 6.2. Showing sample, surface finish and RMS measured by TM-AFM.

Sample	Surface Finish	RMS / nm (n=3)
20-01	**As grown**	1.57 ± 0.30
23-01	**As grown**	2.37 ± 0.88
34-0X	**Scaife polished**	1.03 ± 0.32

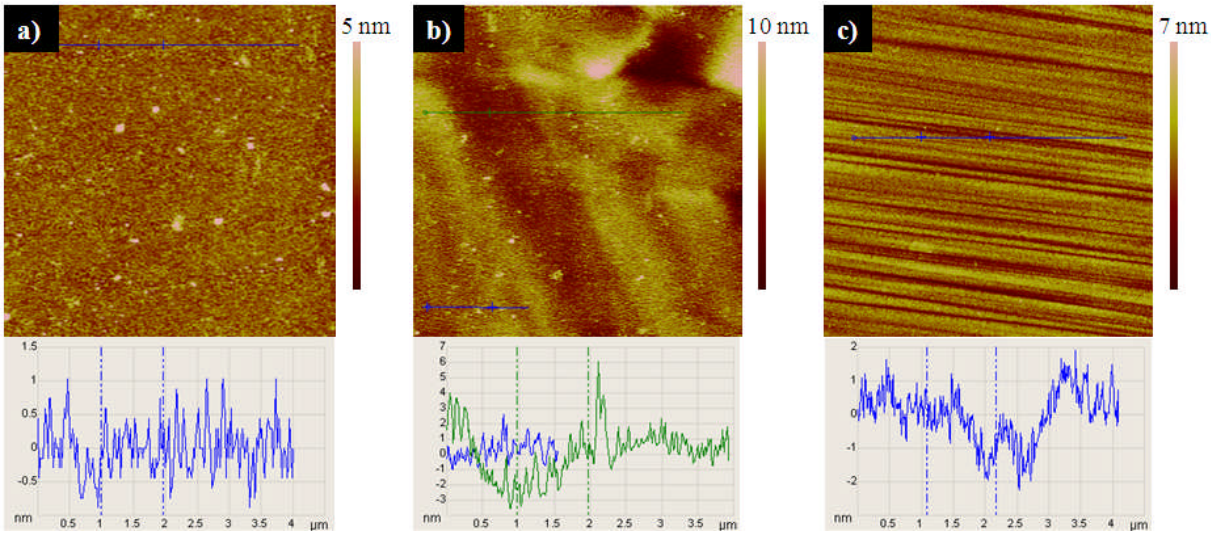

Figure 6.3. 5 × 5 µm TM-AFM images and respective cross sections showing surface roughness of a) 20-01, b) 23-01 and c) 34-0X.

Figure 6.3a is as grown with a low surface roughness. Figure 6.3b also shows the as grown surface but with a thicker capping layer. Prior to cap layer growth the surface was scaife polished and these polishing features may have followed through

to the cap layer during homoepitaxial overgrowth. The AFM image shows the presence of an undulation about 1.5 µm wide and ~3 nm deep on sample 23-01. Figure 6.3cc is of a bulk sample which was scaife polished, subtle undulations in the surface topography are also visible here, with a surface roughness of < 3 nm.

6.1.5 Micro Raman Spectroscopy

Micro Raman spectroscopy was undertaken to assess scBDD diamond quality.[8] Raman was performed using the 514 nm laser, as shown in Figure 6.4.

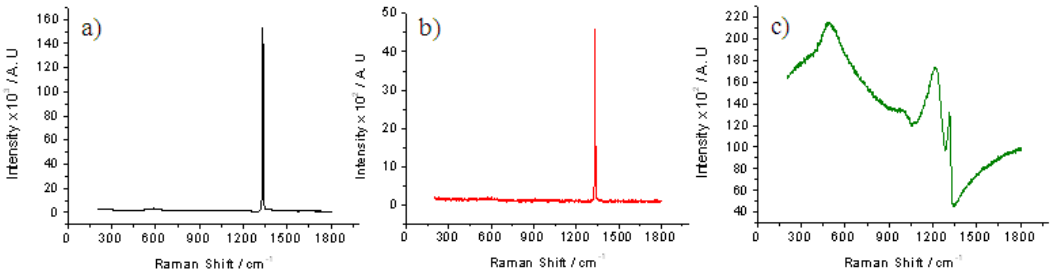

Figure 6.4. Raman spectra showing a) 20-01, b) 23-01 and c) 34-0X recorded using 514 nm laser, spot size 6 µm.

The lack of any sp^2 signature demonstrates the high quality of all three samples shown in Figure 6.4. However as seen previously (section 3.1.5) the laser is penetrating through the cap layer of both 20-01 and 23-01 such that the semiconducting bulk substrate ([B] 2×10^{19} cm^{-3}) is being probed hence the lack of Fano resonance. Figure 6.4c of bulk 34-0X shows a large Fano resonance and attenuated sp^3 peak, suggesting the sample contains a high [B] [9-11] which correlates with SIMS data.

Larger scale Raman mapping was undertaken for the 34-0X sample, to validate sample homogeneity with respect to [B]. Raman mapping was performed

using a 3 µm step size over 200 × 200 µm, with the 514 nm laser and is shown in Figure 6.5.

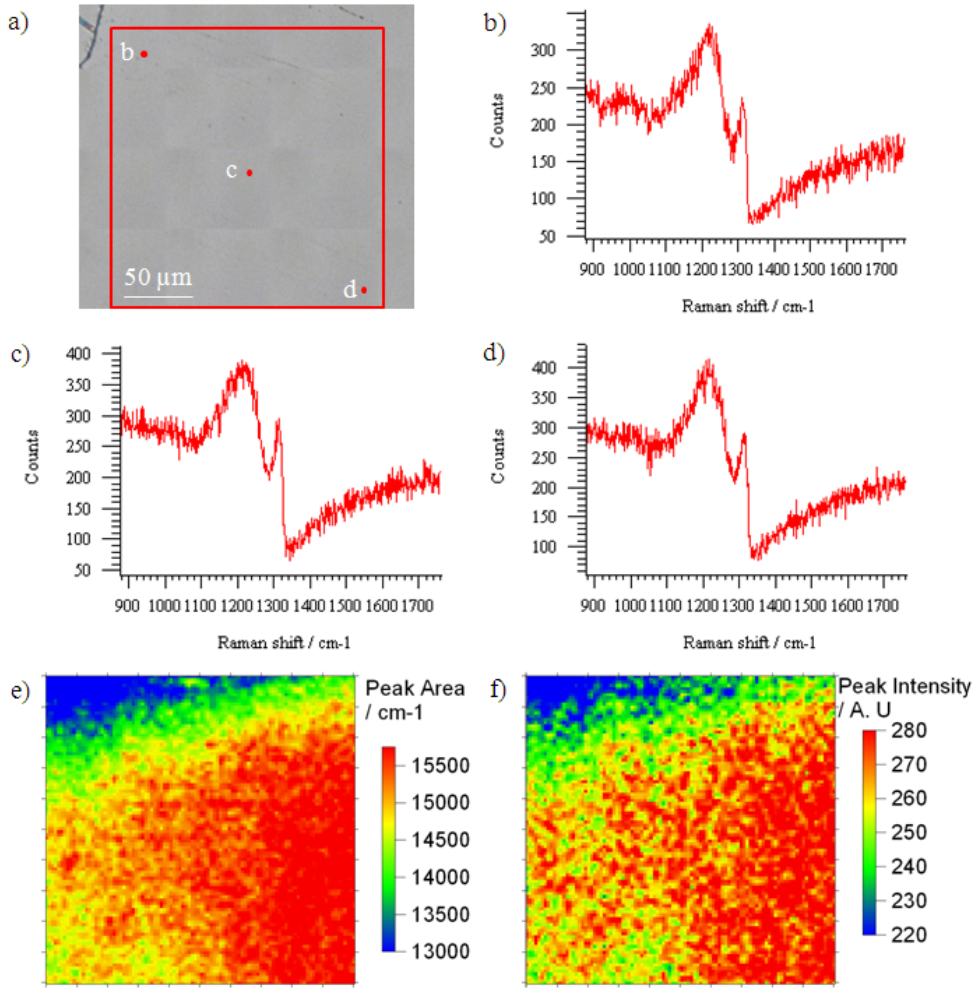

Figure 6.5. a) Optical image of 34-0X showing the boundaries of the 200 × 200 µm Raman map. b), c) and d) Raman spectra at selected points highlighted in a). e) Raman map showing the integrated peak area ~1332 cm^{-1} as a function of spot location using 514 nm laser, spot size 6 µm. f)Raman map showing the measured peak intensity ~1332 cm^{-1}.

The Raman maps show a small gradient in both peak area and intensity, however when the sample was rotated at 90° to the original orientation, the observed gradient correlated with the orientation of the sample, suggesting the electrode was not wholly coplanar to the objective lens.

6.2 ELECTROCHEMICAL CHARACTERISATION

6.2.1 Double Layer Capacitance Measurements (C_{meas})

As detailed in section 3.2.1, C_{meas} was measured and quantified (equation 3.2) by recording CVs in 0.1 M KNO_3 (pH 7.2) swept at 100 mV $s^{-1.}$ The calculated C_{meas} values (n=3) are shown in Table 6.3 using data recorded at 0 V *vs.* SCE.

Table 6.3. Table showing 1 mm macrodisc BDD sample orientation, C_{meas} values and [B] compared with commercial electrodes.

Sample	C_{meas} / µF cm^{-2} (n=3)	[B] / cm^{-3}
20-01	**6.20 ± 0.45**	6×10^{20}
23-01	**5.01 ± 0.14**	7×10^{20}
34-0X	**5.21 ± 0.04**	1.2×10^{21}
MR14 pBDD	**8.58 ± 0.70**	$\sim 3 \times 10^{20}$
GC	**77.9 ± 1.0**	n/a
Au	**36.8 ± 2.6**	n/a
Pt	**88.7 ± 1.5**	n/a

There is no noticeable trend relating to C_{meas} and scBDD [B] for these three new samples. This suggests that under these growth parameters when boron is incorporated into the carbon lattice beyond metal-like conductivity ($\geq 1 \times 10^{20}$ cm^{-3})[12] as [B] increases the effect on C_{meas} is minimal.

As observed previously (section 3.2.1), surface finish does not appear to have a significant influence on C_{meas}, suggesting as grown and polished samples show similar low background currents. The low C_{meas} values demonstrate the high quality of the scBDD samples analysed and are comparable to previously measured C_{meas} values for (100) samples.

6.2.2 Potential Windows in Background Electrolyte (0.1 M KNO_3)

Potential window CVs were performed using 0.1 M KNO_3 (background electrolyte) at 100 mV s^{-1} *vs*. SCE. Data is reported in Table 6.4 where the potential window of BDD is greatly extended when compared to commercial electrodes.

Table 6.4. Mean tabulated values of potential limits for scBDD and commercial electrodes measured using 0.1 M KNO_3, swept between -3 and +3 V at 100 mV s^{-1}, values recorded at 0.3 mA. Values measured from the original CVs (n=3).

Sample	Potential Window Voltage Range (V)	Negative Potential Limit (V)	Positive Potential Limit (V)
20-01	**5.50** ± 0.01	-2.71 ± 0.02	2.77 ± 0.07
23-01	**4.75** ± 0.14	-2.28 ± 0.10	2.46 ± 0.04
34-0X	**4.60** ± 0.10	-2.26 ± 0.11	2.34 ± 0.05
MR14 pBDD	**4.64** ± 0.14	-2.26 ± 0.12	2.36 ± 0.02
GC	**3.10** ± 0.23	-1.16 ± 0.25	1.94 ± 0.11
Au	**2.51** ± 0.18	-0.41 ± 0.70	1.78 ± 0.01
Pt	**1.48** ± 0.32	-0.20 ± 0.08	1.29 ± 0.41

6.2.3 Macro Electrochemistry with Outer Sphere Redox Mediators

Electrochemical characterisation was undertaken using a range of redox mediators and values of ΔE_p and i_p were extracted from the data and compared to theoretical values using (equation 1.4 and 1.5). Table 3.6 details D and $E°´$ values for the outer sphere redox mediators used. All electrodes were prepared as described in section 2.4.2.

CVs and corresponding data table for the three (100) scBDD samples, using a range of scan rates (10-1000 mV s^{-1}) and varying concentrations of $FcTMA^+$, are shown in Figure 6.6 and Table 6.5.

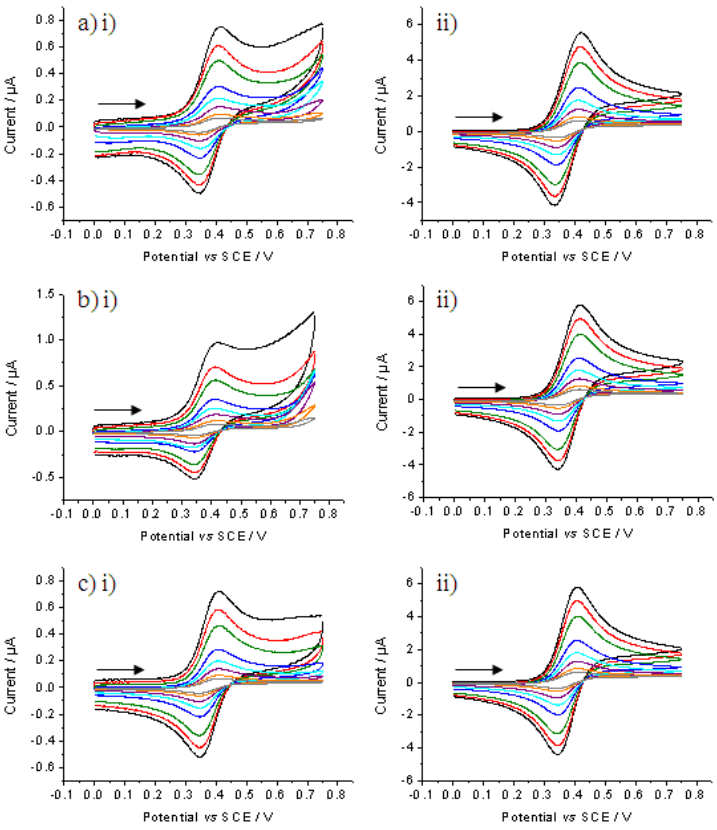

Figure 6.6. CV recorded at a range of scan rates showing the oxidation of i) 0.1 mM FcTMA$^+$ in 0.1 M $KNO_3$and ii) 1 mM FcTMA$^+$ in 0.1 M KNO_3 for 1 mm macrodisc a) 20-01, b) 23-01 and c) 34-0X. The following colour coding applies; ***10 mV s^{-1}****,* ***20 mV s^{-1}****,* ***50 mV s^{-1}****,* ***100 mV s^{-1}****,* ***200 mV s^{-1}****,* ***500 mV s^{-1}****,* ***750 mV s^{-1}*** *and* ***1000 mV s^{-1}****.*

Table 6.5. Theoretical oxidation peak currents using a range of scan rates and varying concentrations of $FcTMA^+$ compared to experimental data including ΔE_p values for 1 mm macrodisc 20-01, 23-01 and 34-0X.

0.1 mM		20-01		23-01		34-0X	
Scan rate / mV s^{-1}	Theory i_p / µA	i_p / µA	ΔEp / mV	i_p / µA	ΔEp / mV	i_p / µA	ΔEp / mV
10	0.05	0.06	67	0.07	78	0.07	66
20	0.07	0.09	67	0.10	73	0.09	67
50	0.12	0.14	68	0.16	72	0.14	67
100	0.16	0.19	64	0.23	75	0.19	62
200	0.23	0.26	61	0.31	67	0.28	63
500	0.37	0.41	66	0.47	75	0.44	67
750	0.45	0.50	63	0.58	64	0.53	68
1000	0.52	0.65	72	0.80	74	0.66	63
1 mM		20-01		23-01		34-0X	
Scan rate / mV s^{-1}	Theory i_p / µA	i_p / µA	ΔEp / mV	i_p / µA	ΔEp / mV	i_p / µA	ΔEp / mV
10	0.52	0.61	69	0.62	70	0.62	69
20	0.73	0.83	70	0.84	71	0.85	67
50	1.16	1.28	72	1.30	71	1.31	68
100	1.64	1.79	68	1.82	66	1.84	62
200	2.31	2.49	74	2.56	69	2.59	66
500	3.66	3.87	84	3.98	74	4.05	67
750	4.48	4.69	87	4.86	71	4.96	63
1000	5.17	5.41	87	5.61	75	5.70	65

When employing the 1 mM solution with 20-01, the ΔE_p range was 68-87 mV suggesting the electrode behaves akin to HB2 (100) and CP09 (111) i.e. close to reversible ET. When using 0.1 mM concentration its behaviour was more like pBDD and 05A (110), where ΔE_p approaches reversibility (61-72 mV). At both concentrations i_p values were close to theoretical values.

Electrode 23-01 offers a ΔE_p range of 66-78 mV across both concentrations and all scan rates, this is similar behaviour to 85G (110). Measured i_p values for the 0.1 mM concentration were close to theoretical values whereas with 1 mM concentration, the experimental i_p was slightly higher with faster scan rates.

At both concentrations 34-0X behaves very close to reversible (ΔE_p 62-69 mV) for all scan rates employed, with measured i_p values close to theoretical values.

To further investigate the electrochemical response of scBDD, another well known outer sphere redox mediator was utilised, $IrCl_6^{2-/3-}$ at two differing concentrations; 0.1 mM and 1 mM. CVs and corresponding data table for the three (100) scBDD samples, using a range of scan rates (20-1000 mV s^{-1}) and varying concentrations of $IrCl_6^{2-}$, are shown in Figure 6.7 and Table 6.6.

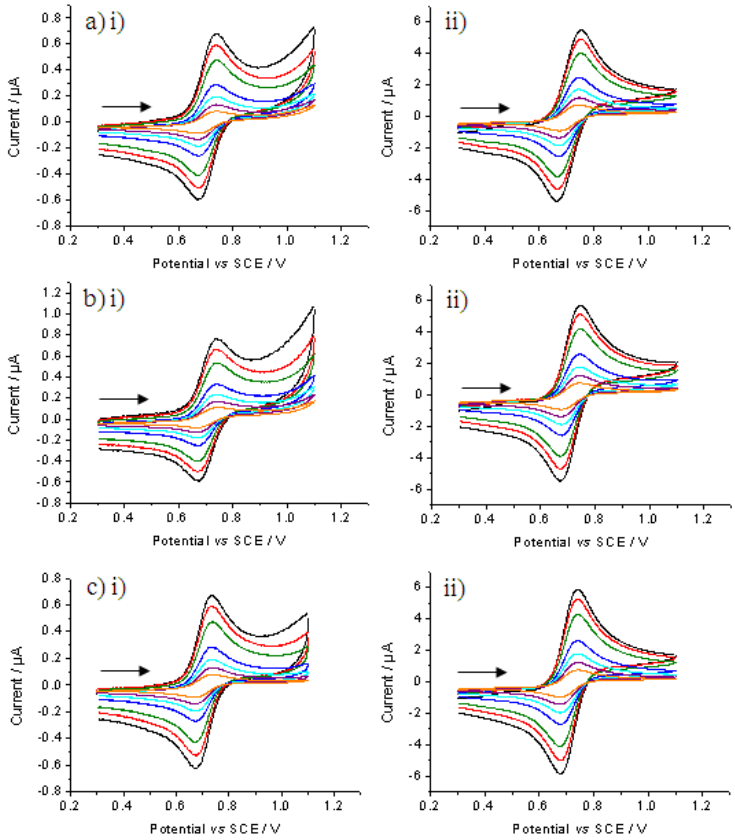

Figure 6.7. CV recorded at a range of scan rates showing the oxidation of i) 0.1 mM $IrCl_6^{2-}$ in 0.1 M $KNO_3$and ii) 1 mM $IrCl_6^{2-}$ in 0.1 M KNO_3 for 1 mm macrodisc a) 20-01, b) 23-01 and c) 34-0X. The following colour coding applies; ***20 mV s^{-1}****,* ***50 mV s^{-1}****,* ***100 mV s^{-1}****,* ***200 mV s^{-1}****,* ***500 mV s^{-1}****,* ***750 mV s^{-1}****and* ***1000 mV s^{-1}****.*

Table 6.6. Theoretical oxidation peak currents using a range of scan rates and varying concentrations of $IrCl_6^{2-}$ compared to experimental data including ΔE_p values for 1 mm macrodisc scBDD 20-01, 23-01 and 34-0X.

0.1 mM		20-01		23-01		34-0X	
Scan rate / mV s^{-1}	Theory i_p / µA	i_p / µA	ΔEp / mV	i_p / µA	ΔEp / mV	i_p / µA	ΔEp / mV
20	0.09	0.09	**68**	0.12	**68**	0.10	**67**
50	0.14	0.14	**70**	0.17	**70**	0.15	**66**
100	0.19	0.20	**64**	0.23	**64**	0.21	**62**
200	0.27	0.28	**63**	0.31	**63**	0.29	**63**
500	0.43	0.44	**72**	0.48	**72**	0.46	**64**
750	0.52	0.54	**65**	0.59	**65**	0.57	**60**
1000	0.60	0.61	**73**	0.67	**73**	0.63	**60**
1 mM		**20-01**		**23-01**		**34-0X**	
Scan rate / mV s^{-1}	Theory i_p / µA	i_p / µA	ΔEp / mV	i_p / µA	ΔEp / mV	i_p / µA	ΔEp / mV
20	0.85	1.01	**71**	1.03	**68**	1.04	**65**
50	1.35	1.52	**73**	1.55	**70**	1.57	**67**
100	1.91	2.09	**64**	2.14	**67**	2.17	**62**
200	2.67	2.46	**73**	2.96	**67**	3.00	**61**
500	4.27	4.00	**85**	4.52	**73**	4.63	**66**
750	5.23	4.93	**87**	5.44	**71**	5.60	**62**
1000	6.04	5.48	**88**	6.13	**76**	6.39	**62**

At the higher concentration, 20-01 gave a slightly wider range of ΔE_p (64-88 mV) compared to the lower concentration (ΔE_p 63-73 mV),the i_p values were very close to theoretical values for the full concentration range.

When employing the higher concentration with 23-01, a similar range of ΔE_p (67-76 mV) was observed, this was similar to pBDD. At the lower concentration a marginally wider reversibility range was recorded (ΔE_p 66-79 mV), more like the (111) electrode for the same redox mediator. At both concentrations, i_p values were near to theoretical values.

Across both concentrations when employing 34-0X, the ΔE_p shows an increasingly reversible range (60-67 mV), improved on all electrodes tested herein. Experimental i_p values are very close to theoretical values.

In order to challenge the electrochemical behaviour a reduction redox reaction, in the negative potential region, was investigated, namely $Ru(NH_3)_6^{3+}$.

CVs and corresponding data table for the three (100) scBDD samples, using a range of scan rates (10-1000 mV s^{-1}) and varying concentrations of $Ru(NH_3)_6^{3+}$,are shown in Figure6.8 and Table 6.7.

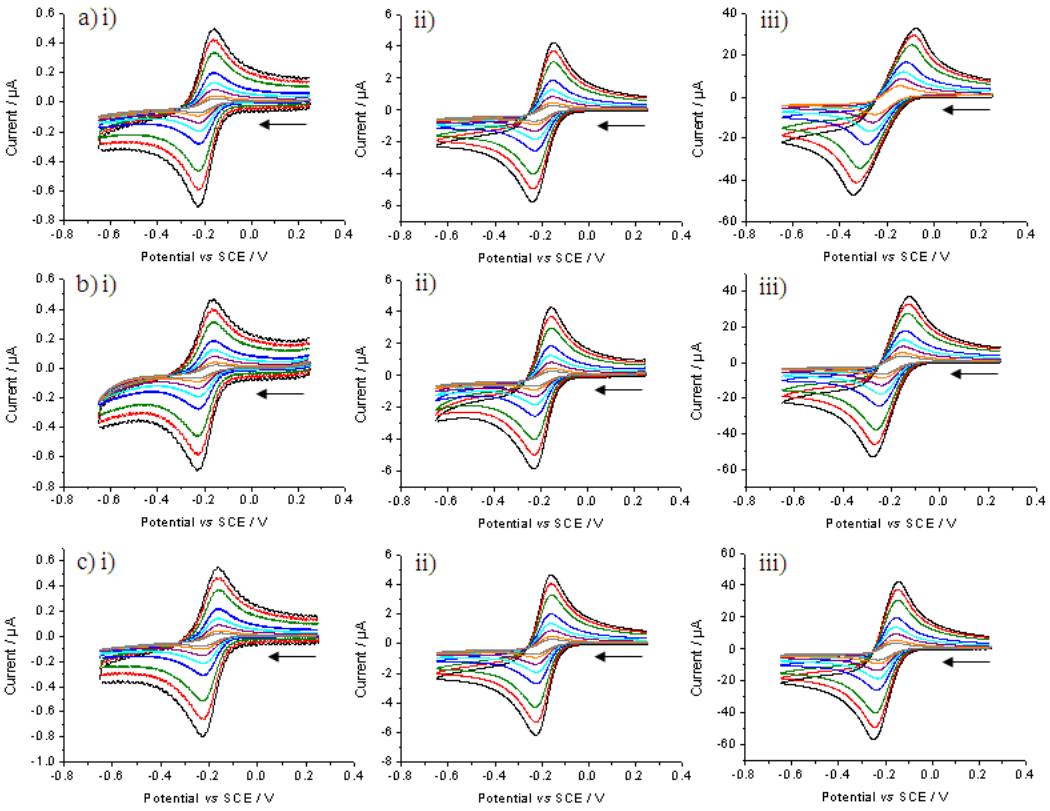

Figure 6.8. CV recorded using a range of scan rates showing the reduction of i) 0.1 mM $Ru(NH_3)_6^{3+}$ in 0.1 M KNO_3, ii) 1 mM $Ru(NH_3)_6^{3-}$ in 0.1 M KNO_3 and iii) 10 mM $Ru(NH_3)_6^{3-}$ in 0.1 M $KNO_3$for 1 mm macrodisc; a) 20-01, b) 23-01 and c) 34-0X. The following colour key for scan rates applies; 10 mV s^{-1},20 mV s^{-1}, 50 mV s^{-1}, 100 mV s^{-1}, 200 mV s^{-1}, 500 mV s^{-1}, 750 mV s^{-1} and 1000 mV s^{-1}.

Table 6.7. Theoretical reduction peak currents using a range of scan rates and varying concentrations of $Ru(NH_3)_6^{3+}$ compared to experimental data including ΔE_p values for 1 mm macrodisc scBDD 20-01, 23-01 and 34-0X.

0.1 mM		**20-01**		**23-01**		**34-0X**	
Scan rate / mV s^{-1}	**Theory i_p / µA**	**i_p / µA**	**ΔEp / mV**	**i_p / µA**	**ΔEp / mV**	**i_p / µA**	**ΔEp / mV**
10	-0.06	-0.07	**80**	-0.06	**83**	-0.08	**76**
20	-0.09	-0.09	**74**	-0.08	77	-0.10	**73**
50	-0.14	-0.14	**72**	-0.13	**72**	-0.15	**71**
100	-0.20	-0.19	**70**	-0.18	**65**	-0.21	**65**
200	-0.28	-0.28	**66**	-0.26	**66**	-0.30	**62**
500	-0.43	-0.44	**68**	-0.42	**67**	-0.49	**66**
750	-0.54	-0.55	**61**	-0.53	**68**	-0.62	**59**
1000	-0.63	-0.63	**69**	-0.61	**72**	-0.72	**63**
1 mM		**20-01**		**23-01**		**34-0X**	
Scan rate / mV s^{-1}	**Theory i_p / µA**	**i_p / µA**	**ΔEp / mV**	**i_p / µA**	**ΔEp / mV**	**i_p / µA**	**ΔEp / mV**
10	-0.63	-0.69	**80**	-0.66	**78**	-0.71	**76**
20	-0.88	-0.89	**74**	-0.87	**71**	-0.93	**71**
50	-1.40	-1.33	**76**	-1.30	**72**	-1.40	**69**
100	-1.98	-1.84	**77**	-1.80	**65**	-1.95	**65**
200	-2.80	-2.57	**77**	-2.53	**68**	-2.73	**64**
500	-4.43	-4.00	**88**	-3.96	**72**	-4.30	**69**
750	-5.40	-4.89	**86**	-4.89	**71**	-5.27	**66**
1000	-6.21	-5.60	**90**	-5.71	**74**	-6.12	**65**
10 mM		**20-01**		**23-01**		**34-0X**	
Scan rate / mV s^{-1}	**Theory i_p / µA**	**i_p / µA**	**ΔEp / mV**	**i_p / µA**	**ΔEp / mV**	**i_p / µA**	**ΔEp / mV**
10	-6.26	-6.47	**97**	-6.49	**83**	-6.80	**74**
20	-8.83	-8.49	**107**	-8.66	**86**	-9.08	**74**
50	-14.0	-12.48	**127**	-13.02	**94**	-13.66	**77**
100	-19.8	-16.78	**143**	-17.96	**94**	-18.87	**76**
200	-28.0	-22.21	**172**	-24.66	**106**	-26.15	**87**
500	-44.3	-29.71	**221**	-37.38	**131**	-40.28	**96**
750	-54.2	-30.91	**244**	-44.83	**142**	-48.78	**99**
1000	-62.6	-31.60	**268**	-50.84	**152**	-55.60	**105**

At both 1 and 0.1 mM concentrations, the 34-0X electrode displays ΔE_p closest to reversible (62-76 mV) compared to ΔE_p ranges of 61-90mV for 20-01 and 65-83 mV for 23-01.

For all samples to pass the current in the 10 mM solution is challenging the availability of charge carries available at the surface of the electrode. This is most severe in the case of 20-01 (ΔE_p97-268 mV), but significantly less for 34-0X where ΔE_p was 74-105 mV.

6.2.4 Macro Electrochemistry of Complex Redox Mediators

Results in section 3.2.4 suggest that BDD reversibly oxidises and reduces the Ru $^{2+/3+}$ ion and this was also observed for these three substrates as shown in Figure 6.9. The ΔE_p range for each sample over the scan rate range 20-1000 mV s^{-1} was as follows; 20-01 (68-77 mV), 23-01 (63-71 mV) and 34-0X (62-67 mV), once again demonstrating ET are fastest on the 34-0X sample. i_p values for all scan rates were close to theoretical values.

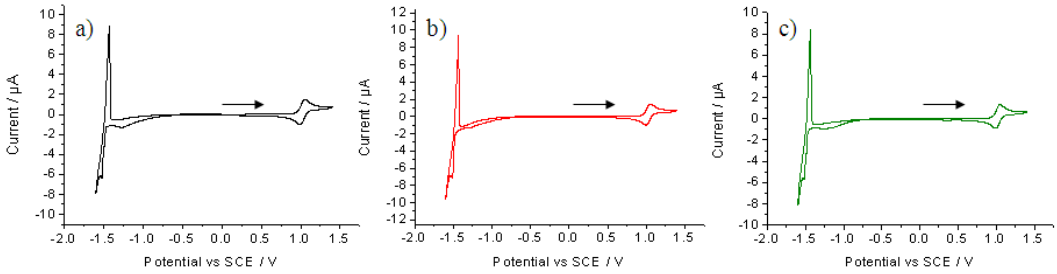

Figure 6.9. CVs in aerated 1 mM $Ru(bpy)_3^{2+/3+}$ with 0.1 M KNO_3 showing multiple oxidation and reduction reactions using a) 20-01, b) 23-01 and c) 34-0X. Scan rate of 100 mV s^{-1}.

6.2.5 Single Crystal Boron Doped Diamond Electrode Pre-treatment and its Effects

Important information on electrode surface chemistry can be gained by analysing the electrochemistry of inner sphere redox mediators. Previous analysis

using a 1 mm macrodisc electrode 85B (100) (section 3.2.5) has demonstrated differing pre-treatments can effect ET kinetics.

For these studies, only sample 34-0X was employed, as it showed the best ET characteristics with outer sphere redox couples. CVs for the oxidation/reduction of $Fe(CN_6)^{3-/4-}$ and $Fe^{2+/3+}$ with 34-0X and selected pre-treatments are shown in Figure 6.10 with the corresponding data table in Table 6.8 (also showing 85B (100) for comparison). *D* and *E°´* values are detailed in section 3.2.5.

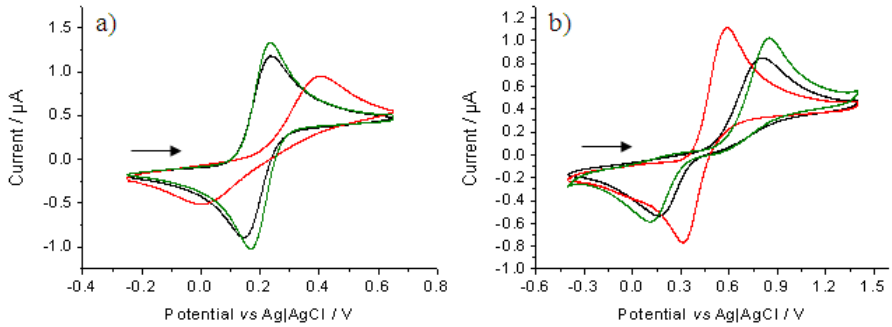

Figure 6.10. CVs showing the response of selected pre-treatments on 34-0X for a)1 mM $Fe(CN_6)^{3-/4-}$ in 0.1 M KNO_3 and b) 1 mM $Fe^{2+/3+}$ in 0.1 M H_2SO_4. In all cases colours are represented as ***alumina polish****,* ***anodic polarisation*** *(****+3 V for 60 s****) and* ***cathodic polarisation*** *(****-3 V for 60 s****). Scan rate of 100 mV s^{-1}.*

*Table 6.8. Extracted i_p and ΔE_p values from the CVs of Figure 6.10 resulting from three different sample pre-treatments (****alumina polish****,* ***anodic polarisation*** *(****+3 V for 60 s****) and* ***cathodic polarisation*** *(****-3 V for 60 s****).*

Sample	Pre-Treatment	1 mM $Fe(CN)_6^{3-}$		1 mM Fe^{2+}	
		i_p / µA	ΔE_p / mV	i_p / µA	ΔE_p / mV
85B (100)	Alumina Polish	1.27	127	1.03	681
	+3 V, 60 sec	1.07	378	1.29	310
	-3 V, 60 sec	1.45	90	1.11	671
34-0X (100)	Alumina Polish	1.18	90	0.85	639
	+3 V, 60 sec	0.95	399	1.14	272
	-3 V, 60 sec	1.36	61	1.01	741

The results for 85B (100) have been discussed previously in section 3.2.5, and 34-0X (100) results also show the same trend. Whereby anodic polarisation significantly increases the rate of ET for Fe^{2+} reducing ΔE_p to 272 mV from 639 mV when alumina polished and cathodic polarisation facilitates near reversible ET for $Fe(CN_6)^{3-/4-}$ (ΔE_p 61 mV).

6.2.6 Finite Element Modelling (FEM) Results

FEM simulations are fully described in section 3.2.6 with explanatory figures and model boundaries shown in Figure 3.34 and Table 3.11, no changes were implemented for these additional samples. Simulated k^0 responses for a range of oxidation and reduction reactions used herein are shown in Table 6.9, for comparative purposes results are also quoted for 85B (100). The model is accurate to 1 mV as is the interpretation of CVs.

Table 6.9. FEM simulation data of k^0 values for selected oxidation and reduction reactions using experimental ΔE_p values.

	Oxidation, k^0/ cm s^{-1}						**Reduction, k^0 / cm s^{-1}**		
Redox Mediator	**$FcTMA^+$**		**$IrCl_6^{2-}$**		**$Ru(bpy)^{2+}$**		**$Ru(NH_3)_6^{3+}$**		
Concentration / mM	**0.1**	**1**	**0.1**	**1**	**0.1**	**1**	**0.1**	**1**	**10**
85B (100)	0.09	0.08	0.16	0.16	0.19	0.19	0.05	0.05	0.012
20-01(100)	0.05	0.03	0.08	0.07	0.03	0.05	0.02	0.03	0.002
23-01 (100)	0.02	0.04	0.05	0.08	0.05	0.05	0.08	0.08	0.007
34-0X (100)	0.10	0.09	0.16	0.16	0.19	0.19	0.08	0.09	0.018

For the outer sphere oxidation reactions at scBDD 20-01 and 23-01 the k^0values are within a small range of each other 0.02-0.08 cm s^{-1}. For 34-0X the range is higher 0.09-0.39 cm s^{-1} and reflects both the higher [B] and the nearer to reversibility of the CVs recorded.

For all BDD electrodes the ET kinetics of 10 mM $Ru(NH_3)_6^{3+}$ are considerably slower with 20-01 and 23-01 being the slowest in Table 6.9, this is reflective most likely of the fact at this concentration the highest currents need to be passed which challenges charge carrier availability.

6.2.7 Electrochemical Characterisation Conclusions

The electrochemical analysis described in this chapter suggest that the bulk sample 34-0X heavily doped with [B] 1.2×10^{21} cm^{-3} is behaving as an ideal electrode material for outer sphere one electron reactions. Inner sphere reactions where surface termination is key can be enhanced due to electrode pre-treatment, offering reversible ET kinetics.

FEM demonstrates the 34-0X sample offers similar k^0 values for all oxidation redox mediators tested herein to 85B of a similar [B]. Comparing the reduction redox mediator $Ru(NH_3)_6^{3+}$, all samples had similar ET kinetics with the exception of the higher 10 mM concentration.

In order to make direct comparisons to the only other scBDD sample with similar [B] (85A/B), 34-0X was subject to Au NP deposition and IC-SECM. Due to the nature of the capped 85B macro delaminating over time, capped scBDD 20-01 and 23-01 were not subject to Au NP deposition or IC-SECM. The impressive results of 34-0X suggest capped layer samples may be obsolete.

6.3 GOLD NANOPARTICLE DEPOSITION USING SINGLE CRYSTAL BORON DOPED DIAMOND 34-0X (100)

6.3.1 Gold Nanoparticle Deposition Utilising Bulk (100) Single Crystal Boron Doped Diamond with AFM and FE-SEM

Initial Au NP deposition on the bulk (100) scBDD sample (34-0X) was performed using the MECM technique (described in section 2.4.8), and the substrate analysed post deposition using FE-SEM primarily and for more detailed information TM-AFM.

Figure 6.11a shows the initial CV (60 × 46 µm capillary) from which a range of V_{dep} were selected for further investigation, this CV is typical of many performed across the sample. Figure 6.11b shows a TM-AFM image of the Au NPs deposited during the CV which was analysed using image analysis software (SPIP™) to provide Au NP heights and distribution (n=3), as shown in Figure 6.11c, with a magnification of the larger Au NP heights.

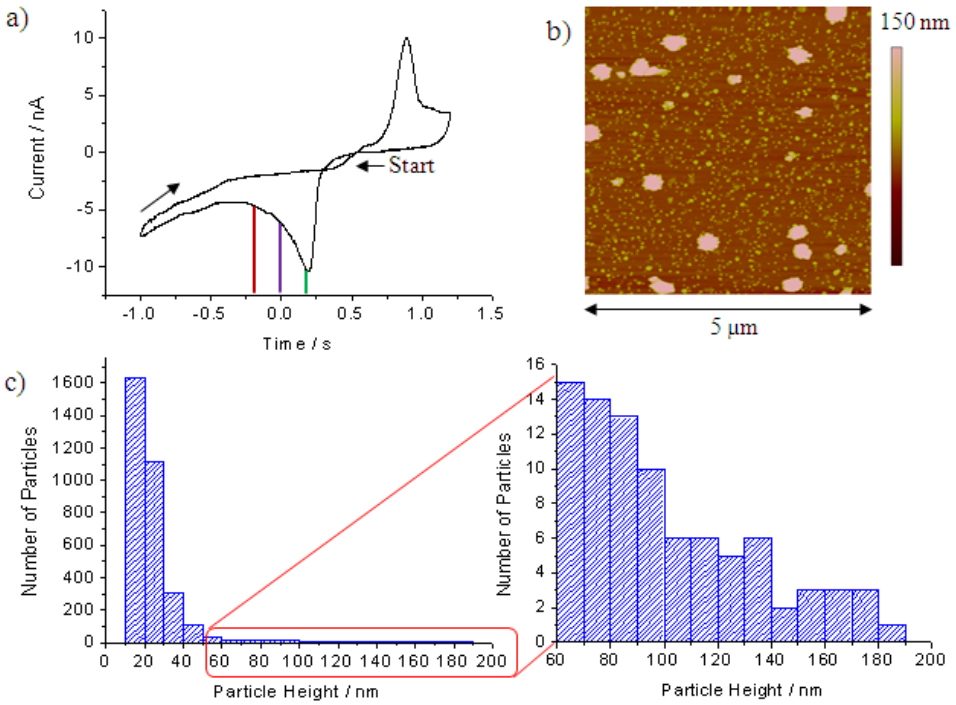

Figure 6.11. a) CV vs. quasi Ag|AgCl for the electrodeposition of Au NPs onto 34-0X using 60 × 46 µm capillary filled with 1 mM $KAuCl_4$ in 0.1 M $NaClO_4$, scan rate 100 mV s^{-1}. b) 5 × 5 µm TM-AFM image of electrodeposited Au NPs after a CV sweep for a) and c) NP size analysed histograms of a CV sweep (n=3).

The NP distribution was determined at 43.88 ± 5.0 µm-2 with an average NP height measured at 24.3 ± 17.6 nm (n=3). FE-SEM images were also recorded and as shown in Figure 6.12, a range of particles sizes are clearly visible, as in the TM-AFM image (Figure 6.11b).

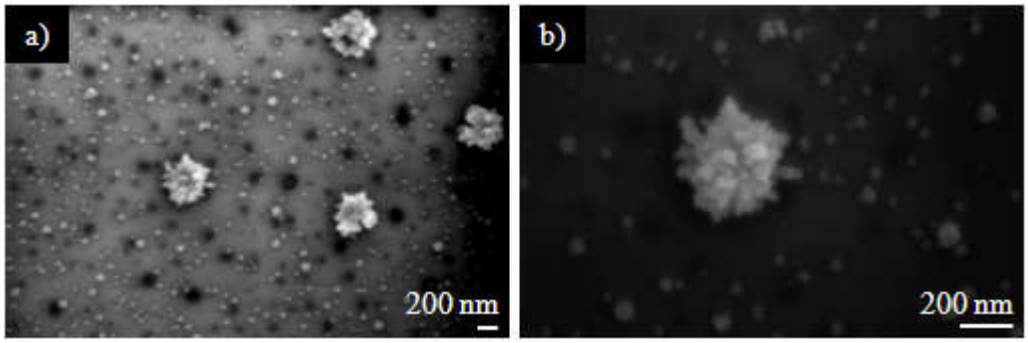

Figure 6.12. In-Lens FE-SEM images of a CV sweep electrodepositing Au NPs onto the surface of 34-0X showing a range of NP sizes.

i-t transients were performed using the V_{dep} selected from Figure 6.11a combined with a range of t_{dep} (0.5, 2 and 10 s) and these are plotted in Figure 6.13a. Figure 6.13a-c (ii) shows the data from a-c (i) plotted against the SH model.

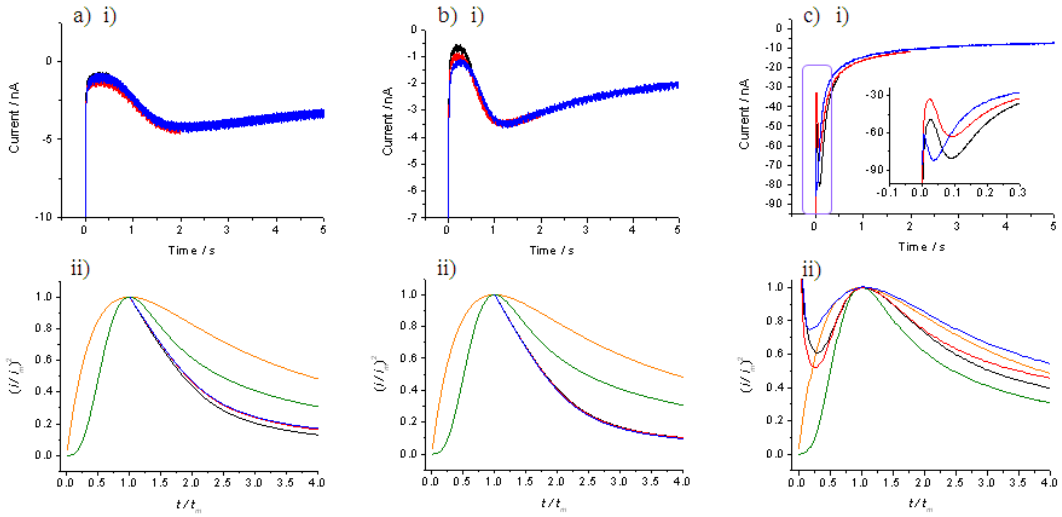

*Figure 6.13. A 60 × 46 µm capillary filled with 1 mM $KAuCl_4$ in 0.1 M $NaClO_4$ vs.quasi Ag|AgCl was employed for i-t transients at V_{dep} a) 0.2 V, b) 0 V and c) -0.2 V. For a)-c)i) i-t transients plotted when t_{dep}= 0.5 s (**black**), 2 s (**red**) and 10 s (**blue**). a)-c) ii)Dimensionless plots of the data from a) plotted with theoretical curves of instantaneous nucleation (**orange**) and progressive nucleation (**green**) as originally described by the SH model, where the t_{dep} 0.5 s (**black**), 2 s (**red**) and 10 s (**blue**).*

Figure 6.13a and b show the *i-t* transients V_{dep} = 0.2 V and 0 V which overlay for all t_{dep} suggesting homogeneous nucleation characteristics in the different areas examined. Comparison to the model shows no fit for both 0.2 and 0 V_{dep} for either progressive or instantaneous nucleation; although the data lies closest to the progressive nucleation theory line.

Where V_{dep} = -0.2 V some differences in nucleation behaviour at the differing t_{dep} are observed. When plotted against the SH model, the assigned nucleation

theorem is inconclusive, falling somewhere between progressive and instantaneous nucleation. When t_{dep} = 10 s the data appears to fit most closely to the instantaneous nucleation theorem. Figure 6.13 is representative of several experiments performed on differing 34-0X samples.

Therefore FE-SEM was also performed on the deposition spots, in order to provide more information on the nucleation behaviour. FE-SEM can provide accurate data on particle number and qualitative information on particle width (charging can result in an overestimation of particle size). NP analysis (n=3) determined NP width and number distributions for the data from FE-SEM images, this is shown in Table 6.10 and table 6.14.

*Table 6.10. MCEM NP analysis (n=3) for the FE-SEM images from Figure 6.14 showing the NP distribution µm^{-2} (**black text**) and widths (**purple text**) at differing V_{deps} using 34-0X.*

Potential / V	Deposition Time / s		
	0.5	2	10
0.2	**0.3 ± 0.0** **157.1 ± 12.3**	**0.5 ± 0.0** **193.1 ± 5.7**	**1.2 ± 0.2** **198.9 ± 8.4**
0.0	**0.7 ± 0.2** **129.0 ± 19.4**	**1.0 ± 0.5** **180.4 ± 12.7**	**1.2 ± 0.2** **204.3 ± 7.8**
-0.2	**1.5 ± 0.1** **121.4 ± 7.8**	**1.6 ± 0.1** **132.2 ± 4.5**	**1.6 ± 0.1** **216.0 ± 9.7**

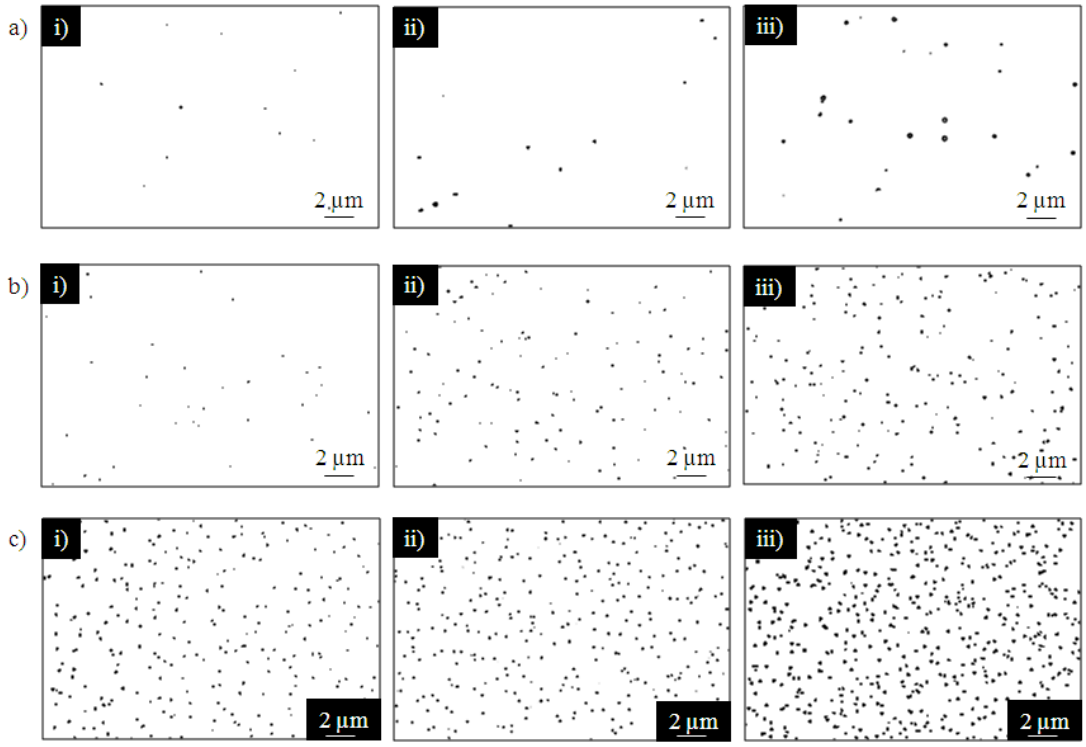

Figure 6.14. Inverted FE-SEM image from the centre of the MECM V_{dep}= a) 0.2 V, b) 0 V and c) -0.2 V. In all cases t_{dep} = i) 0.5 s, ii) 2 s and iii) 10 s.

When taking into consideration the standard deviation of the NP distribution and width data from Table 6.10 combined with Figure 6.14, the results suggest that instantaneous nucleation appears to be more dominant than progressive nucleation for all V_{deps}. Instantaneous nucleation is not unexpected for a homogeneously doped scBDD substrate.

Figure 6.15 plots and compares CVs performed using similar sized capillaries for the electrodeposition and stripping of Au at different scBDD electrodes. Differences between the capped (100) sample and the heterogeneous (110) sample have already been discussed in section 5.3.2.

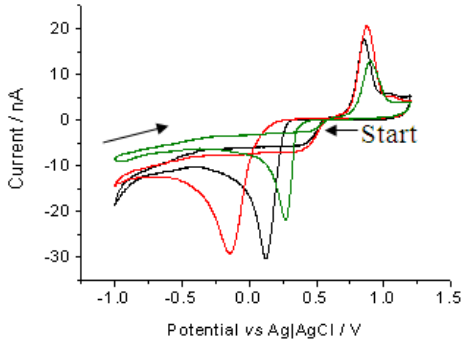

*Figure 6.15. Plot showing CVs vs. quasi Ag|AgCl, performed using the MCEM technique with 1 mM $KAuCl_4$ in 0.1 M $NaClO_4$ using scan rate 100 mV s^{-1}. The **black** plot employed 50 × 60 µm capillary and capped (100) 85A, the **red** plot employed 50 × 60 µm capillary with the bulk (110) 85F and the **green** plot employed 46 × 60 µm capillary with the bulk (100) 34-0X.*

Figure 6.15 shows the onset of Au nucleation differs for each sample, with 34-0X reducing Au from the solution onto its surface at the most positive potential. 34-0X has marginally higher [B] than 85A where Au nucleation occurs ~0.2 V, and finally the heterogeneous 85G onset occurs ~-0.2 V despite similar sized capillaries being employed.

Despite the differences in the onset of electrodeposition of Au NPs, the gold oxide stripping peak occurs around the same potential for the capped (100) and bulk (110) sample. However the bulk 34-0X (100) sample shows a slightly more positive stripping peak. Both (100) samples have similar [B], therefore differences in Au nucleation onset and slight shift in stripping peak potential is unlikely to be caused by any differences in [B] and may instead reflect the morphology of the particles on the two different surfaces. Capped 85A was provided as grown and bulk 34-0X was scaife polished (Figure 3.9c and Figure 6.3c), the RMS values reported in Table 6.2 indicate the polished 34-0X sample is marginally smoother which may in turn affect Au NP deposition.

The substrates employed in these experiments proved challenging to image in the AFM as it was often difficult to locate the exact area where Au NP deposition had occurred with MCEM. To improve the ease of AFM analysis, electrochemical deposition experiments were carried out on a 34-0X 1 mm macrodisc electrode, subsequently placed into an inverted AFM for topographical analysis.

6.3.2 Gold Nanoparticle Deposition onto a 1 mm (100) Single Crystal Boron Doped Diamond Macrodisc Electrode

In order to facilitate AFM imaging, a 1 mm macrodisc electrode was formatted as described in (section 2.2.4). The macro electrode was prepared prior to each deposition as previously described (section 2.4.2).Figure 6.16 shows a CV for the electrodeposition and stripping of Au NPs onto a 1 mm macrodisc electrode. The reduction of water clearly overshadows the plot after -0.75 V *vs.* Ag|AgCl, and the AuO stripping peak is observed ca. ~0.9 V, similar to CVs from the MCEM technique. From this initial CV, V_{dep} were selected (0.2, 0.1, 0 and -0.2 V) as indicated.

The Au deposition peak current is recorded at ~0.2 V for both the 1 mm macrodisc electrode and the MECM (Figure 6.11). The differences in current magnitude are directly related to the electrode surface area exposed to the Au solution *i.e*. MECM utilising tens of µm surface area and the macrodisc electrode is 1 mm in diameter.

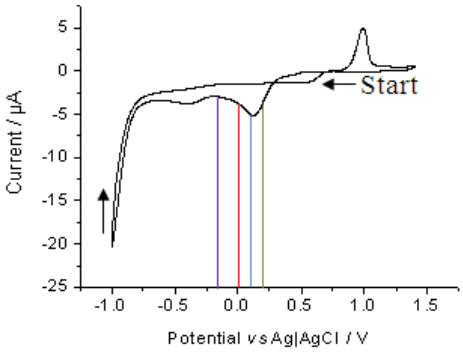

Figure 6.16. Typical CV vs. quasi Ag|AgCl, for the electrodeposition of Au NPs onto a bulk 34-0X 1 mm macrodisc electrode dipped into 1 mM $KAuCl_4$ in 0.1 M $NaClO_4$. Scan rate 100 mV s^{-1}.

i-t transients were undertaken using a range of t_{dep} (0.5, 2, 10 and 30 s). A limitation of using a macrodisc electrode format is the significantly larger capacitative/background currents which flow during chronoamperometric measurements, compared to the MCEM set-up, which makes *i-t* quantitative analysis difficult, examples are shown in Figure 6.17. Instead the AFM images resulting from these depositions were analysed in detail.

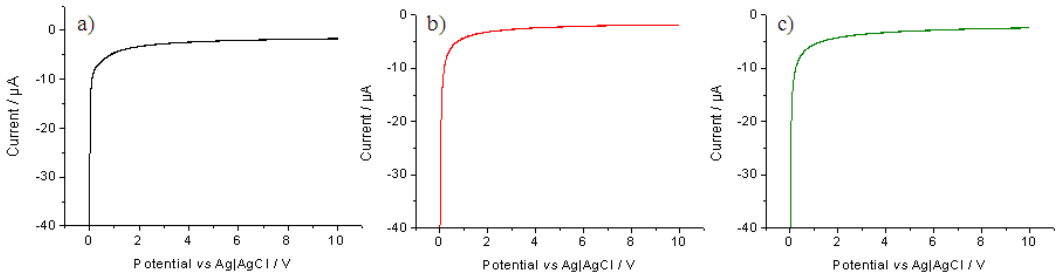

Figure 6.17. i-t transients recorded during t_{dep} = 10 s using 34-0X 1 mm macrodisc electrode with 1 mM $KAuCl_4$ in 0.1 M $NaClO_4$. V_{dep}= a) 0.2 V, b) 0 V and c) -0.2 V.

AFM images in several areas across the sample were taken in various scan sizes (min 2 × 2 µm, max 5 × 5 µm). NP height and distribution data from the TM-AFM histograms shown in Figure 6.18 are detailed in Table 6.11.

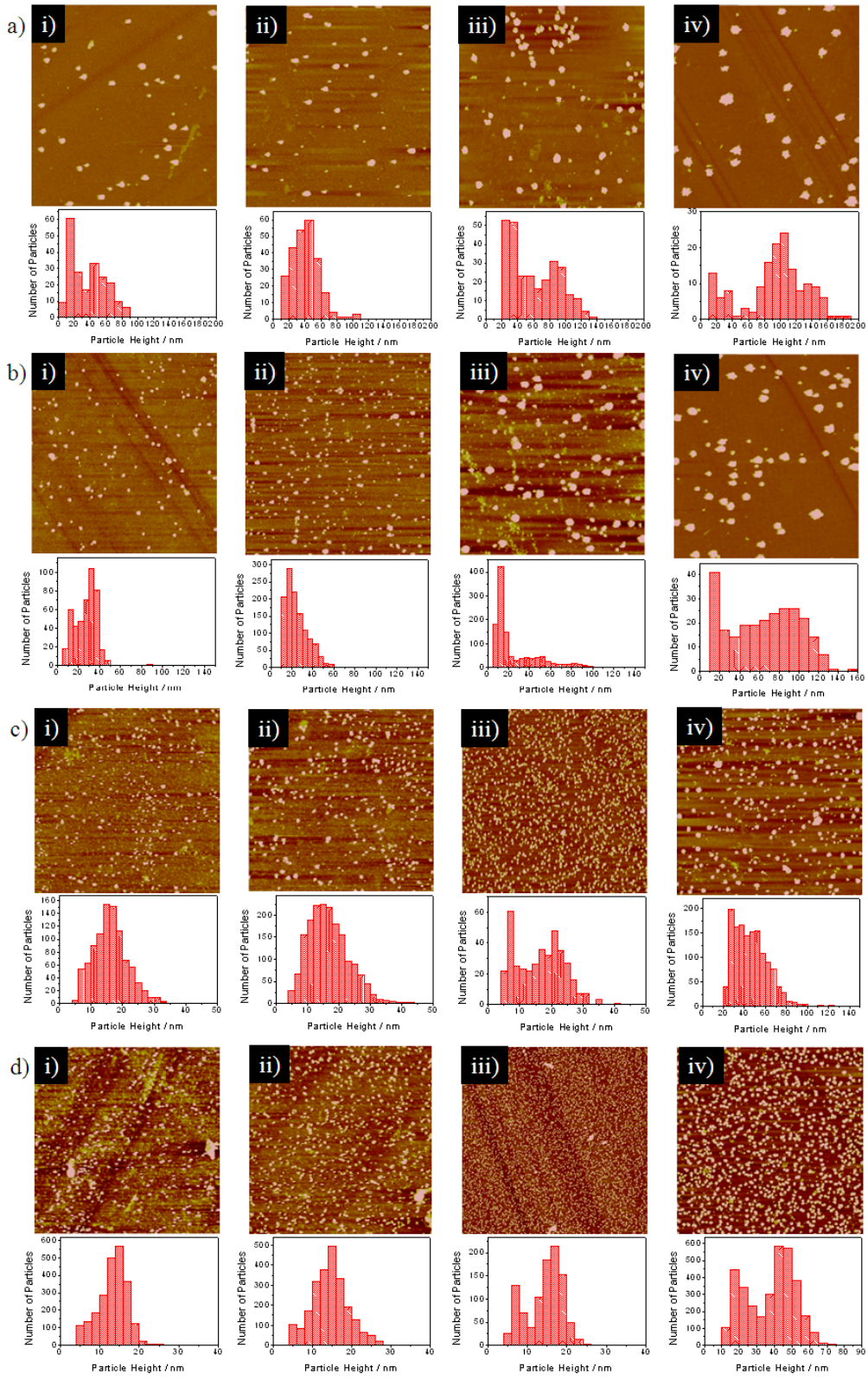

Figure 6.18. Representative TM-AFM images recorded for Au NP deposition from a 1 mM $KAuCl_4$ in 0.1 M $NaClO_4$ onto a 34-0X 1 mm macrodisc electrode at V_{dep} a) 0.2 V, b) 0.1 V, c) 0 V and d) -0.2 V for t_{dep} i) 0.5 s, ii) 2 s, iii) 10 s and iv) 30 s. Respective histograms of NP height distribution (n=3) are shown below each image.

*Table 6.11. NP analysis (n=3) for the TM-AFM images from Figure 6.18 showing the NP distribution µm^{-2} (**black text**) and heights (**purple text**) at differing potentials using a 34-0X 1 mm macrodisc electrode.*

Potential / V	Deposition Time / s			
	0.5	2	10	30
0.2	2.8 ± 0.45 36.7 ± 21.5	3.27 ± 0.5 27.2 ± 10.0	3.68 ± 0.5 16.2 ± 5.4	2.04 ± 0.6 13.2 ± 3.6
0.1	5.93 ± 0.3 40.7 ± 16.5	11.95 ± 1.7 24.8 ± 10.3	15.4 ± 1.0 16.7 ± 6.3	3.36 ± 0.4 14.5 ± 4.6
0.0	26.11 ± 9.5 60.3 ± 29.3	49.5 ± 11.7 24.7 ± 20.9	130.3 ± 7.0 16.3 ± 7.1	18.7 ± 4.1 14.4 ± 4.6
-0.2	9.5 ± 6.7 92.8 ± 40.6	146.5 ± 57 64.4 ± 34.6	329.3 ± 28 46.5 ± 16.2	45.0 ± 8.2 37.7 ± 13.7

Referring to Table 6.11, and as shown in Figure 6.19 and Figure 6.20 at all V_{dep} investigated as the t_{dep} increases the NP distribution (per µm) increases in number over the t_{dep} time period 0.5-10 s. When t_{dep}=30 s one explanation for the possible reduction in NP density is the occurrence of Ostwald ripening (described in section 5.3.2 with Figure 6.16). Although this is more traditionally observed at longer timescales, there is evidence that it can occur on timescales of the order employed herein.[13-15] It is also important to note that the AFM measurements are made ex-situ and although every attempt was made to carefully dry the sample after deposition to avoid NP disruption we cannot be sure that the sample in the ex-situ state is exactly the same as that in-situ. Therefore, future studies would look to the use of in-situ AFM measurements with the substrate held under potential control.

For all V_{dep} as t_{dep} increases the heights of the NPs decreases. The AFM data strongly suggests a nucleation mechanism which is progressive in nature not instantaneous.

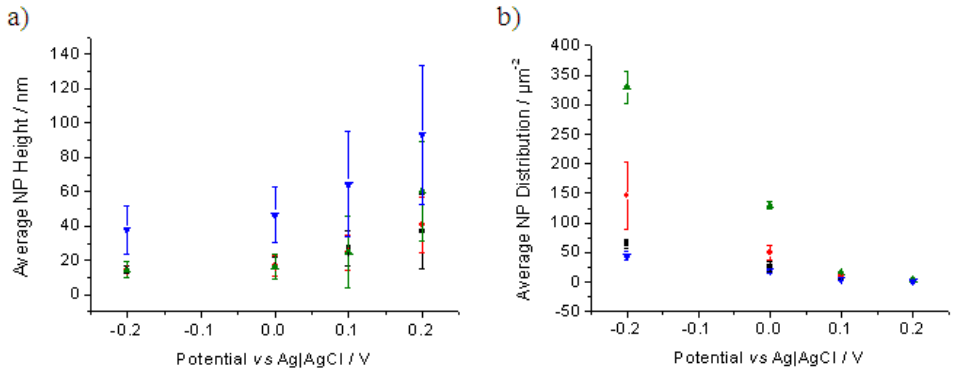

Figure 6.19. a) Average NP heights with Y error bars as s.d showing a decrease in NP size as the V_{dep} applied is increasingly negative. b) Average NP distribution with Y error bars as s.d, all t_{dep} showing similar trends of increasing distribution as the potential applied increasingly drives the deposition reaction. In both cases experimental t_{dep} represented as 0.5 s (■), 2 s (●), 10 s (▲) and 30 s (▼).

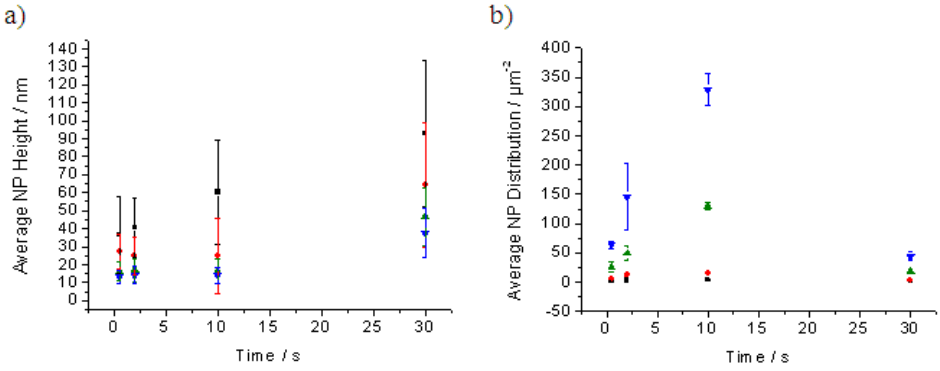

Figure 6.20. a) Average NP heights with Y error bars as s.d showing an increase in NP size as t_{dep}. b) Average NP distribution with Y error bars as s.d, all time frames showing similar trends of increasing distribution until 30 s when Ostwald ripening takes effect. In both cases experimental V_{dep} represented as 0.2 V (■), 0.1 V (●), 0 V (▲) and -0.2 V (▼).

The trends discussed relating to progressive growth at increasingly negative driving potentials can be further illustrated by plotting distribution and height

simultaneously as shown in Figure 6.21. This is an example, all showed similar trends for the range of V_{dep} and t_{dep}.

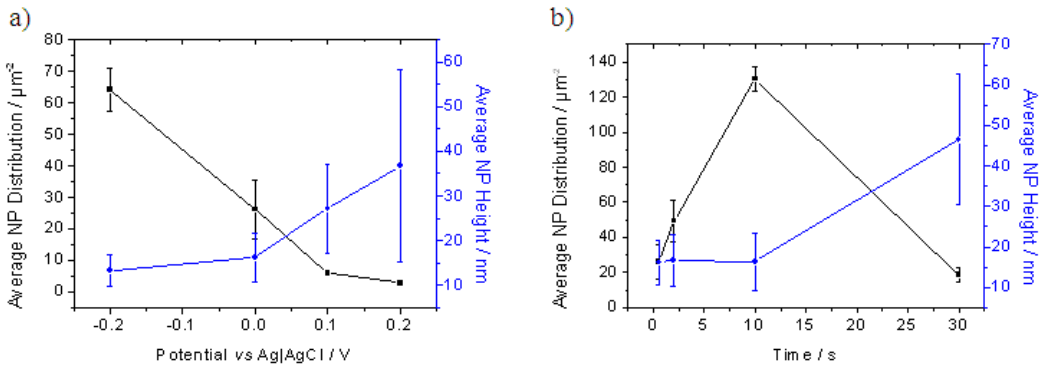

Figure 6.21. Double Y plot of average NP distribution and heights of deposition t_{dep} = a) 0.5 s and b) V_{dep} = 0 V.

6.3.3 Gold Nanoparticle Electrodeposition Conclusions

Bulk (100) scBDD has been electrodeposited with Au NPs at two differing mass transport and length scales, using the MCEM technique to create tens of micron sized domains and a 1 mm macrodisc electrode in stationary solution. The *i-t* transients resulting from the MCEM method for a range V_{dep} of did not fit either progressive or instantaneous nucleation when plotted using the SH model; only at V_{dep} = -0.2 V did the model suggest instantaneous nucleation. In contrast instantaneous nucleation appeared to dominate when examining the resulting FE-SEM images of the nucleated surface in the area of the MCEM capillary.

TM-AFM data recorded in different areas of a much larger electrode, 1 mm macrodisc scBDD electrode, showed that Au NP deposition appeared to follow progressive nucleation. As V_{dep} was increased the NP density increased with increasing t_{dep} between 0.5-10 s. Ostwald ripening lead to clusters forming when

t_{dep} = 30 s thereby reducing the NP density. The height of the NPs decreased as t_{dep} increases for all V_{dep} applied.

Interestingly, microscopic analysis of the two different electrode areas micro *vs*. macro appeared to indicate two different nucleation pathways. In the smaller areas, probed by MCEM, nucleation appeared more instantaneous whilst for the larger area electrode nucleation was progressive in nature. The different observations could reflect the different mass transport characteristics of the two different arrangements, mass transport is significantly higher in the MCEM capillary.

6.4 IC-SECM IMAGING WITH SINGLE CRYSTAL BORON DOPED DIAMOND 34-0X (100)

As described in section 2.4.6, IC-SECM[16] was employed to image the surface of scBDD 34-0X.

6.4.1 Finite Element Modelling of IC-SECM Data

The FEM employed is described in section 4.1.3.

6.4.2 IC-SECM Current and k^0 Maps of Single Crystal Boron Doped Diamond using $FcTMA^+$

Corresponding SG-TC IC-SECM current and k^0 map of 34-0X are shown in Figure 6.22 using 1 mM $FcTMA^+$.

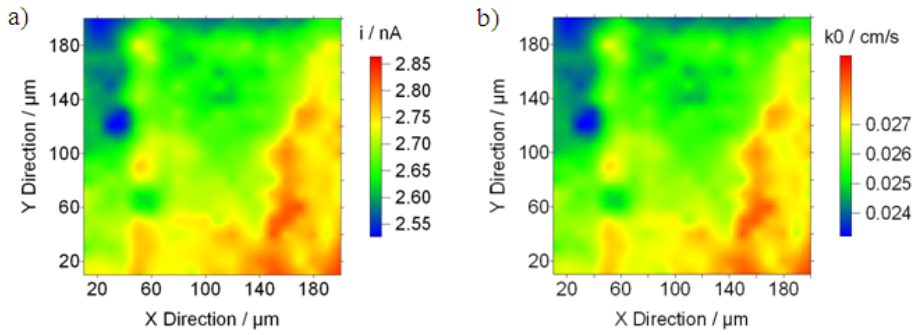

Figure 6.22. a) IC-SECM SG-TCimage of 34-0X for the collection of 1 mM $FcTMA^{2+}$ electrochemically generated at the surface when η = 0.028 V. Using10 µm Pt UME, RG=7, d=0.68 µm. b) Corresponding k^0 FEM map.

The current map of Figure 6.22 shows a minimal change in current for the area analysed (~0.3 nA). No features were recorded suggesting a homogeneous substrate. The corresponding k^0 map provides kinetic ET values of narrow range further supporting sample homogeneity. Furthermore the values of k^0 recorded for 34-0X were similar for a range of differing η investigated.

6.4.3 IC-SECM current and k^0 Maps of Single Crystal Boron Doped Diamond using $Ru(NH_3)_6^{3+}$

To further investigate and challenge ET kinetics of the scBDD electrodes, a redox mediator with a more negative standard potential was employed; $Ru(NH_3)_6^{3+}$with -0.25 V *vs.* SCE, thereby investigating ET kinetics at positive and negative redox potentials.

Corresponding SG-TC IC-SECM current and k^0 map of 34-0X are shown in Figure 6.23 using 1 mM $Ru(NH_3)_6^{3+}$.

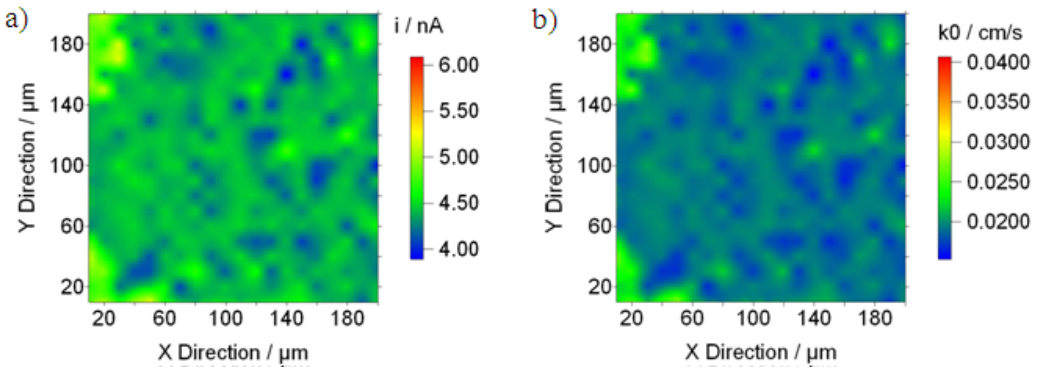

Figure 6.23. a) IC-SECM SG-TC image of 34-0Xfor the collection of 1 mM $Ru(NH_3)_6^{2+}$ electrochemically generated at the surface when η = -0.06 V. Using 10 µm Pt UME, RG=7, d=0.68 µm. b) Corresponding k^0 FEM map.

The current map of Figure 6.23 shows a small current range (~1 nA) for the area analysed. No features were recorded suggesting a homogeneous substrate. The corresponding k^0 map provides kinetic ET values of narrow range further supporting sample homogeneity.

Table 6.12 shows mean k^0 values (n=400) for $FcTMA^+$ and $Ru(NH_3)_6^{3+}$ compared to the IC-SECM data for capped 85A, which contains a similar [B].

Table 6.12. Comparison of current and k^0 values recorded using IC-SECM in SG-TC mode for heavily doped (100) scBDD using 1 mM $FcTMA^+$ in 0.1 M KNO_3 and 1 mM $Ru(NH_3)_6^{3+}$ in 0.1 M KNO_3.

Mediator	Sample	Mean k^0/ cm s^{-1}	η / V	Tip separation / µm
$FcTMA^+$	**85A**	0.041 ± 0.001	0.028	0.77
	34-0X	0.026 ± 0.001	0.020	0.68
$Ru(NH_3)_6^{3+}$	**85A**	0.019 ± 0.001	-0.054	0.77
	34-0X	0.019 ± 0.002	-0.060	0.68

Both heavily doped scBDD (100) samples show similar ET characteristics for outer sphere redox couples; $FcTMA^+$ and $Ru(NH_3)_6^{3+}$, the former showing slightly higher k^0 than the latter. This is likely to be as a result of ferrocenes higher

self-exchange constant.[17,18] The minimal standard deviation values over the duration of the scan adds further weight to the sample homogeneity.

Table 6.13 compares the k^0 values for $FcTMA^+$ and $Ru(NH_3)_6^{3+}$, determined for both CV and IC-SECM using FEM.

Table 6.13. Comparison of CV and IC-SECM k^0 values with selected 1 mM redox mediators.

Mediator	Technique	Mean k^0 / cm s^{-1}
$FcTMA^+$	**CV**	0.090
	IC-SECM	0.026
$Ru(NH_3)_6^{3+}$	**CV**	0.090
	IC-SECM	0.019

The determination of k^0 using two electrochemical analysis methods provides differing results which are not unexpected. CV employs a large electrode surface area therefore an average of ET behaviour is taken from the whole surface area during CV. Furthermore small changes in ΔE_p can have a large effect on k^0 because you are close to the reversible limit.

IC-SECM is able to measure much higher heterogeneous rate constants (k_t) therefore is able to more accurately determine k^0. However IC-SECM measurements take much longer than conventional CV such the possibility of electrode fouling arises. Both approaches allow for comparisons to be made between redox mediators employing the same experimental parameters.

6.5 CONCLUSIONS

Three (100) scBDD samples of differing [B] and surface finishes have been characterised by physical and electrochemical methods. SIMS provided [B] suggesting the two capped samples were of similar [B] (~6×10^{20} cm^{-3}) and the bulk sample was of the highest [B]; 1.2×10^{21} cm^{-3}, akin to the original capped 85A/B.

Electrochemically, these three samples performed well when compared to the results in Chapter 3 for oxidation reactions and several redox mediators were employed. Complex electron processes were visualised for 34-0X in aqueous solution utilising the wide potential window of scBDD. The electrochemical response of pre-treated electrodes using inner sphere redox mediators was performed. Anodic potentials appearing to promote the oxidation of Fe^{2+} greater than all other samples and cathodic potentials promoting the very near reversible oxidation of $Fe(CN_6)^{3-}$.

DICM and FE-SEM did not provide any evidence of any defects for any of the three samples. AFM suggested the scaife polished 34-0X was smoother (~3 nm) than the capped samples, provided as grown. Undulating troughs were evident on capped 23-01 as a result of homoepitaxial overgrowth of the scaife polished bulk layer.

Raman microscopy demonstrated the three samples were of high diamond quality with no sp^2 carbon detected. Raman probed the semiconducting bulk layer for the capped samples (400 and 1200 nm) as seen before with 85A/B, therefore a Fano resonance was not detected. Whereas a large Fano resonance and peak attenuation was observed for the heavily doped 34-0X bulk sample, supporting the

SIMS measured [B]. Raman mapping was performed on 34-0X suggesting a homogeneous substrate.

Au NP deposition via the MECM and macro approach were performed employing 34-0X only, using a range of t_{dep} and V_{dep} selected from initial CVs. The deposited NPs were characterised using TM-AFM and FE-SEM, the images analysed using SPIP™ therefore elucidating NP distribution , heights and widths.

i-t curves using MECM did not fit either theory of the SH model for V_{dep} 0.2-0 V, however when employing -0.2 V, instantaneous nucleation was the closest fit. However when analysing FE-SEM images of said MECM Au NPs, instantaneous nucleation was dominant.

The use of a 1 mm macro electrode suggested 34-0X followed progressive nucleation theory, as V_{dep} increased, NP density increased for t_{dep} 0.5-10s. At 30 s, clusters attributed to due to Ostwald ripening reduced NP density. NP height reduced as t_{dep} increased at all V_{dep} applied.

The employment of IC-SECM to examine k^0 values for two differing redox mediators was only undertaken using 34-0X. Any differences in k^0values for the scan duration were minimal for both redox mediators supporting substrate homogeneity. k^0values were similar to those seen with 85A of a similar [B] with $FcTMA^+$ slightly faster than $Ru(NH_3)_6^{3+}$, due to the formers self-exchange mechanism.[17,18]

6.6 REFERENCES

1. E. Gheeraert, P. Gonon, A. Deneuville, L. Abello and G. Lucazeau, *Diamond and Related Materials*, 1993, **2**, 742-745.
2. D. J. Goldberg and D. W. Burmeister, *Journal of Cell Biology*, 1986, **103**, 1921-1931.
3. F. Shen, L. Hodgson, J. H. Price and K. M. Hahn, *Cytometry Part A*, 2008, **73A**, 658-666.
4. E. M. Schulson, *Journal of Materials Science*, 1977, **12**, 1071-1087.
5. J. W. Steeds, A. E. Mora, S. J. Charles, D. J. F. Evans and J. E. Butler, *Materials Chemistry and Physics*, 2003, **81**, 281-285.
6. G. Binnig, C. F. Quate and C. Gerber, *Physical Review Letters*, 1986, **56**, 930-933.
7. C. F. Quate, *Surface Science*, 1994, **299**, 980-995.
8. S. R. Sails, D. J. Gardiner, M. Bowden, J. Savage and D. Rodway, *Diamond and Related Materials*, 1996, **5**, 589-591.
9. G. Janssen, W. J. P. Vanenckevort, W. Vollenberg and L. J. Giling, *Diamond and Related Materials*, 1992, **1**, 789-800.
10. Y. V. Pleskov, Y. E. Evstefeeva, V. P. Varnin and I. G. Teremetskaya, *Russian Journal of Electrochemistry*, 2004, **40**, 886-892.
11. B. V. Spitsyn, L. L. Bouilov and B. V. Derjaguin, *Journal of Crystal Growth*, 1981, **52**, 219-226.
12. J. P. Lagrange, A. Deneuville and E. Gheeraert, *Diamond and Related Materials*, 1998, **7**, 1390-1393.
13. J. D. Porter and T. O. Robinson, *Journal of Physical Chemistry*, 1993, **97**, 6696-6709.
14. P. L. Redmond, A. J. Hallock and L. E. Brus, *Nano Letters*, 2005, **5**, 131-135.
15. P. V. Dudin, P. R. Unwin and J. V. Macpherson, *Journal of Physical Chemistry C*, 2010, **114**, 13241-13248.
16. K. McKelvey, M. A. Edwards and P. R. Unwin, *Analytical Chemistry*, 2010, **82**, 6334-6337.
17. P. J. Smolenaers and J. K. Beattie, *Inorganic Chemistry*, 1986, **25**, 2259-2262.
18. G. M. Brown and N. Sutin, *Journal of the American Chemical Society*, 1979, **101**, 883-892.

7 Conclusions

In the electrochemical arena, BDD offers a wide potential window thereby offering the detection of a wider range of analytes when compared to traditional metal electrodes. Low capacitative background currents and the absence of any redox active surface species further support the use of BDD for electroanalytical applications.

Due to comparative ease of growth, pBDD diamond is readily available and employed as an electrode material. pBDD is heterogeneous in nature, which makes determination of HET kinetics of different redox species challenging unless high spatial resolution electrochemical imaging techniques are employed. It also provides a heterogeneous surface for chemical functionalisation or derivatisation. In contrast, defect free scBDD would enable the unambiguous determination of HET rates due to its homogeneous nature, and would aid in surface modification strategies.

The aim of this thesis was to characterise unique scBDD samples grown by E6 Ltd with a view to this material being employed as an electrochemical electrode material. scBDD was grown incorporating a range of boron concentrations ($0.8 \times 10^{20} – 1.2 \times 10^{21}$ B atoms cm^{-3}) determined by SIMS. Differing single crystal orientations were provided; (100), (110) and (111) and samples subject to two different surface finishes (as grown or scaife polished by E6). A range of physical and electrochemical methods were used to characterise all samples.

The employment of qualitative DICM served to highlight subtle height differences, not observed under conventional optical microscopy. It was found that

sample HB2 (100) ([B] 1.5 × 10^{20} cm^{-3}) contained polycrystalline-like defects, incorporated throughout the sample. Both (110) samples (05A ([B] 1.1 × 10^{20} cm^{-3}) and 85F/G ([B] 0.8-1 × 10^{20} cm^{-3})) appeared bowed which was also visible to the human eye. These samples also all contained fleck-like defect features, higher in density in 85F/G most likely due to its exposure to a hydrogen plasma, during a failed second CVD growth run.

Sample CP09 ([B] 0.95 × 10^{20} cm^{-3}) was polished to a (111) orientation from an original (110) sample, however the nature of scaife polishing resulted in this sample being heterogeneous, containing both a polished (111) area and a rougher (110) zone. White light interferometery found an angle of 40° between the two crystallographic orientations in close agreement with the expected value (~35° [1,2]). Samples of (100); namely 85A/B ([B] 1.0 × 10^{21} cm^{-3}), 20-01 ([B] 6.0 × 10^{20} cm^{-3}), 23-01([B] 7.0 × 10^{20} cm^{-3}) and 34-0X ([B] 1.2 × 10^{21} cm^{-3}), all appeared homogeneous under DICM. TM-AFM was performed on all samples and surface roughness was < 6 nm for all samples, polished or as grown.

FE-SEM was employed to further probe the scBDD surface using an electron beam, samples 85A/B, 20-01, 23-01 and 23-01 did not show any surface or boron doping heterogeneities. However HB2, with the polycrystalline defect, suggested the defect contained boron at a different concentration to the surrounding non-defect area and even within the defect there were variations in boron uptake. 05A and 85F/G showed some contrast in areas where the flecks were present. CP09 due to it heterogeneous nature offered extensive contrast between the (111) and (110) areas, however this was due to the two surfaces not being coplanar.

Raman microscopy is able to distinguish between the different carbon forms thereby demonstrating sample quality, a poor BDD sample is likely to have an graphitic sp^2 signal, this would be absent on a high quality sample. As such, no sp^2 carbon was detected on any of the scBDD analysed, even on/around the polycrystalline like defect of HB2 demonstrating their exceptional quality.

Laser penetration (~1 μm) resulted in the probing of the semiconducting bulk substrates for 85A/B, 20-01 and 23-01, however some features were detected within the bulk layer of 85B during larger scale Raman mapping. The 'pyramidal hillock' shaped features were also probed using CL which further suggested their presence in the bulk layer rather than the thinner (65 nm) cap layer.

All other samples provided evidence of metal-like conductivity where [B] > ~1×10^{20} cm^{-33} due to the presence of a Fano resonance at 1332 cm^{-1}. The use of Raman mapping on HB2 including a defect area demonstrated a difference in [B] as originally shown with FE-SEM. Raman suggested the non-defect area was of a lower [B] than the defected area. Sample 05A, CP09 (highly polished (111)) and 34-0X all suggested [B] homogeneity via this method. A map incorporating the fleck like features of 85G demonstrated differences in Raman response, however this could not be used to determine differences in [B] due to surface height heterogeneities.

Electrochemistry was performed in the 1 mm macrodisc[4] format and all samples were oxygen terminated. The use of three differing outer sphere oxidation reactions at a range of positive potentials suggested all samples bar CP09 (111) behaved close to reversible with peak currents close to those predicted assuming semi-infinite linear diffusion limits the reaction (Randles Sevcik).

When employing a mediator with a reduction at negative potentials, some differences in behaviour were observed. The heavily doped samples were close to reversible for this mediator, those samples with a lower [B], close to the metal-like threshold showed more quasi reversible reactions, this was especially applicable for HB2 followed by CP09. When using the highest concentration (10 mM $Ru(NH_3)_6^{3+}$), all samples showed quasi reversible behaviour. This is likely to be due to the fact that in terms of energy, $Ru(NH_3)_6^{3+}$ lies just above the acceptor level of semiconducting BDD. Unlike a metal, BDD will therefore have a finite number of charge carriers available for charge transfer. This depletion of available charge carriers is exacerbated at high concentrations.

FEM simulations of 1 mm macrodisc electrochemistry suggested the heavily doped samples offered faster HET kinetics. When employing redox mediators with concentrations of 0.1 and 1 mM, the HET kinetics were independent between concentrations and this was observed for all samples. The 10 mM $Ru(NH_3)_6^{3+}$ HET kinetics were considerably slower for reasons already discussed, the heavily doped sample 85B again offering the fastest (but somewhat reduced) HET rates of the scBDD samples employed.

Complex electron processes, utilising the wide potential window of scBDD, demonstrated the reversible behaviour of the $Ru^{2+/3+}$ cation in $Ru(bpy)_3^{2+/3+}$ at positive potentials, close to the potential window and the irreversible behaviour of a surrounding ligand at very negative potentials. It is not possible to see such behaviour at conventional metal electrodes in aqueous solutions. This was observed for all scBDD electrodes.

Surface pre-treatment of scBDD was found to alter the electrochemical signature for inner sphere redox mediators. In particular, cathodic polarisation promoted the oxidation of $Fe(CN_6)^{3-}$ and anodic polarisation the oxidation of Fe^{2+}. This was most noticeable for the (100) samples 85B and 34-0X.

Harsh fabrication treatments (e.g. abrasive and acid cleaning) of 85B led to a poor response in redox mediators. Investigation via AFM, DICM and FE-SEM suggested the thin (65 nm) cap layer was greatly reduced (delamination) therefore exposing the original semiconducting bulk material.

Selected samples were electrochemically imaged using IC-SECM which accurately maps surface current and topography with a known tip-substrate separation. Two differing redox mediators were employed, utilising positive and negative potentials combined with a range of overpotentials. IC-SECM was seeking to challenge the [B] rather than crystal orientations, especially those of samples with lower [B]. FEM was employed and produced k^0 maps elucidating ET kinetic rates.

When employing HB2, the same defect area as Raman was imaged leading to the same conclusion, whereby the defect contained higher [B] than the surrounding area. The k^0 rates were much slower for the surrounding area, which would be expected due to its lower [B]. No other defects or features were mapped using this technique for any of the samples. Homogeneity was suggested for 85A, 34-0X and 85F. Higher k^0 values were determined for 85A and 34-0X in both mediators and given they are an order of magnitude higher in [B], this is not unexpected. Faster k^0 rates were noted for $FcTMA^+$ than $Ru(NH_3)_6^{3+}$which is related to ferrocenes higher self-exchange mechanism.[5, 6]

Functionalisation at the microscale using Au NPs with 85A (100), 85F (110) and 34-0X (100) served to highlight surface heterogeneities on 85F not observed under DICM or FE-SEM. Analysis of Au NPs using TM-AFM and FE-SEM demonstrated in certain areas of 85F, regardless of deposition potential/time higher densities of smaller NPs. 85A and 34-0X both offered a random homogeneous distribution of particles which varies in size dependent on deposition potential and time scales used and were analysed using TM-AFM and FE-SEM. The use of AFM and FE-SEM suggested differing nucleation theories when plotted against the SH model of either instantaneous or progressive for 85A. 34-0X when analysed with FE-SEM suggested instantaneous nucleation was prevalent.

The onset of deposition was at a more positive potential for 34-0X and the most negative potential for 85F with 85A in-between. The difference between 85A, 85F and 34-0X is surface finish, 85A and 85F are as grown and 34-0X scaife polished which may have been a contributing factor. The range of kinetic processes during deposition on 85F led to a wider peak.

34-0X was further functionalised in the 1 mm macrodisc format and AFM suggested progressive nucleation in contrast to the micro scale results of instantaneous. At longer depositions (30s), Ostwald ripening was considered the most likely factor leading to a decrease in NP density.

The physical and electrochemical characterisation employed has suggested that capped layer scBDD samples are not as robust as bulk scBDD. High quality, heavily doped scBDD material can be consistently grown by E6 and sample 34-0X (100) has proven itself to be of the most desirable homogeneous electrode material.

7.1 REFERENCES

1. J. K. Barton, A. A. Vertegel, E. W. Bohannan and J. A. Switzer, *Chemistry of Materials*, 2001, **13**, 952-959.
2. T. W. Mercer, J. N. Russell Jr and P. E. Pehrsson, *Surface Science*, 1997, **392**, L21-L26.
3. J. P. Lagrange, A. Deneuville and E. Gheeraert, *Diamond and Related Materials*, 1998, **7**, 1390-1393.
4. L. Hutton, M. E. Newton, P. R. Unwin and J. V. Macpherson, *Analytical Chemistry*, 2009, **81**, 1023-1032.
5. P. J. Smolenaers and J. K. Beattie, *Inorganic Chemistry*, 1986, **25**, 2259-2262.
6. G. M. Brown and N. Sutin, *Journal of the American Chemical Society*, 1979, **101**, 883-892.